Sonodynamic Therapy of Hypoxic Tumours

Estelle Françoise Rosanne Béguin

Wolfson College

University of Oxford

A thesis submitted for the degree of Doctor of Philosophy

Supervised by Professor Eleanor Stride

Michaelmas 2018

To my family.

Abstract

Improvements in cancer therapies have enabled a steady increase in the five-year survival rates of patients with most tumour types. Yet, some highly aggressive tumours still present resistance to conventional cancer therapies. One of the explanations for this has been ascribed to the low levels of oxygen seen in the tumours' vicinity. In this manuscript, the development of sonodynamic therapy to enable the treatment of hypoxic pancreatic tumours is presented. With this technique, low intensity ultrasound is used to activate oxygen-loaded microbubbles in order to provide oxygen in hypoxic lesions and enable their treatment using an ultrasound-responsive drug: Rose Bengal.

An investigation on mechanisms demonstrated that light generated from collapsing microbubbles allows the activation of Rose Bengal during ultrasound exposure. Several acoustic parameters were also evaluated to understand their impact on treatment. To enhance the delivery of oxygen and the sonodynamic effect, magnetic targeting of microbubbles was enabled by incorporating iron oxide nanoparticles within their coating. Thus, an external magnetic field focused at the tumour can be used to target this therapy. A structural analysis of microbubbles as drug and oxygen carrier was then undertaken to optimise the system's stability and performance. An evaluation of this method in preclinical *in vivo* experiments demonstrated that magnetically targeted sonodynamic therapy with oxygen microbubbles and Rose Bengal enabled a decrease in size of hypoxic pancreatic tumours in a murine model. Therefore, this thesis presents promising results for the treatment of hypoxic tumours using sonodynamic therapy, as well as key mechanistic and parametric results to enable the further optimisation of this method for clinical use.

Statement of originality

I hereby declare that this submission is my own work and to the best of my knowledge it contains no materials previously published or written by another person, or substantial proportions of work which have been accepted for the award of any other degree or diploma at the University of Oxford or any other educational institution, except where due acknowledgements is made in the thesis.

Any contribution made to the research by others, with whom I have worked at the University of Oxford or elsewhere is explicitly acknowledged in this manuscript.

I also declare that the intellectual content of this thesis is the product of my own work, except to the extent that assistance from others in the project's design and conception or in style, presentation and linguistic expression is acknowledged.

Estelle F. R. Béguin

December 2018

Acknowledgements

First and foremost, it has been a privilege to work under the supervision of Professor Eleanor Stride. I am truly grateful for your exceptional support and dedication to biomedical research which were a constant source of inspiration throughout my graduate studies.

I would also like to thank the past and present BUBBL members who contributed to the work that became this thesis. Especially, to Dr. Michael Gray and Magda Abbas thanks for answering my endless ultrasound related questions. To Dr. Shamit Shrivastava for your enthusiasm during the Langmuir trough and sonoluminescence experiments. To Dr. Luca Bau for your curiosity and constant will to help. To James Fisk and David Salisbury for enabling me to produce these results by building many of the set-ups presented in this dissertation. To Dr. Richard Browning for your patience when showing me how to bubble and your sense of humour. To Dr. Christophoros Mannaris for helping me see real bubbles with ultrasound, and to Dr. Lester Barnsley for answering all my magnetism related questions. I am greatly indebted for all the help you provided.

I would also like to extend my appreciation to my collaborators from the University of Ulster: Dr. Yingjie Sheng, Dr. Heather Nesbitt, Keiran Logan, Professor John Callan, and Professor Anthony McHale, for your commitment to sonodynamic therapy and from the University of Belarus: Professor Nikolai Dezhkunov for your enthusiasm at finding light amongst bubbles. I would also like to acknowledge the Research Councils UK, Digital Economy Programme grant number EP/G036861/1 (Oxford Centre for Doctoral Training in Healthcare Innovation) for supporting this work financially.

I also extend my sincere gratitude for the support and inspiration from past academic and industry mentors, who together have instilled my motivation to pursue this doctorate degree. At Northeastern University, Professor Hicham Fenniri for your support and the time you dedicated to our conversations, Professor Shashi Murthy, Dr. Adedayo Adeniran-Catlett, and Professor Elizabeth Podlaha-Murphy for introducing me to academic research. My past co-op mentors: Dr. Nick Dunwoody and Dr. Snehal Kedkar for showing me the value of diligence in analytical chemistry; Henrique Rodrigues and Phani Sukhavasi for introducing me to manufacturing engineering; and Greg Troiano, Jagannath Dey and the former particle manufacturing team at BIND therapeutics for your dedication to improve drug delivery. Your combined mentoring was tremendous and made the scientist I am today.

I would also like thank my friends at BUBBL and from the centre of doctoral training in healthcare innovation, for making every day at the IBME so enjoyable. To my Wolfson family for keeping me sane over the past four years, in particular Jack Tan, Paige Mustain, Aileen Tse, Crystal Chan, and Nawamin Pinpathomrat. To the members of the Wolfson College Boat Club for making me achieve always more than I thought I could. Your friendships have been such an important part of my life in Oxford.

Finally, I am also forever grateful for the unfailing patience, encouragement and support from my partner Christian Vaas. For my family and your unceased support and love. Papa, Maman, Michel, words cannot express the depth of my gratitude for your cheers over the past few years and this thesis is dedicated to you always reminding me of the big picture beyond it all.

Dissemination

Peer-reviewed journal publications

E. Beguin, E. Stride, An investigation of ultrasound parameters for sonodynamic therapy with oxygen microbubbles and Rose Bengal. *In preparation*

E. Beguin*, M.D. Gray*, K.A. Logan*, H. Nesbitt, Y. Sheng, S. Kamila, L.C. Barnsley, A.P. McHale, J.F. Callan, E. Stride, Delivery of magnetic microbubble mediated sonodynamic therapy using a combined magnetic-acoustic device, J. Control. Release. (2019). *In review. * first co-authors.*

E. Beguin, S. Shrivastava, N. V. Dezhkunov, A.P. McHale, J.F. Callan, E. Stride, Direct evidence of multi-bubble sonoluminescence using therapeutic ultrasound and microbubbles, ACS Appl. Mater. Interfaces. (2019). *In review*

E. Beguin, L. Bau, S. Shrivastava, E. Stride, Comparing strategies for magnetic functionalisation of microbubbles, ACS Appl. Mater. Interfaces. 11 (2018) 1829–1840. DOI: 10.1021/acsami.8b18418

J. Owen, S. Kamila, S. Shrivastava, D. Carugo, J. Bernadino de la Serna, C. Mannaris, V. Pereno, R. Browning, **E. Beguin**, A.P. McHale, J.F. Callan, E. Stride, The Role of PEG-40-stearate in the production, morphology and stability of microbubbles, Langmuir. (2018). DOI: 10.1021/acs.langmuir.8b02516

H. Nesbitt, Y. Sheng, S. Kamila, K. Logan, K. Thomas, B. Callan, M.A. Taylor, M. Love, D. O'Rourke, P. Kelly, **E. Beguin**, E. Stride, A.P. McHale, J.F. Callan, Gemcitabine loaded microbubbles for targeted chemo-sonodynamic therapy of pancreatic cancer, J. Control. Release. 279 (2018) 8–16. DOI: 10.1016/j.jconrel.2018.04.018

L.C. Barnsley, M.D. Gray, **E. Beguin**, D. Carugo, E. Stride, A Combined Magnetic-Acoustic Device for Simultaneous, Coaligned Application of Magnetic and Ultrasonic Fields, Adv. Mater. Technol. 3 (2018) 1800081. DOI: 10.1002/admt.201800081

Y. Sheng*, **E. Beguin***, H. Nesbitt, S. Kamila, J. Owen, L.C. Barnsley, B. Callan, C. O'Kane, N. Nomikou, R. Hamoudi, M.A. Taylor, M. Love, P. Kelly, D. O'Rourke, E. Stride, A.P. McHale, J.F. Callan, Magnetically responsive microbubbles as delivery vehicles for targeted sonodynamic and antimetabolite therapy of pancreatic cancer, J. Control. Release. 262 (2017) 192–200. DOI: 10.1016/j.jconrel.2017.07.040 ** first co-authors*

J. Owen, C. Crake, J.Y. Lee, D. Carugo, **E. Beguin**, A.A. Khrapitchev, R.J. Browning, N. Sibson, E. Stride, A versatile method for the preparation of particle-loaded microbubbles for multimodality imaging and targeted drug delivery, Drug Deliv. Transl. Res. (2017). DOI: 10.1007/s13346-017-0366-7

Conferences

M. Gray, **E. Beguin**, E.P. Stride, H. Nesbitt, K. Logan, S. Kamila, A. McHale, J. Callan, L. Barnsley, Prototypical madness: Design and demonstration of a magnetic-acoustic

targeted drug delivery system, J. Acoust. Soc. Am., Acoustical Society of America, November 2018: pp. 1824–1824. doi:10.1121/1.5068042.

E. Beguin, F. Foglietta, J.F. Callan, A. McHale, E. Stride, N. V Dezhkunov, Investigation of sonoluminescence generated in suspensions of microbubbles, Poster presented at: 16th Meet. Eur. Soc. Sonochemistry, 2018.

E. Beguin, J. Owen, H. Nesbitt, A.P. McHale, J.F. Callan, E. Stride, Magnetic Oxygen Microbubbles for the Targeted Treatment of Hypoxic Tumours using Ultrasound. Poster presented at: STEM for Britain: Engineering exhibition, House of Parliament, London, March 2018.

E. Beguin, L. Bau, S. Shrivastava, H. Nesbitt, A. Mchale, J.F. Callan, E. Stride, Interplay between functionalising and stabilising lipid microbubbles for magnetic targeting, Poster presented at: 23rd Eur. Symp. Ultrasound Contrast Imaging, Rotterdam, January 2018: pp. 108-110. *Best poster prize awarded in the category: New Direction I*

E. Beguin, E. Stride, Sonodynamic therapy of hypoxic tumours. Poster presented at the Inaugural Symposium of the EPSRC/Jeol Centre of Liquid Phase Electron Microscopy, UCL, London, July 2017.

E. Beguin, J. Owen, Y. Sheng, H. Nesbitt, C. McEwan, L. Barnsley, M. Borden, A. McHale, J. Callan, E. Stride, Oxygen Loaded Microbubbles for Sonodynamic Therapy. 22nd Eur. Symp. Ultrasound Contrast Imaging, Rotterdam, January 2017: pp. 20-22.

E. Beguin, L. Bau, Y. Yildiz, J. Owen, P. Rademeyer, R. Browning, J.F. Callan, A.P. McHale, E. Stride, Investigation of Sonodynamic Therapy Mechanisms with Oxygen Loaded Microbubbles. Poster presented at: 22nd Eur. Symp. Ultrasound Contrast Imaging, Rotterdam, January 2017: pp. 93.

Table of contents

List of figures

List of tables

List of abbreviations

·H	Hydrogen atom
·OH	Hydroxyl radical
1mL/2minO_2	1 mL of SF_6MBs sparged with oxygen for 2 minutes
$^1O_2$	Singlet oxygen
5-FU	5-Fluouracil
5mL/2minO_2	5 mL of SF_6MBs sparged with oxygen for 2 minutes
Biotin-RB-Gem	Rose Bengal and Gemcitabine drugs linked to one biotin moiety
DBPC	1,2-dibehenoyl-sn-glycero-3-phosphocholine
DC	Duty cycle
Direct O_2MB	Lipid-coated microbubbles produced under oxygen gas flow
DPBF	1,3-diphenylisobenzofuran
DPPC	1,2-dipalmitoyl-sn-glycero-3-phosphocholine
DSPC	1,2-distearoyl-sn-glycero-3-phosphocholine
f	frequency
FFT	Fast Fourier transform
Gem	Gemcitabine
H_2O_2	Hydrogen peroxide
HIF	Hypoxia-inducible factor
IONP	Iron oxide nanoparticles
LipMB	Phospholipid microbubbles loaded with phospholipid-stabilised IONPs with hydrophobic cores
LipMB- DBPC	Phospholipid microbubbles loaded with 1,2-dibehenoyl-sn-glycero-3-phosphocholine stabilised IONPs with hydrophobic cores
LipMB- LαPC	Phospholipid microbubbles loaded with L-α-phosphatidylcholine stabilised IONPs with hydrophobic cores
LαPC	L-α-phosphatidylcholine
MAD	Magnetic acoustic device
MB	Microbubble
MBSL	Multi-bubble sonoluminescence
MI	Mechanical index
MMB	Magnetic microbubble
NA	Numerical aperture
$O_2^{\cdot -}$	Superoxide anion
O_2MB	Oxygen-loaded microbubble
O_2MB-RB	Oxygen microbubble loaded with Rose Bengal
O_2SV	Sonovue® microbubbles reconstituted with oxygen
OilMB	Phospholipid microbubbles loaded with hydrophobic IONPs in an oil phase

PBS	Dulbecco's phosphate buffered saline
PCD	Passive cavitation detector
PDT	Photodynamic therapy
PEG40S	Polyoxyethylene (40) stearate
PFB	Perfluorobutane
PFC	Perfluorocarbon
PMT	Photomultiplier tube
PMT(filt)	PMT used with optical filters
PMT(full)	PMT used without optical filters
PPG	PBS:propylene glycol:glycerol solution (8:1:1, v:v:v)
PRF	Pulse repetition frequency
RB	Rose Bengal (4,5,6,7-tetrachloro-2',4',5',7'-tetraiodofluorescein)
ROI	Region of interest
ROS	Reactive oxygen species
SBSL	Single-bubble sonoluminescence
SDT	Sonodynamic therapy
SF_6MB	Sulphur hexafluoride-loaded microbubble
SL	Sonoluminescence
SOD	Superoxide dismutase
SOSG	Singlet oxygen sensor green
Sparged O_2MB	Lipid-coated microbubbles produced under sulphur hexafluoride gas flow, then subsequently sparged with oxygen gas
SurfMB	Phospholipid microbubbles loaded with surface-bound hydrophilic IONPs
TEM	Transmission electron microscopy
US	Ultrasound
UV	Ultraviolet
WSR	Wall shear rate
WSS	Wall shear stress

Chapter 1
Introduction

This chapter introduces the field of sonodynamic therapy and the key challenges motivating the work described in this thesis. The research objectives are defined, and a thesis outline is presented.

Contents

1.1. An introduction to sonodynamic therapy

Sonodynamic therapy emerged in 1989 with the findings of Yumita *et al.* on the cytotoxic effects of porphyrin sensitisers when exposed to ultrasound [1]. By combining ultrasound, a sensitising drug and molecular oxygen, this therapy enables the local production of cytotoxic reactive oxygen species. Since then, this approach has been increasingly researched to optimise the cytotoxic effects of sensitisers during ultrasound exposure, and has been evaluated for a range of indications such as cancer [2] and atherosclerosis [3]. Because the reactive oxygen species are confined to the region of the ultrasound focus, sonodynamic therapy offers a means of delivering a highly localised therapy and a much lower risk of harmful side effects compared to conventional cancer treatments [4,5]. This method is similar to the more established, photodynamic therapy, which is currently approved for the treatment of skin and oesophageal cancers using light as an external trigger [4,5]. Ultrasound offers, however, significantly greater penetration depths in tissue than light (< 150 mm vs. < 5 mm), tighter focusing and hence the potential for treating a wider range of disease sites.

1.1.1. Enhancement of sonodynamic therapy with microbubbles

Focusing on the treatment of cancer, one significant drawback to both photo- and sonodynamic therapies is the hypoxic nature of many solid tumours. Hypoxia inhibits the majority of current cancer therapies and favours malignant progression [6]. It is particularly problematic in the case of photo- and sonodynamic therapies since molecular oxygen is necessary to generate reactive oxygen species. Previous studies on sonodynamic therapy have demonstrated the advantage that can be gained from

delivering oxygen microbubbles in addition to a sensitising drug to counteract the hypoxic microenvironment within tumours [4]. This synergistic effect is the focus of this thesis.

1.1.2. Current challenges

While preclinical studies combining the use of oxygen microbubbles and sonodynamic therapy have presented promising results for the treatment of hypoxic tumours in murine (mouse and rat) models, these studies have required the intratumoural injection of the therapy due to the low stability of these microbubbles in the bloodstream [4]. Additionally, a weak understanding of the mechanism for the activation of the sensitiser and hence the optimal ultrasound exposure conditions have hindered the optimisation of this therapy and its translation into the clinic.

1.2. An overview of the thesis

1.2.1. Aims of the research

The aims of this thesis are to address these challenges by providing (1) a review of the current work on sonodynamic therapy, (2) a formulation for microbubbles with improved stability and potential for targeting via magnetic functionalisation, (3) an investigation of the mechanism underlying the activation of the sensitiser Rose Bengal during ultrasound exposure, (4) an evaluation of oxygen loading protocols to produce oxygen microbubbles, (5) the influence of ultrasound exposure conditions on sonodynamic therapy, and finally (6) a characterisation of this approach *in vitro* and *in vivo* in mice bearing hypoxic tumours.

1.2.2. Outline of the thesis

To address the research aims, this document is divided into 7 chapters. Chapter 2 provides a review of the literature on sonodynamic therapy and highlights the challenges associated with this technique for the treatment of hypoxic lesions. The advances made to date to address them are also discussed.

Chapter 3 presents an *in vitro* comparison between several magnetic microbubble formulations. The incorporation of different iron oxide nanoparticles is assessed for its effects on microbubble stability, acoustic response and magnetic targeting efficiency.

Chapter 4 provides an investigation and discussion of the potential mechanisms involved in the activation of Rose Bengal during ultrasound exposure.

Chapter 5 presents a study on the effects of different acoustic parameters for the generation of cytotoxic singlet oxygen from Rose Bengal during sonodynamic therapy in degassed solutions enhanced with oxygen microbubbles.

In Chapter 6, a novel device allowing the simultaneous and co-aligned application of both magnetic and acoustic fields was tested to enhance the sonodynamic effects with magnetically-responsive microbubbles loaded with oxygen and Rose Bengal. The *in vitro* and *in vivo* results are presented, and their implications for the clinical translation of this method are discussed.

Finally, concluding remarks and an outline of the recommended future investigations are provided in Chapter 7.

Chapter 2
A review of the literature

This chapter presents a review of current sensitisers, ultrasound parameters, and indications related to sonodynamic therapy, and a discussion of the mechanisms hypothesised to explain the production of reactive oxygen species with this method. Therapies developed for hypoxic tumours are then reviewed including recent approaches for overcoming this condition. Finally, the use of microbubbles for drug delivery and their use to enhance sonodynamic therapy are evaluated.

Sections of this review have been published in alternate forms in the publications listed in the Dissemination of this thesis.

Contents

2.1. Sonodynamic therapy

Sonodynamic therapy (SDT) uses ultrasound (US) to activate specialised drug molecules (sensitisers) to produce reactive oxygen species (ROS) in the proximity of a region of interest. It is closely related to photodynamic therapy (PDT), but PDT targets are limited by the low penetration depth of light in tissue. Ultrasound, on the other hand, can be focused to treat tumours at tissue depths of up to 10 cm. This gives sonodynamic therapy a significant advantage over PDT.

The initial findings of sensitiser activation using ultrasound were presented by Yumita *et al.* in 1989, and the term "sonodynamic treatment" was established a year later to describe this method [1,7]. Since then, sonodynamic therapy has been increasingly researched to optimise the cytotoxic effects of the sensitiser during ultrasound exposure. Several reviews have compiled lists of sensitisers, ultrasound parameters, and indications targeted with this technique [8–10]. An updated survey focusing on studies with *in vivo* results is provided in **Appendix Table A.1**. This section reviews the current progress of sonodynamic therapy and the remaining challenges facing its clinical translation.

2.1.1. Current status

As shown in **Appendix Table A.1**, a range of sensitisers has been investigated in preclinical *in vivo* models to determine their potential for therapy. Several sensitisers have shown promising *in vitro* results such as porphyrin [11], xanthene derivatives [12], and some natural products such as ginger root extract [13], and chemotherapy drugs [14]. To minimise undesired side-effects, the use of locally activated sensitisers that are otherwise non-toxic is, however, preferable. Porphyrin derivatives are the most studied sensitiser due to their wide use in photodynamic therapy and their good sonodynamic generation

of cytotoxic radicals. Their hydrophobic nature, however, leads to undesirably long clearance times because of accumulation in peripheral tissues in addition to the tumour site [15]. Nonetheless, their safety has been investigated intravenously and orally in human trials of PDT [16,17], and intravenously in sonodynamic therapy trials focusing on atherosclerosis [18].

Rose Bengal (RB), a xanthene based sensitiser, has been shown to generate reactive oxygen species more effectively upon ultrasound exposure compared to protoporphyrin IX *in vitro* [2]. Further, preclinical studies have shown that it undergoes rapid clearance *in vivo* [19–23]. Recent human trials have, however, only looked at Rose Bengal toxicity with intralesional injections for photodynamic therapy; although, it has been previously approved as a contrast agent for ocular diagnostics [24,25]. Promising results have recently been obtained with Rose Bengal in mice bearing hypoxic pancreatic tumours, and it was therefore chosen as the sensitiser for the work presented in this manuscript [4,12].

The ultrasound parameters used for sonodynamic therapy preclinical studies have been typically in the range of low-intensity therapeutic ultrasound with: 1-3 MHz frequency, 0.5-5 W/cm^2 intensity, 10-100% duty cycle, and 2-15 minutes exposure time. The choice of frequency represents a necessary compromise between the treatment depth and focal volume achieved, while the other parameters allow a trade-off between tissue heating and the treatment time. These criteria have not yet been thoroughly investigated and are further discussed in Chapter 5 for the optimisation of the treatment regimen. First though, a key challenge is to understand the working mechanism for the activation of the sensitiser during sonodynamic therapy. The previous work on this subject is reviewed in the following section.

2.1.2. Activation mechanisms

Sonodynamic therapy relies on the propagation of sound waves, through an aqueous medium, producing fluctuations in density and pressure. Under appropriate conditions, this process can trigger the activation of nucleation sites from which gas and/or vapour filled bubbles can grow, oscillate and potentially collapse. This process is known as cavitation [26]. During bubble oscillation and collapse, extremely high internal temperatures and pressures can be produced due to rapid compression. Although a consensus has yet to be reached as to which process or processes causes the activation of sensitisers during sonodynamic therapy, there is strong evidence that cavitation is involved. Sonoluminescence [7,27] and pyrolysis [28] are two main mechanisms that have been proposed to explain the activation of sensitisers also known to be photosensitive, such as Rose Bengal.

2.1.2.1. Sonoluminescence

First reported in 1933 by Marinesco and Trillat [29], sonoluminescence (SL) refers to the generation of light from a liquid solution exposed to ultrasound as the results of acoustic cavitation events [30–34]. Although black-body, bremsstrahlung, and/or recombination radiations (**Figure 2.1**) have all been reported in subsequent studies as explanations for the origin of the light generated [5,35–39], this process remains a subject of controversy amongst researchers. A consensus was at least drawn in 1990 that the light emission was of thermal origin [30], refuting the theories on electrical discharge [40]. This was mainly supported by results indicating that photons were generated during the compression phase of bubble collapse instead of during the expansion, necessary in the case of electrical discharge [30].

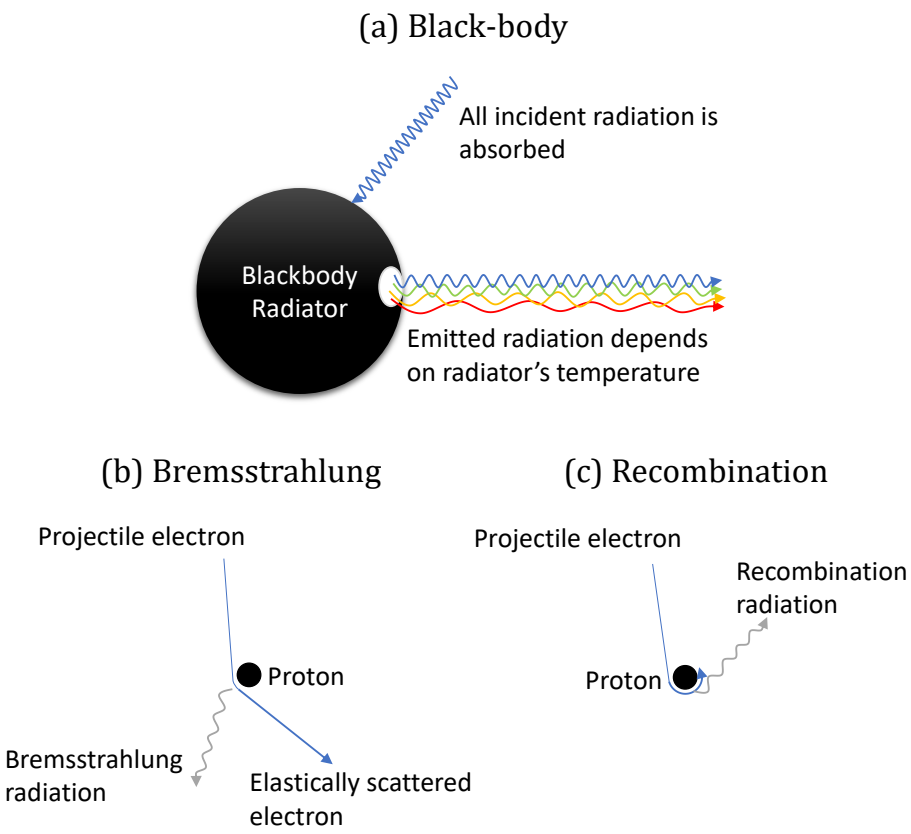

Figure 2.1. *Schematic depicting* ***(a)*** *black-body,* ***(b)*** *bremsstrahlung, and* ***(c)*** *recombination radiation processes.*

Single bubble sonoluminescence (SBSL) has been associated with a featureless optical emission spectrum and the conditions in the interior of the bubble during collapse are, in theory, more extreme than during multi-bubble sonoluminescence (MBSL) [35–38]. The spherically symmetric adiabatic collapse of a single bubble enables the partial ionization of gas molecules which can produce black-body [41], bremsstrahlung [42], and/or recombination radiations [43] (**Figure 2.1**). The intensity of light emission has also been shown to vary with the type of gas molecules inside the collapsing bubbles. For instance, Hiller *et al.* reported that the incorporation of at least 1% noble gas in nitrogen bubbles stabilised the oscillations of a trapped single bubble and significantly increased the amount of light it produced [44]. In contrast to SBSL, the optical emission spectrum from MBSL reflects features of chemical species in their excited-state in solution as indicated

by the results of Matula *et al.* in **Figure 2.2** [33]. This was associated to the thermal dissociation and recombination of molecules during cavitation events [30,38,45]. MBSL has consequently been described as a form of chemiluminescence, similar to flame emissions [38]. The marked differences between the optical spectrum of SBSL with a broad continuum and that of MBSL with features of excited-state species has been explained in terms of the temperatures generated inside the bubble [33,37,46]. The more spherically symmetric the bubble collapse, the higher the compression and the temperature reached. A single bubble in a large volume of liquid is more likely to undergo a spherical collapse than one surrounded by other bubbles, due to the perturbing influence of bubble-bubble interactions [46,47]. Thus, SBSL only occurs under well controlled experimental conditions that are unlikely to be met during sonodynamic therapy, indicating that MBSL is more likely to be responsible for activation of sensitisers by ultrasound.

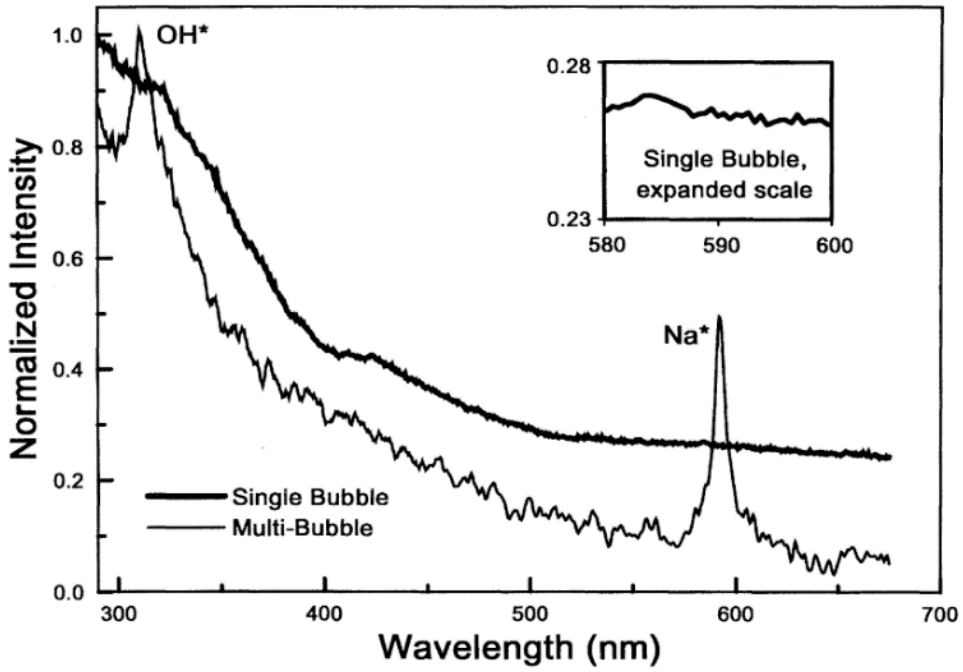

Figure 2.2. *Comparison of single- and multi-bubble sonoluminescence as reported by Matula et al. for a 0.1 M sodium chloride solution insonated with 32 kHz ultrasound [33]*

The majority of reports on sonoluminescence have been based on experiments conducted at low frequency ultrasound (20-200 kHz). A few studies, however, have examined sonoluminescence at higher frequencies (0.7 – 1.2 MHz) relevant to therapeutic ultrasound. Srinivasan *et al.* in 1961 used 0.8 MHz ultrasound and reported a broad sonoluminescence spectrum centred at 310 nm [48], which was associated with the presence of hydroxyl radical formation [49]. Pickworth *et al.* in 1988 with 1 MHz ultrasound identified that sonoluminescence increased with increasing temperature [50]. These results contradicted those of other studies conducted at lower frequencies [51], but it was argued that this was due to the decrease in cavitation threshold at higher temperature [50]. An even smaller number of studies has examined the role of sonoluminescence in the activation of sonodynamic therapy sensitisers. Both Umemura *et al.* in 1990 and more recently Giuntini *et al.* investigated this at 2 MHz. They reported continuous sonoluminescence spectra with a broad peak at approximately 450 nm, and the appearance of an absorption band once a sensitiser was added which corresponded to the absorption of the drug (**Figure 2.3**) [7,27]. Further tests on the sensitisers indicated the production of singlet oxygen after ultrasound exposure confirming their activation. However, a lack of cavitation monitoring during these experiments prevented the demonstration of a direct relationship between bubble dynamics and sensitiser activation. There were also several key differences between the experimental conditions and those relevant to sonodynamic therapy, for example bubbling argon through the solution in order to promote sonoluminescence events [27].

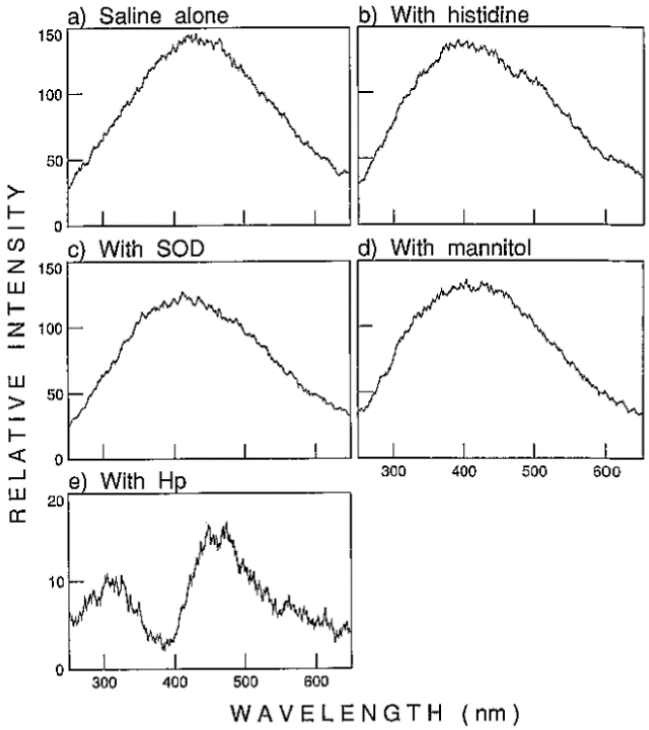

Figure 2.3. *MBSL spectrum reported by Umemura et al. in 1990 for air-saturated saline solution* ***(a)*** *without additive, with ROS scavengers:* ***(b)*** *histidine,* ***(c)*** *superoxide dismutase (SOD), and* ***(d)*** *mannitol, and sensitiser:* ***(e)*** *hematoporphyrin exposed to 2 MHz ultrasound [7].*

2.1.2.2. Pyrolysis

The explanation of sensitiser activation through pyrolysis is also related to very high temperatures and pressures generated at the centre of collapsing bubbles [52,53]. As thermal diffusion is not sufficient to dissipate the heat generated from acoustic cavitation, this process leads to the formation of localized hot spots at the core of a collapsing bubble and the thermal dissociation of molecules generating reactive species [28,54]. It has been proposed that the short-lived radicals generated from the splitting of water vapour such as hydroxyl radicals (·OH) and hydrogen atoms (·H) could react with the drug to generate sensitiser-derived free radicals with longer lifetimes [28]. This enables them to travel further and react with critical cellular sites [54], while hydroxyl radicals and hydrogen atoms generated from water pyrolysis are more rapidly quenched [28,55,56]. Pyrolysis of

the sensitiser itself has also been proposed, enabling the formation of radical intermediates derived from the sensitiser which then react with dissolved oxygen to then form longer-lived peroxyl or alkoxyl radicals [28,54].

The experiments conducted to support the pyrolysis theory as a mechanism for sonodynamic therapy have, however, all been conducted at low ultrasound frequencies (50 kHz). In this regime, the degradation of dye molecules can be expected [57–60], and to the best of the author's knowledge no studies have demonstrated this theory using the frequencies at which sonodynamic therapy has been shown to be effective (i.e. 1-3 MHz). Nevertheless, Kim *et al.* reported interesting results using an optically inert Rose Bengal derivative combined with focused ultrasound, supporting the theory that cytotoxicity from sonodynamic therapy might be independent from sonoluminescence activity [61]. This highlights the need to further examine whether pyrolysis of the sensitisers occurs at higher frequencies and hence could play a role in this therapy.

2.1.3. Bioeffects of reactive oxygen species

ROS are reactive species and radicals with oxidative power derived from molecular oxygen [62]. In aerobic organisms, these are naturally generated through the partial reduction of oxygen into radical or non-radical oxygen species, such as superoxide anion ($O_2^{\cdot -}$), hydroperoxyl radical (HO_2, protonated superoxide), hydrogen peroxide (H_2O_2), and hydroxyl radical ($HO^{\cdot}$) [62]. However, ROS can cause oxidative stress and induce cytotoxicity in surrounding cells when limited amounts of antioxidants are present, an effect that can be used advantageously when aiming to treat cancer cells [63]. In a review focusing on the impact of ROS on cancer, Gupta *et al*. highlighted the paradoxical relationship between reactive oxygen species and the signalling pathways related to

tumour promotion or suppression [64]. In effect, intracellular ROS appears to be a critical factor affecting the expression of proteins related to tumour cell survival, proliferation, and growth. Nonetheless, reactive oxygen species were also found to affect the expression of tumour suppressor genes [64]. These contrasting effects are important considerations when developing a therapy based on the local production of ROS as they could potentially affect the treatment outcome negatively.

Rose Bengal is known to have a high quantum yield for its triplet excited state, which can then be quenched by ground state molecular oxygen to produce a high yield in singlet oxygen ($^1O_2$) as depicted in **Figure 2.4** [65,66].

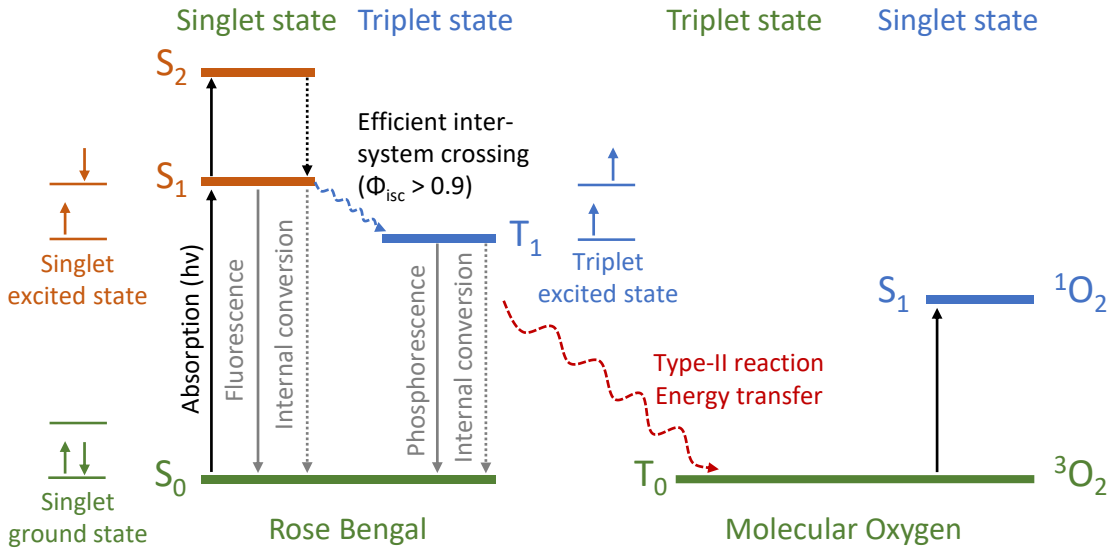

Figure 2.4. *Schematic of energy transfer from the photo-excitation of Rose Bengal to the production of singlet oxygen through the Type-II reaction pathway.*

With an upper limit lifetime of 500 ns, singlet oxygen is rapidly quenched by surrounding biomolecules [67]. Although intracellular singlet oxygen can provoke DNA based oxidative stress and single strand break, it is unlikely that during sonodynamic therapy this reactive species will reach the nucleus as it will first oxidise extracellular lipids membranes [68]. However, through lipid peroxidation additional radicals with longer lifetimes can be

produced that can act on other cellular components [69,70]. An increased reactive oxygen species production during sonodynamic therapy can therefore result in programmed cell death mechanisms such as apoptosis and/or necrosis [64,71–73].

Apoptosis is a protective biological process relying on signalling pathways activated in damaged or severely mutated cells to prevent the further passage of abnormal mutations to subsequent generations. For instance, abnormal intracellular concentrations of calcium ions or reactive oxygen species, activation of BAX proteins, and the production of ceramides have all been found to trigger apoptotic pathways [74–77]. Nofiele *et al.* used cell ceramide content to assess cell survival after ultrasound exposure with microbubbles (MB) [78]. Through histology and immunohistochemistry using anti-ceramide anti-body stained cells, ceramide accumulation was found in endothelial, leukaemia, breast, prostate cancer, and murine fibrosarcoma cells after exposure [78]. Additional biological features for ultrasound-induced apoptosis have been identified, including disturbances in the mitochondrial transmembrane potential, loss of phosphatidylserine asymmetry, morphological changes such as membrane damage, and eventual DNA fragmentation. The mitochondria-caspase pathway was found to be especially important for this process through an increased mitochondrial oxidative stress causing the release of cytochrome C and subsequent caspase activation ultimately leading to cell death [74,77,79–81].

In contrast, necrosis is a more acute event involving the loss of cell membrane integrity and debris expulsion in the extracellular space. This process has also been reported in several sonodynamic therapy studies [11,82] and could be exploited to induce an inflammatory immune response and help tumour cell eradication.

Autophagy which involves the digestion and recycling of cell components is another process that can result in cell death [83] and has been observed during the sonodynamic treatment of mouse sarcoma 180 and human leukaemia K562 cells [84,85]. Nonetheless, the addition of autophagy inhibitors was found to promote sonodynamically-induced apoptosis and necrosis indicating that autophagy might also provide cytoprotection allowing cells to recover from treatment during these experiments [84,85].

As the population of reactive species generated during sonodynamic therapy differs depending on the sensitiser used and cells treated, it is likely that multiple cell-death mechanisms are involved. For example, although increased levels of caspase activity and BAX (Bcl-2-associated X) protein indicating cellular apoptosis have been observed within pancreatic tumours receiving sonodynamic therapy with Rose Bengal [86], it is possible that necrosis and autophagy are also involved.

2.1.4. Challenges

There is encouraging evidence for the potential of sonodynamic therapy in the treatment of cancer. Its clinical translation, however, depends upon a more thorough mechanistic understanding of the approach and characterisation of the sensitiser to ensure its safety. As a range of ultrasound parameters, sensitisers and indications have been investigated, it is important to focus the research efforts on an application that would showcase the potential of this approach compared to current treatment gold-standards. In addition, although the ultrasound intensities used are low compared with other therapeutic applications, the incorporation of some form of *in situ* treatment monitoring would be beneficial to improve both efficacy and safety.

2.2. Hypoxic tumours

In medicine, the term hypoxia is used to describe an environment of low oxygen tension [63,87,88]. In these regions, oxygen demand from cells is greater than the supply provided by the vasculature, which generally leads to cell signalling inducing angiogenesis and erythropoiesis as adaptive responses [63]. Hypoxia has then been found to be a critical factor for prognostic estimation in the context of tumour growth, as it is plays a role in both malignant progression, and resistance to therapy [87,88]. Considering the requirement of sonodynamic therapy for ground state molecular oxygen to produce cytotoxic reactive species, this condition is also expected to hinder the efficacy of this method. Tumour hypoxia is known to be caused by the disturbed diffusivity of the surrounding microcirculations, presenting an increased resistance and reduced structural and functional characteristics. In this section an overview is provided of biological considerations important for oxygen transport in the blood and hypoxic tumours as well as remediation techniques developed for this condition.

2.2.1. Biological considerations

2.2.1.1. Oxygen transport in the blood

Blood is composed of mainly water, proteins, and three cell populations: erythrocytes, leukocytes, and thrombocytes, and allows the dissolution of electrolytes, nutrients, vitamins, and gases necessary for the functioning of organs. The biconcave disk shape of erythrocytes provides the high surface area to volume ratio advantageous for the exchanges of oxygen and carbon dioxide in the lung and the peripheral tissues [89]. During oxygenation, oxygen diffuses and binds to the iron atom on each of the four haem groups found in the haemoglobin of erythrocytes as shown in **Figure 2.5**. When a low oxygen

tension is encountered, the bond between oxygen and the haem group dissociates then releasing the oxygen to the surroundings [90,91].

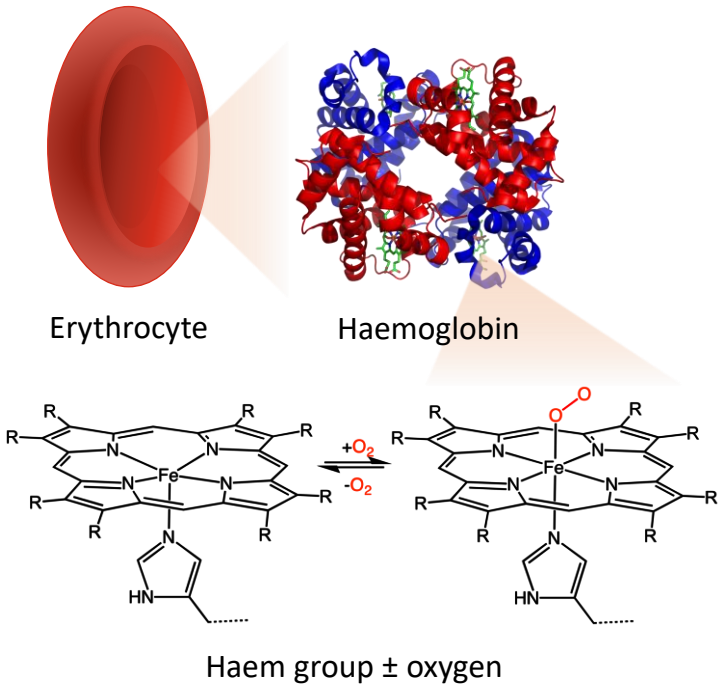

Figure 2.5. *Main features of erythrocytes for oxygen transport [92,93]*

The vascular network has the critical role of supplying oxygen from the aorta to the smallest microvessels and capillaries, where passive diffusion and oxygen gradients allow the efficient supply of oxygen to parenchymal cells in tissues. Therefore, the supply of oxygen starts with low oxygen tension allowing the release of oxygen from the oxyhaemoglobin in erythrocytes which have a high deformability allowing them to circulate and reach all places in the body [89]. The free oxygen then passes through the capillary wall, through the interstitial fluid, and in a parenchymal cell where it can be used during mitochondrial oxidative phosphorylation to generate adenosine triphosphate [94,95]. This well-balanced processed can, however, be altered by irregularities in the vasculatures as found around tumours, causing the collapse of microvessels, inefficient oxygenation, and the formation of hypoxic areas as depicted in **Figure 2.6** [96].

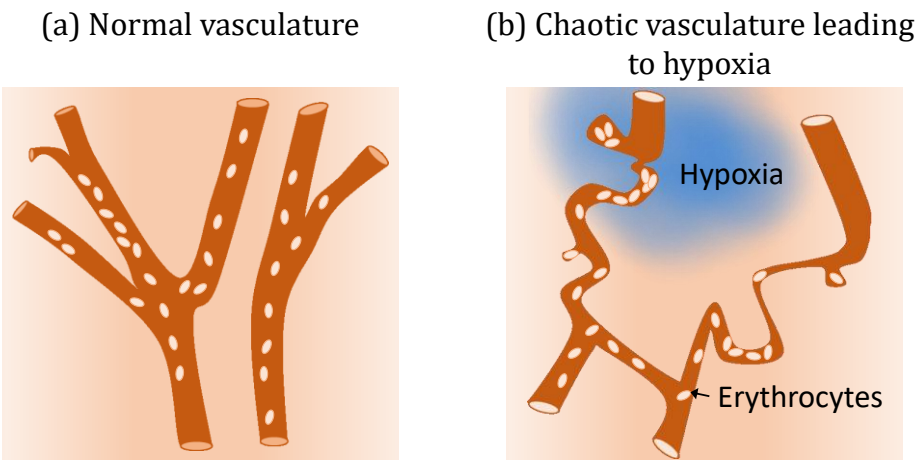

Figure 2.6. *Schematic of vascular network in* ***(a)*** *normal vs.* ***(b)*** *tumour tissues indicating organised vessels in normal tissues compared to a chaotic system in tumours forming hypoxic regions.*

2.2.1.2. Hypoxia in cancer

Oxygen transport within tissues has been modelled by numerical simulation to examine oxygen delivery to tumours of different stages of growth and invasion [97]. The results identified the growth of tumour cells being parallel to pre-existing vasculatures in order to allow sufficient supply of oxygen for tumour growth. However, the high-demand for oxygen near the vasculature leads to the formation of a hypoxic tumour core further away from oxygen-supplying vessels. The uneven oxygen distribution in the tissues triggers an upregulation of vascular endothelial growth factor and thus angiogenesis. Additionally, necrosis of tumour cells due to insufficient oxygen supply causes further invasion of healthy cells forming clusters of surviving cancer cells [97]. Thus, due to the poor structure and functionality of tumour vasculatures, it is important to consider the use of a delivery mechanism enabling a homogeneous distribution of oxygen in the tumour site to address hypoxia.

The presence of a hypoxic core in tumours has been shown to influence patients' response to most forms of cancer treatment [4,63,87,88,98–100]. As reviewed by Saito *et al.*, the increased presence of hypoxia-inducible factors-2α (HIF2α) inhibits the functioning

of p53, a tumour suppressor protein, leading to greater tumour resistance to treatments. Additionally, several studies have highlighted the capacity of HIFs to reprogram normal and cancer cells to pluripotent and stem cell phenotypes by inducing a shift from oxidative to highly glycolytic cell metabolism [87,101,102]. Stem cells have reduced mitochondrial activity and increased glycolysis compared to differentiated cells. A shift of metabolic state is required to reprogram cells with stem cell phenotypes. HIF1α and HIF2α both appear essential for this metabolic switch. The link between hypoxic conditions and the maintenance of cancer stem cells through the expression of HIFs explains the decreased cell differentiation within tumours noted in mesenchymal stem cells by Kim *et al.* [103]. These conditions facilitate tumour growth and persistence by sustaining a population of undifferentiated tumour cells. As indicated by Grist *et al.,* stem cell proliferation has been demonstrated with hypoxic oxygen levels lower than the 20% found in normal tissues [104]. The capacity of HIF signalling pathways to promote the reprogramming of tumour cells into undifferentiated and pluripotent tumour stem cells appears as a critical role in cancer progression. Thus, the ability of these cancer stem cells to generate bulk mass of differentiated and heterogeneous cancer cells is a primary reason for disease progression, metastasis and treatment resistance [102]. This further highlights the need to address hypoxia for successful tumour remediation.

2.2.1.3. Pancreatic cancer

Pancreatic cancer has the lowest survival rate among the 21 most common forms of cancer with only 3% of patients surviving five years after their initial diagnosis [105]. Whilst many other forms of cancer have seen survival rates increase significantly over the past four decades, the survival rate for pancreatic cancer has remained unchanged. The

low availability of surrounding oxygen in pancreatic tumours and an often-late diagnosis of the condition together lead to poor prognosis for patients with the disease [105,106]. In effect, only approximately 20% of patients are eligible for surgical resection of the tumour with curative intent at the time of diagnosis [107]. Of the remaining 80% of patients, 40% have a metastatic disease and approximately 40% present borderline resectable lesions or a locally advanced disease making surgical resection with curative intent not possible [108]. Several reports have investigated neoadjuvant chemo- and radio-therapies alone or in combination to downstage patients' tumours and enable their resection; these treatments, however, still come with significant side-effects due to the non-specific nature of chemotherapy [109,110]. Thus, the development of targeted therapies to reduce undesirable off-target effects and a method to downstage pancreatic tumours could have significant impacts for pancreatic cancer patients.

2.2.2. Addressing hypoxia

Treatments for hypoxia have been researched since the 1930s with protocols to increase the levels of oxygen inspired or the concentration of dissolved oxygen in tissue using hyperbaric conditions. The practical challenges and/or side effects associated with these techniques, however, have stimulated the development of alternative methods enabling the delivery of oxygen-loaded particles or production of oxygen *in situ*.

2.2.2.1. Oxygen breathing and hyperbaria

The use of oxygen to improve the efficacy of radiotherapy in cancer patients was investigated in the 1930s by giving patients 100% oxygen to breath during treatment and in some cases also an intravenous injection of oxygen saturated plasma [88].

Vasoconstriction was, however, sometimes observed when delivering pure oxygen and Carbogen (a mixture of oxygen and small amounts of carbon dioxide) was then investigated as an alternative [88,95,99,111]. The next development in the field involved studies of hyperbaric oxygen delivery in which patients were treated in a chamber pressurised to 2 to 4 atmospheres with elevated levels of oxygen [88,112,113]. The justification behind this method comes from the thought that hyperbaric conditions would allow an increased diffusion and penetration through dense tissues because the diffusion distance of oxygen increases with the initial oxygen tension [88,112]. This method presented promising results to address hypoxia but it suffered technical challenges with the primitive hyperbaric chambers available at that time rendering the simultaneous treatment with radiotherapy impractical [6,88]. Additionally, side effects associated with hyperbaric oxygen therapy have been reported with barotraumatic lesions, oxygen toxicity (central nervous system), and ocular effects [114].

2.2.2.2. Adjusting the haematocrit blood level

Efforts were also made to increase blood transport capacity for oxygen as cancer patients are often anaemic at the start of treatment. Transfusions were then given to adjust patient's haematocrits levels back to normal [88,115]. However, these studies were of limited success as transfused blood typically offers less effective oxygen transport compared to fresh blood, in addition to an increased risk of immunogenicity [88].

2.2.2.3. Delivery of erythropoietin and haemoglobin-based systems

The delivery of erythropoietin was also investigated to stimulate the production of red blood cells in patients and transport of oxygen to hypoxic regions. However, it was

demonstrated that erythropoietin had multiple effects on tumours cells and surrounding normal cell populations which led to a significant increase in mortality observed when this molecule was given to cancer patients undergoing radiotherapy [88,115].

Similarly, the delivery of haemoglobin-based systems was studied for the same purpose. While initial results using stroma-free haemoglobins presented cardiovascular and renal complications and a rapid clearance of these systems [88,111,115,116], more recent studies have improved on this method by delivering polymer-bound haemoglobin to minimise toxicity and improve efficacy [116–118]. Thus, to utilise the advantageous binding affinity between haemoglobin and oxygen, shielding lipids and polymers were incorporated [116–118]. Nonetheless, some of these systems resulted in long circulatory half-lives of 18-48 hours which can be a challenge for addressing immediate and local hypoxic conditions as the oxyhaemoglobin remains encapsulated within a shielding material. Therefore, unless a triggering mechanism is incorporated for oxygen release, this method might not be appropriate to remediate local hypoxia in tumours prior to treatment [116].

2.2.2.4. Delivery of perfluorocarbon-based systems

Perfluorocarbon (PFC)-based emulsions offer a very high capacity for dissolving oxygen, and thus have been investigated as a platform for oxygen delivery [88,115,119]. The favourable characteristic of fluorinated compounds for oxygen delivery stems from their high surface reactivity and self-assembling properties into vesicles. The low polarizability of fluorine molecules in van-der-Waals interactions within fluorinated chains and the low cohesive energy densities in liquid fluorocarbons are factors responsible for the

exceptional properties of fluorinated oxygen carriers [120]. However, their low solubility in water or lipids require emulsification in order to be feasible for intravenous use.

Moreover, it is important to note that while haemoglobin systems provide binding to oxygen, PCFs only offer increased dissolving capacity for oxygen. Thus, although oxygen transport has been shown to be efficient, requirements of complex formulations and production methods have limited the number of clinical trials completed with these systems [88,120]. Additionally, the uses of PFC emulsions from the 1970s presented long term toxicity caused by the fluorocarbon polymer remaining in the reticuloendothelial system and leading to patient death by chemical pneumonitis [115,116].

2.2.2.5. Delivery of lipid-based systems

Oxygen delivery has also been investigated using phospholipid-coated micro- and nano-bubbles encapsulating oxygen gas [99,121]. In effect, a lipid monolayer on the surface of micron-sized gas bubbles can provide the system with a biocompatible barrier against bubble dissolution and gas exchange. This was reported by Borden *et al.* with results highlighting that fully condensed lipid monolayers provide a resistance to oxygen transport from the bubble gas core [99,122,123]. For instance, the shell resistance to oxygen permeation was measured to increase from 690 to 1950 s/cm for lipids with 18 to 24 carbon chain length respectively [123]. In addition, although a 4 µm diameter bubble filled with 95% oxygen and 5% perfluorobutane was predicted to release approximately 1 fmol of oxygen upon contact with an air-saturated medium, it was also predicted to retaine approximately 0.25 fmol within its gas core, based on simulation results [99]. These systems are, however, still challenged by their short half-lives compared to haemoglobin systems [116,124,125]. Nonetheless, preclinical studies with oxygen micro-

and nano-bubbles have demonstrated promising data with the enhancement of treatment in hypoxic pancreatic tumours [4,121,126].

2.2.2.6. In situ production of oxygen

Particles for *in situ* oxygen generation have recently been developed as the delivery of encapsulated oxygen to tumours is challenging. This is mainly due to the unbound state of oxygen leading to uncontrolled release and ultimately low concentrations delivered. Reports have shown that encapsulated materials such as manganese dioxide and calcium peroxide in nanoparticles can enhance the treatment of hypoxic tumours by reacting with endogenous hydrogen peroxide or water respectively to generate oxygen [127,128]. Nonetheless, this approach still faces manufacturing challenges due to the protocol complexity. Further, the reliance of manganese dioxide nanoparticles on the elevated hydrogen peroxide concentration in tumours could also hinder the technique as hydrogen peroxide levels are still low [128,129]. In contrast, although calcium peroxide avoids relying on the local tumour microenvironment, this method then lacks specificity and the safety of increasing oxygen levels in other parts of the body needs to be evaluated.

2.2.2.7. Challenges

Early research on oxygen delivery required high doses, conditions to induce an increased oxygen flux in tissues, and repetitive treatments. As these methods led to an increase in therapy toxicity [88,111], a thorough safety examination is required for novel approaches that aim to address this problem. Encapsulated oxygen solutions might be advantageous as a known maximum volume is delivered and the induced increase in oxygen mobility can be determined based on the local concentration gradients. Additionally, the

development of a method to remediate hypoxia also requires oxygen delivery in local regions away from vasculatures, indicating the need for targeting.

2.3. Therapeutic microbubbles

Although microbubble agents were originally developed to improve the contrast of diagnostic ultrasound images [130], they are increasingly being used for therapeutic applications. Microbubble oscillations can cause bioeffects advantageous for some indications [131,132] and their drug and gas loading capacity allows them to be used as delivery vehicles [133–136]. This section reviews the design considerations for therapeutic microbubbles to transport sensitisers and oxygen for the treatment of hypoxic tumours with sonodynamic therapy.

2.3.1. Echogenicity and stability of microbubbles

The low density and high compressibility of the microbubble gas core allow them to compress and expand in response to ultrasound exposure [137–139]. Additionally, microbubbles have a resonant frequency corresponding to those typically used in medical ultrasound (1-10 MHz) allowing large amplitude oscillations under these conditions [140]. The highly non-linear response of microbubbles to moderate ultrasound pressures produces acoustic radiation over a range of frequencies that can be readily distinguished from those due to the surrounding tissue [141]. However, a disadvantage is that the half-life of these systems in circulation is of the order of 5-10 minutes even when a stabilising coating is incorporated [124,125].

Current commercial microbubbles have a stabilising lipid, protein or polymer-based coating and an inert gas core as indicated in **Table 2.1** [142]. While polymer microbubbles

provide good physical stability [12], cross-linked polymers are more resistant to compression and expansion, thus producing less echogenic systems [143]. Proteins can also produce stable microbubbles; however, to avoid immunogenic reactions they require additional considerations such as the use of thermally treated proteins or a formulation incorporating stealth material [144,145]. Finally, the majority of commercial contrast agents use phospholipids (thereafter referred to as "lipids") or lipid-mix systems which offer excellent echogenicity, biocompatibility, and circulatory stability [143,146]. Furthermore, the spontaneous self-assembly of lipids into monolayers at interfaces, with hydrophobic tails facing the gas phase, facilitates microbubble formation and manufacturing, and promotes physical stability [143,147].

Table 2.1. *List of commercial microbubbles, the coating and encapsulated gas core.*

NAME	COATING	GAS	MANUFACTURER
Albunex	Albumin	Air	Mallinckrodt
Quantison	Albumin	Air	Quandrant Healthcare
Optison	Albumin	C_3F_8	GE Healthcare
Definity	Lipid	C_3F_8	Bristol-Myers Squibb
Imagent	Lipid	C_6F_{14}	IMCOR Pharmaceutical Co.
SonoVue	Lipid	SF_6	Bracco
Aerosomes	Lipid	Perfluorocarbon gas	ImaRx Pharmaceutical Corp
Filmix	Lipid	Air	Cavcon
Sonazoid	Lipid	Perfluorocarbon gas	GE Healthcare
BiSphere	Polymer	Air	Point Biomedical
MP1950	Lipid	C_4F_{10}	Mallinckrodt

Abbreviations: C_3F_8 = Perfluoropropane, C_6F_{14} = Perfluorohexane, SF_6 = Sulphur hexafluoride, C_4F_{10} = Perfluorobutane.

The physical principles governing the stability or dissolution of microbubbles in solution must be understood to design efficient formulations. The first consideration comes from the Laplace pressure differential between inside and outside of a microbubble, expressed as $\Delta P = 2\sigma/R$, where σ is the interfacial tension and R is the instantaneous radius of the microbubble.

Taking the pressure differential into account and following Epstein and Plesset's model, the rate of dissolution for an uncoated microbubble can be derived as presented in Equation 1 [137,148].

$$\frac{dR}{dt} = \frac{D\left(C_i - C_{sat}(R)\right)}{\rho(\infty) + \frac{2M\,2\sigma}{3BT\,R}}\left[\frac{1}{R} + \frac{1}{(\pi Dt)^{\frac{1}{2}}}\right] \quad (1)$$

where: D is the diffusion coefficient, C_i and $C_{sat}(R)$ are the initial and saturation concentration of dissolved gas in the surrounding liquid respectively, t is time, M is the encapsulated gas' molecular weight, B is the universal gas constant, T is the gas temperature, and $\rho(\infty)$ is the gas density at a zero curvature interface. Although this relationship assumes an uncoated microbubble in liquid with constant hydrostatic pressure and temperature over time, it demonstrates the dependence of microbubble stability on the encapsulated gas core properties. The relatively high solubility and diffusivity of oxygen in blood are then expected to hinder the stability of oxygen microbubbles, highlighting the need for additional stabilising factors such as the incorporation of other gases to prevent oxygen escape (**Table 2.2**). Additionally, as the size of the microbubble is limited by safety considerations, the focus of new formulations must be on reducing the magnitude of interfacial tension σ, acting on the microbubble surface by considering stabilising forces. For instance, increasing the microbubble shell packing or thickness decreases the diffusivity of the gas core across the coating and strengthens microbubbles against the applied surface tension and Laplace pressure. Consequently, lipid microbubbles using DBPC (22:0, indicating the number of carbon-carbon single-bond:double-bonds respectively) and DSPC (18:0) demonstrated a higher stability relative to DPPC (16:0) systems [99,149].

Table 2.2. *Solubility and diffusivity of gases in water at 298.15 K*

GAS	MOLECULAR WEIGHT g/mol	HENRY'S LAW CONSTANT mol/(m³Pa)	REFERENCE
C_3F_8	188	1.2×10^{-7}	[150]
C_4F_{10}	238	1.5×10^{-8}	[151]
C_6F_{14}	338	5.4×10^{-10}	[151]
SF_6	146	2.4×10^{-6}	[152,153]
O_2	32	1.3×10^{-5}	[154,155]
N_2	28	6.5×10^{-6}	[156]

Abbreviations: C_3F_8 = Perfluoropropane, C_4F_{10} = Perfluorobutane, C_6F_{14} = Perfluorohexane, SF_6 = Sulphur hexafluoride, O_2 = molecular oxygen, N_2 = molecular nitrogen.

Kwan *et al.* presented results confirming the feasibility of delivering oxygen using microbubbles [99]. Their report described the method to be achievable and clinically relevant; however, they also identified difficulties with this delivery platform. High yield in oxygen delivery is required to overcome hypoxic conditions which could be difficult due to the low stability of pure oxygen microbubbles (O_2MB) in solution. The group then demonstrated that a larger molecular weight gas such as perfluorobutane could be used alongside molecular oxygen to stabilise microbubbles against dissolution. As they suggest, the low solubility gas could lead to an increase in bubble lifetime which could allow additional lipids to adsorb onto the shell, decrease the surface tension, and further prevent bubble dissolution. The addition of lipid material at the bubble surface could then also increase the resistance again gas permeation [157]. Contrastingly, the addition of perfluorobutane in the gas core also lowers the oxygen delivery yield. Ultimately, the group highlighted the unknown effect of injecting intravascularly large quantities of microbubbles and oxygen. Similarly, an improved microbubble stabilisation was reported through the incorporation a nanoparticle coating [148,158]. Nevertheless, these design factors can affect the acoustic properties of the system by increasing the rigidity of the microbubble coating and leading to difficult shrinking and expansion cycles under ultrasound exposure [140]. A summary of these considerations is provided in **Figure 2.7**.

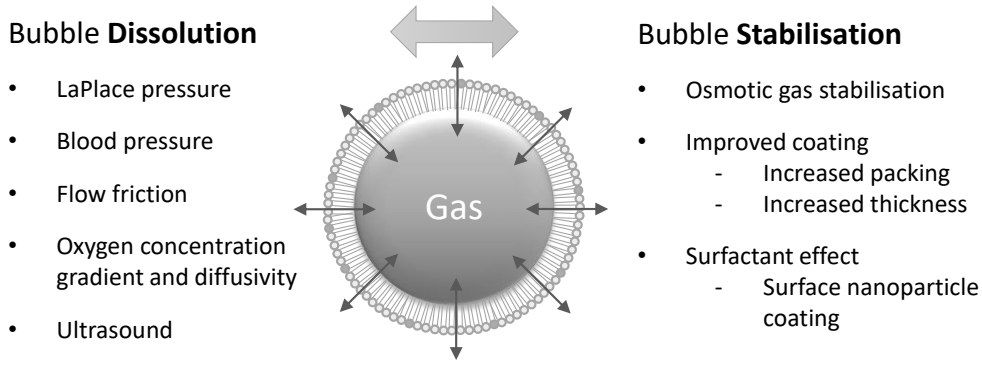

Figure 2.7. *Factors for dissolution and stabilisation of oxygen microbubbles in circulation*

2.3.2. Bioeffects of microbubbles exposed to ultrasound

At higher pressures, the violent oscillations exhibited by microbubbles can produce substantial biological effects [132,159–163], and these are being actively investigated for their potential application in ultrasound mediated therapy. Although these disruptions have yet to be fully understood, the following section discusses current findings on hydrodynamic stresses and sonochemical imbalances from the ultrasound exposure of microbubbles.

2.3.2.1. Hydrodynamic stress

The oscillations of microbubbles under acoustic pressure waves lead to the formation of microstreaming patterns in the surrounding medium [8,164]. The hydrodynamic stresses produced by this motion have been associated with inter- and intracellular effects [8,131,132,165]. For example, they can trigger the remodelling of the cell cytoskeletal network through fluidisation leading to changes in membrane permeability [166,167], or change the cell monolayer integrity ultimately forming intercellular gaps [132]. As these bioeffects are transient when caused by low-intensity ultrasound, they are investigated to enhance treatment efficacy by increasing drug uptake using ultrasound targeted

microbubble destruction [132,165]. The acoustic parameters and the microbubble proximity to the targeted cells are, however, crucial factors affecting these changes. As the use of higher acoustic pressure was found to initiate pathways to cell apoptosis [168], these factors need to be thoroughly characterised to ensure the efficacy and safety of this method to increase drug uptake. In contrast, for the case of cancer therapy where localised cell death triggering is desired, these effects seem less critical.

2.3.2.2. Sonochemical stress

The oscillations of microbubbles also generate sonochemical stresses on cells. For instance, reactive oxygen species such as hydrogen peroxide and superoxide anion can be produced from the splitting of water and have been linked to changes in intracellular calcium concentration after ultrasound and microbubble exposure [132,162]. Mainly depending on the ultrasound exposure conditions, some changes in cellular homeostasis have been found to be reversible [132] but apoptosis signalling has also been observed and related to calcium ion- and mitochondria caspase-dependent pathways [169].

Overall, these stresses are likely to act in combination to induce cellular changes during exposure to microbubbles oscillations. Although the bioeffects and the mechanisms through which these stresses occur need to be further characterised to ensure safety, they can be applied to enhance therapies.

2.3.3. Drug delivery

Ultrasound-induced microbubble oscillations can affect the permeability of cells in a targeted manner as previously mentioned. The loading of therapeutics into the microbubble coating and their targeted destruction with ultrasound can then enable the

local delivery of highly potent drugs at a site of interest. This process can occur through the shedding of materials during microbubble oscillations as reported by Luan *et al.* with the results presented in **Figure 2.8** [170]. Several studies have further demonstrated the deposition of lipids from ultrasound activation of microbubbles *in vitro* [171,172] and *in vivo* [173].

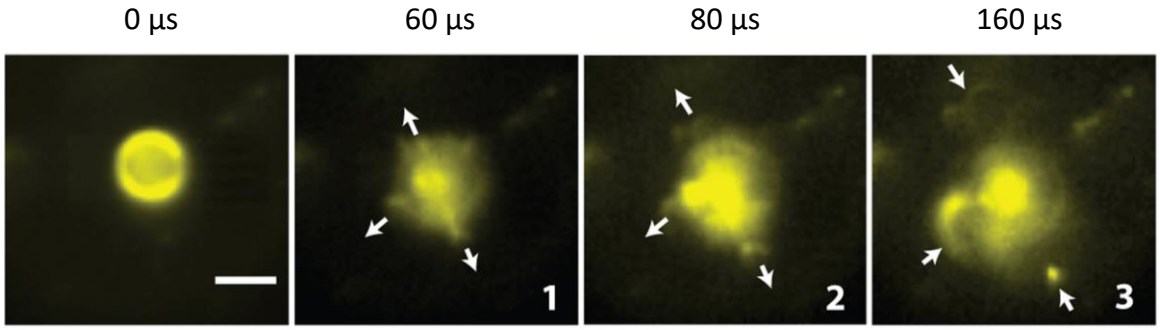

Figure 2.8. *Images from* [170] *showing the shedding of fluorescent lipids during bubble oscillations with arrows indicating the motion toward/away from the microbubble during ultrasound excitation (255 kPa, 500 cycles), the scale bar is 5 µm.*

Additionally, the delivery of drugs using cavitation nuclei and ultrasound was observed to provide an enhanced distribution of therapeutics due to the oscillations and jetting from microbubbles enabling the extravasation of drugs to the surrounding [174–177]. For the development of sonodynamic therapy for hypoxic tumours, the loading of sensitisers and oxygen in microbubbles can be released and distributed using ultrasound, thereby allowing the treatment of tissues farther away from the vasculature. Moreover, as this method provides a locally-enhanced therapy, the concentration of active agents administered can be reduced compared to systemic drug administration, therefore minimising the risk of toxic side effects.

Numerous formulations have been proposed to facilitate the loading of drugs within the microbubble coating and/or to its surface in the form of liposomes, nanoparticles, or single molecules [133,178–181]. An example of these systems is presented in **Figure 2.9**.

Although extending the functionality of microbubbles, this functionalisation generates a series of potentially conflicting requirements for their design. In particular, the microbubbles must have adequate stability both for storage and in circulation. They must be sufficiently responsive to ultrasound to promote therapy and ideally be imaged during treatment. Finally, they must be able to carry sufficient quantities of drug to be effective; and it is also desirable to target them to specific sites such as the tumour endothelium.

(a) MB + Liposomes

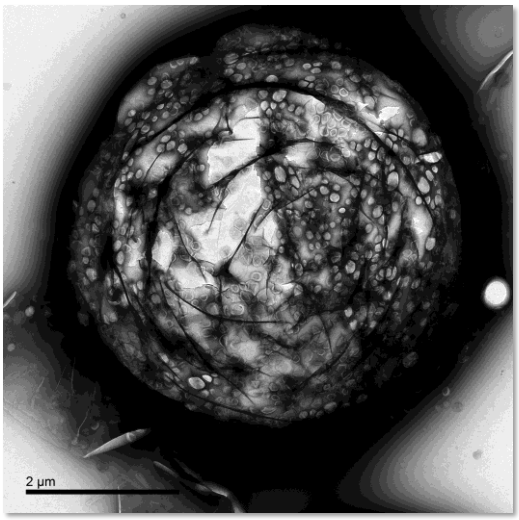

(b) MB + Gold nanoparticles

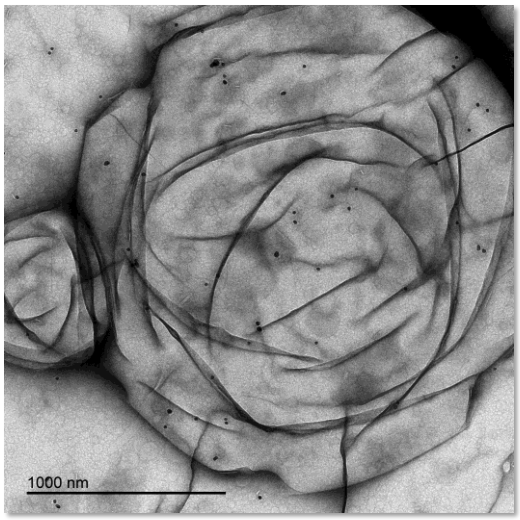

(c) MB + Rose Bengal

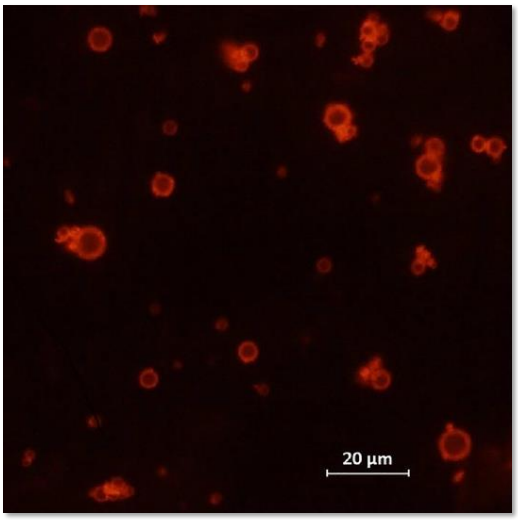

Figure 2.9. *Examples of liposome, nanoparticles and drug loaded microbubbles. Transmission electron microscopy images of microbubbles functionalised with* ***(a)*** *liposomes,* ***(b)*** *gold nanoparticles, and* ***(c)*** *reproduced from* [182] *with a fluorescence microscopy image of microbubbles functionalised with Rose Bengal.*

2.3.4. Targeting microbubbles

There are a number of different approaches that have been applied alone or in combination in order to focus the action of microbubbles at a site of interest. Biochemical targeting with the attachment of ligand receptors on microbubbles enables binding with high specificity to target regions [183]. The short half-life of microbubbles can, however, hinder the efficacy of ligand-receptor binding although acoustic radiation force has been used to concentrate and slow down microbubbles at a vessel wall of interest [184] and increase ligand-receptor binding [183]. Nonetheless, challenges with microbubble stability and these targeting methods have led to a third possibility, which incorporates magnetic material in microbubbles enabling localisation at a target site using an externally applied magnetic field. While magnetic targeting improved the delivery of drug loaded magnetic microbubbles (MMBs), the incorporation of iron oxide nanoparticles (IONPs) in microbubbles requires formulation considerations to ensure the stability of these systems.

Multiple formulation for magnetic microbubbles have been presented in the literature, stabilised with polymer, surfactants, and lipids [185,186]. In the case of polymer coated microbubbles, IONPs are typically embedded within the microbubble coating during manufacturing [187–194]. However, several studies have also investigated the performance of microbubbles with IONPs conjugated to their outer-surface. This external loading approach was found advantageous in terms of improving magnetic properties while preserving acoustic response; and also improved cellular uptake [195–198]. However, the reduced echogenicity of polymeric microbubbles [143] has favoured the use lipid-mix ultrasound contrast agents instead.

Previous studies on lipid-coated magnetic microbubbles have: incorporated hydrophobic IONPs on the internal surface of the coating enabling the targeted delivery of genes or thrombolytic drugs [199–201]; embedded different types of IONPs within the microbubble coating, enabling magnetic targeting of nucleic acid [202], genes, [203–206] and antirestenotic drugs [207]; or attached hydrophilic IONPs to the surface of microbubbles through biotin/avidin [208,209], or protamine/heparin [210] interactions. Surfactant microbubbles with charged IONPs have also been reported [211–215], but toxicity concerns related to these systems limits their clinical feasibility. A comparison between formulations of lipid coated magnetic microbubbles is further discussed in Chapter 3.

2.3.5. Microbubbles for sonodynamic therapy of hypoxic tumours

Section 2.3.2 reviewed the bioeffects of ultrasound and microbubbles on cells, and sections 2.3.3 and 2.3.4 highlighted their potential to deliver drugs to cells in a targeted manner. The addition of ultrasound-responsive microbubbles to enhance the efficacy of sonodynamic therapy has also shown promising results to locally deliver and activate the sensitiser instead of requiring a systemic injection of the drug [216–218]. More specifically, the inertia-driven collapse of microbubbles in the presence of ground state molecular oxygen can enhance the activation of sensitising drugs such as Rose Bengal to generate cytotoxic reactive oxygen species in a targeted manner [10]. Nevertheless, this method relies on the presence of molecular oxygen to generate its toxic effects; a requirement which can be challenging for the treatment of hypoxic pancreatic tumours.

2.3.5.1. Oxygen delivery

As above, the hypoxic nature of solid tumours can hinder sonodynamic treatment due to the poor availability of molecular oxygen to produce reactive oxygen species [4,63,99]. Yet, McEwan *et al.* presented promising *in vivo* results with the intratumoural injection of oxygen microbubbles for enhanced sonodynamic therapy [4]. The group reported tumour volume reduction by 45% five days after treatment using Rose Bengal-loaded oxygen microbubbles and ultrasound activation in mice bearing BxPC-3 pancreatic tumours. In these studies, microbubbles were produced with a stabilising coating composed of DSPC:DSPE-PEG2000:DSPE-PEG2000-biotin to enable the loading of biotinylated sensitiser onto the microbubbles through an avidin bridge. Microbubbles were first made with encapsulated sulphur hexafluoride, followed by sparging of the suspension with oxygen to cause an exchange in the encapsulated gas and form oxygen microbubbles. Nonetheless, due to the low stability of these systems, treatment administration in these studies was done through intratumoural injections. Therefore, the production of oxygen microbubbles for intravenous use would be valuable to facilitate administration of the therapeutic as well as ensuring its thorough distribution within the tumour.

2.3.5.2. Combination therapy

Antimetabolite drugs such as gemcitabine (Gem) and 5-fluorouracil (5-FU) have been investigated for cancer treatment as they hinder or terminate DNA synthesis through several chemical pathways [219]. As cancer cells are rapidly dividing, they are more sensitive to damage during DNA synthesis compared to most normal cells which are in a quiescent state of their cell cycle. The combination of these antimetabolite drugs and sonodynamic Rose Bengal loaded onto oxygen microbubbles still indicated the potential

for an increased therapeutic effect with a combination treatment regimen [220]. Yet, gemcitabine was found to provide a higher clinical benefit for patients with advanced pancreatic cancer compared to 5-FU [221]. Additionally, several studies reported an increase in the quality of life for patients with pancreatic adenocarcinoma when gemcitabine and microbubbles were co-injected and exposed to ultrasound, compared to gemcitabine alone [222,223]. Although the co-injection of therapeutics favours the clinical translation of the method, it does not prevent off-target side-effects caused by the systemic delivery of gemcitabine. In an additional pre-clinical study investigating pancreatic tumours in mice, the combination of gemcitabine and sonodynamic therapy was tested to enhance treatment outcome. The study resulted in a significant tumour growth delay compared to either therapy alone with no observed systemic toxicity [182].

2.3.5.3. Challenges

Therefore, using microbubbles in sonodynamic therapy has the potential to reduce drug dosage and undesired side-effects for the patients, while increasing treatment efficacy with: (1) targeting, (2) lowering of the acoustic energy required to obtain an effect, and (3) delivering the oxygen required for treatment. Nonetheless, this method is still challenged by several factors. Firstly, the stability of oxygen microbubbles needs to be optimised to minimise off-site sensitiser accumulation and toxicity. This is further discussed and assessed in Chapter 3 and Chapter 5. Then, in order to allow clinical acceptance of this method, an understanding of the mechanisms allowing the activation of the sensitiser is required (Chapter 4). Additionally, as highlighted in sections 2.3.2, the ultrasound parameters (Chapter 5) and devices (Chapter 6) used also need to be evaluated in order to promote treatment efficiency and safety, and to ease the translation of sonodynamic therapy for hypoxic tumours into clinical use.

Chapter 3
Magnetic functionalisation of microbubbles

In this chapter the results from a preliminary in vivo study are first presented demonstrating the potential for concentrating sensitiser- and oxygen-loaded microbubbles using an externally applied magnetic field to enhance sonodynamic therapy. The limitations of this method are then discussed, and new lipid-coated magnetic microbubble formulations are presented to address them. Further in vitro studies are then reported which evaluate these formulations in terms of their magnetic and acoustic responses, stability, and drug loading capacity.

The in vivo results in this chapter were obtained in collaboration with the University of Ulster where the experiments took place and this chapter provides an edited version of the publications indicated below.

Y. Sheng, E. Beguin*, H. Nesbitt*, S. Kamila, J. Owen, L.C. Barnsley, B. Callan, C. O'Kane, N. Nomikou, R. Hamoudi, M.A. Taylor, M. Love, P. Kelly, D. O'Rourke, E. Stride, A.P. McHale, J.F. Callan, Magnetically responsive microbubbles as delivery vehicles for targeted sonodynamic and antimetabolite therapy of pancreatic cancer, J. Control. Release. 262 (2017) 192–200. DOI: 10.1016/j.jconrel.2017.07.040. * joint first authors*

E. Beguin, L. Bau, S. Shrivastava, E. Stride, Comparing strategies for magnetic functionalisation of microbubbles, ACS Appl. Mater. Interfaces. 11 (2018) 1829–1840. DOI: 10.1021/acsami.8b18418

Contents

3.1. Introduction

3.1.1. Preliminary experiments

As outlined in section 2.3, the advancement of ultrasound-mediated therapy has stimulated the development of drug-loaded microbubbles that can be targeted to a region of interest with an applied magnetic field prior to ultrasound activation. This approach has been used to deliver sonodynamic therapy for pancreatic cancer *in vitro* and *in vivo*. As the combination of antimetabolite and sonodynamic drugs has been previously reported to provide a therapeutic benefit [220], preliminary experiments were carried out using a combination of 5-fluorouracil and Rose Bengal with magnetic microbubbles. The antimetabolite 5-fluorouracil was used because a biotinylated version of the drug was available from the work of McEwan *et al.* [220]. Microbubbles were then filled with oxygen gas in order to counteract the hypoxic nature of pancreatic tumours. They were also functionalised by incorporating lipid-coated IONPs into the microbubble shell to enable their magnetic targeting. These nanoparticles were chosen as they are commonly available for purchase and are coated with phospholipids similar to those constituting the microbubble coating. Additionally, following the physical considerations discussed in section 2.3.1, the incorporation of nanoparticles on the coating of microbubbles can induce a "jamming" effect that can prevent further bubble shrinkage once an equilibrium is reached [148]. This, however, assumes the overall force holding the IONPs on the surface of microbubbles is stronger than the Laplace pressure required to dislodge them.

In vitro, the combined treatment of magnetic microbubbles functionalised with 5-fluorouracil and Rose Bengal produced a reduction in cell viability of 50% ($p < 0.001$) when tested against pancreatic BxPC-3 cells as shown in **Figure 3.1.**

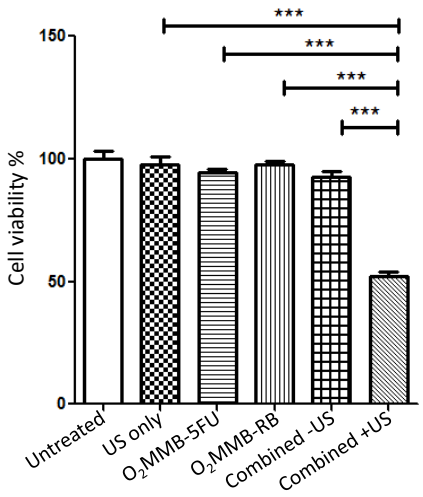

Figure 3.1. *Cell viability for BxPC-3 cells after treatment with (1) untreated, (2) ultrasound only, (3) oxygen magnetic microbubble loaded with 5-fluorouracil (O_2MMB-5FU) only, (4) oxygen magnetic microbubble loaded with Rose Bengal (O_2MMB-RB) only, (5) combined O_2MMB-RB and O_2MMB-5FU, and (6) combined O_2MMB-RB and O_2MMB-5FU plus ultrasound. *** $p < 0.001$ for (6) compared to either (2), (3), (4), or (5). Data produced in collaboration with Dr. Yingjie Sheng and published in [86].*

An *in vivo* study was then completed to provide an additional assessment of the benefit gained from incorporating magnetic targeting into this method. The intravenous administration of the treatment to mice bearing orthotopic human xenograft BxPC-3 tumours yielded a 48% reduction in tumour volume relative to an untreated control group ($p < 0.05$) when the tumour was exposed to both external magnetic and ultrasound fields. In contrast, the application of an ultrasound field with the treatment resulted in a 28% reduction in tumour volume (**Figure 3.2**). In addition, activated caspase and BAX protein levels were both observed to be significantly elevated in tumours harvested from animals treated with the combination of MMBs in the presence of magnetic and ultrasonic fields when compared to expression of those proteins in tumours from either the control or ultrasound field only groups ($p<0.05$, **Figure 3.3**). These results suggest magnetic microbubbles have considerable potential as a platform to enable the targeted sonodynamic / antimetabolite treatment of pancreatic cancer.

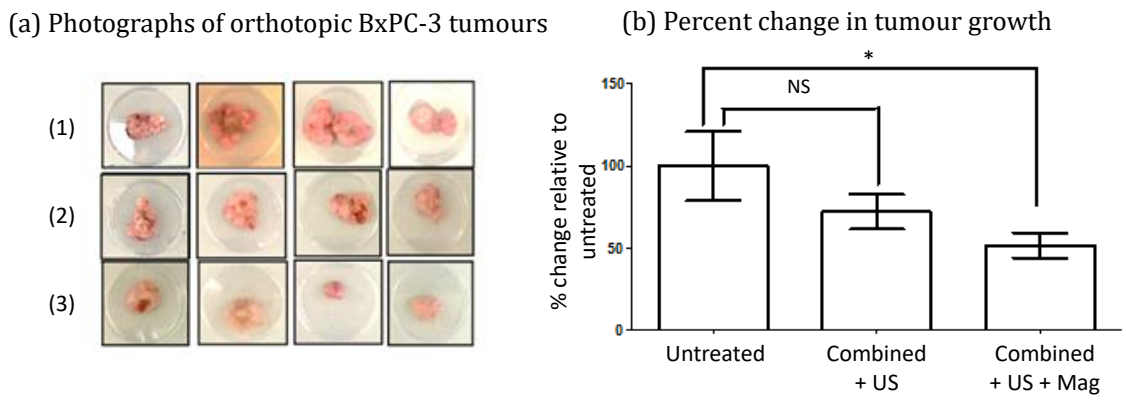

Figure 3.2. *In vivo results for the treatment of BxPC-3 tumours in a murine model.* ***(a)*** *Photographs of orthotopic BxPC-3 tumours removed from SCID mice 28 days following implantation after (1) no treatment, (2) treatment with combined O_2MMB-RB and O_2MMB-5FU plus ultrasound or (3) with O_2MMB-RB and O_2MMB-5FU plus ultrasound and magnet (n = 4). Treatments were administered on days 19, 20, and 21.* ***(b)*** *Plot of % change in tumour volume relative to untreated for mice treated with (2) or (3) above. * $p < 0.05$ for (3) compared to (1). A one-way ANOVA, post-hoc test showed the same significance as above. Data produced in collaboration with Dr. Yingjie Sheng and Dr. Heather Nesbitt and published in [86].*

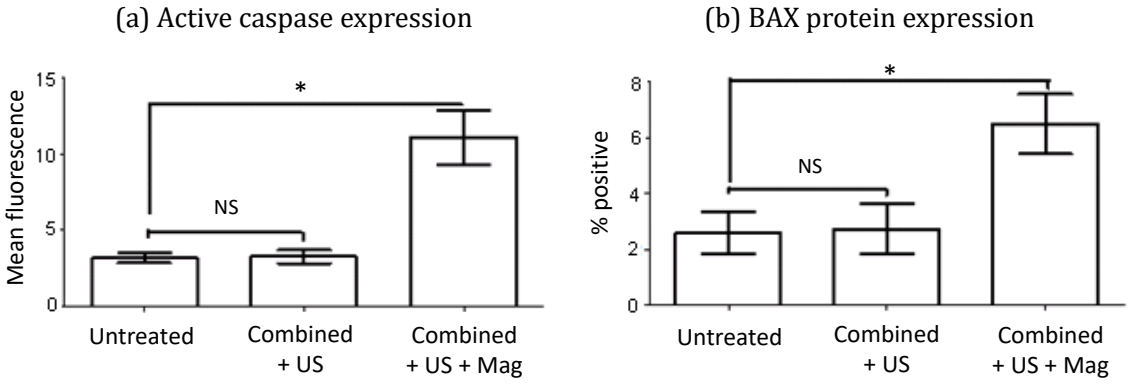

Figure 3.3. *BxPC-3 tumour cell expression.* ***(a)*** *Plot showing presence of active caspase in single cell suspensions of tumours removed from SCID mice 38 days following implantation after treatment with (1) no treatment, (2) treatment with combined O_2MMB-RB and O_2MMB-5FU plus ultrasound or (3) treatment with O_2MMB-RB and O_2MMB-5FU plus ultrasound and magnet. Fluorescence indicates caspase activity which is reflective of apoptosis and was determined using the Pan Caspase probe (Pan Caspase NIR from Vergent Bioscience) via flow cytometry. Treatments were administered on days 19, 20 and 21.* ***(b)*** *BAX protein expression of the same single cell suspensions via flow cytometry. *$p < 0.05$ for (3) compared to (1). Data produced in collaboration with Dr. Yingjie Sheng and Dr. Heather Nesbitt and published in [86].*

The *in vitro* and *in vivo* studies presented promising results for the magnetically targeted delivery of sonodynamic and antimetabolite therapies to pancreatic tumours. However, the intravenous injection of the treatment during the *in vivo* study highlighted the low stability of oxygen loaded magnetic microbubbles functionalised with Rose Bengal or 5-fluorouracil, as some microbubble samples would dissolve as soon as pressure was applied to the syringe. Thus, the need to incorporate therapeutic molecules while optimising responsiveness to both magnetic and acoustic fields and maintaining adequate stability, poses a considerable challenge for microbubble synthesis. Thus, a study was undertaken to evaluate three different methods for incorporating iron oxide nanoparticles into phospholipid-coated microbubbles using: (1) hydrophobic IONPs within an oil layer below the microbubble shell, (2) phospholipid-stabilised IONPs within the shell, or (3) hydrophilic IONPs non-covalently bound to the surface of microbubbles. This chapter provides a comparison of previously published magnetic microbubble formulations and a new method. As the delivery of therapeutics is also necessary during sonodynamic therapy, the drug-loading potential of these systems is also discussed.

3.1.2. Objectives

The objective of this chapter is to provide a comparison of the *in vitro* performance for different magnetic microbubble formulations based on their (1) stability, (2) magnetic response, and (3) acoustic properties. Because of their strong echogenicity, ease of manufacturing, and biocompatibility, the comparison was limited to the use of the lipid-based systems depicted in **Figure 3.4**, and did not consider polymer- or surfactant-based microbubbles previously reviewed in section 2.3.4. Further limitations affecting the results of this study are also discussed at the end of this chapter.

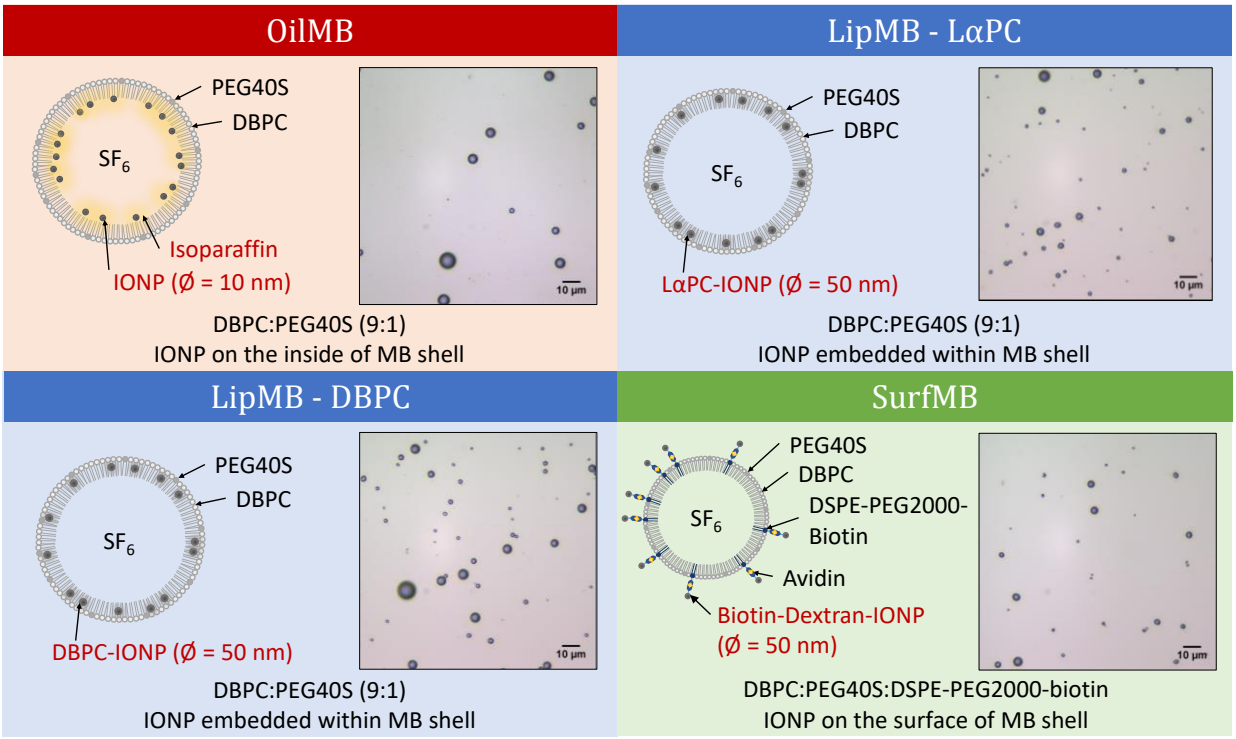

Figure 3.4. *Schematics and optical images of magnetic microbubbles formulations. Scale bar indicates 10 µm. Formulations: phospholipid microbubbles loaded with hydrophobic IONPs in an oil phase (OilMB), phospholipid-stabilised (LαPC or DBPC) IONPs with hydrophobic cores (LipMB-LαPC and LipMB-DBPC) and surface-bound hydrophilic IONPs (SurfMB).*

3.2. Materials

1,2-dibehenoyl-*sn*-glycero-3-phosphocholine (DBPC), and 1,2-distearoyl-*sn*-glycero-3-phosphoethanolamine-N-[biotinyl(polyethylene glycol)-2000] (DSPE-PEG2000-biotin) were obtained from Avanti Polar Lipids Inc. (Alabaster, Alabama, USA). N-(7-nitrobenz-2-oxa-1,3-diazol-4-yl)-1,2-dihexadecanoyl-sn-glycero-3-phosphoethanolamine, triethylammonium salt (NBD-PE) was purchased from Thermo Fisher Scientific. Polyoxyethylene (40) stearate (PEG40S), chloroform, Dulbecco's phosphate buffered saline (PBS), and avidin were all obtained from Sigma Aldrich Ltd. (Gillingham, Dorset, UK). Fluorescein-PEG40S was made by [224], using Fluorescein-PEG-NH_2 (molecular weight = 2000 Da) purchased from NANOCS (ChemQuest, Co., Ltd, Cheshire, UK). Sulphur

hexafluoride gas was purchased from The BOC Group (Guilford, Surrey, UK). Finally, Sonovue® microbubbles were purchased from Bracco UK Limited (High Wycombe, UK).

Biotinylated carboxymethyl dextran magnetic nanoparticles (dextran IONPs) were modified in-house (50 nm hydrodynamic diameter post-preparation, method and characterisation provided in Appendix B) with the following additional materials. Hydrochloric acid, 4-methylmorpholine (NMM) and 4-(4,6-dimethoxy-1,3,5-triazin-2-yl)-4-methylmorpholinium chloride (DMTMM) were purchased from Sigma Aldrich Ltd. (Gillingham, Dorset, UK). N-biotin-tetra(ethylene glycol)-diamine (Biotin-TEG-NH_2·TFA) was obtained from Iris Biotech GmbH (Marktredwitz, Germany). IONPs coated with carboxymethyl dextran were purchased as FluidMAG-CMX (50 nm hydrodynamic diameter) from Chemicell GmbH (Berlin, Germany).

Other nanoparticles used in this work were L-α-phosphatidylcholine coated iron oxide nanoparticles (LαPC IONPs) purchased as fluidMAG-lipid (50 nm hydrodynamic diameter) from Chemicell GmbH (Berlin, Germany). 1,2-dibehenoyl-*sn*-glycero-3-phosphocholine coated iron oxide nanoparticles (DBPC IONPs, 50 nm hydrodynamic diameter) were manufactured by Ocean NanoTech (San Diego, USA). Iron oxide nanoparticles dispersed in isoparaffin (isoparaffin IONPs) were purchased as WHJS1-B (10 nm diameter) from Liquids Research Ltd. (Bangor, UK).

To assess the haemolysis induced by the different formulations, horse blood was used. A 100 mL sample was purchased (Ref: HB046, Lot 34701900) from TCS Biosciences Ltd (Botolph Claydon, Buckingham, United Kingdom). Positive controls were achieved by adding a solution of Triton X-100 purchased from Sigma Aldrich Ltd. (Gillingham, Dorset, UK) and diluted in deionised water.

3.3. Methods for microbubble manufacturing

3.3.1. Overview of microbubble formulations

Five different microbubble formulations were compared. The first formulation (**OilMB**) consisted of phospholipid microbubbles loaded with hydrophobic IONPs suspended in an isoparaffin oil phase that partitions into bubbles upon sonication. The **OilMB** method, previously presented by [199], is similar to the acoustically activated lipospheres reported by others where a layer of soybean oil is embedded in bubbles to act as a reservoir for a hydrophobic drug [225,226]. The IONPs used for this formulation have a diameter of 10 nm and are suspended in isoparaffin. The ferrite particles are reported to constitute 10% by volume of the solution, thus providing a magnetic flux density of 400 Gauss according to the manufacturer corresponding to a saturation magnetisation of 6.3 emu/g.

Two further hydrophobic IONP formulations (**LipMB-DBPC** and **LipMB-LαPC**, collectively referred to as **LipMB** hereafter) were prepared using phospholipid-coated IONPs directly incorporated into the bubble coating. **LipMB-LαPC** was previously described in [86,227,228] and has LαPC coated IONPs added into the microbubbles. These nanoparticles were chosen because they are commercially available; their coating is composed of a range of phosphatidylcholines with approximately 17% DPPC (16:0), 4% DSPC (18:0), 9% DOPC (18:1), 60% DLPC (18:2) and 7% 18:3 PC. **LipMB-DBPC** was produced to test the impact of the IONP lipid coating on the performance of the magnetic microbubble produced. This formulation then uses IONPs coated with the same phosphatidylcholine (DBPC) as that composing the microbubble shell. The method relies on the phospholipid coating to transfer the IONPs to the microbubble shell upon sonication and allows loading of hydrophobic IONPs into microbubbles without

introducing an oil phase. The lipid-coated IONPs both had a hydrodynamic diameter of 50 nm with a crystal core of approximately 30 nm made of magnetite.

In the fourth formulation (**SurfMB**), hydrophilic dextran IONPs were biotinylated by reacting the carboxylic acids on the carboxymethyl dextran coating with biotin-TEG-NH_2 and attached to the surface of biotinylated microbubbles via an avidin bridge. The motivation behind this method was to produce IONPs with similar surface chemistry as the clinical product Feraheme [229] which is made of IONPs coated with a carboxymethyl dextran sorbitol ether. The carboxylic acids on Feraheme could be used as handles for biotinylation to enable loading onto the external surface of biotinylated microbubbles. The dextran IONPs used for this formulation had a hydrodynamic diameter of 50 nm and crystal core of 30 nm made of magnetite. The fifth formulation (unloaded) represented the control population and consisted of phospholipid microbubbles without IONPs.

The different IONPs were chosen to have a hydrodynamic diameter of 50 nm for all formulations except for **OilMB** which contained IONPs of 10 nm in diameter in isoparaffin to allow a comparison with the method used by others [199]. **Table 3.1** and **Table 3.2** provide a summary of the nanoparticles and the resulting magnetic microbubbles presented in this thesis. Surfactants were used to promote the formation of microbubbles. To ensure the bio-compatibility of the final product, they were chosen from the ingredients of clinically approved products [230,231].

Table 3.1. *Summary of iron oxide nanoparticles properties as provided by the manufacturers*

PARTICLE	HYDRODYNAMIC DIAMETER [nm]	SATURATION MAGNETISATION [emu/g]	PARTICLE CORE DIAMETER [nm]	PARTICLE CORE COMPOSITION
Isoparaffin IONP	26	6.3	10	Magnetite
DBPC-IONP	50	~ 45	30	Magnetite
LαPC-IONP	50	~ 58	~ 30	Magnetite
Dextran-IONP	50	~ 58	~ 30	Magnetite

Table 3.2. *Summary of magnetic microbubbles properties*

FORMULATION	CONCENTRATION [MB/mL] [a]	DIAMETER [μm]	IRON LOADING [pg/MB]	MAGNETIC RETENTION [b]	HALF-LIFE IN FLOW [c] [hr]
OilMB	$(0.1 \pm 0.1) \times 10^9$	5.1 ± 1.4	0.61	(19 ± 7) %	0.1
LipMB-DBPC	$(1.4 \pm 0.4) \times 10^9$	1.9 ± 0.3	0.036	(15 ± 6) %	2.0
LibMB-LαPC	$(1.4 \pm 0.6) \times 10^9$	1.9 ± 0.2	0.014	(10 ± 8) %	0.3
SurfMB	$(1.1 \pm 0.6) \times 10^9$	2.1 ± 0.4	0.71	(61 ± 11) %	0.9
Unloaded	$(0.9 \pm 0.5) \times 10^9$	2.2 ± 0.4	-	-	0.4

[a] Concentration measured immediately after production, prior to cleaning. [b] Percentage difference in B-mode image intensity of a channel containing flowing microbubbles produced by the application of a magnetic field. [c] Obtained by fitting an exponential curve to the measured change in microbubble concentration over time.

3.3.2. General protocol

A mixture of lipids and surfactants dissolved in chloroform were added to a glass vial to produce a 5 mL batch of microbubbles at a total concentration 4 mg/mL. The sample was covered with pierced parafilm and set on a hot plate at 50°C for 12 hours to evaporate the chloroform. Once all the solvent evaporated, the dried lipid film was suspended in 5 mL of PBS for 1 hour at 80°C under constant magnetic stirring. The magnetic stir bar was then removed.

The lipid mix solution was sonicated at low intensity (QSonica Q125, 20kHz, 3 mm probe tip, amplitude: 20%, 1 min) with the sonicator probe tip immersed in the solution (**Figure 3.5a**). The sonicator probe tip was then moved to touch the air and water interface and a light flow of sulphur hexafluoride gas was added to fill the headspace of the sample vial (**Figure 3.5b**). The sonicator was then turned on at high intensity (amplitude: 80%, 20 s). The samples were capped and cooled on ice for 10 minutes after which a layer of foam was visible at the top of the sample with a thick layer of densely packed microbubbles underneath.

Cleaning of microbubbles was done through centrifugation using 10 mL syringes modified to fit into 50 mL centrifuge tubes. The sample was aspired into the syringe using

a blunt 18-G needle. The syringe was capped, placed into a 50 mL centrifuge tube and centrifuged at 100 g for 5 minutes at 4°C. The subnatant was removed, the bubbles were resuspended in the original volume of PBS at 4°C, and the washing procedure was completed a total of three times.

(a) Low intensity sonication

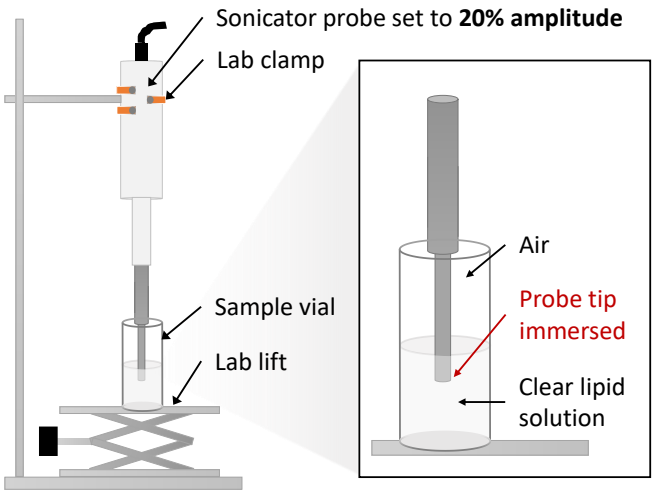

(b) High intensity sonication

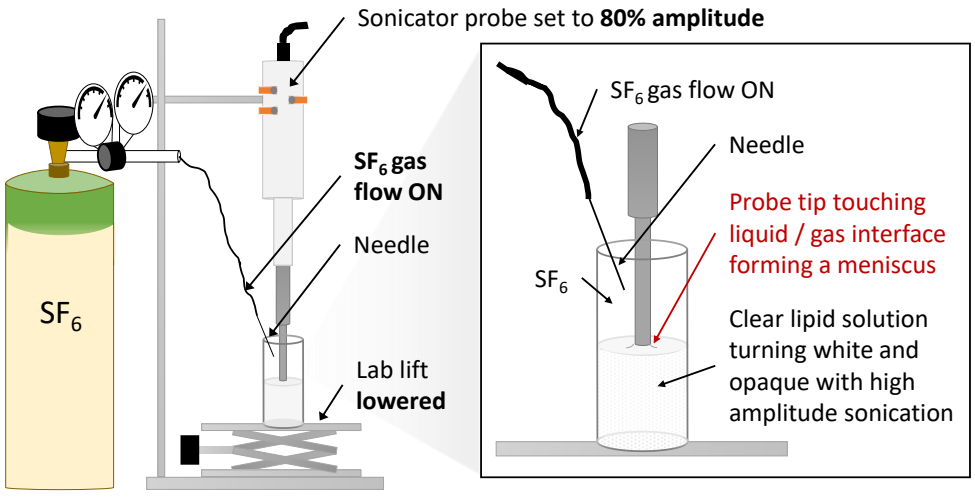

Figure 3.5. *Schematic depicting the general protocol for microbubble manufacturing showing the placement of the sonicator probe tip for the* ***(a)*** *low intensity sonication (20%) with the tip immersed in the lipid solution which is clear after 1 min of sonication. This is followed by the* ***(b)*** *high intensity sonication (80%) with the tip just touching the SF_6 gas and liquid interface forming a meniscus. Upon high amplitude sonication (20 s), the clear lipid solution turned opaque white. After these two sonication steps, the sample vial was immediately capped and placed on ice.*

3.3.3. Preparation of unloaded microbubbles

Unloaded microbubbles were prepared following the general protocol, using a 9:1 molar ratio mixture of DBPC:PEG40S to prepare the lipid mix.

3.3.4. Preparation of **LipMB** (phospholipid-mediated loading)

To make magnetic microbubbles through phospholipid-mediated loading, the lipid mix was prepared according to the protocol for unloaded microbubbles. A volume of LαPC or DBPC IONPs corresponding to 3.75 mg of iron oxide was then added between the low-intensity and the high-intensity sonication. Cleaning was carried out according to the general protocol.

3.3.5. Preparation of **OilMB** (oil loading)

To make magnetic microbubbles with nanoparticles suspended in oil, the lipid mix was prepared according to the protocol for unloaded microbubbles. A volume of isoparaffin IONPs corresponding to 3.75 mg of iron oxide was added after the two sonication steps. The vial was capped and cooled on ice for 5 minutes before repeating the two sonication steps to form magnetic microbubbles. Cleaning was carried out according to the general protocol.

3.3.6. Preparation of **SurfMB** (surface loading)

To make magnetic microbubbles via surface loading, the lipid mix was prepared with a 82:9:9 mixture of DBPC:PEG40S:DSPE-PEG2000-biotin. The general protocol was followed until the cleaning step. The suspension was then cleaned to remove excess lipids in solution via centrifugation. 2 mL of a 2.5 mg/mL solution of avidin in PBS was added to

the resuspended biotinylated microbubbles and left to mix on ice on a rotary shaker for 5 minutes. The microbubbles were then centrifuged again before adding 300 µL of biotin-dextran IONPs (12.5 mg/mL) to the resuspended avidin-loaded microbubbles. The sample was left to mix on ice on a rotary shaker for 5 minutes again. The magnetic microbubbles were centrifuged once more and finally resuspended with PBS at 4°C.

3.4. Methods and results for microbubble characterisation

3.4.1. Overview of microbubble characterisation

The different magnetic microbubbles shown in **Figure 3.1** were compared in terms of their physical stability, acoustic, and magnetic response. The physical stability of microbubbles was quantified by measuring their concentration decay over time at 37°C and under flow (10 mL/min). Langmuir trough measurements were used to measure the mechanical properties of the lipid monolayer systems at the gas and water interface similar to the microbubble shell [232]. In particular, these were conducted to capture changes in surface tension of lipid-mix monolayers upon compression and expansion, and the findings were compared with the microbubble physical stability results. The acoustic properties of the different formulations were assessed at both 1 MHz, typical for therapeutic ultrasound applications, and 7 MHz to evaluate them for diagnostic ultrasound imaging. The iron content of microbubbles was measured using inductively coupled plasma optical emission spectroscopy to determine the quantity of iron oxide nanoparticles still incorporated into the microbubbles after cleaning of the suspension. The quantity of microbubbles retained under flow (0.2 mL/min) under the influence of a magnetic field was also measured. Finally, the toxicity of the formulations was examined by measuring the levels of haemolysis recorded in horse blood following incubation with microbubbles at 37°C.

3.4.1.1. Statistical analysis

Statistical analyses were performed using Microsoft Excel and GraphPad Prism with significance defined as $p < 0.05$ unless otherwise indicated. GraphPad Prism was also used to perform nonlinear regression modelling. One-way ANOVA was used for experiments investigating the difference between more than two groups with post-hoc Tukey HSD test. Data are presented as mean ± standard deviation unless otherwise indicated.

3.4.2. Microbubble size and concentration

3.4.2.1. Method

Microbubble size and concentration were determined through analysis of optical microscopy images [233] as previous studies have confirmed the reliability of this method compared to other options available [233–236]. For this, the microbubble suspension was diluted 1:20 in PBS and 10 µL were loaded onto a haemocytometer with a cover slide. 30 microscope images were acquired through an optical microscope (Leica DM500 optical microscope, Larch House, Milton Keynes, MK14 6FG, UK) with a 40x objective lens at room temperature. The images were then analysed using purpose written MATLAB code (R2016b, The MathWorks, Natick, MA, USA) to determine microbubble mean size and concentration [233]. With this method approximately 1800 bubbles are analysed per microbubble batch.

3.4.2.1. Results

The size distribution and concentration of unloaded microbubbles before and after centrifugal cleaning are shown in **Figure 3.6**. indicating a reduction in concentration during the cleaning process although the size distribution remained comparable.

(a) Size distribution of unloaded microbubbles (b) Unloaded microbubbles cleaned

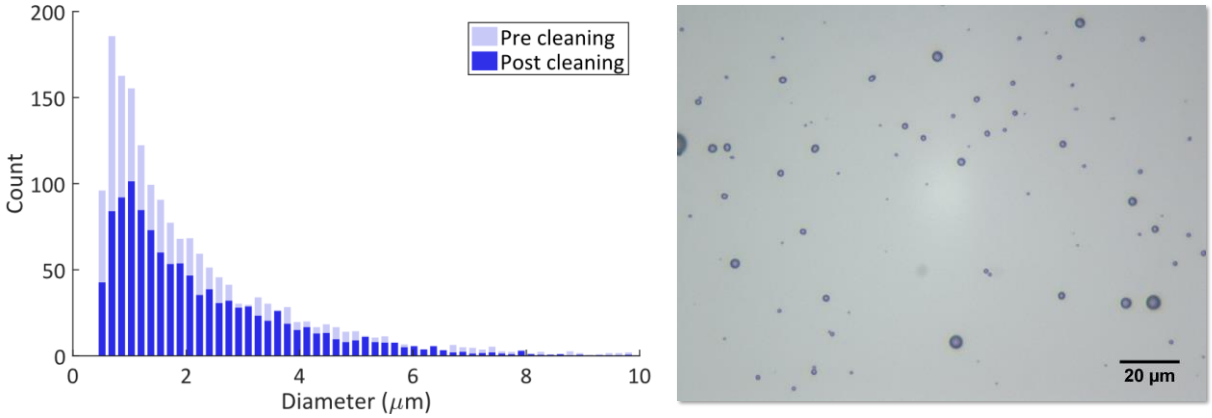

Figure 3.6. (a) *Size distribution of unloaded microbubbles pre- and post- cleaning.* ***(b)*** *Optical microscope image of post-cleaning microbubbles. Scale bar indicates 20 µm and cleaning was achieved with three centrifuge runs (100 g, 5 minutes, 4°C). Due to the optical resolution of the system particles smaller than 0.5 µm were ignored.*

The concentration and mean diameter for the different magnetic microbubble formulations considered in this chapter are shown in **Figure 3.7**. **OilMB** exhibited a significantly lower yield and larger mean diameter compared to all other groups, with approximately 10 times fewer bubbles produced of double the size. This effect could be due to excess surfactant[1] present in the isoparaffin IONPs suspension disrupting the phospholipid coating or to the oil phase itself reducing the coating integrity. The remaining formulations tested, however, presented comparable concentrations and sizes. Average concentrations of (1.2±0.2) $\times$ 10^9 and (0.4±0.1) x 10^9 MB/mL were obtained before and after cleaning respectively for unloaded microbubbles, **LipMB** and **SurfMB**. In contrast, **OilMB** presented a lower yield with (0.1±0.1) x 10^9 and (0.04±0.05) $\times$ 10^9 MB/mL before and after cleaning respectively.

[1] The isoparaffin IONPs used in this work are stabilised with a surfactant. We unfortunately could not obtain information on the nature of the surfactant from the manufacturer.

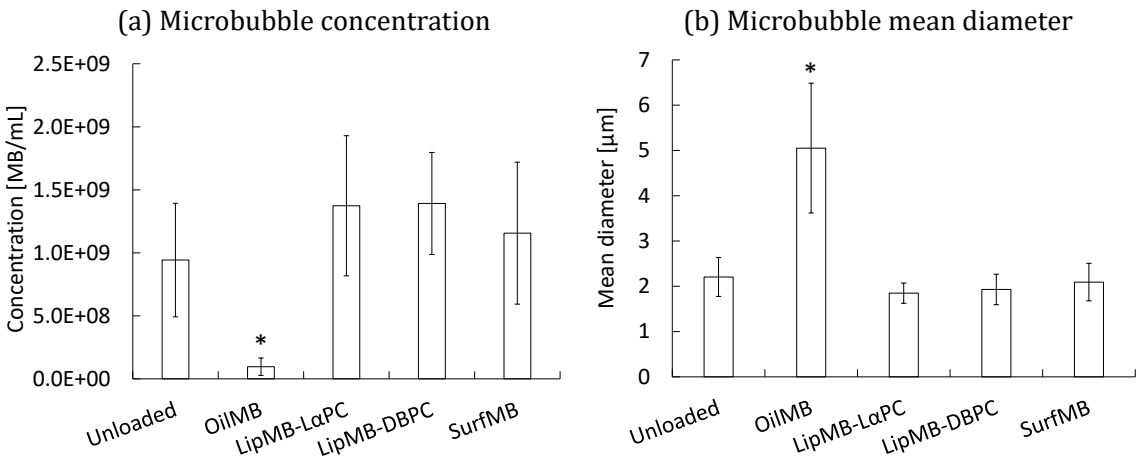

Figure 3.7. *Microbubble pre cleaning* ***(a)*** *concentration [MB/mL] and* ***(b)*** *mean diameter [µm] obtained from n = 3 microbubble batches per formulation, with each 30 optical microscope images analysed using purposely written MATLAB script. * p < 0.05 compared to all other groups.*

3.4.3. Stability studies

3.4.3.1. Method

The stability of the different microbubble formulations was investigated by measuring changes in microbubble concentration over time under flow at 37°C in PBS. Flow was induced by a Gilson Minipuls 3 peristaltic pump from Fisher Scientific (Loughborough, UK) used with a 1.6 mm inner diameter latex tube producing a flow rate of 10 mL/min. These conditions were chosen to represent the flow parameters found in small arteries and veins [237,238], and the Reynolds number *Re* was calculated following Equation 2 to determine if the flow was laminar or turbulent.

$$Re = \frac{DV}{\nu} \qquad (2)$$

Where: *D* is the diameter of the tube, *V* is the axial velocity of the flow, and *v* is the kinematic viscosity of the fluid (dynamic viscosity / density of the fluid). The same calculation was also done for several biological vessels for comparison. When the flow

was found to be laminar (*Re* < 2000), the wall shear rate *γ* (WSR) was calculated following Equation 3.

$$\gamma = \frac{4Q}{\pi r^3} \quad (3)$$

Where: *Q* is the volumetric flow rate, and *r* is the radius of the tube. The wall shear stress (WSS) was then computed as shown in Equation 4 with *v* still representing the kinematic viscosity.

$$WSS = \nu \times WSR \quad (4)$$

The results from these calculations are presented in **Table 3.3**. Since injected microbubbles are exposed to a range of flow conditions in biological systems, the parameters used for the stability study were chosen to represent those found in small arteries.

Table 3.3. *Flow parameters for biological vessels compared to the chosen testing conditions. The diameters and flow velocities for biological vessels were obtained from the referenced work.*

VESSEL	DIAMETER	FLOW VELOCITY	REF	VOLUMETRIC FLOW RATE	REYNOLDS NUMBER [a]	SHEAR RATE [s^{-1}]	SHEAR STRESS [Pa]
Ascending aorta	25 mm	100 cm/s	[239]	0.5 L/s	6600	-	-
Femoral artery	8 mm	33 cm/s	[239]	1000 mL/min	690	330	1.3
Small arteries	1.8 mm	10 cm/s	[240]	15 mL/min	50	440	1.8
Testing tubing	**1.6 mm**	**8 cm/s**	**-**	**10 mL/min**	**130** [b]	**410**	**1.7**
Arteriole	30 µm	3 mm/s	[239]	0.13 µL/min	0.02	800	3.2
Capillaries	8 µm	1 mm/s	[241]	0.003 µL/min	0.002	1000	4

[a] Calculated with a blood kinematic viscosity of 4 x 10^{-6} m^2/s [239] unless indicated otherwise. [b] Calculated with a water kinematic viscosity of 1 x 10^{-6} m^2/s.

Using these flow conditions, microbubble concentration measurements were made at t = 15, 30, 45 minutes, 1, 1.5, 2, 2.5, 3 hours. Each formulation was tested four times and the collected data was fitted to a one-phase exponential decay nonlinear curve model using GraphPad Prism (Version 6, GraphPad Software Inc., La Jolla, CA, USA) which showed a randomness of residuals.

3.4.3.1. Results

The results of the stability studies on microbubbles exposed to flow at 37°C are shown in **Figure 3.8**. One-phase exponential decay nonlinear regression models were fitted to the datasets and indicated that DBPC IONPs and dextran IONPs both produced magnetic microbubbles with significantly improved stability by more than doubling their half-lives to 2 and 0.9 hour respectively compared to 0.4 hour for unloaded bubbles. In contrast, the hydrophobic incorporation of isoparaffin IONPs resulted in a significant decrease in stability (half-life of 0.1 hr).

Microbubbles were observed over three hours circulating in a 2 mL flow loop at 37°C which is a longer timeframe than that reported in *in vivo* models. This difference in timescale is explained by the absence of clearance mechanisms that exist *in vivo* and the fact that microbubbles were undiluted in the flow loop [242].

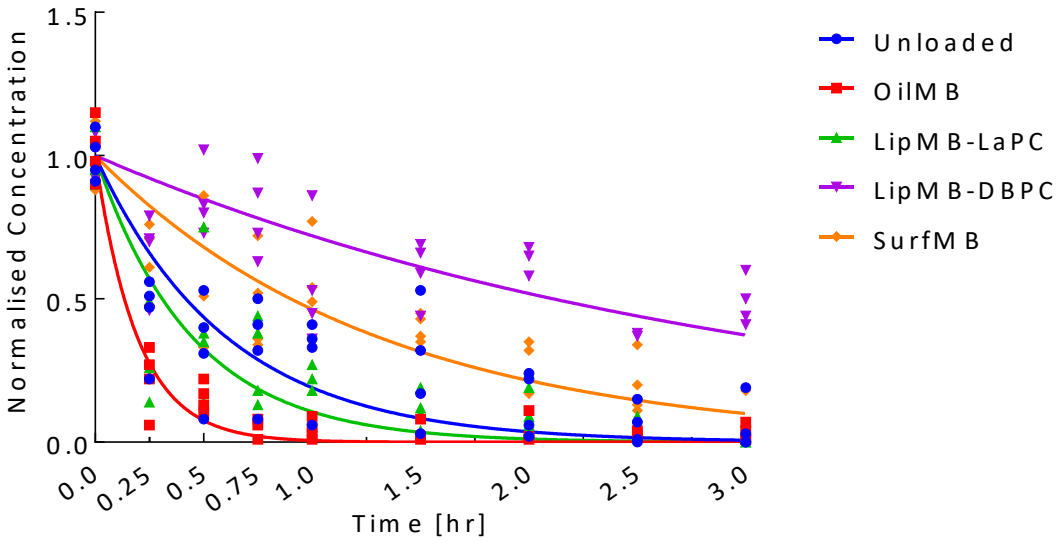

Figure 3.8. *Microbubble stability measured in terms of normalised concentration over 3 hours under flow (10 mL/min) at 37°C for n = 4 batches per formulation. One-phase exponential decay nonlinear regressions were fitted to the datasets and the rate constants for magnetic microbubbles were compared. * $p < 0.05$ to that of unloaded systems.*

The incorporation of nanoparticles into microbubbles has been shown previously to reduce gas diffusion and microbubble coalescence through a form of Pickering stabilisation [148], which might explain the stability of **LipMB-DBPC** and **SurfMB**. The solid nanoparticles reduce the surface area available for gas diffusion and physical jamming of the particles can inhibit microbubble shrinkage. The addition of LαPC IONPs had a destabilising effect which could be due to the presence of acyl chains of different length in LαPC (approximately 33% 16:0, 13% 18:0, 31% 18:1, 15% 18:2 PC) reducing the molecular packing on the microbubble surface and hence the resistance to gas diffusion. Isoparaffin IONPs also had a destabilising effect on microbubbles initially indicated by the low production yield of this formulation (**Figure 3.7a**). Similarly, this may be due to surfactants in the isoparaffin product affecting the packing of the phospholipid coating.

The relative instability of this formulation was further indicated by the results shown in **Figure 3.9**. Additional measurements were made for **OilMB** at 37°C and under flow, of the number of magnetic droplets settled at the bottom of the haemocytometer and the number of buoyant magnetic microbubbles at the top of the sample underneath the coverslip. **Figure 3.9** indicates a decrease in the buoyant **OilMB** over time while the number of magnetic droplets sunken at the bottom of the haemocytometer increased. The size of the droplets suggests that this might have been caused by diffusion of the encapsulated gas out of **OilMB**, forming magnetic droplets that then sank due to the absence of a gas core. The Langmuir trough measurements discussed in the next section support this.

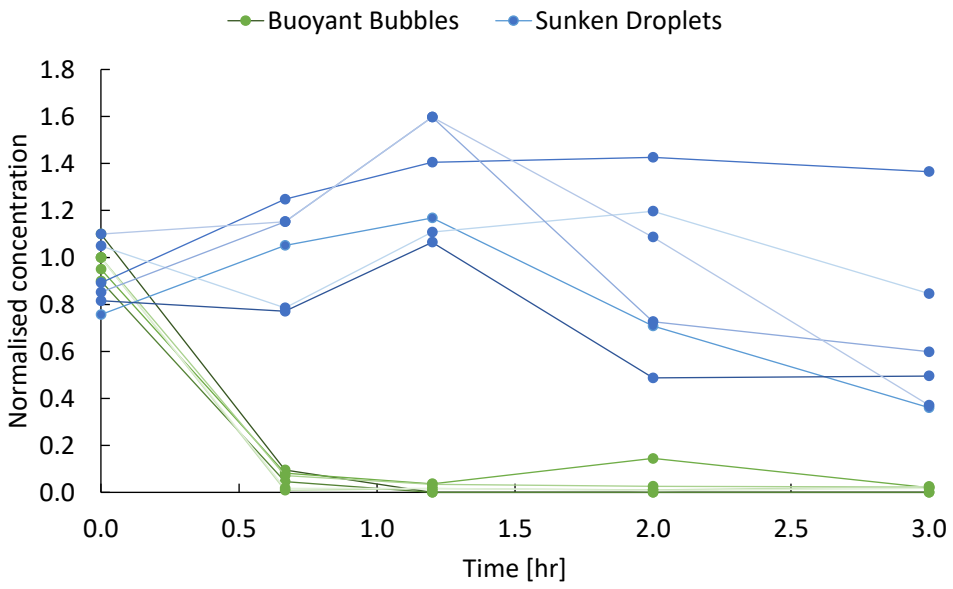

Figure 3.9. *Concentration over time of buoyant and sunken particles from OilMB. Experiment run over 3 hours under flow (10 mL/min) at 37°C for n = 6 batches per group.*

3.4.4. Langmuir trough

3.4.4.1. Methods

To further investigate the differences in magnetic microbubble stability, Langmuir trough experiments were completed to provide the surface pressure of the monolayers. An intermediate compression or expansion rate of 56 mm^2/s was chosen to evaluate the system's integrity over gradually increasing or decreasing pressure. Since this data is indicative of the integrity and physical properties of the lipid monolayer, it can be used to understand the characteristics of microbubbles immediately after manufacturing and during stabilisation. The experiments were conducted at room temperature and 37±1°C on a MicroTrough XL model with inner dimensions of 39.3 x 5.9 cm from Kibron (Kenilworth, Warwickshire, UK) connected to a recirculating chiller-heater for temperature control (**Figure 3.10**).

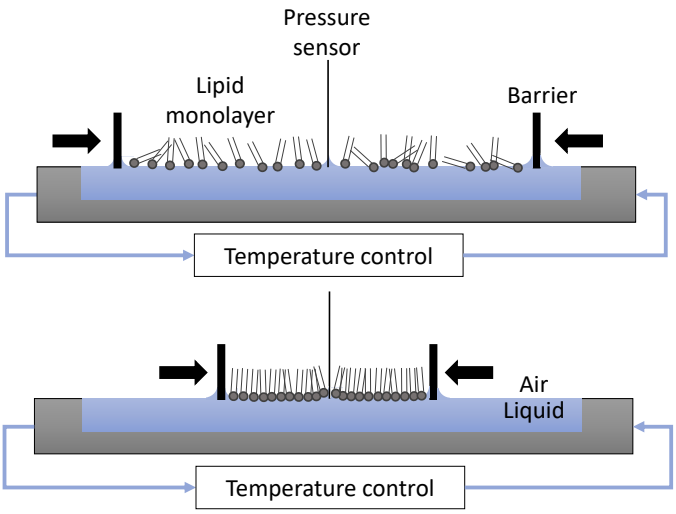

Figure 3.10. *Schematic of Langmuir trough. Experimental set-up used for the characterisation the surface pressure of a lipid monolayer upon compression and expansion.*

A lipid monolayer was formed at the gas and water interface of 75 mL of deionised water by adding 1 µL of lipids dissolved in chloroform (25 mg/mL) and letting it equilibrate for 5 minutes after which it was compressed (56 mm^2/s) from 11000 mm^2 to 2000 mm^2. The average area per lipid molecule was calculated using the average lipid molecular weight. The surface pressure (Π) of the monolayer was then measured over the molecular area ($Å^2$/molecule). The effect of phospholipid-mediated loading of IONPs on a lipid monolayer was studied by adding IONPs to the deionised water subphase at a concentration of 20 µg/mL before forming the lipid monolayer. Isoparaffin IONPs were added in corresponding amounts on top of the lipid monolayer before compression due to their hydrophobicity.

Optical microscope pictures were also acquired during Langmuir trough compression and expansion of the monolayer. The lipid dye NBD-PE (λ_{ex} = 463 nm, λ_{em} = 536 nm) was used to highlight the presence of lipids within the monolayer. A 20x objective (LWD M PLAN FL 20x Olympus) was used with a camera (C11440-36U, Hamamatsu) to image the monolayer with excitation wavelength 470±15 nm and emission 500 nm long pass filter.

3.4.4.2. Results

Surface pressure-area (Π-a) isotherms of DBPC:PEG40S monolayers without IONPs were characterised and imaged at 18°C and 37°C for different pressure ranges. A lipid dye (NBD-PE) was used to highlight the presence of lipid domains on images shown in **Figure 3.11**, whereas a fluorescent-PEG40S was used to highlight emulsifier domains shown in **Figure 3.12**. As the molar ratio used of each fluorescent probe was a fraction of the other components of the monolayer (DBPC:PEG40S:fluorescent probe, 8.9:1:0.1 molar ratio), these measurements are representative of the behaviour of DBPC:PEG40S systems.

Upon formation of the monolayer and before compression, the images in **Figure 3.11** highlight the spreading behaviour of the emulsifier PEG40S initially dominating the image as **A1** is mostly dark with only few bright domains for the presence of lipids. **Figure 3.12** correspondingly shows bright surfactant domains highlighting the presence of PEG40S. Upon compression, the isotherms show an initial gradual rise in surface pressure followed by an intermediate plateau around 35 mN/m which has been reported as the collapse pressure of PEG40S [232]. The presence of this plateau was associated with the "squeeze-out" of emulsifier from the monolayer [232,243], confirmed by **Figure 3.12 C** and **D** with a decrease in image brightness from the removal of PEG40S beyond 35 mN/m. Following PEG40S elimination, the slope of the isotherm steepens due to the dominant behaviour of the remaining DBPC monolayer which then undergoes an irreversible collapse beyond 60 mN/m at 18°C. This effect is highlighted by a plateau at the highest pressure followed by a broad hysteresis due to the loss of material upon monolayer expansion. Although the compression cycles shown in **Figure 3.11** were stopped before the irreversible collapse, the slight hysteresis between **C1** and **C2** indicates a loss of material. In the corresponding images, the reappearance of lipid domains could be due to lipid budding and vesicle

formation during compression [243–246] followed by their reintegration into the monolayer upon expansion. This effect might, however, be dependent on the expansion occurring before the irreversible collapse pressure is reached.

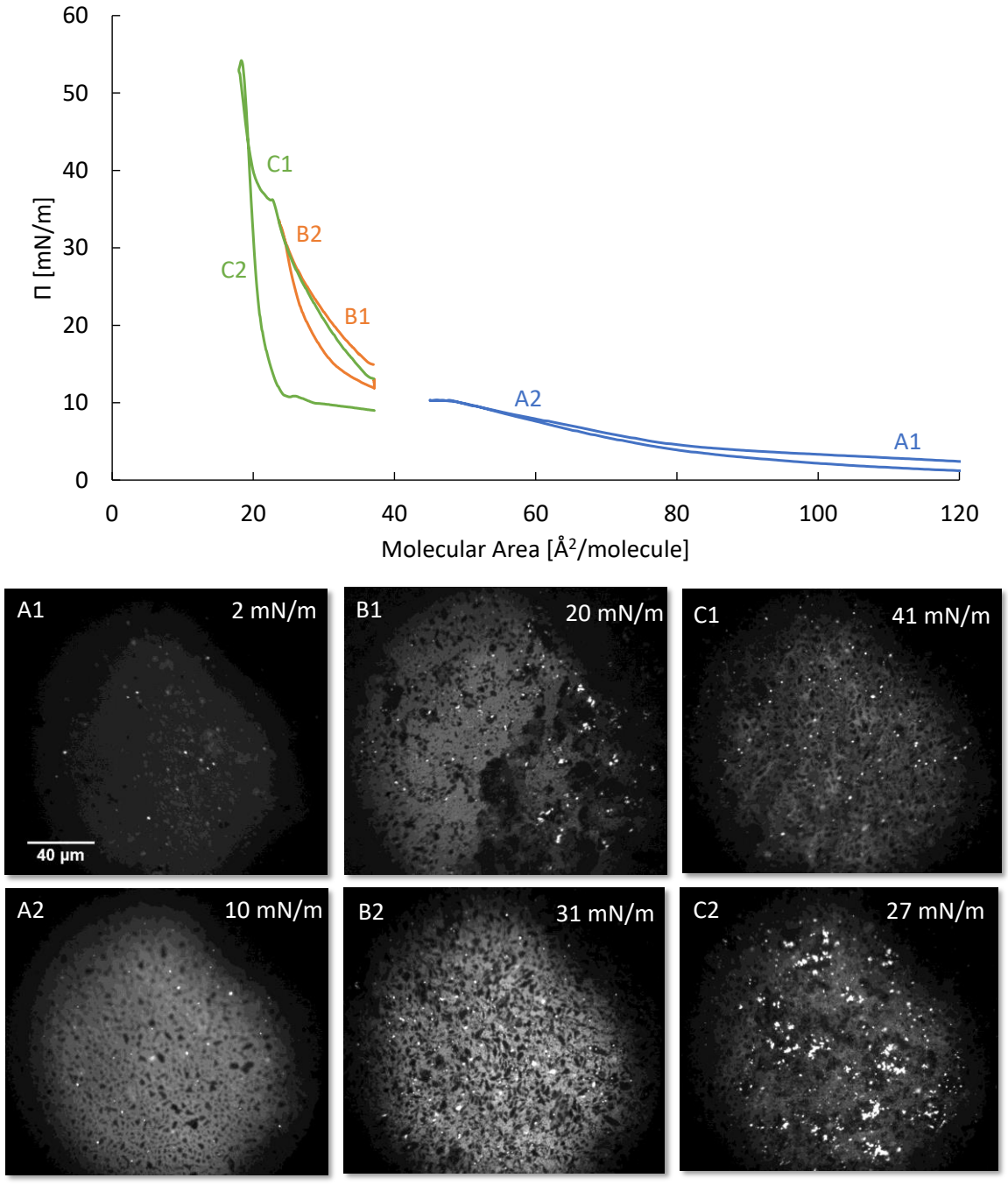

Figure 3.11. *Langmuir isotherms of DBPC:PEG40S:NBD-PE (8.9:1:0.1 molar ratio) monolayers at 18°C for three runs: A, B, C over which the target pressure was increased. Labelled pictures were captured at the corresponding point on the isotherms, and bright domains indicate the presence of lipids through the fluorescence of NBD-PE. The scale bar indicates 40 µm.*

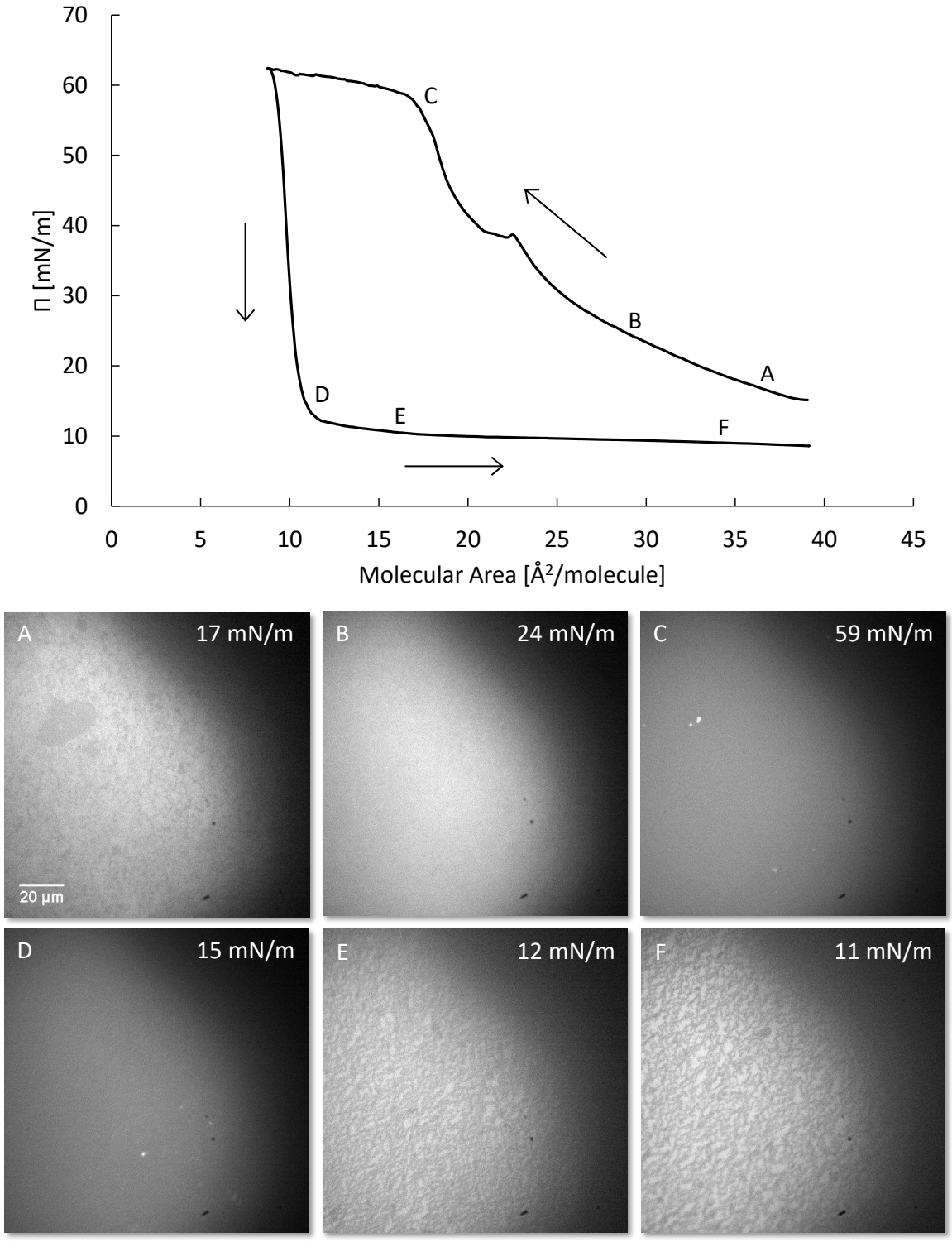

Figure 3.12. *Langmuir isotherms of DBPC:PEG40S:FITC-PEG40S (8.9:1:0.1 molar ratio) monolayers at 18°C for one acquisition over which the pressure was increased (A, B, C) and decreased (D, E, F) in the direction indicated by the arrows. Labelled pictures were captured at the corresponding points on the isotherms, and bright domains are the fluorescent emulsifier FITC-PEG40S. The scale bar indicates 20 µm.*

The effect of adding IONPs to the monolayer was then tested at 37°C and the results presented in **Figure 3.13** were compared to that of a control monolayer without nanoparticles. The addition of isoparaffin and LαPC particles lowered the final collapse pressure of the monolayer and the presence of LαPC IONPs also reduced the surfactant "squeeze-out" plateau around 35 mN/m with a flatter isotherm. In contrast, the addition of DBPC IONPs produced a steep isotherm overlapping that of the control and an increased final collapse pressure.

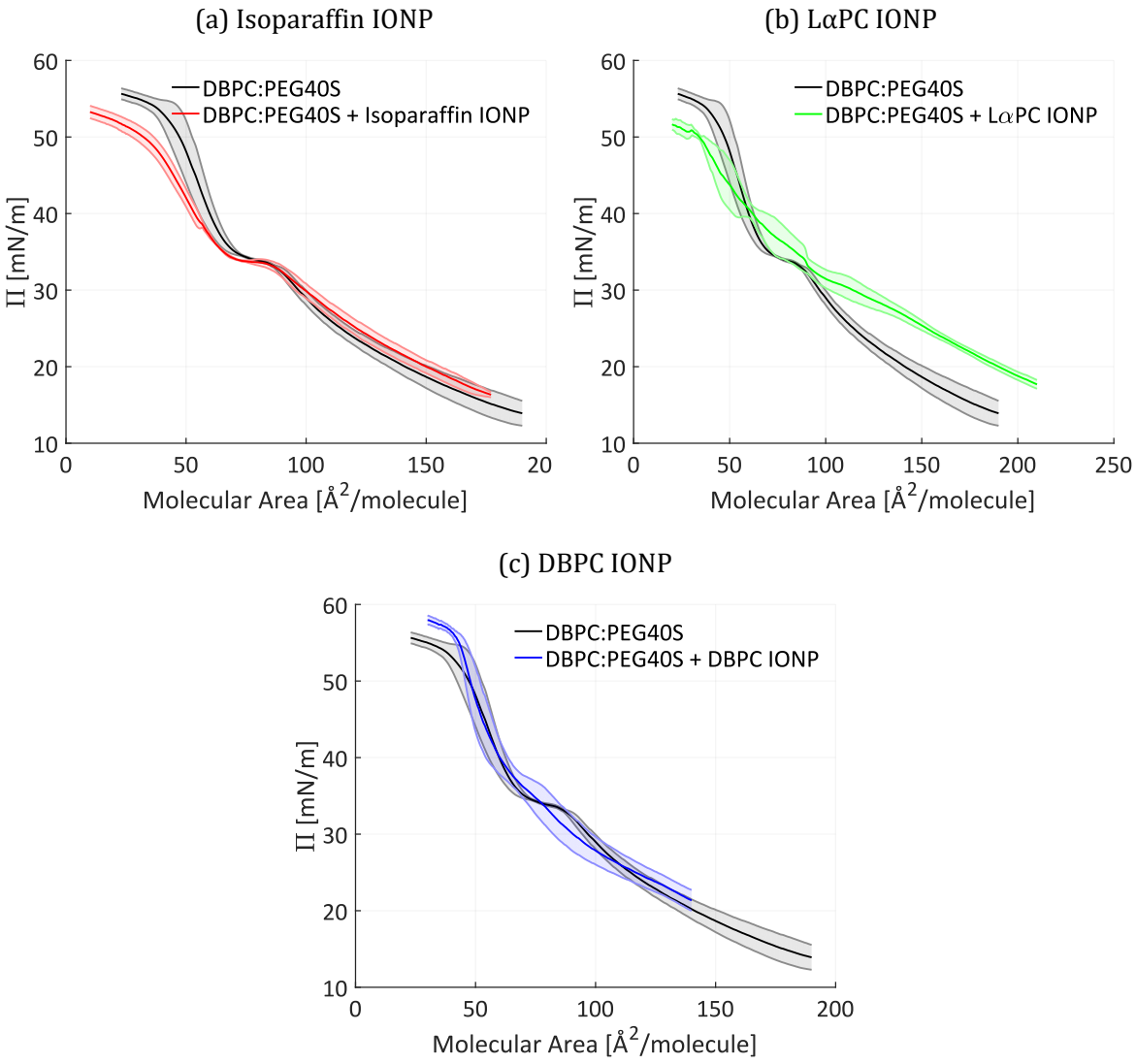

Figure 3.13. *Pressure-area isotherms of DBPC:PEG40S monolayers ± IONPs for* ***(a)*** *hydrophobic isoparaffin IONPs, phospholipid-stabilised* ***(b)*** *LαPC IONPs, and* ***(c)*** *DBPC IONPs. The isotherms of the magnetic microbubble formulations are overlaid with the isotherm of unloaded microbubbles. For each formulation, the mean and standard deviation around it are shown for n = 3 runs.*

Upon formation of microbubbles, the lipid-mix coating is compressed due to the Laplace pressure driving the system towards dissolution. Langmuir trough results for control monolayers demonstrate that as the lipid packing increases, the emulsifier would be squeezed out of the unloaded microbubble coating until the remaining condensed-phase lipids reach a meta-stable state with very low surface tension enabling bubble stabilisation [232]. However, remaining PEG40S within the coating would hinder the system from reaching this metastable state. This is reflected in the results for the addition of LαPC IONPs indicating that **LipMB-LαPC** might not squeeze out PEG40S during compression due to an overall less organised microbubble coating. Contrastingly, the addition of DBPC IONPs indicated that **LipMB-DBPC** would exhibit compressional properties comparable to those of unloaded microbubbles. Moreover, the added DBPC from the IONPs may provide an increased stability, highlighted on the isotherm with an increased final collapse pressure compared to a control monolayer. This demonstrates that the lipid coating on the IONPs can affect the stabilisation of magnetic microbubbles incorporating them. Finally, Langmuir trough results for the addition of isoparaffin IONPs suggest that **OilMB** should demonstrate similar compressional properties to that of unloaded systems with, however, a lower stability under compression indicated by a decrease in the monolayer collapse pressure. Nonetheless, these measurements assume the gas phase remains stable and separated from the liquid phase. Therefore, these results suggest that the poor physical stability of **OilMB** might not be related to the compressional properties of the microbubble coating but could be caused by other factors such as the stability of the encapsulated gas core as previously proposed with **Figure 3.9**.

3.4.5. Microbubble acoustic properties

3.4.5.1. Method with 1 MHz

A custom-made tank with a built-in 1 MHz transducer (**Figure 3.14**) was filled with degassed deionised water. A 14 mL sample was prepared and 10 mL were injected into a chamber adapted from [247], and placed in the pre-focal region of the transducer to allow a uniform pressure field at the top surface of the chamber (Appendix C.1.). The transducer was driven by a 33220A waveform generator from Agilent Technologies (Cheshire, UK) amplified with a gain of 55 dB (A300, E&I Ltd., Rochester, NY, USA). The output voltage of the amplifier was verified using a high-voltage probe and HDO4024 oscilloscope from Teledyne Lecroy for each ultrasound exposure. The temperature of the sample before and after ultrasound was measured using a PCE-T390 thermometer from PCE Instruments.

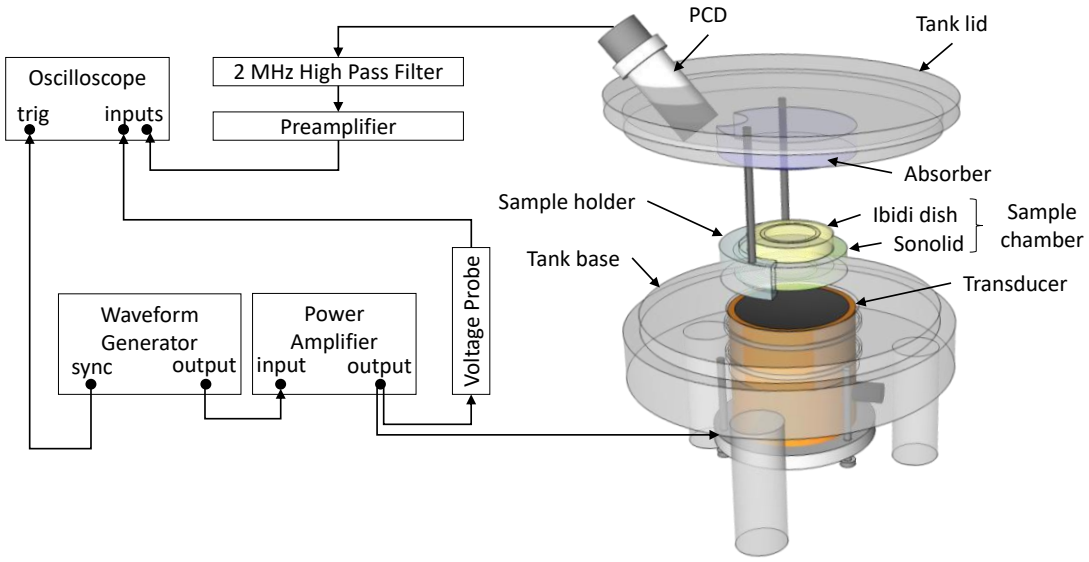

Figure 3.14. *Schematic of experimental set-up used to characterise microbubbles at 1 MHz which was designed and characterised by Dr. Michael Gray.*

The acoustic emissions from microbubbles exposed to 1 MHz ultrasound were recorded using a passive cavitation detector (PCD, 7.5 MHz centre frequency, 12.7 mm diameter, 75 mm focal distance, Olympus NDT, Essex, UK). A 2 MHz high-pass filter was

used to remove the drive frequency from the recorded PCD traces before preamplifying (SR445A, SRS, Sunnyvale, CA, USA), digitising it (Handyscope HS3, TiePie Engineering, Sneek, Netherlands) and saving it on a computer drive for analysis. As in **Figure 3.15**, the acquired PCD traces were multiplied by a Tukey window to reduce discontinuities and analysed with a Fast Fourier Transform (FFT) using MATLAB. The harmonics (multiples of the drive frequency ± 100 kHz, > 2 MHz), ultraharmonics (half-integer harmonics of the drive frequency ± 50 kHz, > 2 MHz), and broadband (remaining signal > 2 MHz) components were extracted for each acquisition. The power and cumulative energy in these frequency subsets were calculated for each acquisition over the exposure time.

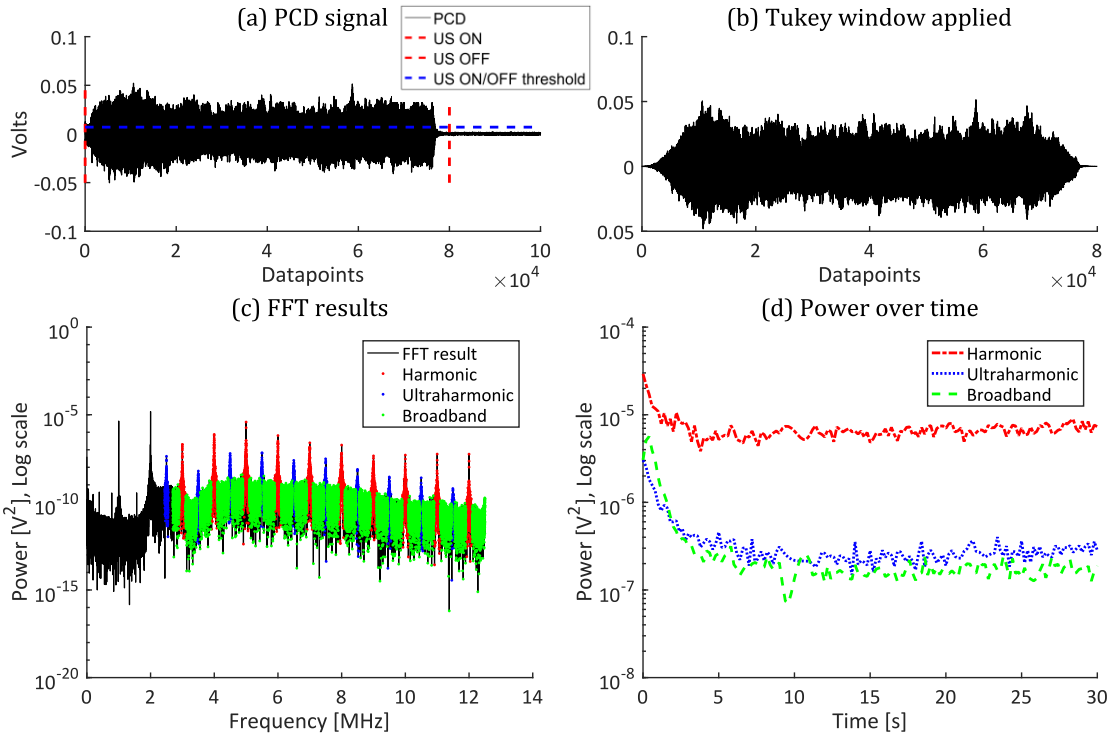

Figure 3.15. *Analysis of the acoustic emissions with a PCD.* ***(a)*** *A threshold was used to determine if the ultrasound was ON.* ***(b)*** *A tukey window was then applied to avoid discontinuites at the start and end of each acquisition.* ***(c)*** *A Fast Fourier Transform (FFT) was done and the contributions of harmonic, ultraharmonic, and broadband emissions were segmented. Finally,* ***(d)*** *the power over exposure time within each frequency range was computed and an integral of the power over time gave the cumulative energy for each frequency range.*

The emission power over time was analysed for each frequency subset and formulation. As the emissions decayed to a plateau within the first 5 seconds of exposure, the mean and standard deviation were plotted over that period to provide an observation of the spread of the data for each group. The data was then fitted to a plateau followed by a one-phase exponential decay in order to provide a comparison between the datasets. This model was chosen as it incorporates a possible delay before the acoustic emissions decay over time. The nonlinear regression model is governed by Equations 5-6.

$$When\ t < t_0, \qquad P = P_0 \tag{5}$$

$$when\ t \geq t_0, \qquad Plateau + (P_0 - Plateau)\, e^{-K(t-t_0)} \tag{6}$$

where: t_0 is the time at which the decay begins, P_0 is the average power value up to time t_0, *Plateau* is the power value at infinite times, K is the rate constant of the decay. Then, the time constant of the decay is $\tau = 1 / K$, the half-life is $t_{1/2} = ln\ (2) / K$, and the *span* is the difference between t_0 and the *Plateau*, as depicted in **Figure 3.16**.

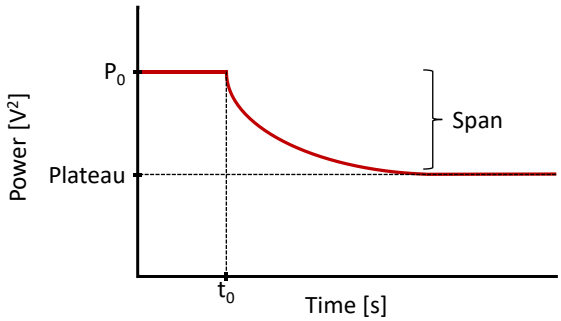

Figure 3.16. *A plateau followed by a one-phase exponential decay was chosen to fit and compare the emission power over time for each formulation. This schematic shows the different parameters for this nonlinear regression.*

With this method, the acoustic emissions for the different formulations could be examined by comparing the fitting parameters of the nonlinear regression. The cumulative energies (integrated power over the entire exposure time) for each frequency subset and formulation were also evaluated.

3.4.5.2. Method with 7 MHz

The magnetic microbubbles were also evaluated at 7 MHz to give an indication of their behaviour while exposed to diagnostic ultrasound (**Figure 3.17**). Deionised water was used as a diluent and flown through a 1.6 mm diameter channel in a 2.5% agar phantom at a rate of 0.2 mL/min. A vessel size of 1.6 mm diameter was chosen to fit the physiological range of small arteries that surround pancreatic tumour lesions [239,248]. A testing flow rate of 0.2 mL/min was used fitting the range of blood flow rates around and within pancreatic lesions [249,250]. This led to a Reynolds number of 2.65, relevant for the circulatory system [251]. A bolus of 200 µL of cleaned $(9\pm1)\times10^6$ MB/mL was injected through a three-way valve and imaged using a commercially available system (iU22, Philips, Bothell, WA, USA) and linear array (L12-5, 7 MHz). A mechanical index (MI) of 0.04 was used as it allowed microbubble imaging using contrast (Harmonic) and tissue (B-mode) imaging modes without an observable decrease in image intensity for the least stable formulation (**Figure 3.17b**).

Commercially available Sonovue® microbubbles (Bracco Imaging, Milan, Italy) were also imaged to provide a comparison. Images were analysed with MATLAB (R2016b, the Mathworks, Natick, USA) by computing grayscale intensities in predefined regions-of-interest (ROIs) for all acquisitions to determine the point at which the injected microbubbles reached constant concentration. Sets of 100 frames at constant microbubble concentration were examined to output the average mean intensity within the ROIs (**Figure 3.17**) and the analysis was completed on both, tissue and contrast images.

(a) Annotated acquisition from Philips iU22 scanner

(b) Analysis results of mean intensity in ROI

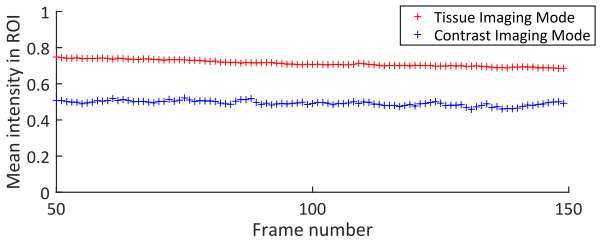

Figure 3.17. *Example of analysis on magnetic microbubbles flowing through an 2.5% agar phantom and imaged using the Philips iU22 scanner, L12-5 ultrasound linear array.* ***(a)*** *Acquired frame showing a ROI for both contrast (red) and tissue (blue) imaging modes for the same sample.* ***(b)*** *Results from the analysis of the mean intensity within the predefined ROIs of both imaging mode over 100 frames.*

3.4.5.3. Results

The acoustic emissions from microbubbles exposed to 1 MHz ultrasound were investigated as this frequency is relevant for therapeutic ultrasound drug delivery, and the energy and duration of the emissions have been shown to be correlated to therapeutic response [252–254]. The acoustic emissions from each magnetic microbubble formulation were measured for suspensions ((1±0.5) $\times 10^7$ MB/mL) exposed to 1 MHz ultrasound, 0.85 $MPa_{pk\text{-}pk}$, 30% duty cycle for 30 seconds (**Figure 3.14**). The signals were analysed for harmonics, ultraharmonics, and broadband emissions separately over the exposure time. **Figure 3.18**, showing the mean and standard deviation of the results for these frequency subsets, indicates a wide range of emission power for each formulation.

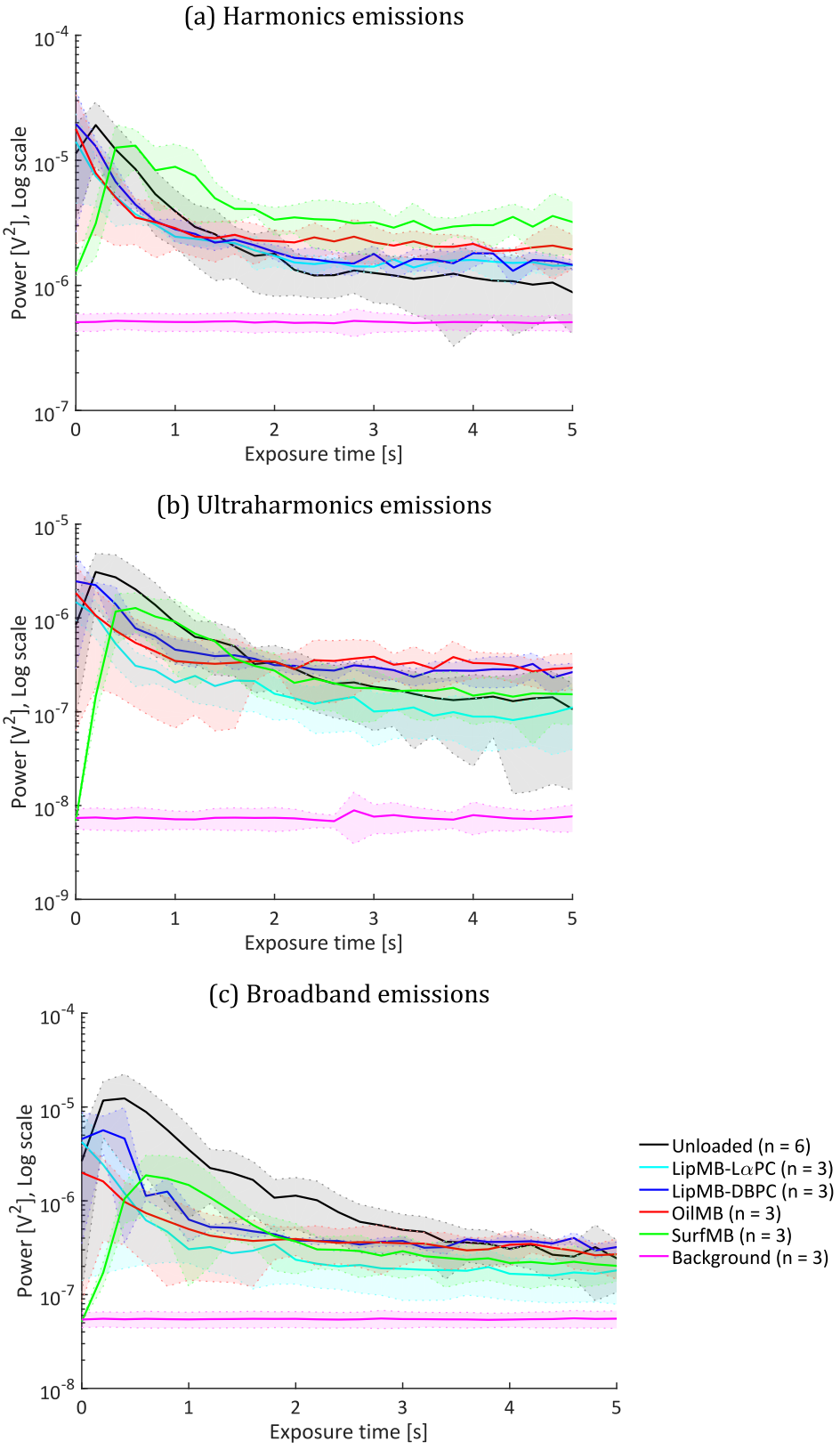

Figure 3.18. *The mean ± standard deviation for the power for the* ***(a)*** *harmonic, and* ***(b)*** *ultraharmonic bands and the remaining* ***(c)*** *broadband emissions are displayed over the first 5 seconds of the 30 seconds exposure for ~ 10^7 MB/mL exposed to 1 MHz, 0.85 MPa_{pk-pk}, 30% duty cycle, 100 Hz PRF.*

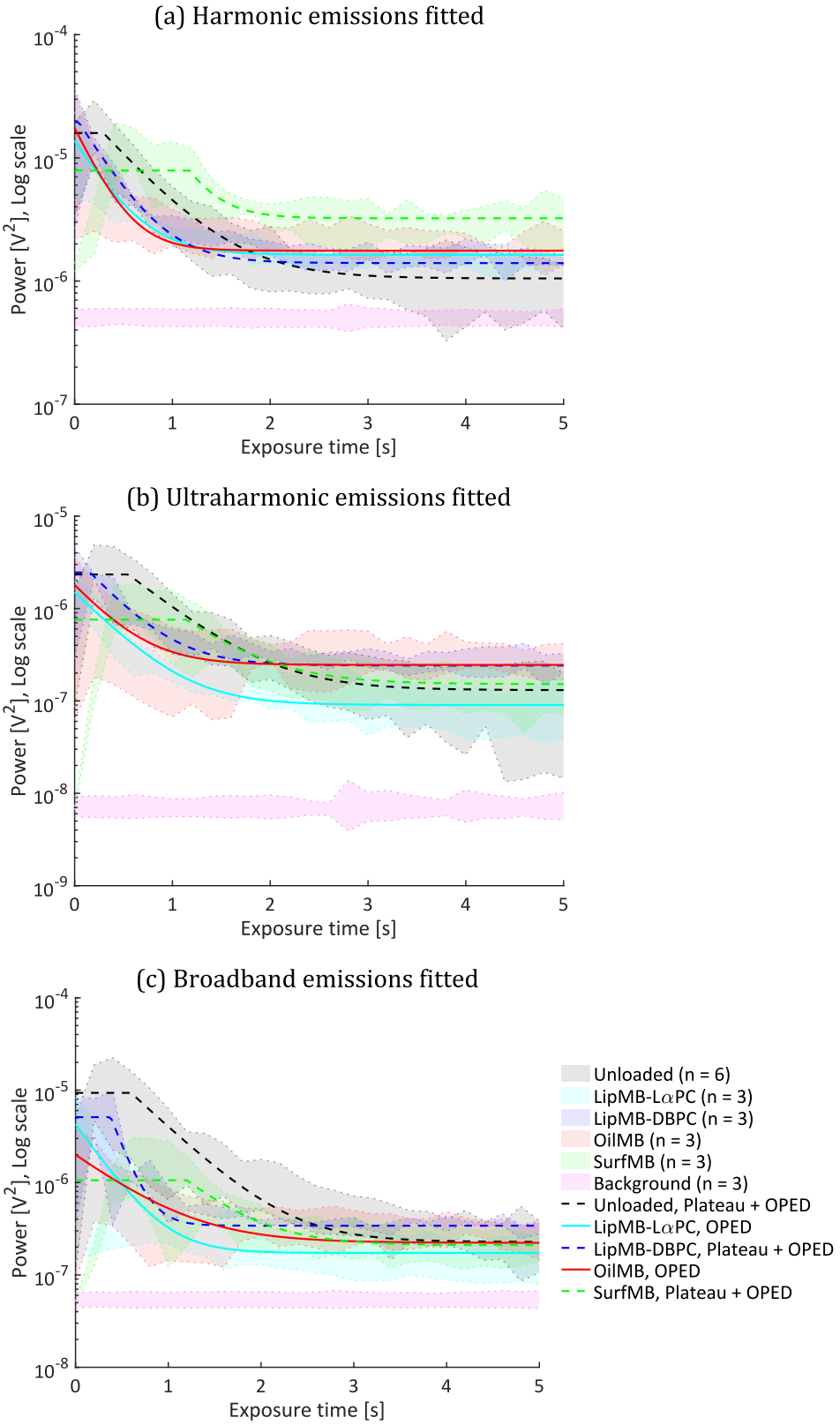

Figure 3.19. *Model with a plateau followed by a one-phase exponential decay (OPED) fitted to the emission powers for the* ***(a)*** *harmonic and* ***(b)*** *ultraharmonic bands and the remaining* ***(c)*** *broadband displayed over the first 5 seconds of the 30 seconds exposure for ~ 10^7 MB/mL exposed to 1 MHz, 0.85 MPapk-pk, 30% duty cycle, 100 Hz PRF.*

Table 3.4. *Summary of parameters for fitting the plateau followed by the one-phase exponential decay to the emission power over time.*

	Parameters	Unloaded	LipMB-LαPC	LipMB-DBPC	OilMB	SurfMB
Harmonics	*Adjusted R^2* [a]	0.70	0.69	0.70	0.53	0.36
	t_0 [s]	0.30 **	0.00	0.04**	0.00	1.17 **
	Half-life, $t_{1/2}$ [s]	0.34	0.23	0.23	0.17	0.18
	$t_{1/2,\ adjusted} = t_0 + t_{1/2}$ [s]	0.64	0.23	0.27	0.17	1.35
	P_0 [x10^{-5} V^2]	1.59	1.38	1.95	1.75	0.79 **
	Plateau [x10^{-6} V^2]	1.05 **	1.63	1.40 **	1.76	3.23 **
Ultraharmonics	*Adjusted R^2*	0.58	0.50	0.72	0.44	0.42
	t_0 [s]	0.55 **	0.00	0.16 **	0.00	1.14 **
	Half-life, $t_{1/2}$ [s]	0.35	0.28	0.25	0.25	0.36
	$t_{1/2,\ adjusted} = t_0 + t_{1/2}$ [s]	0.90	0.28	0.41	0.25	1.50
	P_0 [x10^{-6} V^2]	2.34	1.50 *	2.46	1.81 *	0.76 **
	Plateau [x10^{-6} V^2]	0.13	0.09 **	0.24	0.24	0.15
Broadband	*Adjusted R^2*	0.55	0.40	0.63	0.53	0.40
	t_0 [s]	0.60 **	0.00	0.38 **	0.00	1.20 **
	Half-life, $t_{1/2}$ [s]	0.32	0.21	0.11 **	0.39	0.33
	$t_{1/2,\ adjusted} = t_0 + t_{1/2}$ [s]	0.92	0.21	0.49	0.39	1.53
	P_0 [x10^{-6} V^2]	9.35 **	4.27 *	5.10 *	2.00 *	1.06 *
	Plateau [x10^{-6} V^2]	0.23	0.17	0.34	0.22	0.21

* $p < 0.05$, ** $p < 0.01$ compared to all other formulation. [a] The adjusted R^2 represents how well the curve fits the data but is adjusted to account for the number of parameters used in the regression, and thus can be compared between models with different numbers of parameters.

The adjusted R^2 in **Table 3.4** highlight that a plateau followed by an exponential decay does not fit some of the datasets well as some groups presented a rise-to-peak and decay-to-plateau in their emission power over time. Additionally, the low values in the adjusted R^2 also confirm the wide spread of data within the groups. Nonetheless, these results show that the time delay t_0 before the decay in emissions was significantly longer for **SurfMB** and unloaded microbubbles compared to all other groups ($p < 0.01$). This led to a longer adjusted half-life $t_{1/2,\ adjusted} = t_0 + t_{1/2}$ for **SurfMB** compared to the other formulations. Further, these results show that the emissions from **LipMB-LαPC**, **LipMB-DBPC,** and

OilMB decayed consistently more rapidly compared to unloaded microbubbles and **SurfMB**. Although the initial rise in emissions was of lower magnitude P_0, **SurfMB** presented a more sustained increase in signal over time and a higher plateau for the power of harmonic emissions compared to all other groups. This could be caused by the surface functionalization of dextran-IONPs providing a dampening effect during the compression cycles of **SurfMB**. Contrastingly, while the hydrophobic loading of IONPs in **LipMB-LαPC**, **LipMB-DBPC** and **OilMB** affected the physical stability of these systems in different ways (**Figure 3.8**), this loading method led to an overall decrease in adjusted half-life of the microbubbles' acoustic emissions compared to unloaded.

The energies of emissions for each frequency range and formulation are displayed in **Figure 3.20**. This demonstrates that over the 30 seconds exposure time, the formulations produced comparable emission energies apart from the harmonic emissions of **SurfMB** which were significantly higher ($p < 0.05$) compared to the other microbubbles tested.

Overall, these results suggest that the external loading of particles on **SurfMB** could provide an increased stability during microbubble oscillations over time. This was observed in the acoustic emission power with an increased time delay t_0 *and* plateau level, and in the increased total emission energy for this formulation compared to other microbubbles. In contrast, although the hydrophobic loading of IONPs in **LipMB** and **OilMB** led to a more rapid decay of their emission power compared to unloaded systems, their total emission energies were comparable.

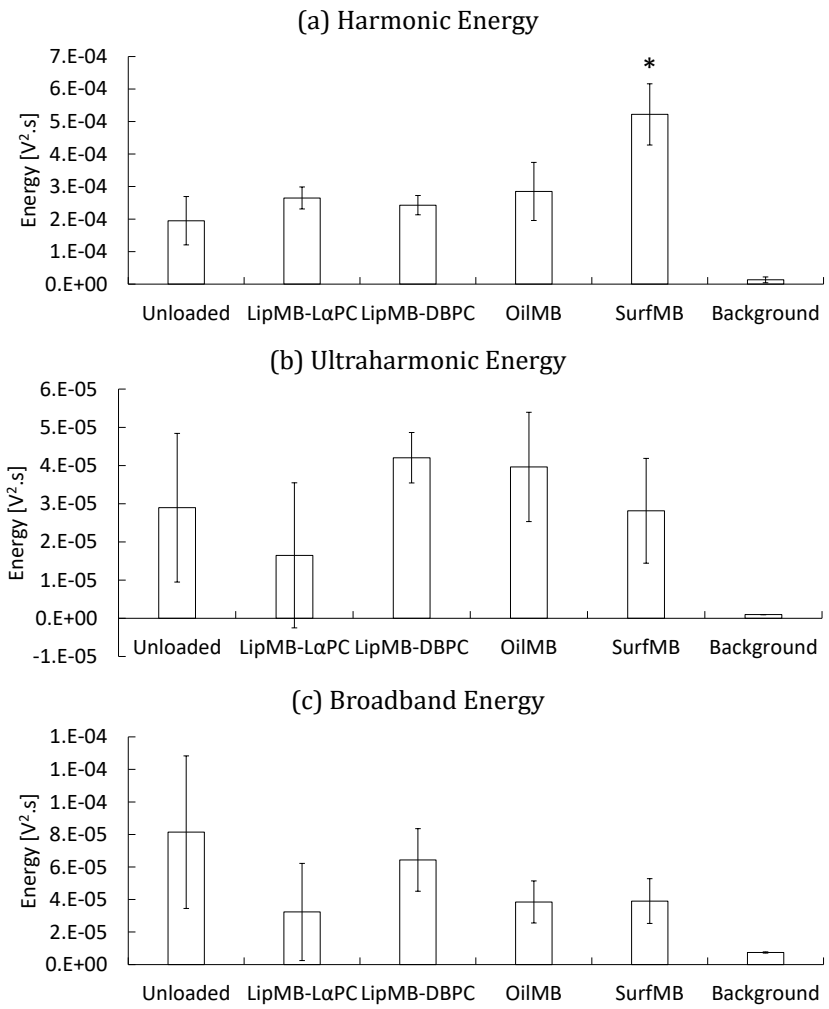

Figure 3.20. *The energy of the* ***(a)*** *harmonic,* ***(b)*** *ultraharmonic, and* ***(c)*** *broadband emissions from ~ 10^7 MB/mL exposed to 1 MHz, 0.85 MPa_{pk-pk}, 30% duty cycle, 100 Hz PRF for 30 s. * $p < 0.05$.*

An analysis of B-mode and contrast ultrasound images also provided a characterisation of microbubble response to 7 MHz ultrasound in a 2.5% agar phantom. A 200 µL sample ((9±1) $\times 10^6$ MB/mL) was flown at 0.2 mL/min and room temperature. The results shown in **Figure 3.21a** present the average mean intensity calculated for two predefined regions of interest within the tissue and contrast imaging modes. Although these intensities were not normalised with the brightness measured in commercially available tissue phantoms, these results indicate that the magnetic formulations all behaved similarly while using an MI of 0.04. While all microbubbles were clearly visible, the image intensity was lower than for the clinical contrast agent SonoVue® for the same

concentration of microbubble injected and comparable size distribution (**Figure 3.21b**). To relate this data to the contrast provided by these formulations in biological tissues, additional measurements should be made in commercial tissue phantoms.

The decreased image intensity obtained with microbubbles produced in-house was attributed to the stiffer shell of DBPC:PEG40S microbubbles preventing bubble expansion compared to softer systems made of DSPC phospholipid as for Sonovue® [255]. Contrastingly, no acoustic difference was observed between the magnetic microbubble formulations and the unloaded systems, indicating that the lipid composition governed the acoustic oscillations of the system more than the presence of the nanoparticles at these ultrasound exposure conditions.

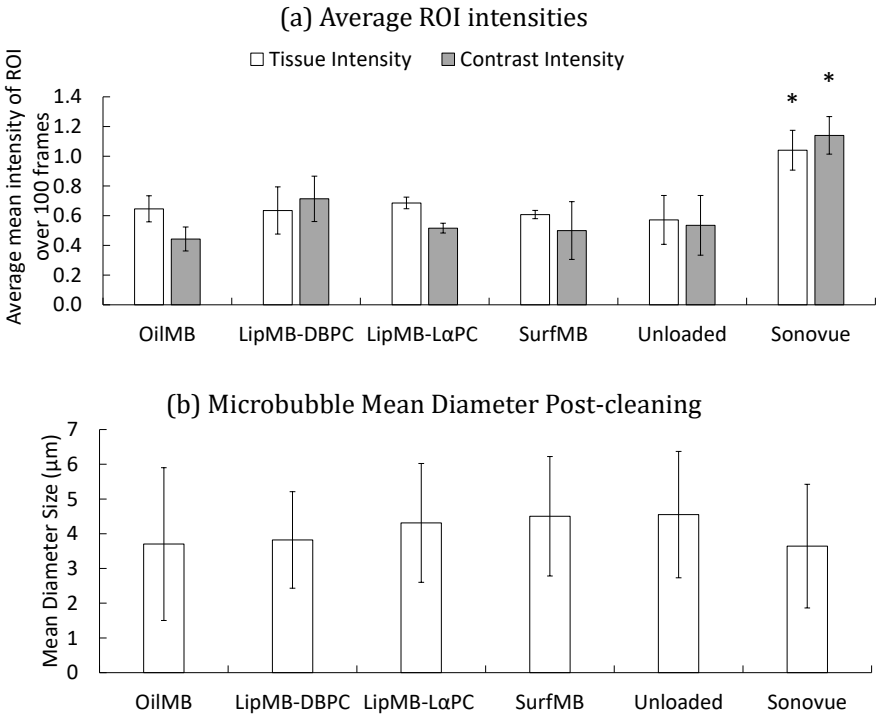

Figure 3.21. *Analysis of 100 frames ultrasound images for different MMBs with* ***(a)*** *the average mean intensity in a predefined ROI in tissue and contrast imaging modes over 100 frames for each formulation (n = 3 runs). 200 µL of 9x10^6 MB/mL were injected and flown at 0.2 mL/min during which B-mode images were acquired. Sets of 100 frames were chosen for analysis where concentration of microbubbles flowing through the channel was found most stable.* ***(b)*** *The size distributions of the different microbubbles considered were comparable post-cleaning. * p < 0.05.*

3.4.6. Magnetic properties

3.4.6.1. Methods

3.4.6.1.1. Transmission electron microscopy

Transmission electron microscopy (TEM) was used to visualise the incorporation of IONPs onto MBs. To obtain dried microbubbles samples for TEM imaging, a previously described method was used [256]. Briefly, a carbon coated copper grid (C267/050 thin clean films of carbon 300 mesh 3 mm copper grid, TAAB Laboratories Equipment Ltd, Berks, UK) was exposed to a glow-discharge cycle and the carbon side of the copper grid was placed onto a 10 µL drop of the diluted microbubble sample on a piece of parafilm for 2 minutes. The TEM grid was then lifted and placed onto a 20 µL drop of 2% w/v uranyl acetate for 10 seconds. The grid was again lifted, carefully dried with a piece of filter paper and left to dry for 10 minutes under an aluminium cover for reduced light exposure. The samples were imaged through a FEI Tecnai 12 transmission electron microscope operated at 120 kV and images were acquired using a Gatan OneView CMOS camera.

3.4.6.1.2. Inductively coupled plasma optical emission spectrometry

The iron content of the different microbubble formulations was detected using inductively coupled plasma optical emission spectroscopy (ICP-OES, Perkin Elmer, Optima 8000). These measurements were used to determine the amount of IONPs loaded onto microbubbles to compare with magnetic retention results. Iron measurements were performed at a wavelength of 238 nm and a 7-point calibration curve was completed for iron in 2% nitric acid solution (0-1 mg/L) with a R^2 value of 0.9999 prior to sample measurements.

3.4.6.1.3. Magnetic retention under flow

The same set-up as for the acoustic characterisation of microbubbles at 7 MHz (section 3.4.5.2) was used to study the magnetic retention of microbubbles under flow. The magnetic field was applied using a five-element Halbach array magnet placed 1 cm below the channel. The magnet was previously described by Stride *et al.* and consisted of five rectangular N52 grade NdFeB permanent magnets (25 x 10 x 10 mm, supplied by NeoTexx, Berlin, Germany) with transversal magnetisations of 1.50 T oriented at an angle of 90° from one another and held by an aluminium frame [199]. A bolus of 100 µL of $5x10^7$ MB/mL was injected through a three-way valve and microbubbles were left to flow for 1 minutes above the magnet before acquiring ultrasound images with a linear array (L12-5, 7 MHz) angled perpendicular to the magnet (**Figure 3.22**).

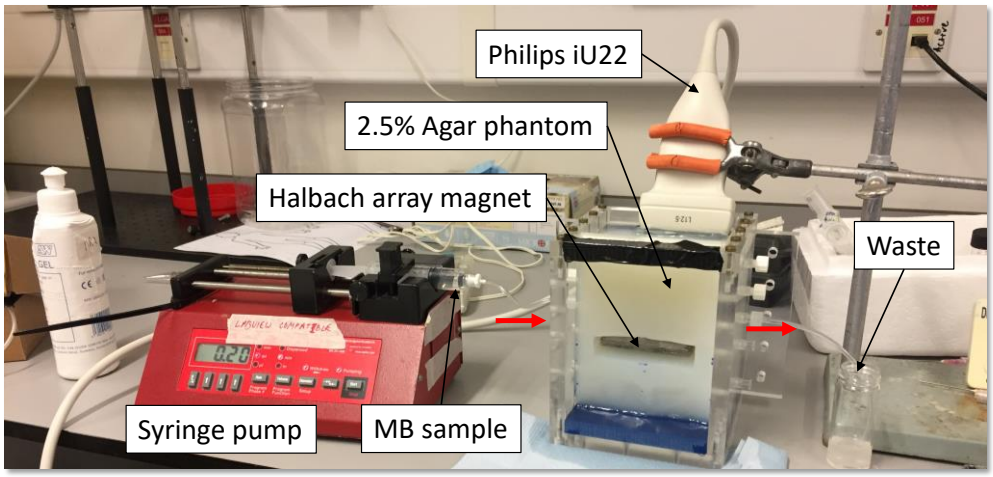

Figure 3.22. *Picture of set-up used to characterise retained magnetic microbubbles by magnet*

An ultrasound MI of 0.04 was used to minimise microbubble destruction. Tests were completed for cleaned magnetic microbubbles and flashes of increased acoustic drive level were used to destroy and confirm the retention of microbubble material. As grayscale intensities of magnetic microbubbles flowing through the system without magnet have been acquired for their acoustic characterisation, a quantification of

magnetic retention was performed through analysis of B-mode image intensity within the ROIs with and without magnet over 10 frames compared background measurements. ROIs were automatically segmented from the bottom of the channel with the first 1/3 of the channel being without magnet, and the remaining 2/3 being directly 1 cm above the Halbach array magnet (**Figure 3.23**).

(a) Water

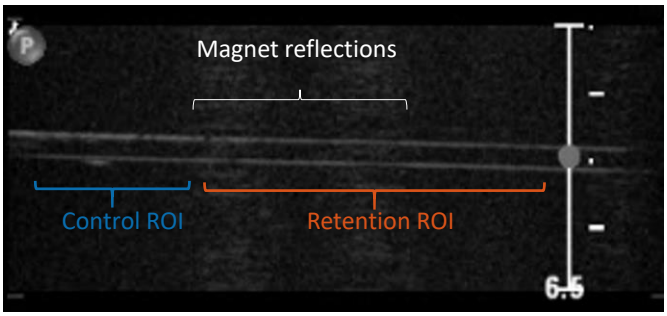

(b) SurfMB

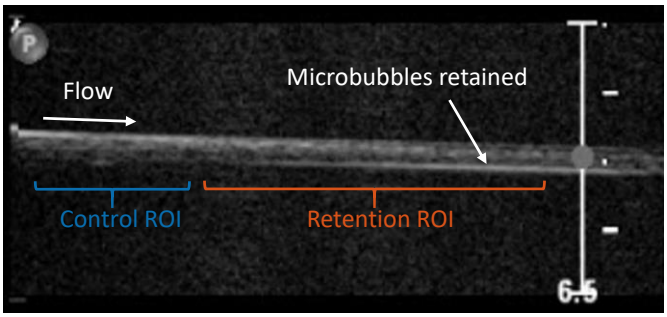

Figure 3.23. *B-mode images of 1.6 mm channel in agar with* ***(a)*** *water, and* ***(b)*** *hydrophilic dextran IONPs loaded microbubbles (****SurfMB****).*

3.4.6.2. Results

The magnetic microbubbles were examined under electron microscopy. The images in **Figure 3.24** and **Figure 3.25** suggest that hydrophobic isoparaffin and LαPC IONPs remain in clusters on microbubbles unlike DBPC (**Figure 3.26**) and dextran IONPs (**Figure 3.27**). The discontinuities seen on the microbubbles is likely associated with the sample drying process required to enable electron microscopy imaging, whereas the dark areas surrounding bubbles is due to pooling of the uranyl acetate stain.

Upon visual inspection of images, the coverage of IONPs on **OilMB**, and **LipMB** appears minimal compared to the larger quantities of the dextran IONPs on **SurfMB**. These observations were then compared to the measurements of iron loading per microbubbles to evaluate the consistency of these findings.

OilMB

(a) scale 200 nm

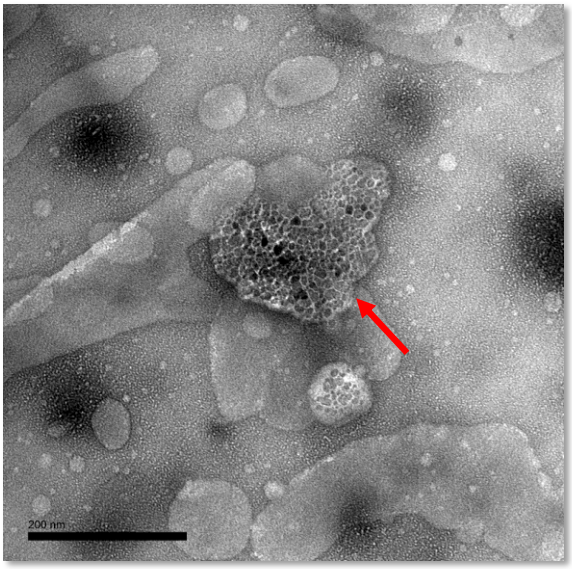

(b) scale 500 nm

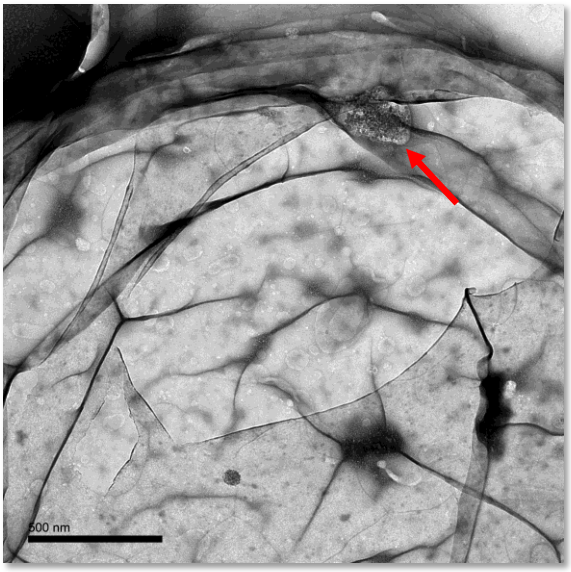

(c) scale 1000 nm

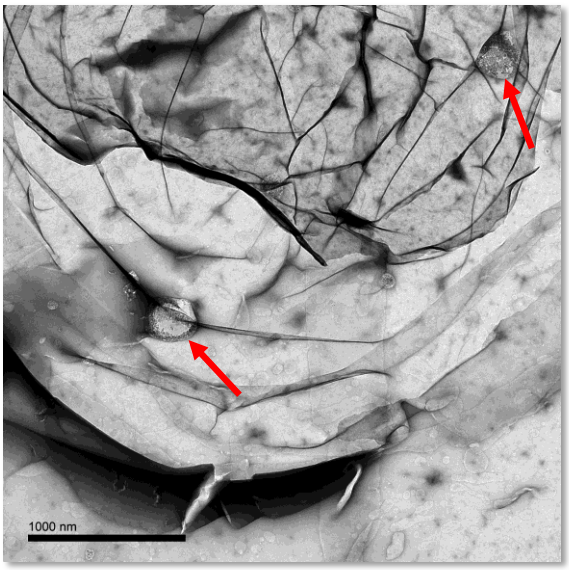

(d) scale 2 µm

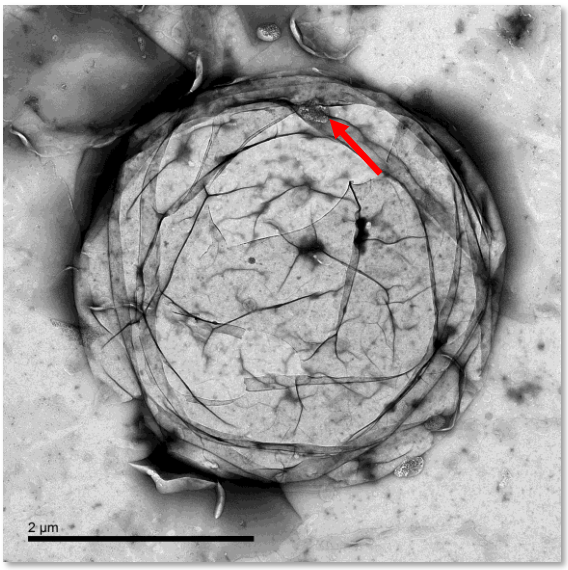

Figure 3.24. *TEM images of* ***OilMB****. TEM images were obtained by negatively staining samples with 2% w/v uranyl acetate, and imaging them at 120 kV. Arrows point at clusters of IONPs and images show nanoparticles* ***(a)*** *without microbubbles and* ***(b-d)*** *on microbubbles.*

LipMB-LαPC

(a) scale 200 nm

(b) scale 500 nm

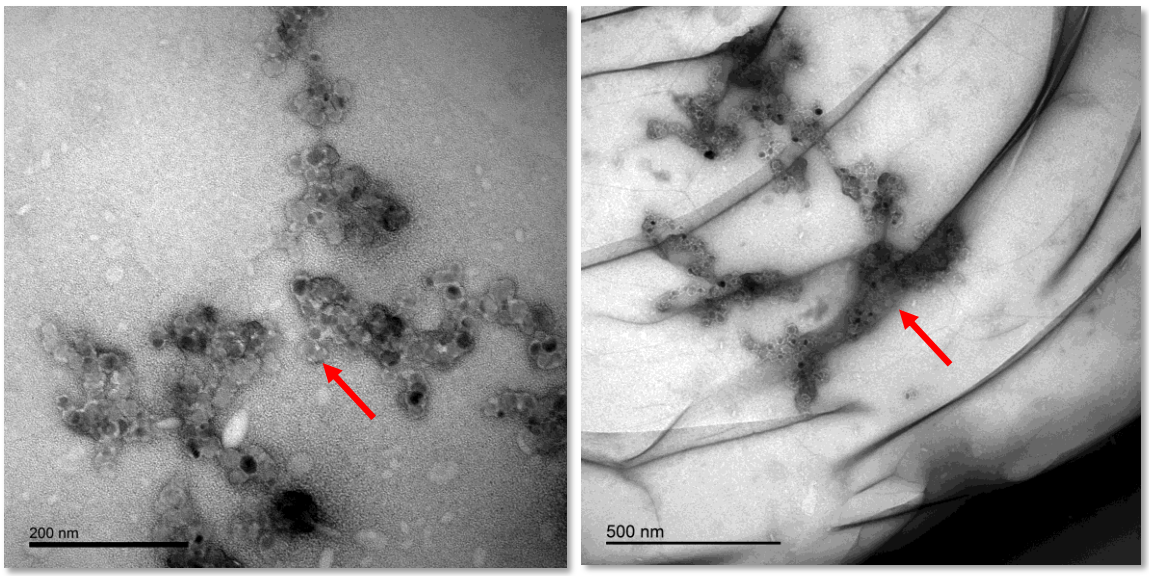

(c) scale 500 nm

(d) scale 1000 nm

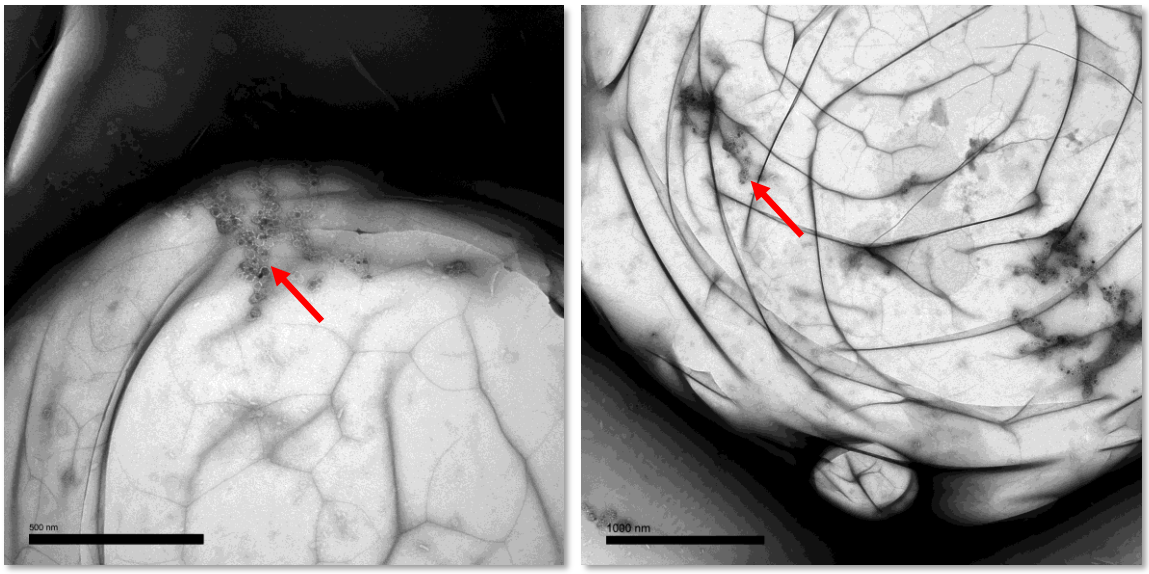

Figure 3.25. *TEM images of* ***LipMB-LαPC****. Arrows point at clusters of IONPs and images show nanoparticles* ***(a)*** *without microbubbles and* ***(b-d)*** *on microbubbles.*

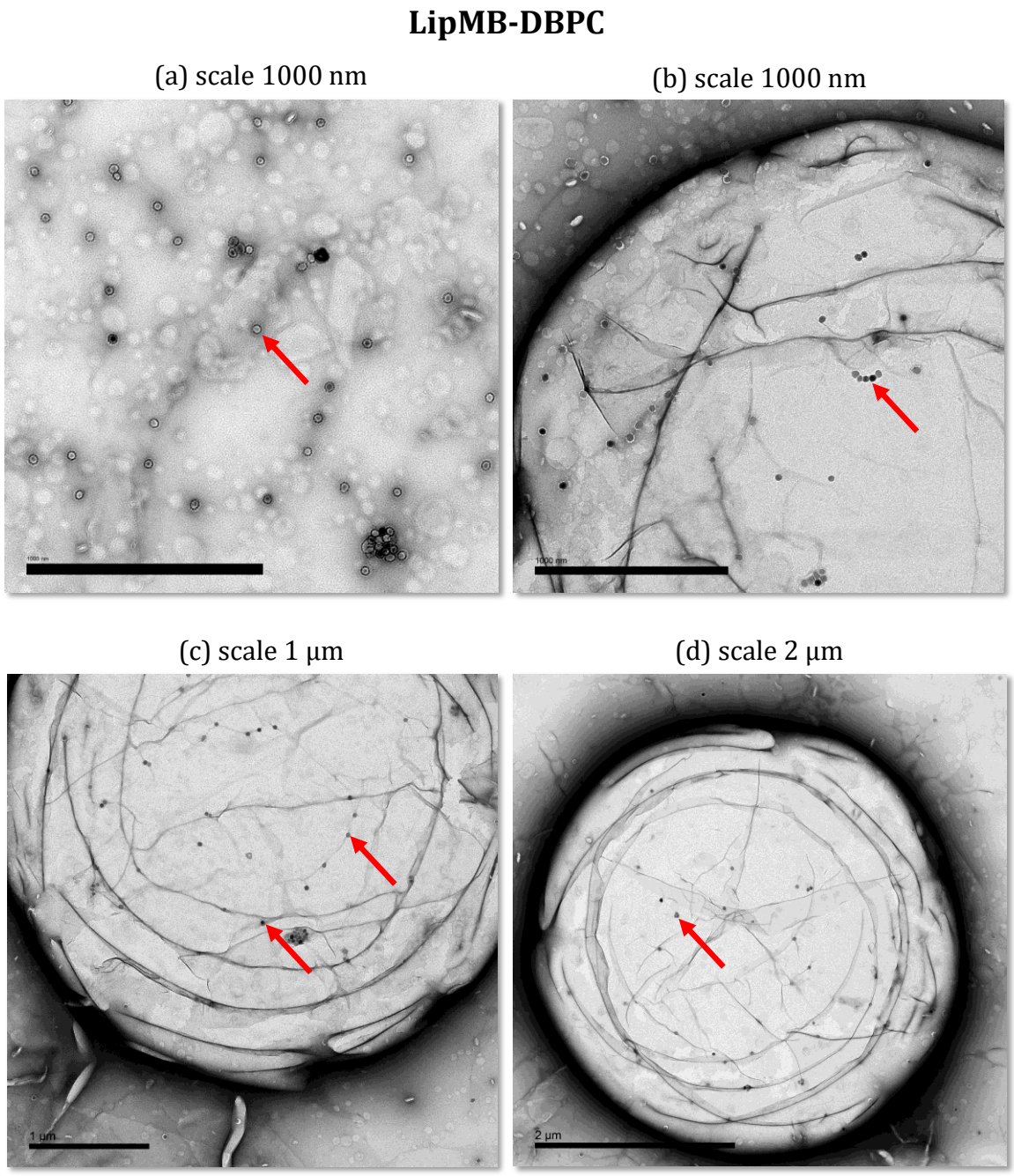

Figure 3.26. *TEM images of* ***LipMB-DBPC****. Arrows point to individual or a cluster of IONPs and images show nanoparticles* ***(a)*** *without microbubbles and* ***(b-d)*** *on microbubbles.*

SurfMB

(a) scale 200 nm

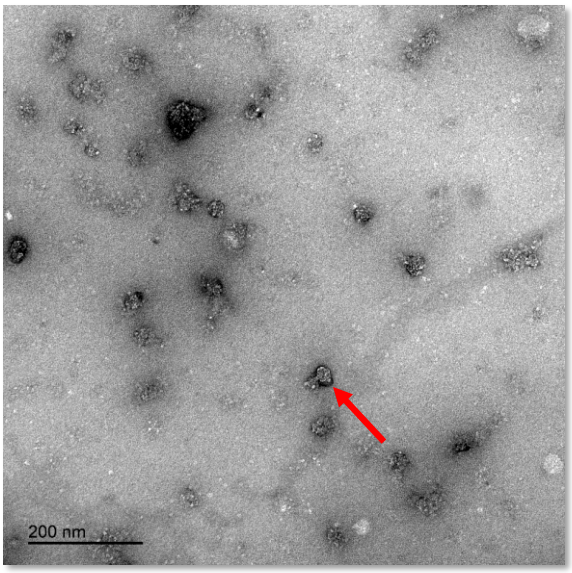

(b) scale 500 nm

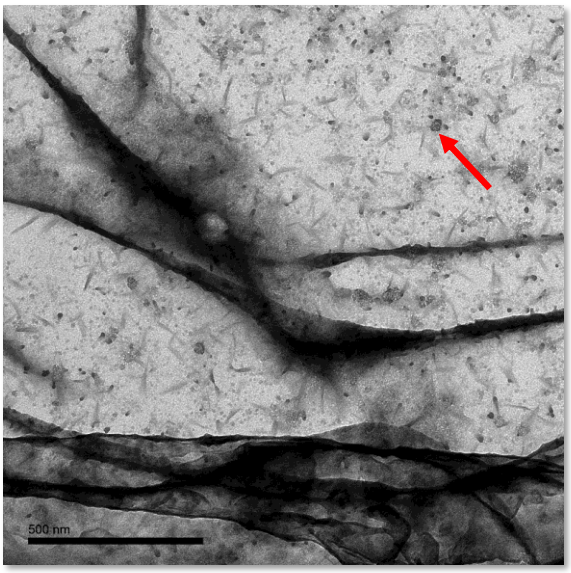

(c) scale 500 nm

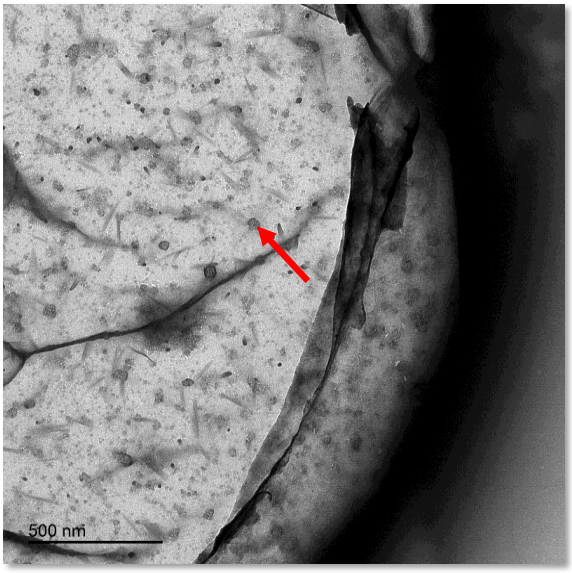

(d) scale 2 µm

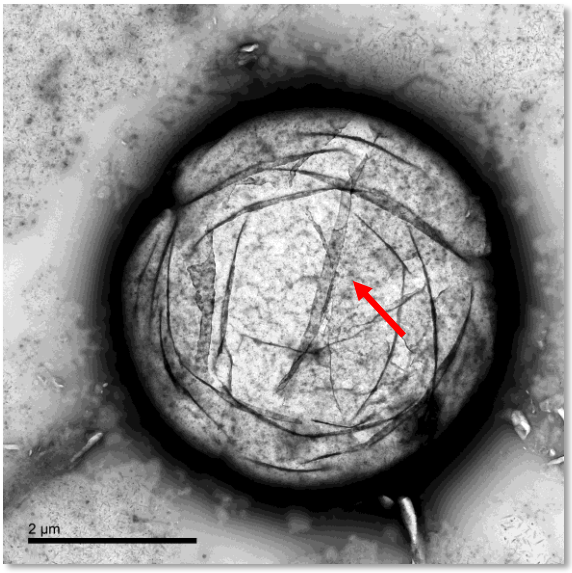

Figure 3.27. *TEM images of* ***SurfMB****. Arrows point to individual or cluster of IONPs and images show nanoparticles* ***(a)*** *without microbubbles and* ***(b-d)*** *on microbubbles.*

Quantification of the iron loading in the different formulations was determined by inductively coupled plasma optical emission spectroscopy and the results are presented in **Figure 3.28a**. This data indicates a significantly higher iron loading in **OilMB** (0.61 pg/MB) and **SurfMB** (0.71 pg/MB) compared to **LipMB** (approximately 0.025 pg/MB) and

the background measurement in the unloaded control (0.006 pg/MB) ($p < 0.05$). The lower loading of LαPC and DBPC IONPs in microbubbles could be due to the low incorporation of particles during microbubble production or their removal from the microbubble coating during the washing procedure.

(a) Iron content

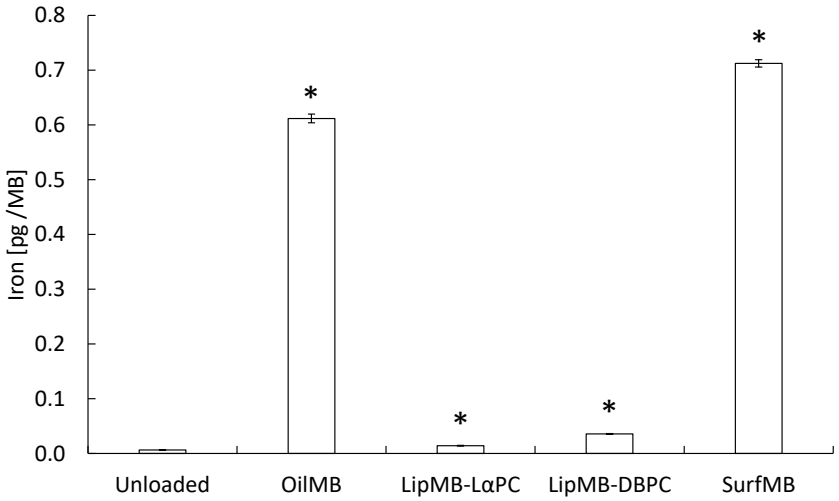

(b) **LipMB-DBPC** (c) Diluted drop of **SurfMB** suspension

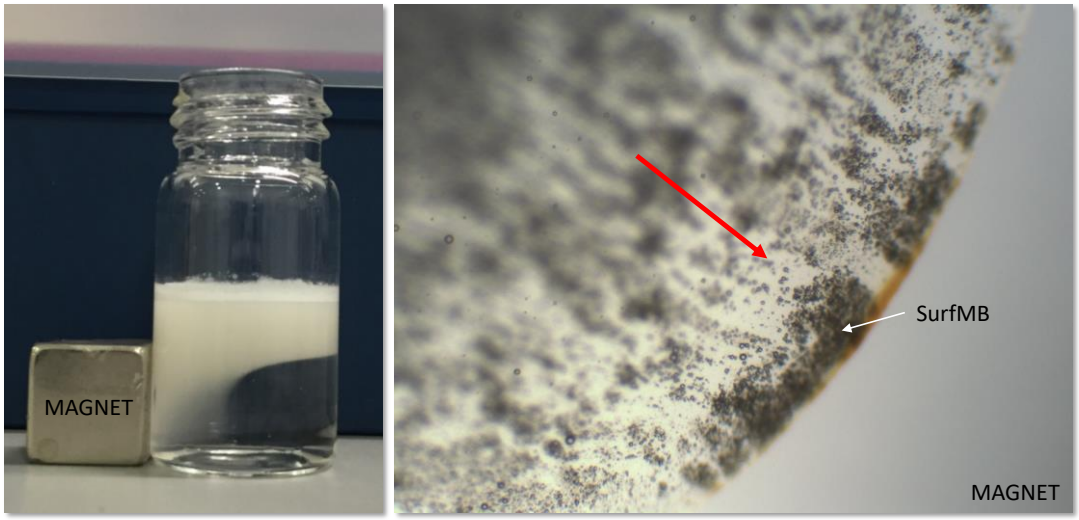

Figure 3.28. (a) *Iron content results for different magnetic microbubbles and photograph of the magnetic response for cleaned* ***(b) LipMB-DBPC****, and* ***(c) SurfMB*** *next to a single N52 grade NdFeB permanent magnet cube. The red arrow in* ***(c)*** *highlight the alignment of* ***SurfMBs*** *with the magnetic field induced by a magnet situated next to the drop of sample as indicated. ICP-OES was done for n = 3 measurements of the same sample, * $p < 0.05$ and pg/MB = mg/10^9MB.*

LipMB, however, presented a detectable level of iron compared to unloaded systems ($p < 0.05$) and exhibited a response to a magnetic field as shown in **Figure 3.28b**. Still, the magnetic response of **SurfMB** demonstrated in **Figure 3.28c** is expected to be significantly higher due to the increased volume of IONPs incorporated on the microbubbles. In effect, although the iron content of microbubbles is not a direct representation of their magnetic properties, these measurements were used to determine how much iron material was incorporated within the microbubbles. As the IONPs used in this work were all superparamagnetic, the magnetic force on the microbubble should then increase with the number of incorporated particles.

Based on the properties of the IONPs used, an approximate iron loading per nanoparticle was calculated (**Table 3.5**) and used with the measured iron loading per microbubble to determine an approximate number of particles per microbubble for each formulation (**Table 3.6**).

Table 3.5. *Calculated iron loading per IONP based on properties provided by the manufacturers.*

PARTICLE	HYDRODYNAMIC DIAMETER [nm]	PARTICLE CORE DIAMETER [nm]	PARTICLE CORE VOLUME [nm^3/IONP]	CALCULATED IRON LOADING / IONP [10^{-5} pg/IONP] [a]
Isoparaffin IONP	26	10	524	0.27
DBPC-IONP	50	30	14 137	7.21
LαPC-IONP	50	~ 30	~ 14 137	~ 7.21
Dextran-IONP	50	~ 30	~ 14 137	~ 7.21

[a] Iron density of 5.1 g/cm^3.

Table 3.6. *Calculated particle loading per microbubble based on the measurement of iron loading per microbubble and IONP properties.*

FORMULATION	MEASURED IRON LOADING / MB [pg/MB]	IONP/MB
OilMB	0.61	~ 228 000
LipMB-DBPC	0.04	~ 500
LipMB-LαPC	0.01	~ 200
SurfMB	0.71	~ 10 000

The particle loading per microbubble presented in **Table 3.6** was then compared to a theoretical approximation of the maximum loading achievable on the microbubbles based on the size distribution for each formulation. For this, the average microbubble surface area (S_{avg}) was computed for microbubbles between 0.5 and 10 µm following Equations 7-8:

$$S_{total} = \sum_{0.5\mu m}^{10\mu m} 4\pi \left(\frac{D_{bin}}{2}\right)^2 \times conc_{bin} \quad (7)$$

$$S_{avg} = \frac{S_{total}}{conc} \quad (8)$$

where: S_{total} is the total microbubble surface area, D_{bin} is the mean diameter of microbubbles in one bin of the size distribution and $conc_{bin}$ is the concentration of microbubbles associated to that bin. Then *conc* is the microbubble concentration of the sample.

The IONP coverage on the mean microbubble surface is approximated by unfolding the bubble surface and fitting as many squares of side equal to the mean IONP diameter. The results in **Table 3.7** highlight that based on the iron content measurements and the size distribution of each microbubble formulation, there is a maximum loading of IONPs on both **OilMB** and **SurfMB**. While the TEM images of **OilMB** did not present a full coverage of the microbubbles with IONPs, this formulation could have an accumulation of IONPs in highly concentrated clusters or droplets, thereby providing the high loading percent. Even with this high loading, the low stability of **OilMB** is expected to hinder the magnetic retention of these systems and this is further discussed in the following section. The IONP loading of **SurfMB** is above the maximum theoretical loading calculation which could be due to the surface functionalisation used allowing the packing of IONPs with increased density, which is unaccounted for in the calculations presented here. In

contrast, there is a very low loading percent of IONPs in **LipMB** with about 5% of coverage only. As previously mentioned, this has been related to the removal of IONPs from the microbubbles during the centrifugal cleaning steps. The **LipMB-DBPC** formulation, however, still showed a response when exposed to a magnet in **Figure 3.28b**.

Table 3.7. *Percent IONP loading on microbubbles for each formulation , summary of calculations.*

FORMULATION	MEAN MB SURFACE AREA [μm^2/MB]	IONP AREA AS A SQUARE [$10^{-3}\mu m^2$]	THEORETICAL MAXIMUM LOADING [IONP/MB]	LOADING [IONP/MB]	% LOADING
OilMB	135	0.7	~ 220 000	~ 228 000	~ 105
LipMB-DBPC	19	2.5	~ 8 000	~ 500	~ 5
LipMB-LαPC	16	2.5	~ 7 000	~ 200	~ 5
SurfMB	15	2.5	~ 6 000	~ 10 000	~ 165

The magnetic responses of the microbubble formulations were then tested through their ability to be retained under flow at a rate of 0.2 mL/min in a tissue-mimicking flow phantom and imaged using a commercially available diagnostic ultrasound device. A channel size of 1.6 mm diameter was chosen to fit the human physiological range for small pancreatic arteries [248]. The concentration of microbubbles injected into the system was kept fixed with 100 µL bolus injections of clean microbubble suspension at $5x10^7$ MB/mL tested for each formulation. Microbubbles were left to circulate for 1 minute with a Halbach array magnet situated 1 cm underneath the channel. The 7 MHz diagnostic ultrasound probe was kept off during this 1-minute period to avoid microbubble destruction. After 1 minute of circulation, a series of B-mode images was captured during which a "flash" of increased ultrasound intensity was used to destroy the retained material and obtain background images. As the magnetic microbubbles produced similar grayscale intensities while exposed to 7 MHz diagnostic ultrasound and an MI of 0.04, their magnetic retention was compared by analysing the intensity of a sequence of 10

frames for each formulation. The regions chosen for analysis were located at the bottom of the channel to avoid noise from remaining microbubbles flowing through the system (**Figure 3.23**). The average image intensity of the ROI with magnet was then compared to that of a region without magnet within the same frame.

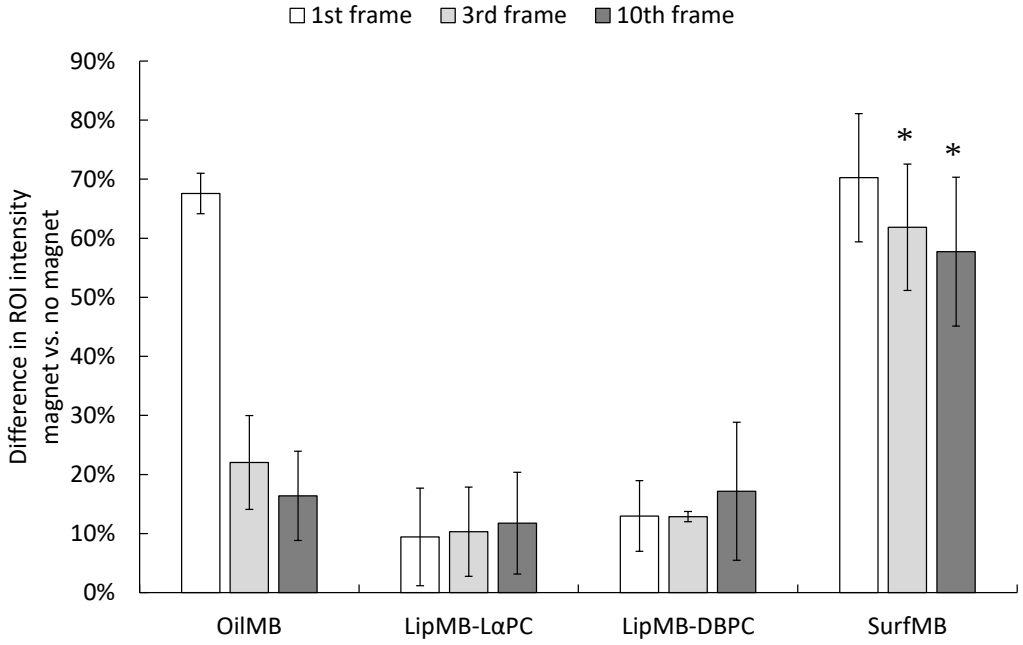

Figure 3.29. *Change in ROI intensity with a magnetic field and the different MMBs formulations. There are n = 2 runs, for each a 10 frame sequence was analysed and the results for the 1st, 3rd and 10th frames are shown. * p < 0.05 compared to all other formulation in that frame group.*

The results in **Figure 3.29** confirm that **SurfMB** still shows significantly higher retention after 10 imaging frames (58% increase in B-mode image intensity) compared to other magnetic microbubbles tested (12 to 17% increase under the same conditions). While **OilMB** did not exhibit a significant difference in retention compared to **LipMBs** after three imaging frames, the first imaging frame showed a comparable ROI intensity to **SurfMB**, thus agreeing with the iron loading measurements. The results from ultrasound imaging with the same experimental set-up, however, demonstrated that an MI of 0.04 was appropriate for imaging **OilMB** without a significant intensity loss over 100 imaging

frames. The low stability of this formulation presented here might then be associated with imaging the retained bolus. Finally, no bolus of retained material was observed using **LipMB**, but only a downward movement of the microbubbles towards the magnet.

3.4.7. Haemolysis

3.4.7.1. Method

Horse blood was used to assess potential haemolysis induced by the different magnetic microbubble formulations. The blood was stored at 5°C and used the day following delivery at room temperature (21°C). 200 µL of blood were diluted with 163 µL of microbubbles at $1.8x10^7$ MB/mL, or with PBS for positive and negative controls. The samples were then incubated at 37°C for 5 minutes. An aliquot of 80 µL of each blood sample was added to 1.12 mL of PBS. The positive control was further diluted with 120 µL of 1% Triton X-100 in water as a 100% haemolysis reference, while the other samples were further diluted with 120 µL of PBS. All samples were then centrifuged at 500 g and 4°C for 5 minutes. The absorbance of the supernatants was measured in triplicate (120 µL per well in a Greigner UV-Star 96-well plate) at 541 nm. This procedure was performed twice.

3.4.7.2. Results

The different formulations were added to horse blood and the results in **Figure 3.30** show that test samples induced on average (5.5±0.9)% haemolysis comparable to the levels observed for the negative control samples made of PBS with (4.9±0.8)%. The samples were incubated at 37°C for 5 minutes, reflecting the short half-life of microbubbles in circulation in biological systems [124,125]. Additionally, several *in vivo* studies using **OilMB** [199,200] and **LipMB-LαPC** [86,227,228] were completed with no reported toxicity.

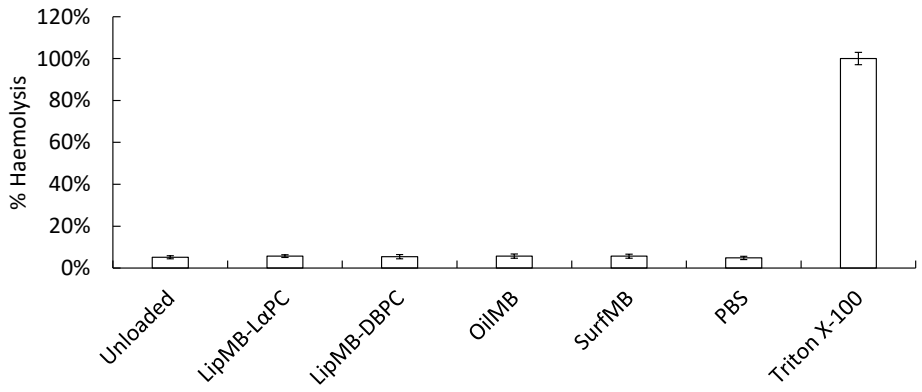

Figure 3.30. *No increase in blood haemolysis was observed with the MMB formulations added to horse blood. Results were compared to 0% control (addition of PBS) and 100% control (addition of 1% Triton X-100). The samples were incubated at 37°C for 5 minutes and haemolysis was characterised with absorbance measurements at 541 nm. The entire procedure was done twice, and samples were transferred in triplicates onto a 96-well plate for absorbance measurement.*

3.5. Evaluation

A summary of the findings is presented in **Table 3.8**. Different loading methods were compared for producing magnetic microbubbles with the aim of prolonging their stability and enabling strong magnetic and acoustic responses. Although, hydrophobic isoparaffin IONPs enabled a high loading of iron, this method produced unstable microbubbles with a substantially reduced half-life at 37°C and under flow compared to unloaded microbubbles. In contrast, **SurfMB** provided a significant advantage over the other formulations as they were found to be both more stable than unloaded systems and magnetically more responsive than **LipMB**. While **LipMB-DBPC** presented a lower retention efficiency during magnetic targeting, this system demonstrated a significant improvement in stability compared to unloaded microbubbles. It should also be noted that magnetic retention could be affected by the different magnetic properties of the IONPs in the different formulations and further optimisation could be carried out to investigate the effects of particle size, charge and magnetic properties.

Table 3.8. *Summary table of findings comparing different loading methods of IONPs to produce magnetic microbubbles and the downstream consequences on microbubble properties.*

PROPERTY OF DBPC BASED MICROBUBBLES	**OilMB**	**LipMB-LαPC**	**LipMB-DBPC**	**SurfMB**
Stability enhancement **In vitro, 10 mL/min, 37°C**	Unstable	None	Very good	Good
Cavitation signal **$1x10^7$ MB/mL suspension, 1 MHz, 30% DC, 100 Hz PRF, 0.85 MPa_{pk-pk}**	Exponential decay	Exponential decay	Exponential decay	Rise to peak + exponential decay
Diagnostic imaging **0.2 mL/min, $9x10^6$ MB/mL, 0.04 MI**	Comparable	Comparable	Comparable	Comparable
Magnetic retention **0.2 mL/min, $5x10^7$ MB/mL, 0.04 MI**	Bolus observed but unstable	No bolus observed	No bolus observed	Bolus observed
Hydrophobic drug loading	×	×	×	✓
Hydrophilic drug loading	✓	✓	✓	×

✓: possible, ×: challenging

For drug delivery purposes, the most versatile way of loading microbubbles with hydrophilic drugs or liposomes relies on the post-functionalisation of microbubble shell phospholipids. The surface loading method of IONPs in **SurfMB** could then present a challenge for this type of additional surface functionalisation, although it would not interfere with the loading of hydrophobic drugs within the shell. Contrastingly, the phospholipid-mediated loading of DBPC IONPs within the microbubble shell remains a useful method to produce stable magnetic microbubbles which allows the attachment of hydrophilic drugs to shell phospholipids but challenges the loading of hydrophobic drugs.[2]

Although the incorporation of IONPs can potentiate oxidative stress due to the release of free iron from the particles followed by iron-catalysed Fenton reaction [257–259], the iron content after microbubble washing was found to be low, with a maximum of 0.7 mg/mL for a microbubble concentration of 10^9 MB/mL. Additionally, considering the recommended dose of SonoVue® microbubbles of 2-2.4 mL in adults [260] which

[2] Preliminary experiments showed that a lower loading of iron was obtained in **LipMB** compared to unloaded microbubbles when hydrophobic drug Paclitaxel was also incorporated.

equates to approximately 10^9 MB administered, the corresponding dose of iron would be 0.7 mg. Compared to clinical intravenous injections of Feraheme (ferumoxytol) recommending two doses of 510 mg of iron over 8 days in adults with chronic kidney disorder [229], the administered dose of iron within magnetic microbubbles is orders of magnitude lower than currently approved for iron deficiency anaemia. Nevertheless, the composition of material used is important to ensure minimal toxicity even at low doses. The lipids used to make the microbubble shell and to coat phospholipid-stabilised IONPs were chosen to be saturated phospholipids to minimize the chance of lipid peroxidation during ultrasound-induced microbubble collapse in the presence of IONPs [69,261,262]. The externally conjugated dextran IONPs were chosen to mimic Feraheme, but additional improvements in biocompatibility could be implemented to inhibit macrophage clearance of these particles and improve the efficiency of this method *in vivo* [263].

3.6. Conclusions

Although many have reported the use of magnetic microbubbles to enhance therapeutic investigations, a comparison between the formulation methods has not been undertaken. Therefore, magnetic microbubbles produced using different IONP loading methods were investigated to compare their stability, acoustic emissions, and magnetic retention.

The external binding of IONPs to the lipid microbubble coating was found to produce a significant improvement on their stability compared to unloaded systems while preserving their acoustic behaviour. This method also produced the most magnetically responsive microbubbles. However, although this method allows for hydrophobic drug loading within the microbubble coating, it renders further attachment of hydrophilic drugs to microbubble shell phospholipids challenging. As the sensitiser Rose Bengal for

sonodynamic therapy is hydrophilic, the phospholipid-mediated loading of DBPC IONPs within the coating of microbubbles might be more appropriate. Although this formulation offers a weak magnetic response, it provides an improved stability which is favourable for the delivery of therapeutics. Thus, the phospholipid-mediated loading of DBPC IONPs within the coating of microbubbles could offer a compromise between targeting efficiency, stability, acoustic response, and surface loading of hydrophilic drugs for sonodynamic therapy.

3.6.1. Contributions

To the best of the author's knowledge, this chapter provides the first comparison on the performance of previously reported magnetically functionalised lipid-based microbubbles. This examination provides an insight on the interplay between functionalising microbubbles for magnetic targeting and how this process affects the performance of microbubbles as contrast and therapeutic agent.

3.6.2. Limitations

The results presented in this chapter, however, did not consider the effects of iron oxide nanoparticle charge, magnetic properties, and size on the microbubbles incorporating them. As the IONPs were purchased from several manufacturers, differences in their properties would then affect the magnetic microbubbles loaded with these particles.

The diagnostic ultrasound images of the different formulations were acquired for a sample flowing in an 2.5% agar tissue mimicking phantom. Additional experiments could evaluate the contrast provided by these magnetic microbubbles in a commercial tissue phantom for an improved approximation of their potential contrast in biological tissues.

Further, the physical stability studies completed at 37°C and under flow do not reflect all factors affecting the *in vivo* stability of microbubbles. Although, a biocompatible phospholipid coating was chosen to stabilise the microbubbles and these present a lower immunogenic response compared to protein-based systems, they still suffer from a rapid clearance *in vivo* with a half-life of approximately 3.5 minutes [264,265]. The accumulation and clearance of these was reported to mainly occur in the liver and the spleen [173,265,266] from interactions or even phagocytosis by Kupffer cells [267], processes which were not examined in this chapter.

Finally, a comparison of magnetic microbubbles performance in blood is still lacking, thus ignoring potentially destabilising factors such as the formation of protein corona on microbubbles [268], or the influence of red blood cells on magnetically retained microbubbles [269].

Chapter 4
Mechanism for sonodynamic therapy with Rose Bengal

Chapter 4 examines theories proposed for the activation mechanism of the sensitiser during sonodynamic therapy. The contributing effects of added microbubbles are also discussed. Characterisation of this process will enable an optimisation of the treatment protocol and the sensitiser used with sonodynamic therapy.

Parts of the results in this chapter have been presented or submitted for publication as indicated below. Collaborative results have been indicated in the following sections.

E. Beguin, L. Bau, Y. Yildiz, J. Owen, P. Rademeyer, R. Browning, J.F. Callan, A. McHale, E. Stride, Investigation of Sonodynamic Therapy Mechanisms with Oxygen Loaded Microbubbles, in: 22nd Eur. Symp. Ultrasound Contrast Imaging, 2017: p. 93.

E. Beguin, F. Foglietta, J.F. Callan, A. McHale, E. Stride, N. V Dezhkunov, Investigation of sonoluminescence generated in suspensions of microbubbles, in: 16th Meet. Eur. Soc. Sonochemistry, 2018.

E. Beguin, S. Shrivastava, N. V. Dezhkunov, A.P. McHale, J.F. Callan, E. Stride, Direct evidence of multi-bubble sonoluminescence using therapeutic ultrasound and microbubbles, ACS Appl. Mater. Interfaces. (2019). In review

---

Contents

4.1. Introduction

Reports on sonodynamic therapy have demonstrated promising results for the treatment of aggressive and resistant tumour cell lines [5,9,76]. As described in section 2.1.2, this therapy relies on the combination of ultrasound, ground state molecular oxygen, and a sensitising drug to produce cytotoxic reactive oxygen species in a targeted manner [10]. Thus, sonodynamic therapy uses a similar approach to photodynamic therapy, a modality clinically approved for the treatment of superficial lesions and lesions that can be reached with an endoscope [270]. Ultrasound can, however, be more tightly focused in deeper regions of human tissues compared to light, allowing sonodynamic therapy to treat a wider range of lesions, more deeply seated in the body compared to photodynamic therapy.

In 1989, the initial findings of sensitiser activation using ultrasound were reported [1] and since then, a range of sensitising drugs have been developed [10,76]. In the last decade, microbubbles have been shown to enhance sonodynamic therapy and offer the potential for treatment of hypoxic tumours [216–218]. The underlying mechanisms responsible for the activation of the sensitiser through this method and how microbubbles might contribute to this event, however, remain uncertain. Several theories have been proposed, including pyrolysis [28] and sonoluminescence [7,27] , but a consensus has yet to be drawn.

4.1.1. Objectives

As sonodynamic therapy advances further towards clinical use, a fundamental understanding of the underlying mechanism for this technique becomes increasingly important. Additionally, with many sensitisers under investigation, gaining insight in the

working principles of the therapy would help the drug design and screening process. Following the review of proposed mechanisms in section 2.1.2, this chapter presents an investigation on the activation of the sensitiser Rose Bengal through pyrolysis and sonoluminescence pathways, using the ultrasound exposure conditions from recent sonodynamic therapy studies. The contributing effects of microbubbles are also evaluated.

4.2. Methods

4.2.1. Overview

As reviewed in section 2.1.2, pyrolysis and sonoluminescence are thermal processes occurring during acoustic cavitation that could be involved with the activation of sensitisers during sonodynamic therapy. These were examined in this chapter for their effect on Rose Bengal.

Cavitation events and the localised hot spots generated can lead to the thermal dissociation of molecules forming reactive species [28,54]. In aqueous solutions, the splitting of water with ultrasound generates hydroxyl radicals which can then oxidise surrounding chemicals [28]. Their recombination can also lead to a cascade of reactions thereby producing a population of reactive species which could react, oxidise, or activate the sensitiser.

To investigate this process, the activity of Rose Bengal in solution was tested with and without the presence of hydroxyl radicals. In effect, these reactive species can trigger the oxidation of Rose Bengal as depicted in **Figure 4.1**, producing superoxide anion [66,271]. In biological systems, superoxide anion dismutates spontaneously or with the action of superoxide dismutase (SOD), and causes a cascade of transitions through which other

reactive species including singlet oxygen can be generated [272–275]. As the recombination of hydroxyl radicals produces hydrogen peroxide [28] and subsequent reactions can form singlet oxygen [276], these reactive species were also examined for their effect on the sensitiser in solution. These experiments were, however, conducted at ambient conditions, ignoring the effects of cavitation temperatures and pressures on these reactions.

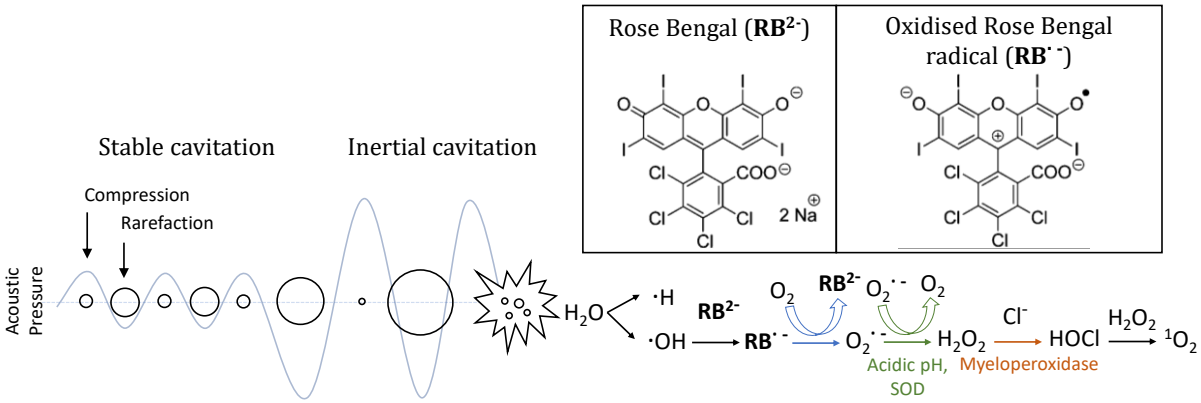

Figure 4.1. *Schematic of bubble cavitation and following reaction to produce ROS: superoxide anion radical ($O_2^{\cdot -}$) from oxidised Rose Bengal radical ($RB^{\cdot -}$). The possible reaction pathway for the production of singlet oxygen ($^1O_2$) in biological systems is also depicted. Other species are: hydrogen atom (·H), hydroxyl radical (·OH), Rose Bengal (RB^{2-}), superoxide dismutase (SOD), hydrogen peroxide (H_2O_2), chloride ion (Cl^-), hypochlorous acid (HOCl).*

The stability of Rose Bengal exposed to several ultrasound exposure conditions was also characterised to determine whether the toxicity induced by sonodynamic therapy could originate from the degradation of sensitiser into reactive species.

Finally, the generation of sonoluminescence from multi-bubble cavitation in aqueous solutions at 37°C was investigated as a mechanism for sensitiser activation with ultrasound parameters applicable to sonodynamic therapy. The contributing effects of microbubbles during this process was also evaluated. The results from this chapter would then demonstrate the likelihood for this phenomenon to occur in biological systems.

4.2.2. Reagents

Rose Bengal, 1,3-diphenylisobenzofuran (97%) (DPBF), hydrogen peroxide, benzoic acid, Methylene Blue, and ethanol were all obtained from Sigma-Aldrich (Dorset, UK). Singlet oxygen sensor green (SOSG) was purchased from Thermo Fisher Scientific (Loughborough, UK). Microbubbles encapsulating sulphur hexafluoride gas (SF_6MBs) were formed using the materials described in section 3.2., and were sparged with oxygen gas from The BOC Group (Guilford, Surrey, UK) to form oxygen microbubbles. Sonovue® microbubbles were purchased from Bracco UK Limited (High Wycombe, UK).

4.2.3. Detection of Rose Bengal

The presence of Rose Bengal was determined through its characteristic absorption around 560 nm (**Figure 4.2**) and its activation was determined by the generation of singlet oxygen through Type-II reaction with ground state molecular oxygen (section 2.1.3, **Figure 2.4**).

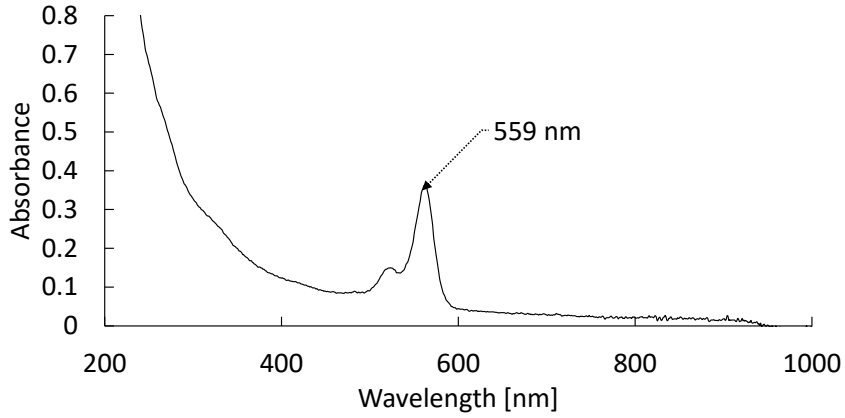

Figure 4.2. *Absorbance spectrum of Rose Bengal in an aqueous lipid solution (4 mg/mL).*

4.2.4. Detection of reactive oxygen species

Several chemical sensors were used to characterise the ROS examined in this chapter. This method ensured the appropriate reactive species were added to Rose Bengal in solution and allowed the characterisation of sensitiser activation.

The generation of hydroxyl radical was verified using non-fluorescent benzoic acid as it becomes permanently fluorescent (Ex: 305 nm / Em: 420 nm) upon aromatic hydroxylation. The detection of singlet oxygen specifically was accomplished using the commercial product SOSG which reacts with singlet oxygen to form SOSG-endoperoxides with a strong fluorescence emission around 525 nm (Ex: 504 nm / Em: 525 nm) [277,278]. Finally, the less specific presence of either singlet oxygen and/or superoxide anion was determined through a decrease in the absorbance of DPBF at 410 nm as it oxidises in the presence of these two species forming the non-fluorescent derivative: 1,2-phenylenebis(phenylmethanone) [279–284]. Because DPBF is not soluble in pure water, these experiments were conducted in mixtures of ethanol and water (50:50, v:v). In this, DPBF had a molar absorption coefficient equal to 1.74×10^4 M^{-1} cm^{-1} at a wavelength of 410 nm, and sample measurements were completed for a DPBF concentration of 20 µM and a path length of 0.441 cm (150 µL in a 96-well plate).

For each group, fluorescence and absorbance measurements were performed for n = 4 wells on COSTAR or Greigner UV-Star 96-well plates from Sigma-Aldrich (Dorset, UK), using a FLUOstar Omega multi-purpose plate reader from BMG Labtech (Aylesbury, Bucks, UK) at room temperature. For some of the examination, these measurements were taken before and after sample treatment to determine the relative change in intensity compared to the pre-exposure intensity. Sample absorbance measurements were all normalised to that of a blank control.

4.2.5. Reactions between reactive oxygen species and Rose Bengal

Cavitation events in aqueous medium can produce hydroxyl radicals, hydrogen peroxide [28,54], and subsequently singlet oxygen [276]. The effects of these reactive species on

Rose Bengal was investigated by measuring the absorbance of DPBF indicative of the generation of singlet oxygen and/or superoxide anions. DPBF was used because hydroxyl radicals, hydrogen peroxide, and singlet oxygen could react with Rose Bengal to subsequently generate singlet oxygen and/or superoxide anions.

4.2.5.1. Hydroxyl radicals

In these experiments, hydroxyl radicals were generated *in situ* through the ultraviolet degradation of hydrogen peroxide. For this, all samples were prepared in quartz reaction vessels. A sample with 10 mM H_2O_2 and 1.4 mM benzoic acid in 50% ethanol was then exposed to 640 µW/cm^2 of ultraviolet (UV) light (254 nm, Spectroline Short Wave X-15F) for 15 minutes. The formation of hydroxyl radical was confirmed through an increase in the fluorescence intensity of benzoic acid after treatment. Hydroxyl radicals were then produced in the presence of Rose Bengal and the formation of singlet oxygen and superoxide anion from this combination was examined using DPBF (**Figure 4.3**). A summary of the different samples tested for this evaluation is provided in **Table 4.1** and each preparation is detailed in the following sections.

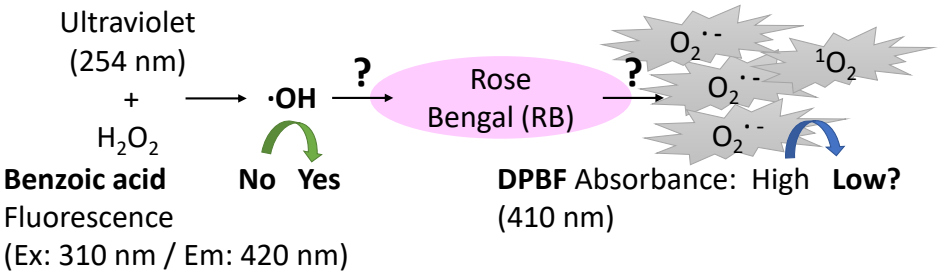

Figure 4.3. *Steps for hydroxyl radical generation in the presence of Rose Bengal to determine if their reaction could produce singlet oxygen or superoxide anion.*

Table 4.1. *Summary for the samples tested for the production of ROS from Rose Bengal in the presence of hydroxyl radical.*

SAMPLE	CONCENTRATION in 50% ethanol in deionised water	EXPOSURE CONDITION	CHARACTERISATION
+ control	10 mM H_2O_2 and 1.4 mM benzoic acid	UV light, 15 mins	Fluorescence intensity of benzoic acid
- control	1.4 mM benzoic acid	UV light, 15 mins	
- control	10 mM H_2O_2 and 1.4 mM benzoic acid	-	
+ control	2.5 µM RB and 20 µM DPBF	Ambient light, 1 min	Absorbance of DPBF
- control	2.5 µM RB and 20 µM DPBF	UV light, 15 mins	
Test	2.5 µM RB and 20 µM DPBF, 10 mM H_2O_2	UV light, 15 mins	

4.2.5.1.1. Positive controls

A 5 mL sample with 10 mM H_2O_2 and 1.4 mM benzoic acid in 50% ethanol in deionised water was prepared and the fluorescence intensity of benzoic acid (Ex: 305 nm / Em: 420 nm) was measured. The sample was then exposed to 640 µW/cm^2 of ultraviolet light (254 nm) for 15 minutes, before measuring its fluorescence again. This positive control verified that hydroxyl radical was indeed produced through the UV degradation of hydrogen peroxide. A second positive control was a 5 mL sample with 2.5 µM RB and 20 µM DPBF in 50% ethanol, exposed to 1 minute of ambient light. A decrease in the absorbance of DPBF at 410 nm confirmed the generation of reactive oxygen species from the photoactivation of the sensitiser.

4.2.5.1.2. Negative controls

A 5 mL sample of 1.4 mM benzoic acid in 50% ethanol was prepared and processed in the same way as the first positive control, to demonstrate the stability of benzoic acid through the 15 minutes UV light exposure. Additionally, a 5 mL sample with 1.4 mM benzoic acid was prepared in 50% ethanol and the fluorescence intensity of benzoic acid was measured pre- and post-addition of 10 mM H_2O_2 to demonstrate the stability of benzoic acid with

hydrogen peroxide. Finally, a 5 mL sample with 2.5 µM RB and 20 µM DPBF in 50% ethanol was prepared and exposed to 15 minutes of UV light to provide a measure of the activation of Rose Bengal from UV exposure.

4.2.5.1.3. Test

A 5 mL sample with 10 mM H_2O_2, 2.5 µM RB, and 20 µM DPBF was prepared in 50% ethanol. The absorbance of DPBF at 410 nm was recorded before and after exposing the sample to 15 minutes of UV light. This sample determined if the hydroxyl radicals produced react with Rose Bengal to form additional reactive oxygen species. A further decrease in the absorbance of DPBF compared to the negative control without added hydrogen peroxide (and hence hydroxyl radical) would suggest a reaction between hydroxyl radicals and Rose Bengal.

4.2.5.2. Hydrogen peroxide

Hydrogen peroxide is a strong oxidiser generated from the recombination of hydroxyl radicals during cavitation. Thus, the addition of hydrogen peroxide to Rose Bengal was examined in reduced light conditions to determine whether their reaction could produce more reactive species characterised by the absorbance of DPBF (**Figure 4.4**). The samples tested are summarised in **Table 4.2** and further described in the following sections.

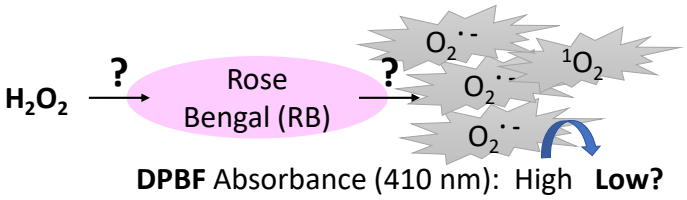

Figure 4.4. *Steps to determine if hydrogen peroxide can react with Rose Bengal and produce superoxide anion or singlet oxygen.*

Table 4.2. *Summary for the samples tested for the production of ROS from Rose Bengal in the presence of hydrogen peroxide.*

SAMPLE	CONCENTRATION in 50% ethanol in deionised water	EXPOSURE CONDITION	CHARACTERISATION
+ control	2.5 µM RB and 20 µM DPBF	Ambient light, 1 min	Absorbance of DPBF
- control	20 µM DPBF	Ambient light, 1 min	
- control	5 mM H_2O_2 and 20 µM DPBF	Reduced light	
Test	5 mM H_2O_2, 2.5 µM RB and 20 µM DPBF	Reduced light	

4.2.5.2.1. Positive control

To demonstrate the activity of Rose Bengal, a 5 mL sample of 2.5 µM RB and 20 µM DPBF was prepared in 50% ethanol. The sample was exposed to ambient light for 1 minute and characterised by the absorbance of DPBF at 410 nm pre- and post-exposure.

4.2.5.2.2. Negative controls

To demonstrate the stability of DPBF in ambient light, a 5 mL sample with 20 µM DPBF in 50% ethanol was prepared and processed the same way as the positive control. Another negative control was a 5 mL sample of 5 mM H_2O_2 and 20 µM DPBF in 50% ethanol kept in reduced light conditions to show the stability of DPBF with hydrogen peroxide in solution.

4.2.5.2.3. Test

A 5 mL sample with 5 mM H_2O_2, 2.5 µM RB, and 20 µM DPBF in 50% ethanol was prepared and processed under reduced light conditions to examine if hydrogen peroxide reacted with Rose Bengal to generate additional reactive oxygen species.

4.2.5.3. Singlet oxygen

As cavitation events can also lead to the formation of singlet oxygen, the addition of this reactive species to Rose Bengal in solution was examined. Singlet oxygen was generated *in situ* using the sensitiser Methylene Blue exposed to a red LED (660 nm, < 1 mW) for 30 seconds, and quantified by a decrease in DPBF absorbance. This was then compared to the DPBF absorbance of the same sample with added Rose Bengal to determine whether more reactive species were produced in the presence of Rose Bengal (**Figure 4.5**). The samples are summarised in **Table 4.3** and further described in the following sections.

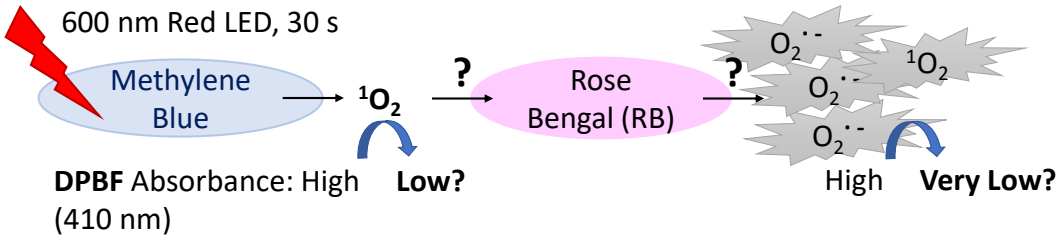

Figure 4.5. *Steps used to determine the production of singlet oxygen and its reactivity with Rose Bengal towards the production of $^1O_2$ or $O_2^{\cdot -}$.*

Table 4.3. *Summary for the samples tested for the production of ROS from Rose Bengal in the presence of singlet oxygen.*

Sample	Concentration in 50% ethanol in deionised water	Exposure condition	Characterisation
+ control	2.5 µM Methylene Blue and 20 µM DPBF	Red light, 30 s	Absorbance of DPBF
- control	2.5 µM RB and 20 µM DPBF	Red light, 30 s	
- control	20 µM DPBF	Red light, 30 s	
Test	2.5 µM Methylene Blue, 2.5 µM RB and 20 µM DPBF	Red light, 30 s	

4.2.5.3.1. Positive control

A 5 mL sample with 20 µM Methylene Blue and 20 µM DPBF in 50% ethanol was prepared in reduced-light conditions and exposed to a red LED (660 nm, 1 W) for 30 seconds. The production of singlet oxygen was then verified a decrease in the absorbance of DPBF.

4.2.5.3.2. Negative controls

A 5 mL sample with 2.5 µM RB and 20 µM DPBF in 50% ethanol was prepared and processed the same way as the positive control to demonstrate the stability of Rose Bengal to the red LED exposure for 30 seconds. The same test was done for a 5 mL sample with 20 µM DPBF in 50% ethanol to obtain the stability of DPBF under these conditions.

4.2.5.3.3. Test

A 5 mL sample with 20 µM Methylene Blue, 2.5 µM RB, and 20 µM DPBF in 50% ethanol was prepared, and processed the same way as the previous samples. The absorbance of DPBF was measured to determine whether the singlet oxygen produced could have reacted with Rose Bengal to produce additional reactive species.

4.2.6. Pyrolysis of Rose Bengal

Section 4.2.5 investigated the effects of reactive oxygen species on Rose Bengal in solution. Nevertheless, these experiments ignored the contributions of cavitation temperatures and pressures to these reactions. In this section, the stability of Rose Bengal with the exposure to several ultrasound conditions is assessed to determine if the oxidative degradation of the sensitiser occurs during sonodynamic therapy. The presence and quantity of Rose Bengal in solution was based on its absorbance spectrum after ultrasound exposure. Following the general protocol (section 3.3.2) for microbubble

manufacturing, a batch of *unloaded microbubbles* (section 3.3.3) was produced and used without the centrifugal cleaning steps as the excess material was not expected to affect this study.

A 1 mL sample with 2.5 µM RB and $5x10^8$ SF_6MB/mL in water were prepared and exposed to: (1) 20 kHz US (QSonica Q125 probe, 20kHz, 3 mm diameter, intensity: 14 W/cm^2) for 1 and 2 minutes, (2) 40 kHz US (Eumax UD150SH-6L ultrasound bath, 40 kHz, 150 W) for 10 minutes, or (3) 1 MHz US (Sonidel SP100 probe, 1 MHz, 16 mm diameter, intensity: 3.5 W/cm^2) for 5 minutes. The absorbance spectrum of the sample was recorded and compared to that of a control sample without exposure to ultrasound to evaluate if Rose Bengal was being degraded during this process.

4.2.7. Sonoluminescence activation of Rose Bengal

Sonoluminescence events generated during multi-bubble cavitation are examined in this section with and without the addition of cavitation nuclei and exposure to 1 MHz ultrasound. The activation of Rose Bengal during this process is then evaluated.

4.2.7.1. Design requirements

A chamber was designed and built for the characterisation of sonoluminescence events in a sample exposed to 1 MHz ultrasound. Photomultiplier tubes (PMTs) were used to characterise the light generated during this process as extremely low intensities are produced, especially when using exposure conditions relevant to sonodynamic therapy. This also prevented the use of a monochromator to characterise the optical spectrum of the light generated.

The design requirements were to:

- Align the ultrasound transducer, light and cavitation detector to cover the same sample volume,
- Minimise external light entry by building the tank from black Delrin,
- Accommodate two photomultiplier tubes (PMTs). One with optical filters and one without as a baseline. To characterise the optical spectrum of sonoluminescence, the signal of a filtered PMT was normalised with the unfiltered total amount of light generated. This enabled a comparison between experimental runs and normalised the data for the PMT sensitivity with respect to the wavelength. The data was then further normalised for the bandwidth of the optical filter.
- Optimise PMT input by maximising the numerical aperture (NA).
- Incorporate an absorber to minimise the formation of standing waves.

4.2.7.2. Custom-built chamber

To fit these design requirements, a tank was built from black Delrin with a 100 mL volume capacity. As shown in **Figure 4.6**, the driving ultrasound transducer is located at the top of the chamber and the passive cavitation detector (PCD) on the side, held in place by two O-rings. The two PMTs were connected to the chamber through SM1 threads on two other sides of the chamber allowing the attachment of lens tubes, connecting rings, and custom-made PMT holders. The PMTs and lenses were protected from the liquid sample with optical adhesive films stuck on the side-faces of the chamber with PMTs connections.

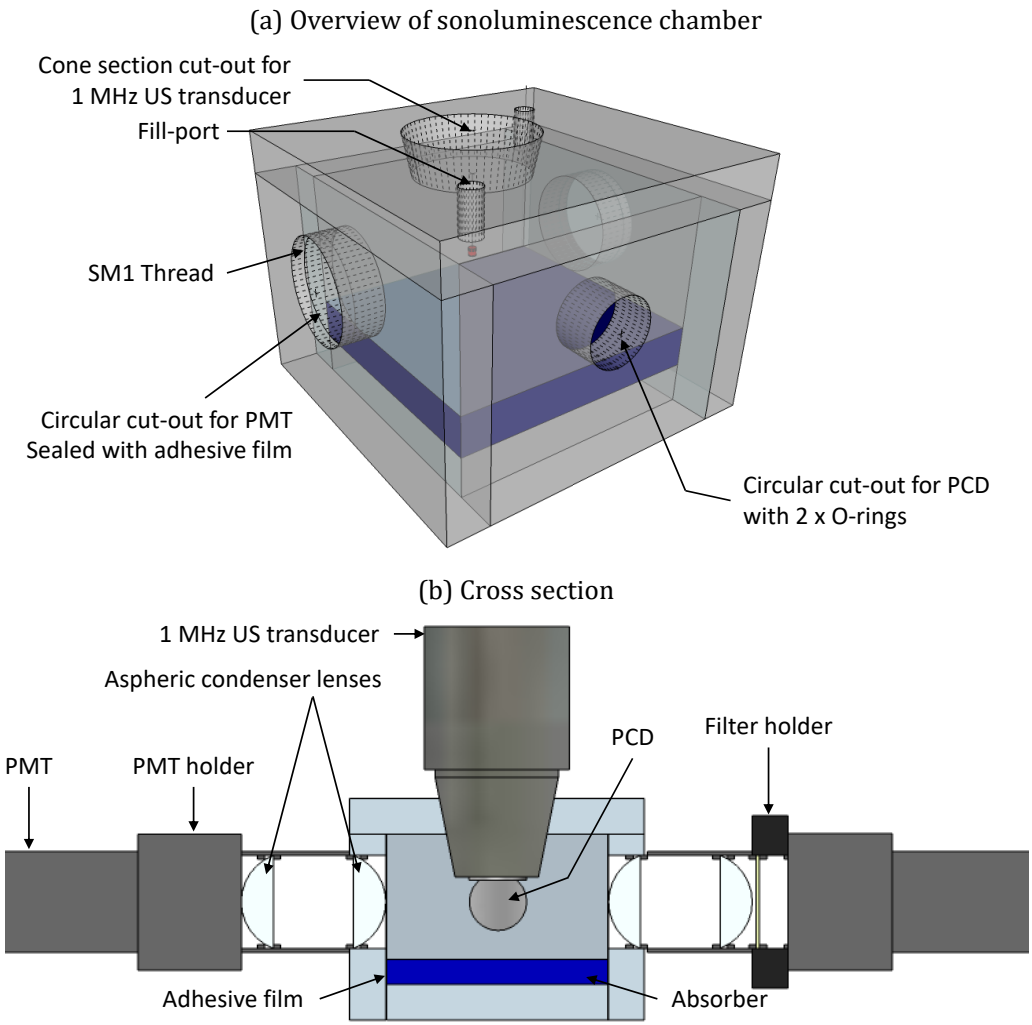

Figure 4.6. *Schematic of the sonoluminescence chamber* ***(a)*** *overview with chamber built from black Delrin, designed to accommodate a 1 MHz US transducer, a PCD, and two PMTs.* ***(b)*** *Cross-section of the chamber in the middle-plane.*

An ultrasound absorber material was added at the bottom of the chamber, and finally, two fill-ports on the lid of the system were added to avoid the trapping of air pockets during sample loading, and one of the fill-ports was used to hold a third transducer in the chamber used as a trigger sensor.

4.2.7.3. Equipment

The equipment incorporated within this set-up is described in **Table 4.4**.

Table 4.4. *Equipement used for the characterisation of sonoluminescence at 1 MHz*

EQUIPMENT	MANUFACTURER	PARAMETERS
Sonoluminescence chamber	Custom-built	
+ 2x adhesive films	MicroAmp™ Optical Adhesive Film, ThermoFisher Scientific, Loughborough, UK	
+ 1 absorber	Precision Acoustics (F28)	
1 MHz ultrasound transducer with built-in generator	Sonidel (SP100, 1 MHz, Ø = 16 mm)	1 MHz, 3.5 W/cm^2, 30% duty cycle, 100 Hz PRF
2x PMT with built-in amplifier	Hamamatsu (H10493-03)	0.6 gain
+ 4x aspheric condenser lenses with connecting rings	ThorLabs (ACL25416U-A, Ø = 1", f = 16 mm, NA = 0.79)	
+ 2x lens tubes	ThorLabs (SM1 lens tube, 1" thread depth)	
+ 2x connecting rings	ThorLabs (SM1T2, SM1 coupler ring, with external threads, 0.5" long)	
+ Sliding filter mount	ThorLabs (CFS1 with two CFS1-F1 inserts)	
+ optical filters	ThorLabs	λ / bandwidth 350 nm / 20 nm 470 nm / 22 nm 520 nm / 15 nm 560 nm / 15 nm
Unfocused PCD	Olympus (V320, 7.5 MHz, Ø = 0.5")	
Trigger transducer	Sonic Concepts (Minisensor, 2.9 MHz, Ø = 1.0 mm)	
+ High pass filter and preamplifier	JSR Ultrasonics (DPR300) Pulse Receiver	1 MHz high pass 34-dB relative gain
Digital oscilloscope	Pico Technology (PicoScope)	
Computer with 2x input channels (CH1, CH2) and 1x external trigger input (Ext) + LabVIEW + Pico scope capabilities		

4.2.7.4. Experimental set-up 1: PMT(full) + PCD

For the simultaneous recording of the PMT and PCD signals, the set-up 1 depicted in **Figure 4.7** was used. This method allowed the acquisition of both PMT and PCD signals on one LabVIEW *.tdms file. However, with set-up 1, the optically filtered PMT, PMT(filt), was not used because the computer only had two input channels.

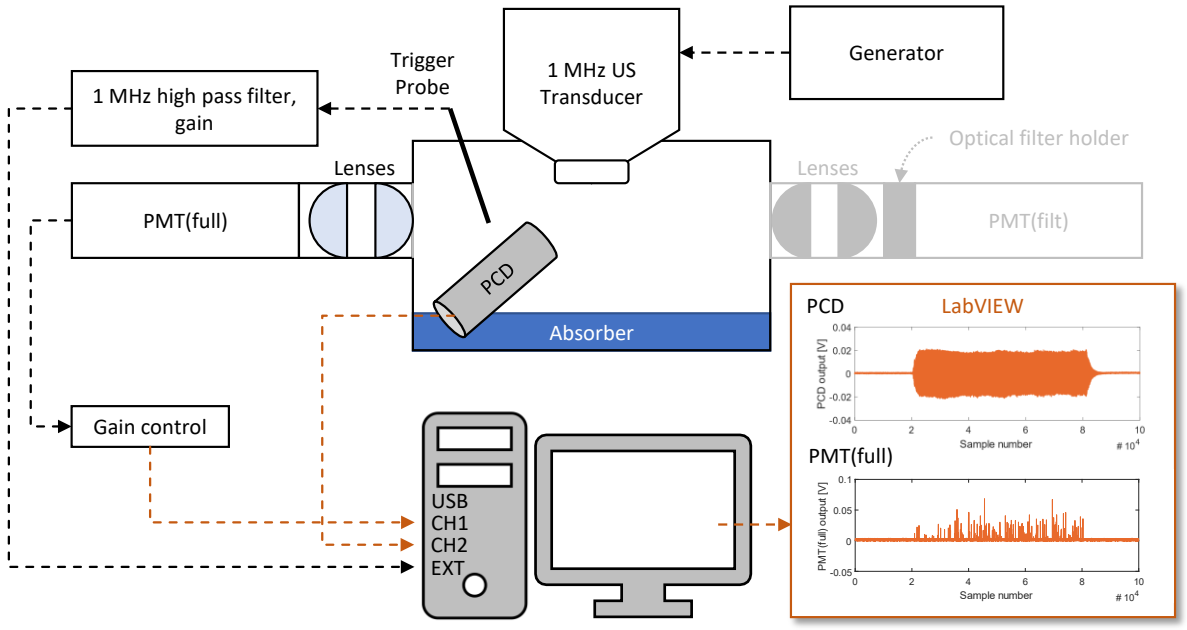

Figure 4.7. *Schematic of sonoluminescence experimental set-up 1 for the simultaneous recording of PMT (PMT(full)) and PCD signal on a computer operating LabVIEW. The PMT with filters (PMT(filt), greyed out) was unused in this set-up.*

4.2.7.5. Experimental set-up 2: PMT(filt) + PMT(full) + PCD

For the recording of the PMT output with and without optical filters, in addition to the PCD signal, a PicoScope was used to acquire the third input channel. The set-up was modified (**Figure 4.8**) and the PMT and PCD signals were acquired through LabVIEW and PicoScope respectively. This method, however, did not provide a perfect match between the recording time of LabVIEW and PicoScope data files due to differences in the triggering levels. A picture of the assembled set-up is shown in **Figure 4.9**.

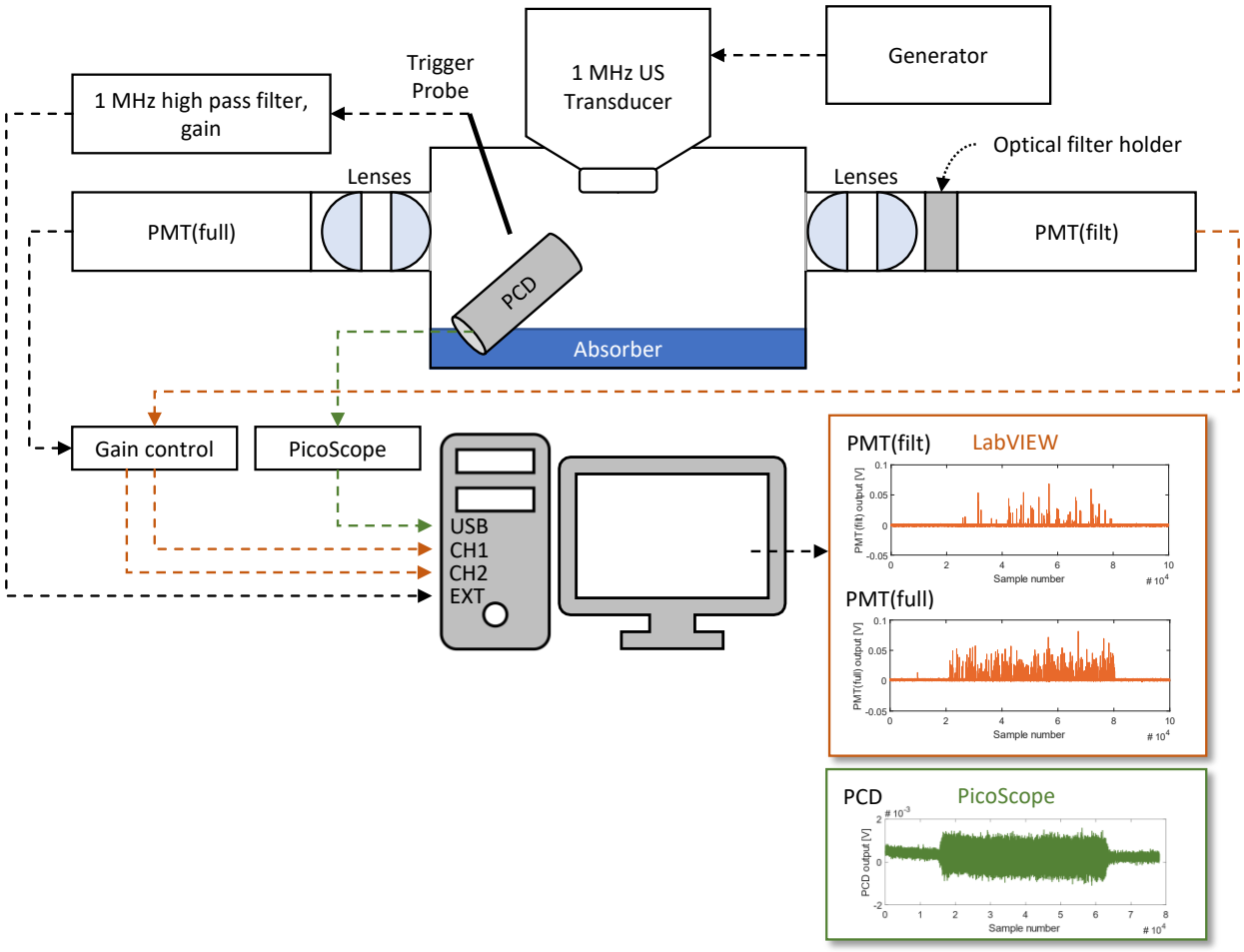

Figure 4.8. *Diagram of sonoluminescence experimental set-up 2 used for the recording of PMT with and without optical filter (PMT(filt), PMT(full) respectively) and PCD signals through LabVIEW and PicoScope.*

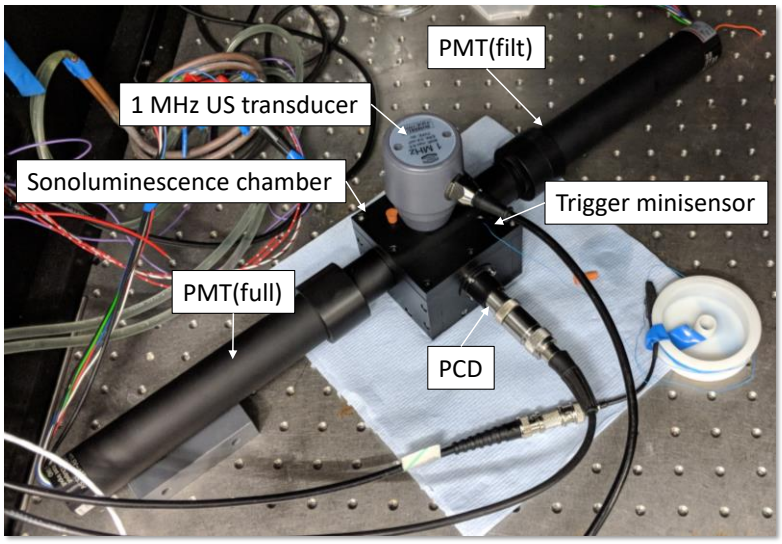

Figure 4.9. *Labelled picture of the experimental set-up used to characterise sonoluminescence.*

4.2.7.6. Exposure conditions

Sonoluminescence testing was done with the ultrasound turned on for 2 minutes (1 MHz centre frequency, 3.5 W/cm^2 intensity, 30% duty cycle, 100 Hz pulse repetition frequency) during which 1000 PMT acquisitions were recorded.

Sonoluminescence events were investigated in aqueous solutions ± microbubbles ± Rose Bengal. Samples were prepared in deionised water to obtain 5x10^5 MB/mL and 2.5 µM RB. Microbubbles produced in-house encapsulating sulphur hexafluoride or oxygen were examined and compared to SonoVue®. Following the general protocol (section 3.3.2*), unloaded microbubbles* encapsulating sulphur hexafluoride were manufactured (section 3.3.3) and used without the centrifugal cleaning of excess lipids. Sonoluminescence from oxygen loaded microbubble suspensions was also investigated as these have been used for the sonodynamic treatment of hypoxic tumours. For this, a 1 mL sample of SF_6MBs was sparged with oxygen for 2 minutes to form O_2MBs. The protocol for oxygen sparging of microbubbles is further discussed in Chapter 5.

The effect of bulk temperature was examined to determine if sonoluminescence could also occur at biologically-relevant temperatures. Thus, experiments were conducted with a sample temperature of 10, 23, and 37°C, monitored using a PCE-T390 digital thermometer from PCE Instruments before and after ultrasound exposure.

4.2.7.7. Data analysis

The PCD data was analysed as described in section 3.4.5.1. In set-up 1 with the recording of PMT(full) and PCD signals on LabVIEW, the cumulated count of PMT spikes above 6 mV in the ultrasound pulse (**Figure 4.10**) was compared to the energy of acoustic emissions. The distribution of PMT output intensity above the threshold was also analysed.

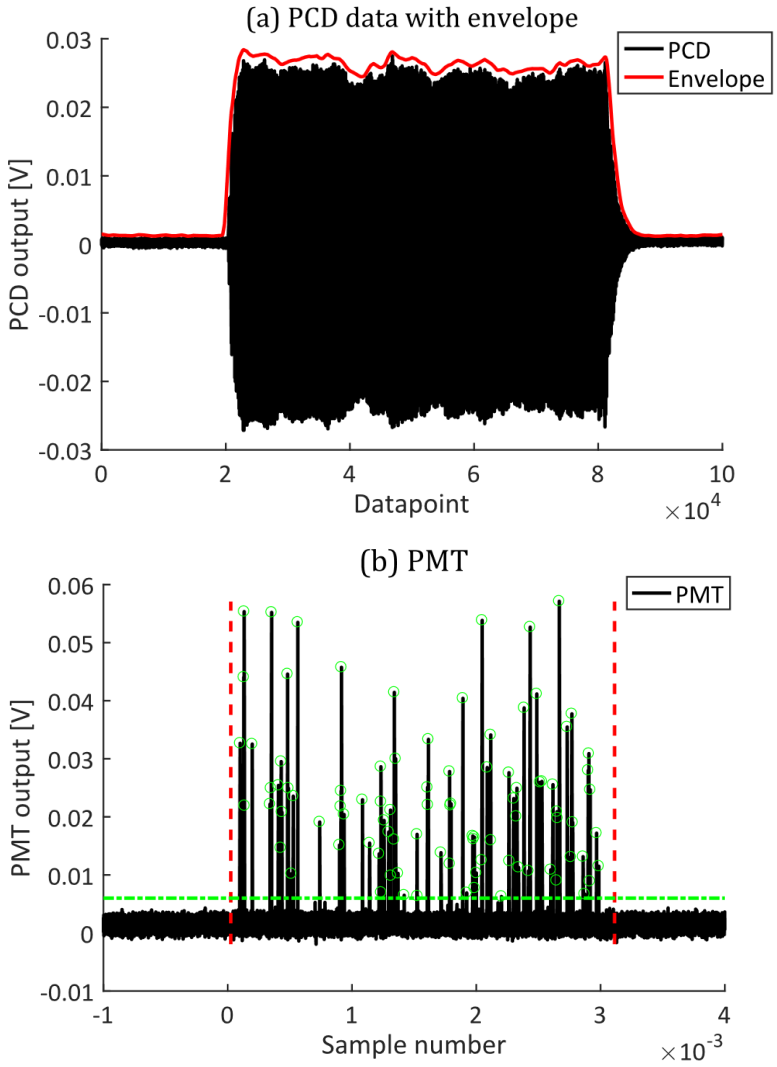

Figure 4.10. *Data analysis using sonoluminescence set-up 1.* ***(a)*** *The PCD traces were used to determine the location of the ON signal by analysing the slope of signal envelope.* ***(b)*** *This allowed a computation of PMT output above set threshold of 6 mV (green line) where the ultrasound was ON (delimited by the red lines).*

In set-up 2 with the recording the PMT(filt) and PMT(full) on LabVIEW, the cumulative count of PMT(filt) spikes above 6 mV were normalised by the overall count from PMT(full), thus allowing comparison between runs and normalising for the PMT wavelength sensitivity. The counts were then further normalised for the optical filter bandwidth indicated in **Table 4.4**, to output a percentage of the overall sonoluminescence recorded per wavelength studied.

4.2.8. Statistical analysis

Each set of experiments in this chapter was repeated n = 3 times. The fluorescence or absorbance readings were performed in quadruplicate for each sample.

4.3. Results

4.3.1. Reactions between reactive oxygen species and Rose Bengal

Pyrolysis of water during cavitation produces reactive oxygen species such as hydroxyl radicals which can recombine to form hydrogen peroxide, and subsequent cascade reactions can lead to the formation of singlet oxygen. These species were investigated to determine whether they would react with Rose Bengal to produce additional ROS as a possible mechanism for sonodynamic therapy. **Figure 4.11a** shows that the ultraviolet exposure of hydrogen peroxide successfully produced hydroxyl radical characterised by an increase in the fluorescence intensity of benzoic acid. The ambient light exposure of Rose Bengal also confirmed that the photoexcitation of the sensitiser produced singlet oxygen and/or superoxide anion determined through a decrease in the absorbance of DPBF (**Figure 4.11b**). Nonetheless, the addition of hydroxyl radical to Rose Bengal did not affect the activity of the sensitiser (**Figure 4.11c**). The unchanged 28% decrease in DPBF absorbance observed for the Rose Bengal solution with or without added hydroxyl radical, highlight the activation of the sensitiser from the UV exposure. Similar results were recorded for the addition of hydrogen peroxide in reduced-light conditions (**Figure 4.11d**), and singlet oxygen in the presence of Rose Bengal (**Figure 4.11e**). Therefore, under ambient temperatures and pressures the presence of hydroxyl radical, hydrogen peroxide, and singlet oxygen did not affect the activity of Rose Bengal.

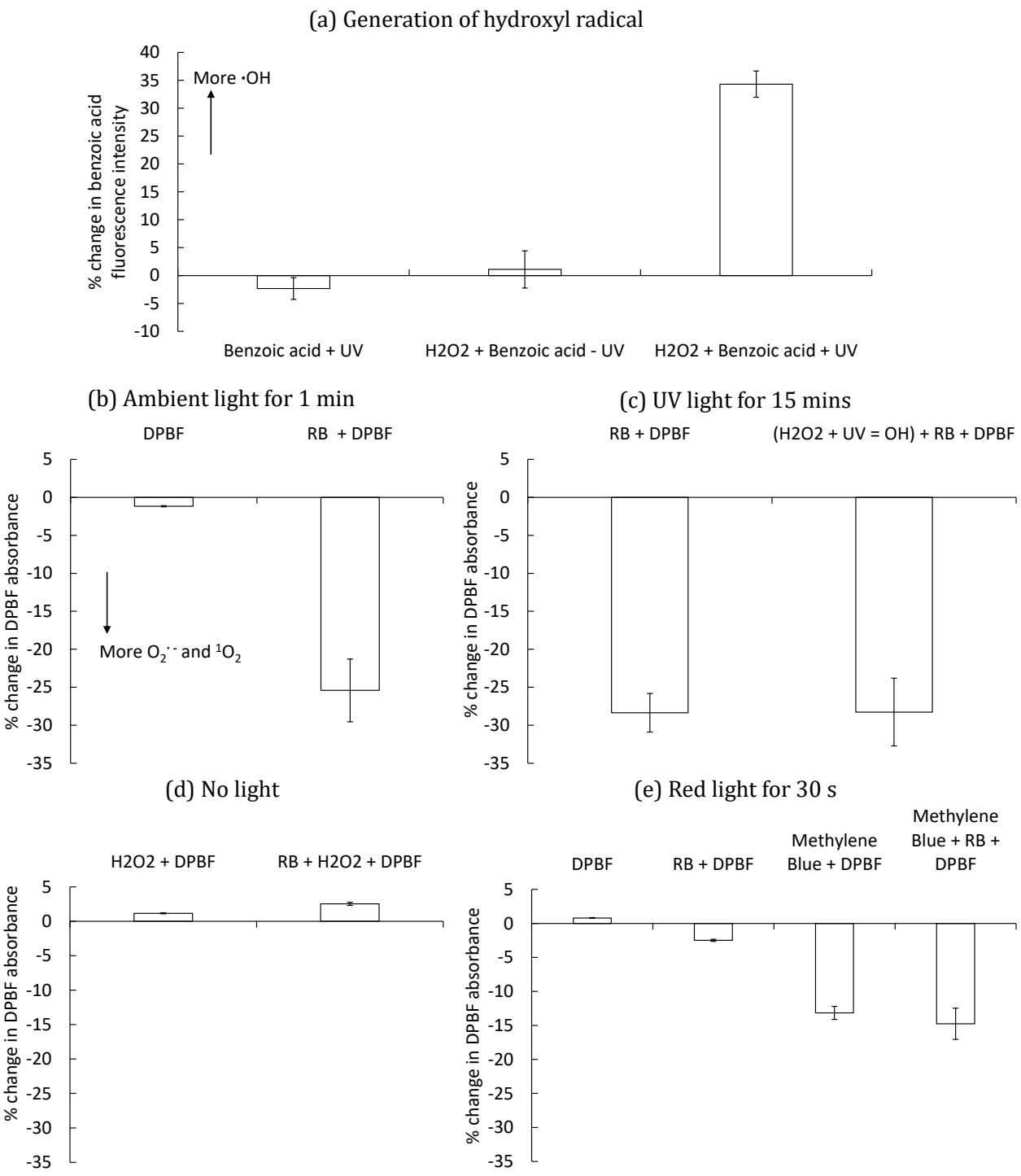

Figure 4.11. *Results on the activation of Rose Bengal with several reactive oxygen species. Demonstration of* ***(a)*** *hydroxyl radical generation from the UV degradation of hydrogen peroxide using benzoic acid as a fluorescent sensor.* ***(b-e)*** *Singlet oxygen and/or superoxide anion characterisation through the absorbance of DPBF for sample exposure to* ***(b)*** *ambient light for 1 minute,* ***(c)*** *hydoxyl radical from the UV degradation of hydrogen peroxide,* ***(d)*** *hydrogen peroxide in reduced-light conditions, and* ***(e)*** *singlet oxygen from the photoactivation of Methylene Blue using red light for 30 seconds. n = 3 for each group and error bars indicate the standard deviation.*

4.3.2. Pyrolysis of Rose Bengal

An evaluation of Rose Bengal in solution after ultrasound exposure in **Figure 4.12** indicated that the sensitiser was not permanently degraded at those exposure conditions (20 kHz for 2 minutes, 40 kHz for 10 minutes, or 1 MHz for 5 minutes).

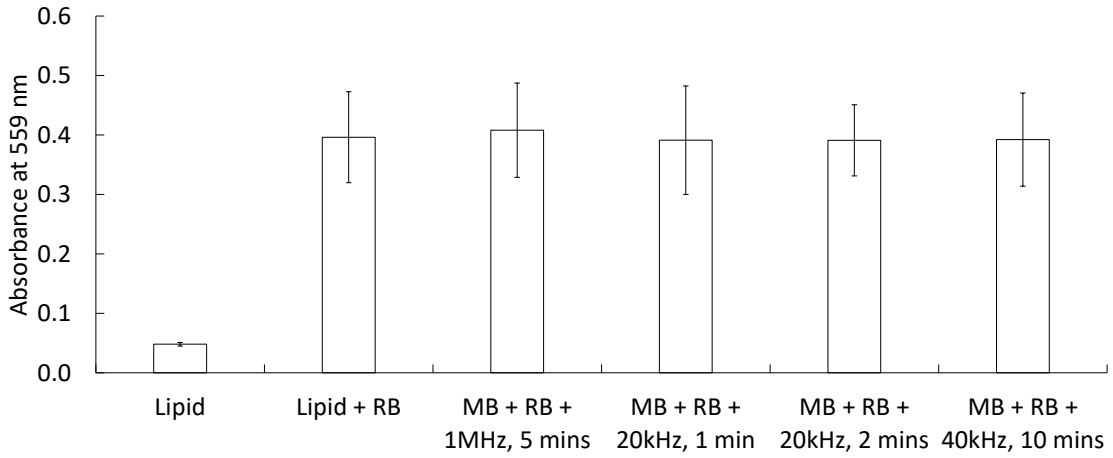

Figure 4.12. *Absorbance of aqueous Rose Bengal solutions at 559 nm after exposure to several conditions, indicating that the sensitiser was not substantially degraded compared to the unexposed Lipid + RB sample.*

4.3.3. Sonoluminescence

Three different formulations of microbubbles were examined for their potential in generating sonoluminescence when insonated with 1 MHz ultrasound at an intensity of 3.5 W/cm^2, 30% duty cycle, and 100 Hz pulse repetition frequency for 2 minutes. For this, simultaneous measurements of sonoluminescence and acoustic emissions at 23°C were taken for microbubbles manufactured in-house encapsulating sulphur hexafluoride or oxygen gas and the commercially available contrast agent Sonovue®. The size distribution of microbubbles with a mean diameter of approximately 2 μm (**Figure 4.13**) was found to be comparable to the size of Sonovue®.

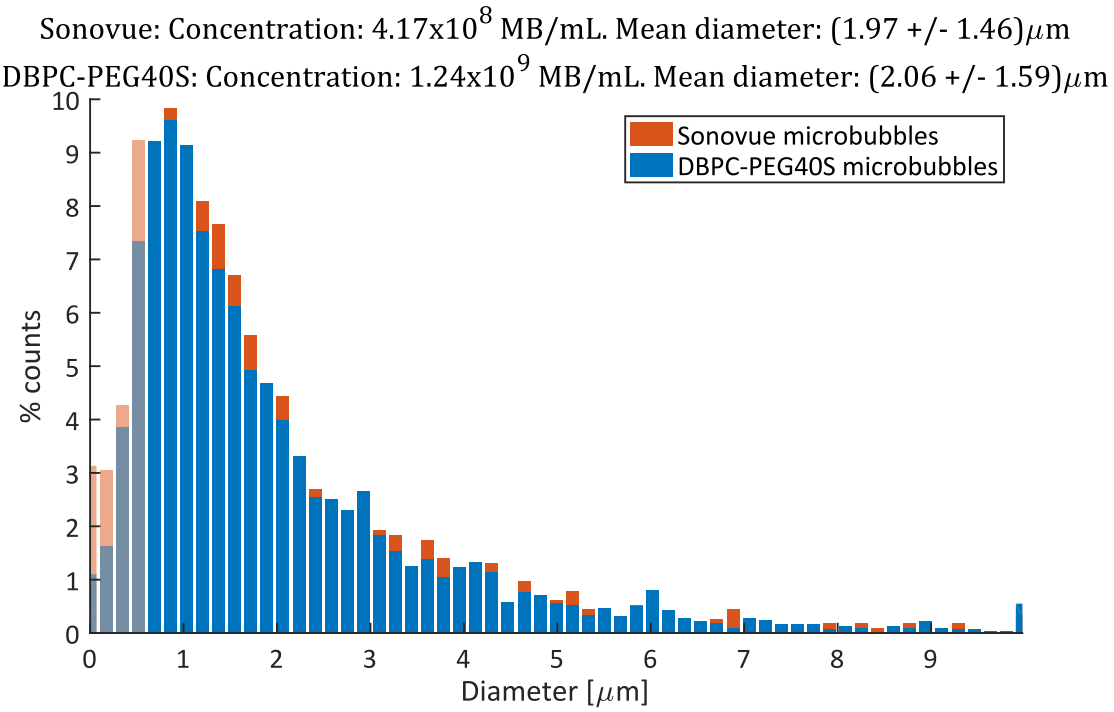

Figure 4.13. *The concentration and size distribution of Sonovue® and in-house produced microbubbles computed through an analysis of optical microscope images* [233].

During the sonoluminescence experiments, the samples were diluted to $5x10^5$ MB/mL in deionised water to reflect the diluted concentrations that would be obtained in the human blood stream following injection. While all microbubbles tested produced sonoluminescence when exposed to ultrasound (**Figure 4.14**), slightly reduced sonoluminescence counts were observed for O_2MBs compared to Sonovue® and SF_6MBs. While still within experimental error, the slight diminution might be attributed to the lower stability of oxygen-loaded microbubbles and the higher solubility of oxygen in aqueous solutions compared to sulphur hexafluoride. The reduced broadband energy levels produced by O_2MBs (**Figure 4.14**) are consistent with these results.

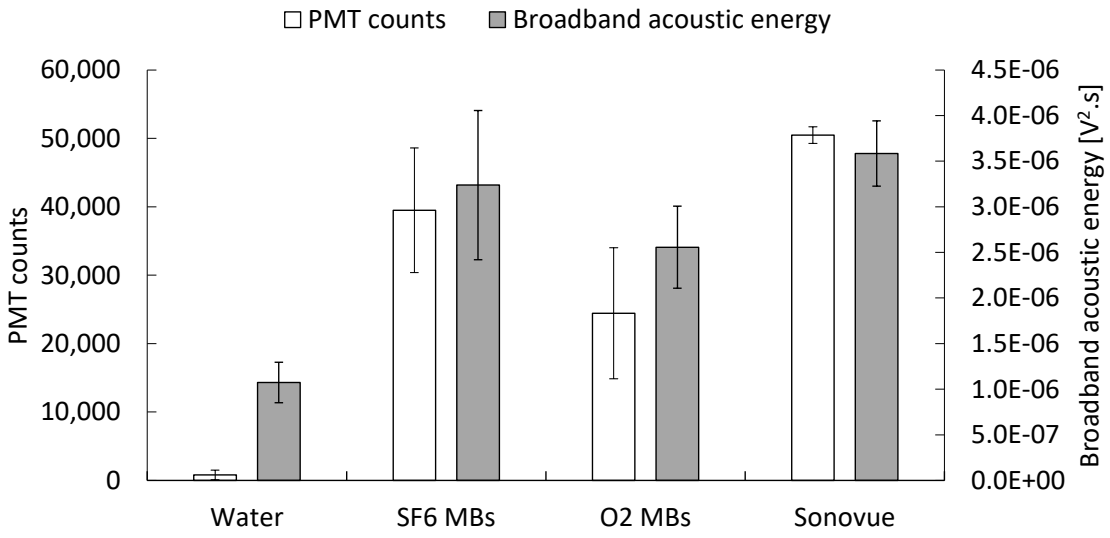

Figure 4.14. *Sonoluminescence produced by microbubbles driven at 1 MHz, an intensity of 3.5 W/cm^2, 30% duty cycle, and 100 Hz pulse repetition frequency for 2 minutes. The total PMT counts above 6 mV in amplitude and broadband energy emission for water and three formulations are displayed. (n = 3 runs of 1000 acquisitions each, error bars indicate standard deviations).*

The PMT pulse height distribution of sonoluminescence events was evaluated for each group. The results in **Figure 4.15a** show that samples containing microbubbles exhibited comparable behaviour. In contrast, water samples presented local highs and lows within the distribution which could be due to the low number of sonoluminescence events recorded in this group (**Figure 4.14**). Nonetheless, different microbubble formulations might affect the intensity of the collapse due to shell stabilisation or gas solubility. Thus, focusing on the upper tail of the pulse height distribution (**Figure 4.15**a **inset**), the sum of PMT peaks above an arbitrary threshold of 60 mV was calculated in order to compare high amplitude events in each group (**Figure 4.15b**). The results indicate that cavitation of these systems generated comparable high amplitude sonoluminescence within experimental variation [50,51]. The slightly lower result recorded for water samples could be associated with the low number of events recorded or the reduced stability of uncoated bubbles in water, leading to collapse conditions of reduced intensity.

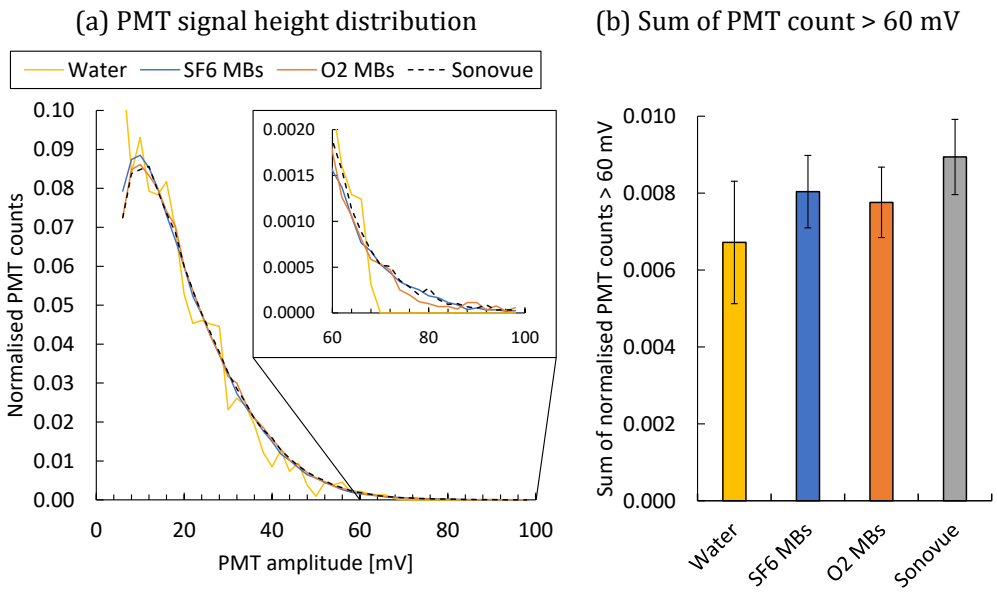

Figure 4.15. *Comparison of sonoluminescence amplitude for water ± SF_6, O_2, or Sonovue MBs.* ***(a)*** *Average number of PMT sonoluminescence counts for increasing peak amplitude for each type of microbubbles (n = 3). Number of PMT counts in each bin is normalised by the total number of counts recorded in each run. The inset shows a zoom-in of high amplitude PMT counts from 60 to 100 mV.* ***(b)*** *Bar chart of the sum of normalised PMT counts above 60 mV for each MB tested.*

The spectrum of the light generated using SF_6MBs was measured using a set of five optical filters at room temperature. **Figure 4.16** shows a broad spectrum with an increased sonoluminescence generation at the shorter wavelengths. As the intensity of sonoluminescence reported here was low, the use of a monochromator to obtain a higher wavelength resolution was not feasible, thus specific molecular features in the optical spectrum were not discernible. However, sonoluminescence in water has been reported at 1 MHz with a broad continuous spectrum and no molecular features [49,285,286]. This has been associated with radiation emissions from cavitation events e.g. blackbody [48], bremsstrahlung [42,46], and/or recombination radiations [43,287]. Although, no consensus has been reached on the exact mechanisms, the generation of reactive oxygen species during microbubble cavitation such as hydrogen peroxide [131] and hydroxyl radical [288,289] concurs with the recombination radiation theory [49,287].

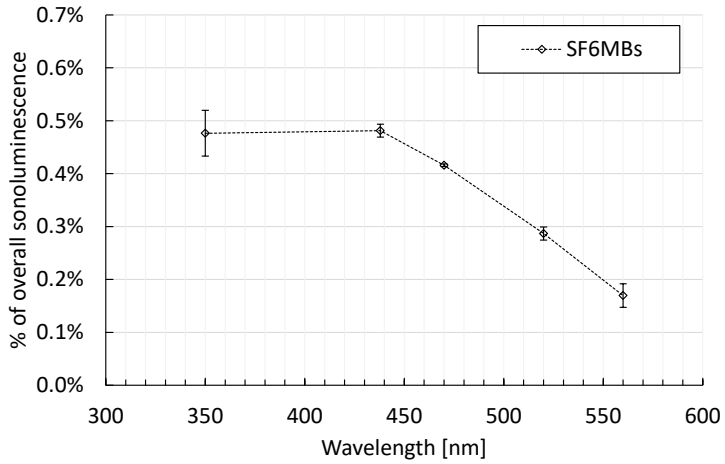

Figure 4.16. *Spectrum of sonoluminescence for diluted SF_6 microbubbles at 23°C. The percentage of overall sonoluminescence reflects the counts from the filtered PMT normalised with the counts from a non-filtered PMT, thus normalising for the PMT sensitivity at that wavelength over 1000 acquisitions. The normalised count was then also corrected for the bandwidth of the optical filters used. n = 3 runs were performed for each wavelength and error bars indicate the standard deviation between the runs.*

An increase in bulk solution temperature has been reported to affect sonoluminescence (1) by increasing the number of sonoluminescence events due to an increase in the number of cavitation events [50] and (2) by lowering the amplitude of individual sonoluminescence events due to lowering of the intensity of collapse [51]. Measurements were taken at 10, 23, and 37°C and their comparison in **Figure 4.17a** shows the expected increase in sonoluminescence occurrence and broadband activity at 37°C when SF_6MBs were used as cavitation nuclei. As the amplitude of sonoluminescence was examined (**Figure 4.17b**), a slight decrease in the number of high amplitude events (> 60 mV) was observed with higher bulk solution temperatures (**Figure 4.17b** inset).

Thus, these results agree with both effects (1) and (2) mentioned above and they demonstrate that at biologically relevant temperatures and at 1 MHz, a greater number of sonoluminescence events occur when microbubbles are exposed to mild therapeutic ultrasound; however, the amplitude of individual events is slightly reduced.

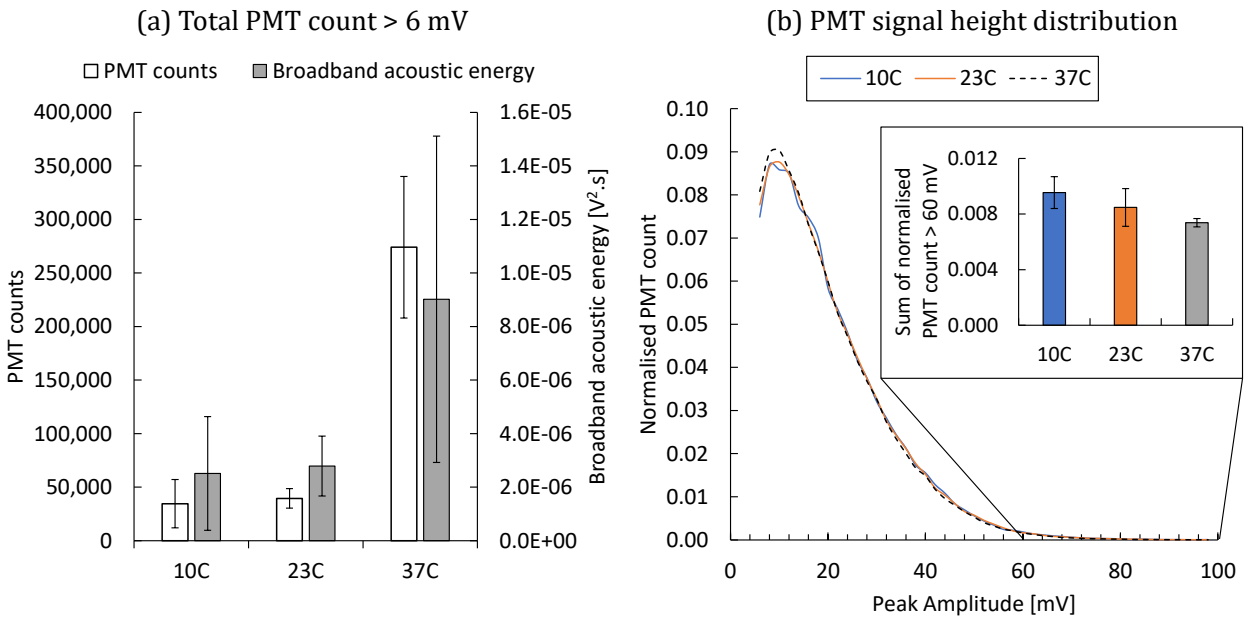

Figure 4.17. *Sonoluminescence from SF_6MBs diluted in deionised water at 10, 23, 37°C (n = 3, error bars indicate standard deviations for each run).* ***(a)*** *Total PMT counts above 6 mV in amplitude and broadband energy for three different temperatures are displayed.* ***(b)*** *Number of PMT counts for increasing peak amplitude. Number of PMT counts in each bin is normalised by the total number of counts recorded in each run. The inset shows the sum of normalised PMT counts above 60 mV for each temperature tested. These results indicate that with increasing temperatures, while the number of cavitation events increases, their amplitude slightly decreases. The sample temperature before and after ultrasound exposure did not fluctuate substantially (±1°C).*

4.3.3.1. Sonoluminescence with Rose Bengal

Sonoluminescence output with and without the presence of Rose Bengal was then examined to determine whether sufficient light of the appropriate wavelength was generated to activate the sensitiser. **Figure 4.18a** highlights that the presence of Rose Bengal and SF_6 microbubbles in solution at 37°C led to a decrease in sonoluminescence measured at the absorption wavelength of the drug (560 nm) compared to a reference wavelength (350 nm). Hence, sonoluminescence from cavitating microbubbles can be absorbed by surrounding sensitisers to cause their activation. These results support the hypothesis that sonoluminescence and the resulting transfer of energy to an accepting

sensitiser is a key mechanism underlying sonodynamic therapy and are consistent with reports by Umemura *et al.* [7] and Giuntini *et al.* [27] at room temperatures and without the use of exogenously-added cavitation nuclei. Additionally, **Figure 4.18b** shows that at with the same ultrasound parameters, the combination of Rose Bengal and sulphur hexafluoride microbubbles in solution produced significantly more singlet oxygen radicals compared to microbubbles alone, confirming the activation of the sensitiser.

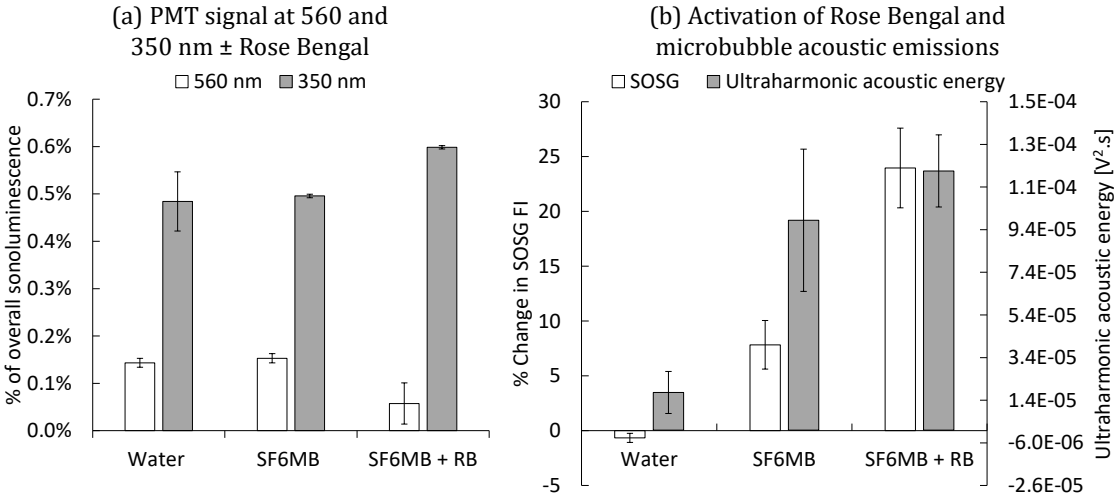

Figure 4.18. *The addition of Rose Bengal (RB) to SF_6 microbubbles (SF6MB), and the resulting effect on sonoluminescence and singlet oxygen radical generation.* ***(a)*** *Percent of overall sonoluminescence measured with optical filters for 560 nm and 350 nm. Filtered PMT signal was normalised by the overall counts recorded by the non-filtered PMT (normalising for PMT wavelength sensitivity) and for the bandwidth of the filter used. These were acquired for water, SF_6 microbubbles (SF6MB), SF_6 microbubbles and Rose Bengal samples at 37°C (n = 3 runs, each of 1000 acquisitions). Rose Bengal peak absorbance is known to be at 559 nm. The sonoluminescence measurement at 560 nm was made to assess the absorption of sonoluminescence by the sensitiser and compared to 350 nm for reference.* ***(b)*** *The activation of Rose Bengal was assessed through the generation of cytotoxic singlet oxygen radical. This was characterised by an increase in the fluorescence intensity (FI) of Singlet Oxygen Sensor Green (SOSG, left axis). The different groups were exposed to 1 MHz, 462 $mV_{pk\text{-}pk}$, 30% duty cycles, 100 Hz pulse repetition frequency for 30 seconds (n = 3). The ultraharmonic emissions of microbubbles were captured using a passive acoustic detector and displayed as the overall ultraharmonic energy during the exposure (right axis).*

4.4. Discussion

In the absence of cavitation, ultrasound is a non-ionising modality and epidemiologic studies of ultrasound imaging have not identified any significant health hazards associated with the technique [43,44]. Yet, bubble cavitation was shown to cause ionisation of molecules as seen with a broad continuum of sonoluminescence and the production of excited species and radicals [37,39]. Nevertheless, the majority of previous studies on sonoluminescence have employed ultrasound frequencies and intensities that are significantly different from those used in diagnostic or therapeutic ultrasound [34,35,38,41,290,291]. Still, with the increasing use of microbubbles in both ultrasound imaging and therapy [142], and studies showing sonoluminescence at ultrasound frequencies in the MHz range [7,27,48–50,292,293], there is a need to understand whether these extreme events can in fact occur in tissue. In particular, sonoluminescence and the reactive oxygen species associated with violent bubble collapse have been suggested as the means by which certain classes of drug can be activated by ultrasound [1,294–297].

In this chapter focusing on the mechanisms for the activation of sensitisers during sonodynamic therapy, the presence of reactive oxygen species did not affect the activity of Rose Bengal at ambient temperatures and pressures. These results suggest that pyrolysis-induced ROS generation might not be involved in the activation of Rose Bengal. Further, microbubble cavitation in the presence of this sensitiser did not lead to significant degradation demonstrating that significant pyrolysis of the sensitiser itself does not occur at these exposure conditions.

In contrast, the occurrence of sonoluminescence events was observed during the excitation of microbubbles at 37°C using ultrasound parameters previously shown to have

a therapeutic effect *in vivo* [4,86,216,298]. The sonoluminescence measured is, however, unlikely to cause phototoxicity as the number of photons was well below that associated with the safe use of lasers in medical applications [45,46]. Nonetheless, the light generated could be absorbed by a sensitiser in solution, and therefore, cavitation-induced sonoluminescence is likely to be involved with the activation of Rose Bengal during sonodynamic therapy. Although these results contradict those of Kim *et al*. presenting the activation of an "optically inert" Rose Bengal during ultrasound exposure [61], an examination of their approach reveals that an optically active Rose Bengal could be regenerated from the reaction of their novel compound with hydroxyl radicals [299]. As these reactive species are produced during cavitation, the regeneration of an optically active Rose Bengal during ultrasound exposure of their proposed compound is expected

Still, the results presented in this chapter are limited by several factors. Firstly, the experiments investigating the effects of reactive oxygen species on Rose Bengal were conducted at ambient temperatures and pressures, thereby ignoring these effects during cavitation. Secondly, additional control experiments should be added: (1) using a non-photosensitive dye with similar chemical structure as Rose Bengal instead of Rose Bengal and evaluating the ROS generation with DPBF and SOSG, and (2) using a photosensitive dye that does not produce singlet oxygen in addition to Rose Bengal to compete for photon absorbance during ultrasound exposure and evaluate the generation of singlet oxygen from Rose Bengal with SOSG. Furthermore, sonoluminescence measurements were obtained on a static sample, and further examination of sonoluminescence at 37°C and under flow is necessary to better characterise the occurrence of these events during sonodynamic therapy. Finally, a study on the ROS population generated by cavitating microbubbles is required in order to determine the appropriate balance between safe and

efficient ultrasound parameters for treatment. Preliminary results on this topic are presented in the following chapter.

4.5. Conclusions

The generation of sonoluminescence by microbubbles and ultrasound is potentially of great importance for the fields of photo- and sonodynamic therapy. In PDT, significant efforts have been made to design sensitisers with increased absorption at wavelengths that allow improved penetration of light in tissue. Although the therapeutic effects of sonodynamic therapy have been reported since 1989 [1], the explanation behind the activation of the sensitiser with this method is currently without consensus.

Since cavitation events lead to the formation of reactive species through pyrolysis of molecules, some these chemicals were examined for how they affect the activity of the sensitiser Rose Bengal. The work presented in this chapter has demonstrated that Rose Bengal is a stable sensitiser for sonodynamic therapy and is not activated through reactions with hydroxyl radicals, hydrogen peroxide or singlet oxygen at ambient conditions. Therefore, these results do not indicate the activation of Rose Bengal through pyrolysis-mediated pathways. Additionally, microbubbles were found to produce light, i.e. sonoluminescence, when driven at medically relevant ultrasound frequencies and pressures. Previous work has indicated that the ultrasound exposure conditions associated with sonoluminescence are very different from those used in medical applications. Nonetheless, this chapter shows that phospholipid-coated microbubbles do produce broadband sonoluminescence when exposed to low-intensity, 1 MHz ultrasound at 37°C, the intensity of which was positively correlated with the broadband energy of microbubble acoustic emissions. Further, the results presented also confirmed that

sonoluminescence is likely to be involved in the activation of Rose Bengal which allows the local production of reactive oxygen species during sonodynamic therapy. Although numerous preclinical reports demonstrated the therapeutic effect of this method, a lack of understanding in how the sensitiser is activated during exposure to ultrasound has caused resistance against this emerging technique. Therefore, this chapter provides key results important for the advancement of sonodynamic therapy towards clinical use, in addition to demonstrating that sensitisers used for photodynamic therapy can be locally activated by ultrasound and microbubble cavitation.

4.5.1. Contributions

To the best of the author's knowledge, this chapter provides the first characterisation of sonoluminescence activity correlated to microbubble acoustic emissions during exposure to ultrasound conditions used for treatment. Additionally, the activation pathway of sensitisers with ultrasound has been debated since the 1990s, and this examination confirmed that sonoluminescence is involved in the activation of Rose Bengal during sonodynamic therapy.

4.5.2. Limitations

The effects of hydroxyl radicals, hydrogen peroxide and singlet oxygen on Rose Bengal were examined at ambient temperatures and pressures, and thus ignored the extreme conditions produced during bubble cavitation. Further, although sonoluminescence measurements were completed at 37°C, the results presented in this chapter are limited to a static environment. Therefore, these experiments could be repeated in a more biologically-relevant system incorporating flow and biological media. Finally, a study on

the reactive species population generated during microbubble cavitation and sonodynamic therapy is needed to confirm the stability of Rose Bengal for this therapy. This would also provide an insight on the ultrasound parameters necessary to obtain a therapeutic effect using this method.

Chapter 5
Oxygen microbubbles and ultrasound parameters for SDT

Chapter 5 focuses on the methods used to produce microbubbles with encapsulated oxygen and the ultrasound parameters required for effective sonodynamic therapy using these microbubbles and Rose Bengal. The aim of the work was to improve the understanding of the critical parameters for this therapy and how they might be optimised for the treatment of hypoxic tumours.

Parts of the results presented in this chapter are under preparation for publication.

Contents

5.1. Introduction

The injection of oxygen microbubbles has been shown to enhance the efficacy of sonodynamic therapy in the treatment of hypoxic tumours [4]. Nonetheless, as outlined in section 2.3.1, the stability of oxygen microbubbles is impaired by the high diffusivity of oxygen in biological systems, and thus an appraisal of the methods for producing lipid-based oxygen microbubbles is needed. In addition, the ultrasound parameters used with sonodynamic therapy have typically been in the range of low-intensity therapeutic ultrasound with 1-3 MHz centre frequency, 0.5-5 W/cm^2 intensity, 10-100% duty cycle, and 2-15 minutes exposure time as presented in **Appendix Table A.1**. However, an optimisation of these parameters for the activation of the sensitiser with oxygen microbubbles during sonodynamic treatment is lacking.

5.1.1. Objectives and scope

This chapter begins with a comparison of methods for producing lipid-coated oxygen microbubbles. A study is then made on the activation of Rose Bengal during sonodynamic therapy mediated by oxygen microbubbles with varying ultrasound (1) pressure, (2) duty cycle (DC), and (3) pulse repetition frequency (PRF). The ultrasound excitation frequency was fixed at 1 MHz for these experiments as it provides an appropriate compromise between focal depth and treatment volume achieved for small animal models [300]. Although beyond the scope of the current preliminary work, the frequency used can be optimised for human applications. Additional studies are then needed to determine how frequency impacts sonoluminescence events and Rose Bengal activation, and whether additional effects (e.g. thermal) contribute to the activation pathway.

5.2. Methods

Microbubbles were characterised for their size, concentration, oxygen loading and stability. Their acoustic emissions under different ultrasound exposure conditions relevant to sonodynamic therapy were measured simultaneously with the generation of singlet oxygen from Rose Bengal. The latter was determined by measuring the increase in the fluorescence intensity of the commercial dye Singlet Oxygen Sensor Green at 520 nm.

5.2.1. Materials

As described in previous chapters, the primary constituent of microbubbles was 1,2-dibehenoyl-sn-glycero-3-phosphocholine (DBPC) a phospholipid purchased from Avanti Polar Lipids Inc. (Alabaster, Alabama, USA). Polyoxyethylene (40) stearate (PEG40S), chloroform, Dulbecco's phosphate buffered saline (PBS), and Rose Bengal were all obtained from Sigma Aldrich Ltd. (Gillingham, Dorset, UK). Singlet Oxygen Sensor Green was purchased from Thermo Fisher Scientific (Loughborough, UK). The oxygen and sulphur hexafluoride gases were obtained from BOC Industrial Gases (Guilford, Surrey, UK). Finally, vials of commercial microbubbles Sonovue® were purchased from Bracco UK Limited (High Wycombe, UK).

5.2.2. Manufacturing oxygen microbubbles

The manufacturing of oxygen microbubbles through several methods was investigated. The first entailed replacing the gas head-space above the freeze-dried Sonovue® product with oxygen before reconstituting the microbubbles in saline. The microbubbles formed by this method are hereafter referred to as "O_2SV".

The second method aimed to generate lipid-coated microbubbles directly through sonication under an oxygen gas flow (referred to as "*direct* O_2MB"). This method followed the same procedure as outlined in the *unloaded microbubble* protocol (section 3.3.3) but replacing sulphur hexafluoride with oxygen gas flow, and without the cleaning of the microbubble batch.

Sparging of microbubble suspensions initially made with sulphur hexafluoride was also tested (referred to as "*sparged* O_2MB"). The aim being to promote gas exchange within the microbubbles by imposing an increased concentration gradient. For this, several sparging methods were compared. 5 mL batches of SF_6MBs were either (1) sparged with oxygen for 2 minutes (method referred to as "5mL/2minO_2") or (2) divided into 5 x 1 mL samples, each of which was sparged with oxygen for 2 minutes ("1mL/2minO_2"). These samples were then immediately capped and placed into a beaker of ice for an additional 5 minutes before use. A summary of the different techniques is provided in **Table 5.1**.

Table 5.1. *Summary of methods for the manufacturing of oxygen microbubbles*

O_2MB METHOD	PROTOCOL	CONSIDERATIONS
O_2SV	Reconstitution of Sonovue microbubbles with a headspace of oxygen gas, saline solution not sparged	Fewer processing steps, ease of clinical translation
Direct O_2MB	Formation of microbubbles under oxygen gas flow for 30 s	Less processing steps
Sparged O_2MB 5mL/2minO2	Sparging of 5-mL SF_6MBs suspension with oxygen gas for 2 mins	More processing steps
Sparged O_2MB 1mL/2minO2	Sparging of 1-mL SF_6MBs suspension with oxygen gas for 2 mins	More processing steps

5.2.3. Characterisation of oxygen loading in microbubbles

The size and concentration of microbubbles was determined through an analysis of optical images using a MATLAB script as described in section 3.4.1 [233]. These were compared for the different manufacturing methods to produce oxygen microbubbles.

The oxygen content of microbubbles was measured using the set-up depicted in **Figure 5.1**. The oxygen content was acquired for the liquid and gas phases of a sealed vial containing a 14 mL water sample and compared to that of the same sample after the addition and subsequent rupture of 1 mL microbubble suspension. Microbubble rupture was achieved by placing the sealed vial in an ultrasound bath (Eumax, UD150SH-6L, 40 kHz, 150 W) for 30 seconds. The oxygen content (% saturation in water) was measured using an OxyMini device from PreSens (Regensburg, Germany) with temperature compensation. The acquired data was subsequently adjusted for the sample dilution (1:15 v/v) and converted to units of µL O_2/mL of microbubble suspension and units of µL $O_2/10^8$ MB to account for differences in microbubble concentrations. The sensor spots for oxygen sensing were glued on the inside of the sample vial at two levels: in the solution and in the gas phase above the solution as depicted in **Figure 5.1**.

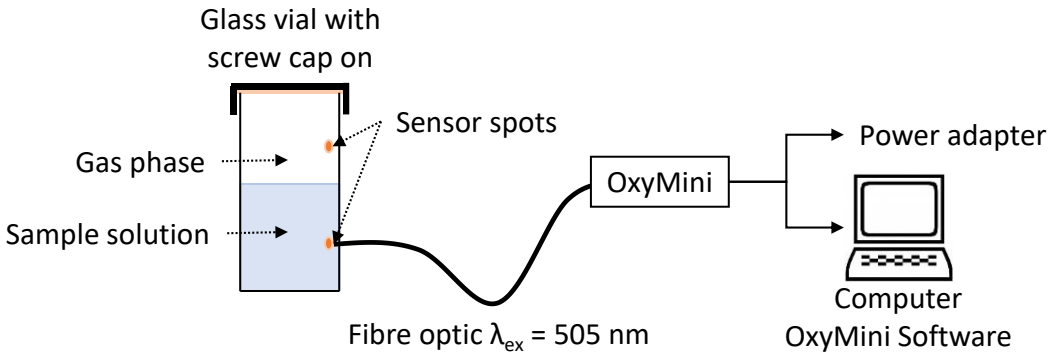

Figure 5.1. *Schematic of experimental set-up used for oxygen loading measurements. A sample glass vial with 14 mL deionised water was measured to determine the oxygen content in the liquid and gas phases prior to, and after addition and rupture of 1 mL oxygen microbubbles. The sample vial was capped and sealed with Teflon tape during these tests and the oxygen content (% saturation in water) was measured using an OxyMini fiber optic, recording device, and two sensor spots attached on the inside of the vial. Each group was measured n = 3 times.*

To determine the amount of oxygen dissolved in the solution surrounding the oxygen microbubbles, measurements were made on control samples containing no bubbles, these were then handled through the same process as test samples. In the case of Sonovue®, the control was the manufacturer's saline solution injected into an empty freeze-drying vial handled in the same way as the O_2SV sample. In the case of microbubbles produced in-house, an aqueous lipid mixture sparged with oxygen or sulphur hexafluoride gas reflecting the handling of a test sample was used as control. The difference in the total oxygen release recorded for microbubble samples and that of control samples then represented the encapsulated oxygen.

After comparing the different loading strategies to produce oxygen microbubbles, the method with the highest loading was characterised for its stability under flow using a second experimental set-up. For this a 1 mL sample of *sparged* O_2MB 1mL/2minO_2 was injected into a 4 mL flow loop pre-loaded with deionised water at room temperature and connected to a CDI Blood Parameter Monitoring System 500 from Terumo UK Ltd. (Tamesis, UK) as depicted in **Figure 5.2**. The sample was flown in a tubing of 1.6 mm inner diameter for 6 minutes at 10 mL/min using a Gilson Minipuls 3 peristaltic pump from Fisher Scientific (Loughborough, UK). This set-up led to a Reynolds number of 130 (using the kinematic viscosity of water as in **Table 3.3**) and wall shear stress of 1.7 Pa resulting in flow conditions representative of those found in small arteries. Three minutes after injection and flow of the sample, the sonicating bath was turned on for 30 seconds to release the remaining encapsulated oxygen. During the 6 minutes, the dissolved oxygen partial pressure (kPa) within the sample was measured every 5 seconds.

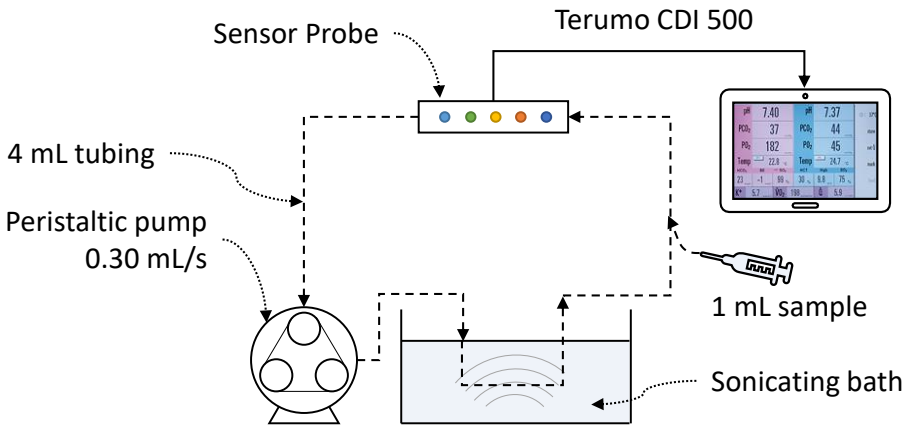

Figure 5.2. *Schematic of the experimental set-up used to characterise the release of oxygen from microbubbles over time (n = 3). A 1 mL sample was injected into a tubing containing 4 mL of deionised water, flown at 0.3 mL/s for 6 minutes while monitoring the dissolved oxygen partial pressure (kPa) every 5 seconds. At t = 3 minutes post-injection, the ultrasound bath was turned on for 30 seconds to release any remaining encapsulated oxygen.*

5.2.4. SDT with Rose Bengal and oxygen microbubbles

During exposure to low-intensity 1 MHz ultrasound, the activation of Rose Bengal was characterised by measuring the intensity of fluorescence emissions from SOSG. This dye is sensitive to singlet oxygen; the cytotoxic product of Type-II reactions from the activated Rose Bengal. The contribution of oxygen microbubbles to sonodynamic therapy was then measured in degassed PBS to mimic the low availability of surrounding oxygen in hypoxic tumours. All experiments were completed (n = 3) in reduced-light condition to prevent the photoactivation of the sensitiser during ultrasound exposure.

5.2.4.1. Ultrasound parameters, exposure, and acoustic emissions

The aim of the study was to examine the independent effects of changing the ultrasonic (1) pressure, (2) duty cycle, and (3) pulse repetition frequency while exposing the samples to the same total number of acoustic cycles ($9x10^6$). **Figure 5.3** illustrates the difference in ultrasound pulses when varying duty cycle or pulse repetition frequency.

(a) Varying duty cycle, fixed pulse repetition frequency of 100 Hz and total number of acoustic cycles delivered

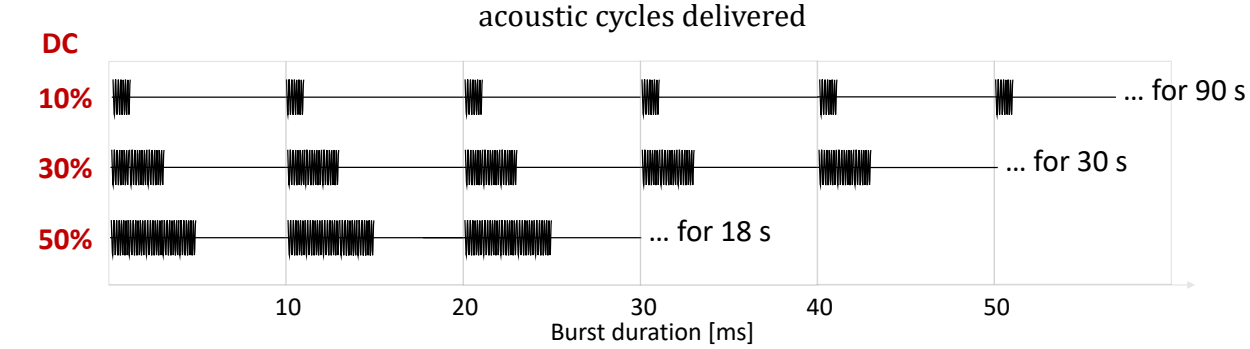

(b) Varying pulse repetition frequency, fixed duty cycle of 30% and total number of acoustic cycles delivered

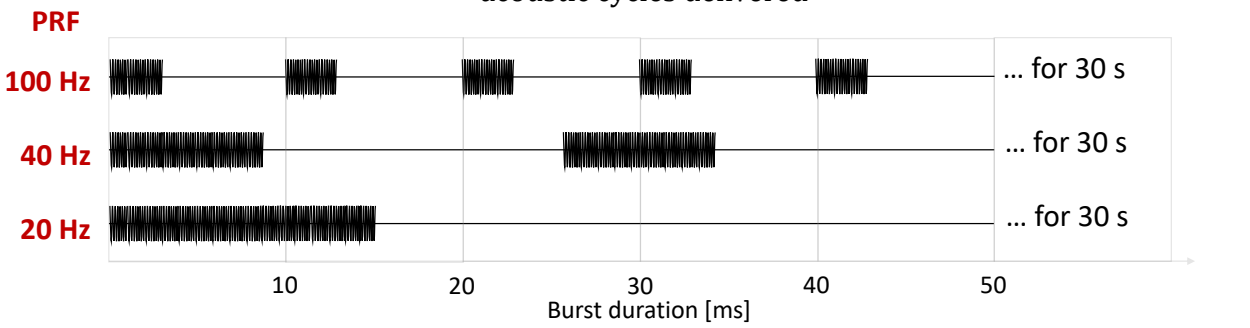

Figure 5.3. *Schematic of ultrasound burst for varying the duty cycle or pulse repetition frequency* ***(a)*** *duty cycles with a fixed pulse repetition frequency of 100 Hz, and* ***(b)*** *pulse repetition frequency with a fixed duty cycle of 30%. In both cases a total number of* $9x10^6$ *acoustic cycles is delivered.*

Table 5.2 then highlights how an increase in duty cycle decreases the amount of OFF time within the exposure compared to a fixed total OFF time when varying the pulse repetition frequency.

Table 5.2. *Summary for $t_{US\ ON}$ and $t_{US\ OFF}$ when varying duty cycle or pulse repetition frequency*

CHANGING ULTRASONIC DUTY CYCLE				
Duty cycle [%]	10	30	50	100
Number of cycles/burst **@ 100 Hz PRF**	1000	3000	5000	10000
Burst US ON time [ms]	1	3	5	10
Burst US OFF time [ms]	9	7	5	0
Number of cycles total	$9x10^6$			
Number of bursts	9000	3000	1800	900
Exposure time (t) [s]	90	30	18	9
Time with US ON ($t_{US\ ON}$) [s]	**9**	**9**	**9**	**9**
Time with US OFF ($t_{US\ OFF}$) [s]	**81**	**21**	**9**	**0**
CHANGING ULTRASONIC PULSE REPETITION FREQUENCY				
Pulse repetition frequency [Hz]	20	40	100	118
Burst duration [ms]	50	25	10	8.5
Number of cycles/burst **@ 30% DC**	15000	7500	3000	2542
Burst US ON time [ms]	15	8	3	3
Burst US OFF time [ms]	35	18	7	6
Number of cycles total	$9x10^6$			
Number of bursts	600	1200	3000	3540
Exposure time (t) [s]	30	30	30	30
Time with US ON ($t_{US\ ON}$) [s]	**9**	**9**	**9**	**9**
Time with US OFF ($t_{US\ OFF}$) [s]	**21**	**21**	**21**	**21**

A sample of 12 mL was prepared comprising of degassed PBS (0.5 L PBS degassed for 30 minutes at -0.9 bar leading to 10% O_2 compared to 20% O_2 in air saturated PBS) with SOSG (1.25 µM), ± RB (2.5 µM), ± O_2MBs (5 x 10^7 MB/mL). A sub-sample of 9 mL was then exposed to ultrasound, and this process was repeated n = 3 times over the parameters indicated in **Table 5.3**. The ultrasound exposure was conducted in custom-made tank with a built-in 1 MHz transducer and the acoustic emissions from the sample were recorded through a PCD and processed as previously described in section 3.4.5.1.[3] Briefly, the recorded emissions were analysed using MATLAB to calculate the power spectral density

[3] The data acquisition and writing limitations of the TiePie Handyscope HS3 unfortunately prevented the recordings of acoustic emissions for ultrasound duty cycles above 30% and pulse repetition frequency below 40 Hz.

of each acquisition, and the power and cumulative energy for broadband, ultraharmonic, and harmonic frequency ranges. The analysis of PCD data was completed over the total ultrasound exposure time to be comparable to the SOSG measurements made after ultrasound treatment.

Table 5.3. *Ultrasound parameters tested for sonodynamic therapy with oxygen loaded microbubbles and Rose Bengal in degassed PBS.*

CHANGING ULTRASONIC PRESSURE					
Frequency (f) [MHz]	1				
Duty cycle [%]	30				
Pulse repetition frequency [Hz]	100				
Exposure time (t*) [s]	30				
Pressure $_{pkpk}$ (P) [MPa]	0.45	0.85	1.1	1.4	1.7
Exposure time (t**) [s]	30	8	5	3	2
CHANGING ULTRASONIC DUTY CYCLE					
Frequency [MHz]	1				
Duty cycle [%]	10	30	50	100	
Pulse repetition frequency [Hz]	100				
Exposure time [s]	90	30	18	9	
Pressure $_{pkpk}$ [MPa]	1.4				
CHANGING ULTRASONIC PULSE REPETITION FREQUENCY					
Frequency [MHz]	1				
Duty cycle [%]	30				
Pulse repetition frequency [Hz]	20	40	100	118	
Exposure time [s]	30				
Pressure $_{pk-pk}$ [MPa]	1.4				

* Increasing the US energy delivered. ** Constant US energy delivered.

5.2.4.2. Singlet oxygen detection

The fluorescence intensity of SOSG (Ex: 490 nm / Em: 520 nm) was measured after ultrasound exposure and compared to that of the remaining unexposed sample. Immediately after ultrasound treatment, the test sample was pipetted (6 x 150 µL) onto a COSTAR 96-well plate from Sigma-Aldrich (Dorset, UK). For each run, the remaining 3 mL of the sample not exposed to ultrasound was used as a control to calculate the percentage

change in SOSG fluorescence intensity caused by the treatment. To minimise the scattering from remaining microbubbles in the control sample, the control sample was taken up into a syringe which was used to rupture the microbubbles by applying pressure on the syringe plunger with the end capped, before sampling it (6 x 150 µL) onto the same 96-well plate. Fluorescence intensity measurements were acquired on a FLUOstar Omega multi-purpose plate reader from BMG Labtech (Aylesbury, Bucks, UK) at room temperature.

5.2.5. Statistical analysis

For each experimental protocol n = 3 runs were completed. The figures present the average measurement and the error bars indicate the standard deviation within each group. Statistical significance was determined using 1-way analysis of variance (ANOVA) followed by Tukey's post-hoc test.

5.3. Results

5.3.1. Oxygen microbubble characterisation

The different manufacturing techniques presented in **Table 5.1** were compared for the size and yield of oxygen microbubbles produced. The results in **Figure 5.4** demonstrate that oxygen microbubbles could be formed following different techniques but there was a significant difference in their production yields. The reconstitution of Sonovue® with a headspace of oxygen and the production in-house of microbubbles under *direct* oxygen gas flow, both produced a lower yield compared to their sulphur hexafluoride counter-parts. Additionally, *direct* O_2MB exhibited a higher mean diameter compared to other in-house methods, suggesting a decreased stability for these systems.

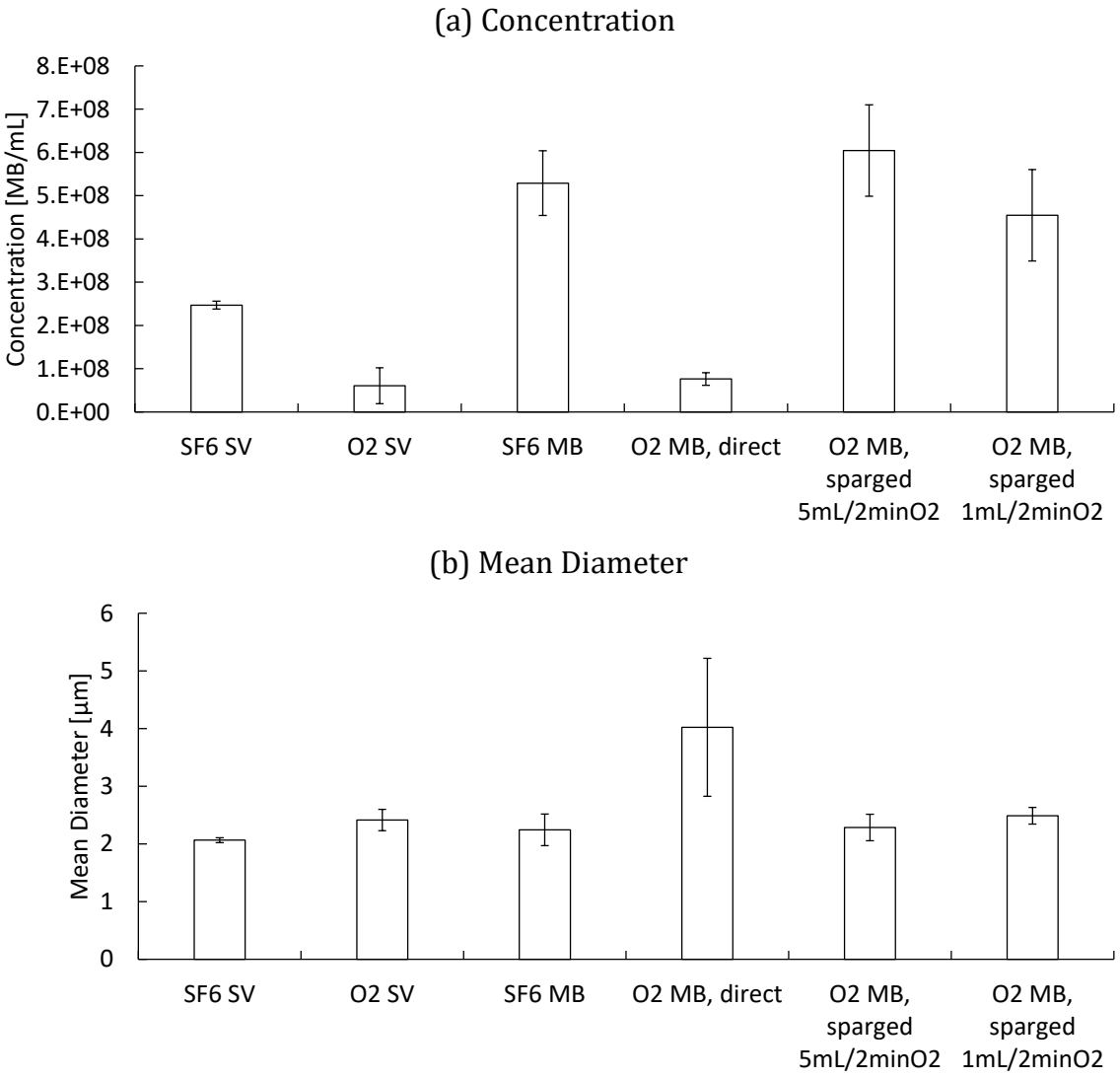

Figure 5.4. (a) *Concentration and* ***(b)*** *mean diameter of the microbubbles considered in this section encapsulating sulphur hexafluoride or oxygen using the different production methods described in Table 5.1 (n = 3). Abbreviations: Sonovue® microbubbles (SF6 SV), Sonovue® microbubbles reconstituted with a headspace of oxygen gas (O2 SV), microbubbles produced in-house made: under SF_6 gas flow (SF6 MB), under O_2 gas flow (O2 MB, direct), under SF_6 gas flow and subsequently a 5 or 1 mL sample was sparged with oxygen for 2 minutes (O2 MB, sparged 5mL/2minO_2 or 1mL/2minO_2 respectively).*

In contrast, the sparging of sulphur hexafluoride microbubbles with oxygen did not affect the concentration of microbubbles obtained significantly.

To compare the oxygen encapsulation efficiency of the different methods, the oxygen content of microbubbles was compared to that of control samples without microbubbles.

Figure 5.5 shows the change in oxygen concentration from the addition of samples with and without microbubbles, and the difference between these two series highlights the amount of encapsulated oxygen within the bubbles. The control groups with sulphur hexafluoride led to a decrease in oxygen concentration following sample addition which might reflect the displacement of oxygen initially dissolved in the sample by the added sulphur hexafluoride.

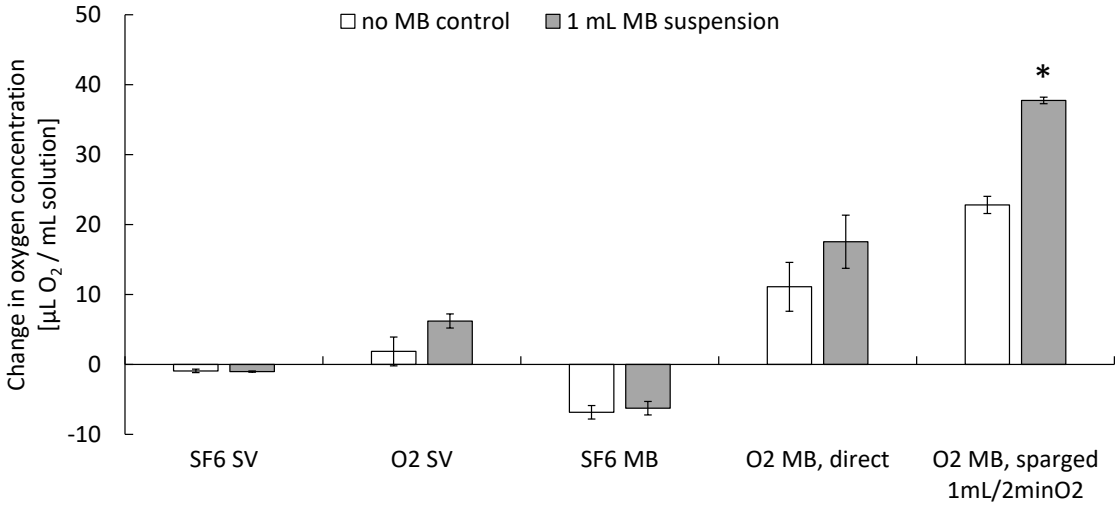

Figure 5.5. *Change in oxygen concentration in the vial after the addition of 1 mL of sample ± microbubbles (n = 3, * p < 0.01). For Sonovue, controls were made with saline injected in an empty freeze-drying vial and handled in the same way as test Sonovue® samples. For in-house produced microbubbles, controls were obtained using an aqueous lipid solution without microbubble.*

Figure 5.5 demonstrates an agreement between the oxygen concentration measured and the concentration of microbubbles present in the sample (**Figure 5.4a**) thereby emphasizing the importance of microbubble yield and stability. The difference in the oxygen concentration between samples with microbubbles and controls without microbubbles represents the encapsulated oxygen in microbubbles. A normalisation of this data based on the microbubble concentration in the 1 mL sample added is shown in **Figure 5.6**.

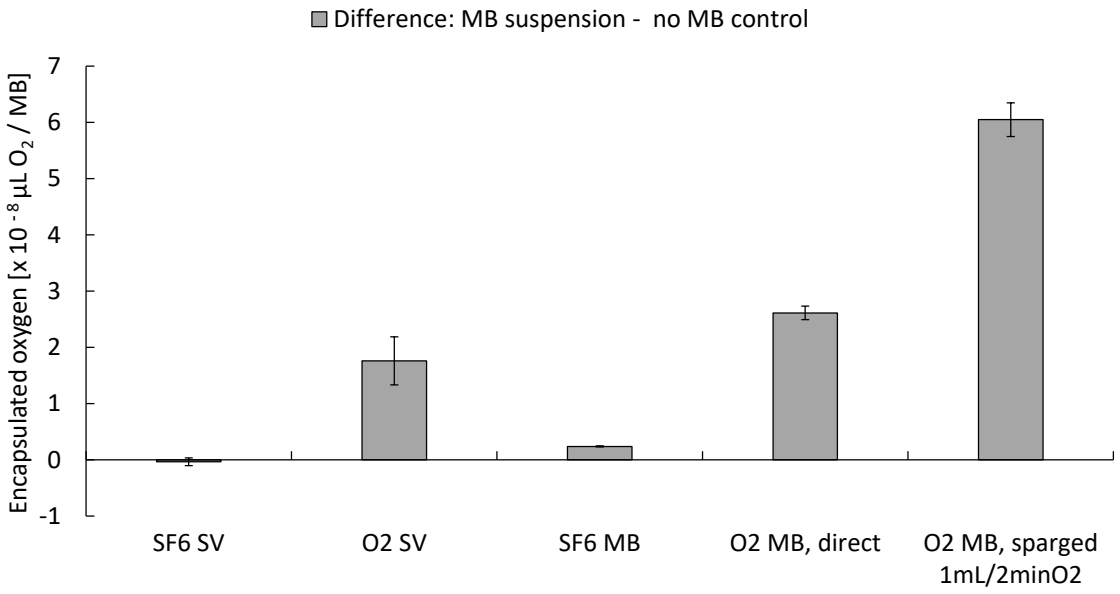

Figure 5.6. *Encapsulated oxygen concentration per microbubble [x10^{-8} µL O_2/MB]. This is computed as the difference in oxygen concentration between samples with and without microbubbles, then normalised for the concentration of microbubbles in the 1 mL sample added.*

For each group, the available gas volume per microbubble was computed based on the sample's size distributions. The oxygen loading was then calculated as a percentage of that available volume. The results in **Table 5.4** highlight that oxygen Sonovue® and microbubbles directly exposed to oxygen during sonication both present an oxygen loading of approximately 30-40% which is unexpectedly low but could be related to the presence of other gases during production. Similarly, sulphur hexafluoride microbubbles also show approximately 10% oxygen loading indicating that air is also incorporated into these systems during production or during bubble stabilisation. Finally, oxygen sparged microbubbles present an oxygen loading of about 200% which suggests a disagreement between the calculations of the microbubble gas volume and the measure encapsulated oxygen. Nevertheless, several factors could explain this discrepancy. Firstly, the measurement method used to establish the sample's size distribution has a lower limit of detection of 0.5 µm and any smaller bubble would be ignored. Such small bubbles are not

expected to affect the encapsulated volume calculations significantly, but their presence in very large numbers might still contribute in a very minor way to this effect. Secondly, the calculated gas volume assumes atmospheric pressure and thus ignores the effect of some surface pressure on the bubbles leading to pressurised encapsulated gas and allowing the encapsulation of a larger gas volume than accounted for in the calculations. Finally, the presence of large bubbles entrained in the gas sparging process and unaccounted for in the size distribution measurement could also affect these results. Thus, further investigations of these different factors are needed to appropriately characterise the oxygen loading of microbubbles.

Table 5.4. *Percent oxygen loading for several production methods, based on the measured encapsulated oxygen and the gas volume capacity calculated from the sample size distribution.*

MICROBUBBLE	GAS VOLUME [a] [10^{-8} µL/MB]	OXYGEN ENCAPSULATED [b] [10^{-8} µL/MB]	OXYGEN LOADING [%]
SF6 SV	1.61 ± 0.29	-0.04 ± 0.07	~ 0%
O2 SV	3.98 ± 2.50	1.76 ± 0.43	~ 40%
SF6 MB	2.44 ± 0.20	0.24 ± 0.01	~ 10%
O2 MB, direct	9.94 ± 3.63	2.61 ± 0.12	~ 30%
O2 MB, sparged 1mL/2minO2	3.12 ± 0.51	6.05 ± 0.30	~ 200%

[a] Calculated based on the size distribution of the samples. [b] Measured.

Nonetheless, the oxygen sparging of SF_6MBs allowed the release of approximately $6x10^{-8}$ µL O_2/MB with increased yield, resulting in a higher total dose of approximately 38 µL O_2/mL of microbubble solution. Therefore, to produce lipid-based O_2MBs, the oxygen sparging of SF_6MBs still appears to be an effective method, although further characterisation of this method is necessary.

A comparison of two sparging methods was also conducted to determine the effect of sample volume on the gas exchange process. **Figure 5.7** indicates that significantly more oxygen was encapsulated in microbubbles when the smaller 1 mL volume was sparged with oxygen for 2 minutes compared to a 5 mL sample ($p < 0.01$). As these methods

produced comparable microbubbles (**Figure 5.4**), this data further confirms that a substantial increase in the dissolved oxygen in solution is necessary in order to promote gas exchange and loading into bubbles. Therefore, for the remainder of the study, oxygen microbubbles were made by sparging 1 mL samples of SF_6MBs with oxygen for 2 minutes. With this method, approximately 15 ± 0.5 µL O_2/mL was encapsulated.

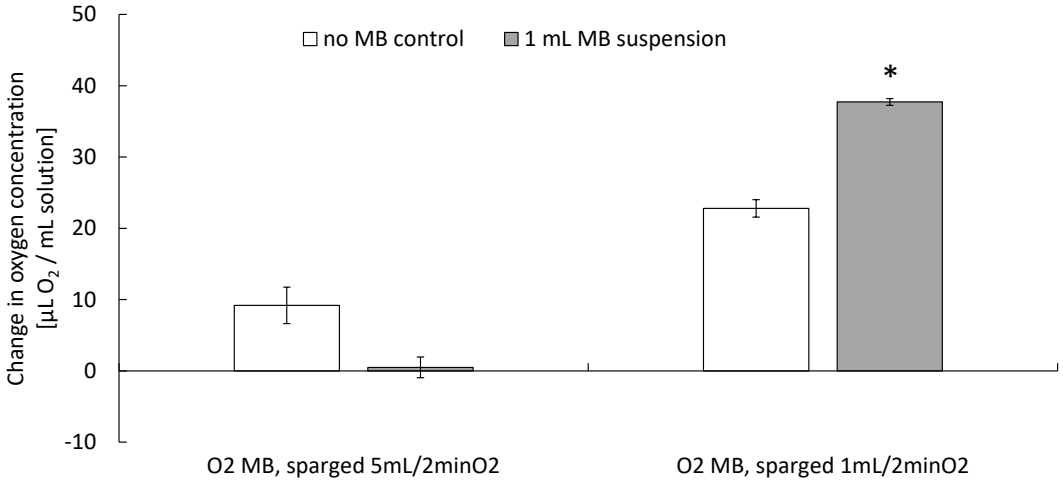

Figure 5.7. *The effect of sample volume on oxygen sparging of SF_6MBs with 5mL/2minO_2 and 1mL/2minO2 describing a 5 mL and 1 mL sample respectively of SF_6MBs sparged for 2 minutes to produce oxygen-loaded microbubbles (n = 3, * p < 0.01). These methods produced microbubbles with comparable concentrations and sizes.*

Finally, the stability of *sparged* O_2MBs (1mL/2minO_2) was tested under flow. The dissolved oxygen partial pressure was measured over time reflecting the rate at which the encapsulated oxygen escaped microbubbles following injection of a 1 mL sample into a 4 mL flow loop pre-loaded with deionised water at room temperature. The results in **Figure 5.8** highlight that 93% of the oxygen within microbubbles is released within the first 3 minutes after injection, reflecting the dissolution of microbubbles within the flow loop or the diffusion of oxygen out of microbubbles. Nonetheless, these results still indicate a significant difference in the total oxygen delivered (**Figure 5.8b**) using oxygen microbubbles compared to solution without microbubbles ($p < 0.05$), and the remaining

7% of total oxygen could still be released after 3 minutes under flow by application of ultrasound. These results are, however, only representative of microbubble suspensions diluted at 1:4 v/v in deionised water at room temperature. Therefore, destabilisation factors such as: low concentration of oxygen and a temperature of 37°C, or stabilising factors such as: oxygen saturation in blood were not incorporated. Further, the experimental set-up used only allowed the measurement of dissolved oxygen partial pressure and did not consider the possible formation of oxygen gas pockets in the tubing.

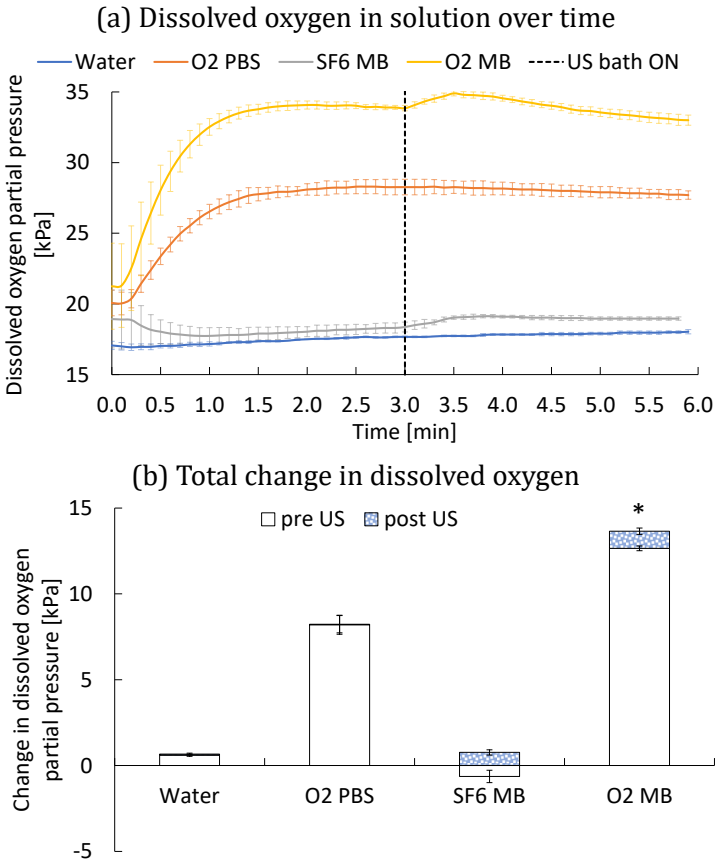

Figure 5.8. *Oxygen release over time from sparged O_2MBs (1mL/2minO_2).* ***(a)*** *The dissolved oxygen partial pressure within a closed flow loop (0.3 mL/s) was monitored to determine how much oxygen is released from microbubbles following injection of a 1 mL sample into a 4 mL flow loop (n = 3). To release any remaining encapsulated oxygen after 3 minutes, the ultrasound bath was turned on for 30 seconds.* ***(b)*** *Change in oxygen partial pressure before injection and pre-ultrasound (pre US) vs. post-ultrasound (post US), showing how much oxygen was released from microbubbles disappearing under flow or oxygen diffusing out (* $p < 0.05$).*

5.3.2. SDT with Rose Bengal and oxygen microbubbles

The activation of Rose Bengal with ultrasound was assessed through the generation of singlet oxygen indicating Type-II reactions with the activated sensitiser. As degassed or hypoxic environments can hinder the production of reactive oxygen species, the dependence of sonodynamic therapy on the presence of oxygen was assessed. **Figure 5.9** highlights that individually Rose Bengal and sparged oxygen loaded microbubbles (1mL/2minO_2) did not generate measurable levels of singlet oxygen in degassed PBS after exposure to ultrasound (1 MHz, 1.4 $MPa_{pk-pk,}$ 30% DC, 100 Hz PRF, t = 30 s). However, the combination of the sensitiser with oxygen microbubbles did generate the reactive species, indicating that the oxygen provided by microbubbles was necessary to enable a sonodynamic effect in a degassed environment. These results were further confirmed as the combination of Rose Bengal with sulphur hexafluoride microbubbles did not produce measurable levels of singlet oxygen.

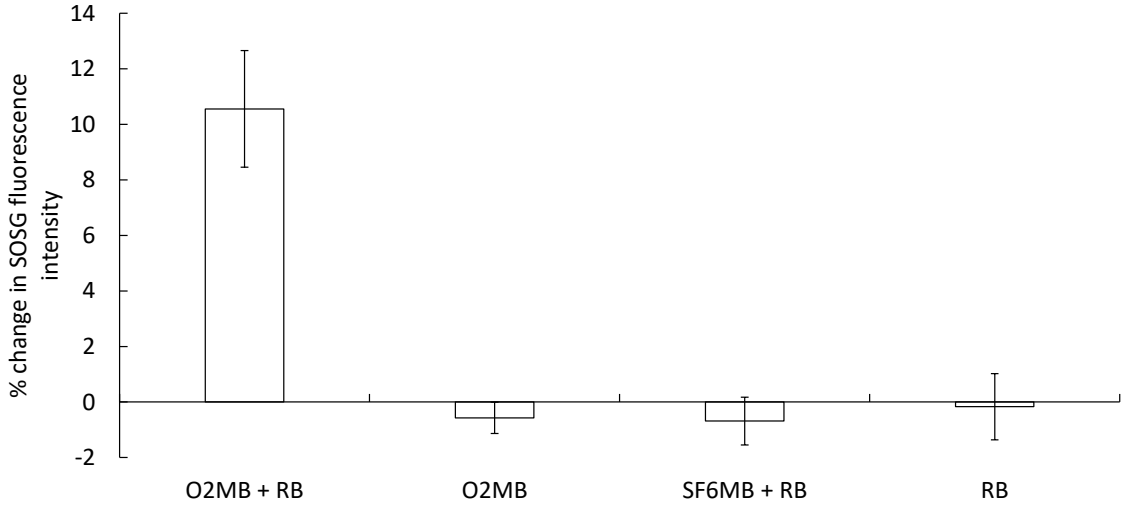

Figure 5.9. *The dependence of Rose Bengal activation of oxygen availability. Percentage change in SOSG fluorescence intensity at 520 nm related to the generation of singlet oxygen before vs. after ultrasound exposure (1 MHz, 1.4 MPa_{pk-pk}, 30% DC, 100 Hz PRF, t = 30 s) in samples prepared in degassed PBS (1.25 µM SOSG, ± 2.5 µM RB, ± 5 x 10^7 MB/mL).*

An increase in the ultrasound pressure while preserving an exposure time of 30 seconds corresponded to an increase in energy delivered. This was correlated with the activation of Rose Bengal (**Figure 5.10a**) and the energies of broadband and ultraharmonic emissions (**Figure 5.10b-c**) for samples of degassed PBS with Rose Bengal and oxygen microbubbles. Nonetheless, the generation of singlet oxygen was not as pronounced when the acoustic energy delivered was kept constant by lowering the exposure time with increasing ultrasound pressure.

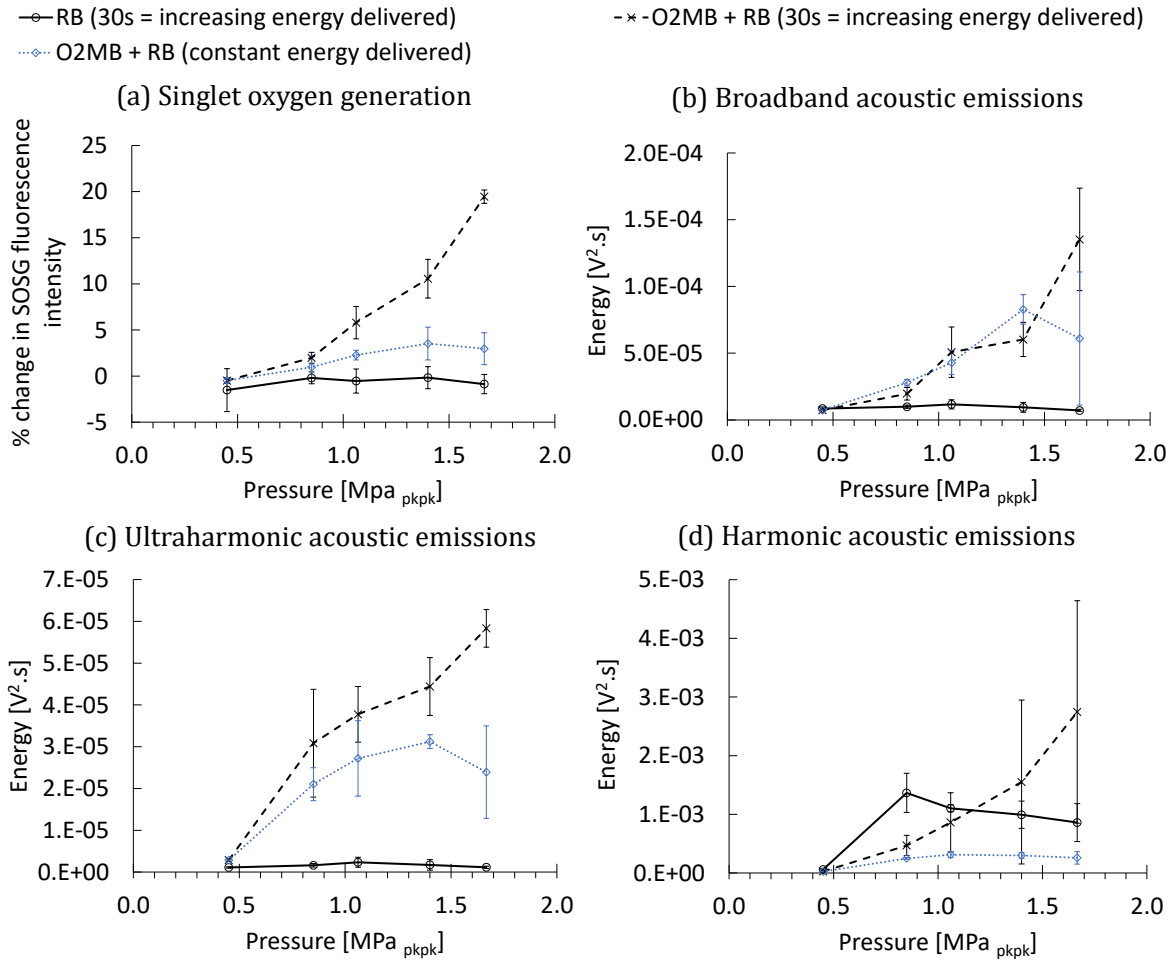

Figure 5.10. *The effects of increasing ultrasound pressure [MPa_{pkpk}] on the activation of Rose Bengal* ***(a)*** *determined by the generation of singlet oxygen, and the energy associated with* ***(b)*** *broadband,* ***(c)*** *ultraharmonic, and* ***(d)*** *harmonic acoustic emissions computed for the entire exposure time. Other parameters were: f = 1 MHz, DC = 30%, PRF = 100 Hz, t* = 30 s, or t** as indicated in* ***Table 5.3****. The samples were prepared (n = 3) in degassed PBS with 1.25 µM SOSG, 2.5 µM RB, ± 5x10^7 MB/mL.*

The energy of harmonic acoustic emissions (**Figure 5.10d**) did not reflect the production of singlet oxygen and this was associated to an increased harmonic amplification from the amplifier [4]. Therefore, although the energy of harmonic emissions is reported in this chapter for completeness, this data did not provide a useful metric for analysis.

The effect of duty cycle was investigated at a set ultrasound pressure of 1.4 MPa_{pkpk}, while preserving the number of ultrasound cycles delivered by changing the exposure time. An increase in duty cycle led to an increase in Rose Bengal activation when oxygen microbubbles were present, while no activation was observed for samples without microbubbles (

Figure 5.11). Due to acquisition limitations on the TiePie Handyscope HS3, the acoustic emissions could only be acquired for 10 and 30% duty cycles. Thus, no conclusion could be drawn regarding the acoustic emissions from oxygen microbubbles during ultrasound exposure at higher duty cycles. Nonetheless, the energies for broadband, ultraharmonic, and harmonic emissions were comparable between 10 and 30% DC (**Appendix Figure D.1**).

In contrast, increasing the pulse repetition frequency from 20 to 120 Hz did not affect the activation of Rose Bengal with or without the addition of oxygen microbubbles (**Figure 5.12**). The acquisition of the acoustic emissions was again limited by the sampling rate of the digital oscilloscope as the PRF was decreased, nonetheless the energies of the acoustic emissions from 40 to 120 Hz did not change significantly (**Appendix Figure D.2**).

[4] The older amplifier used E&I Ltd A300 (015230) was reported to distort the transmitted waveforms with more harmonic output.

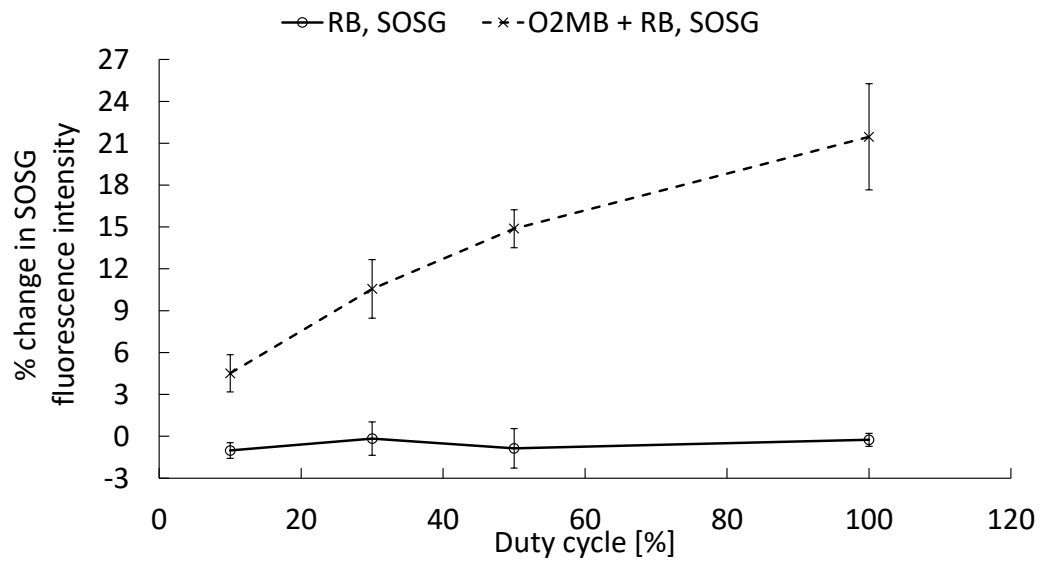

Figure 5.11. *The effect of increasing ultrasound duty cycle [%] on the activation of Rose Bengal determined by the generation of singlet oxygen. Other parameters were: f = 1 MHz, PRF = 100 Hz, P = 1.4 MPa_{pkpk}, total number of cycles = $9x10^6$. The samples were prepared (n = 3) in degassed PBS with 1.25 µM SOSG, 2.5 µM RB, ± $5x10^7$ MB/mL.*

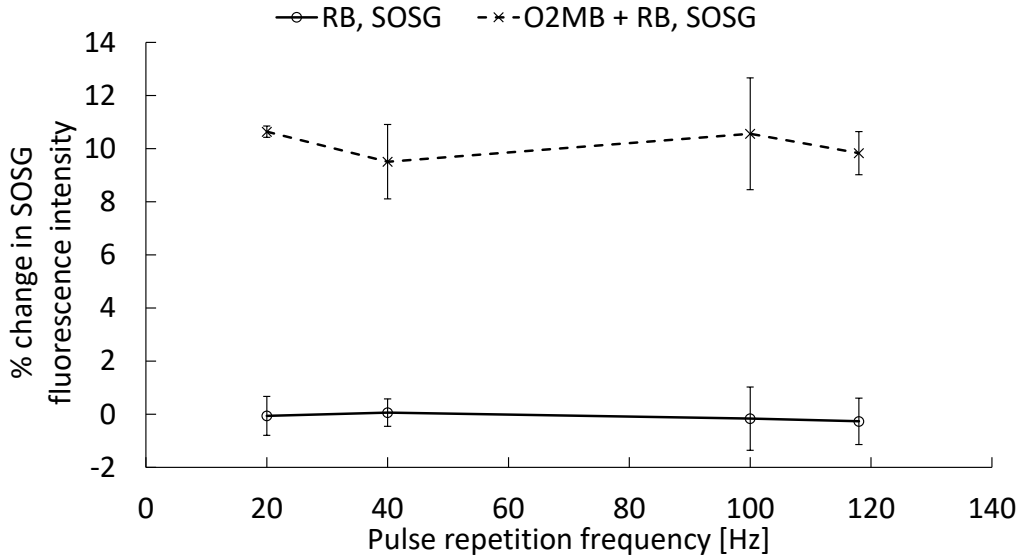

Figure 5.12. *The effects of increasing ultrasound pulse repetition frequency [Hz] on the activation of Rose Bengal determined by the generation of singlet oxygen. The constant ultrasound parameters were: f = 1 MHz, DC = 30%, P = 1.4 MPa_{pk-pk}, t = 30 s, total number of cycles = $9x10^6$. The samples were prepared (n = 3) in degassed PBS with 1.25 µM SOSG, 2.5 µM RB, ± $5x10^7$ MB/mL.*

5.4. Discussion

An investigation of oxygen loading methods was undertaken to produce lipid-based oxygen microbubbles. The direct formation of microbubbles under oxygen gas flow through the sonication of aqueous lipids presented a low production yield which was associated to the decreased stability of these systems [301]. Similar results were obtained through the reconstitution of freeze-dried Sonovue® with a headspace of oxygen instead of sulphur hexafluoride. Moreover, these methods demonstrated only about 30-40% oxygen loading within the microbubbles, thus suggesting that air is also incorporated into these systems during production or bubble stabilisation in solution. These findings also highlight the importance of incorporating gases with high molecular weight and low diffusivity to enable the formation and stabilisation of a bubble population prior to oxygen loading [159]. This was observed in this chapter when comparing the results for *sparged* vs. *direct* oxygen microbubbles, and the use of sulphur hexafluoride to promote microbubble stability and yield. The sparging method was also improved by exposing smaller sample volumes to oxygen gas flow in order to increase the concentration gradient and promote gas exchange within the sample. The sparging of 1 mL solution of sulphur hexafluoride with oxygen gas flow for two minutes led to a high oxygen loading of 200%, thus beyond the theoretical gas capacity of these systems. This discrepancy could be due to limits in the size and concentration measurement technique used to characterise microbubbles then ignoring very large or very small bubbles that contribute to the oxygen loading. It could also be due to some surface pressure on bubbles allowing an increased gas density encapsulated which has not been incorporated in the theoretical gas volume calculations. Although these effects need to be further investigated to

determine the exact loading achieved, this method allowed for a high oxygen content within the suspension and was chose to produce oxygen microbubbles moving forward.

The injection and flow of diluted *sparged* O_2MBs, however, presented a rapid release of oxygen. This was associated with the high oxygen concentration gradient with the surrounding solution [159]. Therefore, although *sparged* O_2MBs allowed the delivery of significantly more oxygen compared to other loading strategies considered, an improvement of oxygen trapping within these systems would be beneficial to enhance treatment.

The contributions of *sparged* O_2MB to the activation of Rose Bengal during sonodynamic therapy was then examined in degassed PBS. The results indicated a dependence of this method on the acoustic duty cycle used with 1 MHz ultrasound, although varying the pulse repetition frequency did not affect the results with a set 30% duty cycle. The increased generation of singlet oxygen and hence Rose Bengal activation at higher duty cycles could be caused by a decrease in ultrasound OFF time, thereby promoting bubble oscillations [302]. Unfortunately, an examination of this hypothesis was challenged as the acoustic emissions were only acquired for a subset of duty cycles and pulse repetition frequencies, and the overall energies of emissions did not provide evidence supporting it. Nevertheless, an analysis of the emission power over time for the acquired data (**Figure 5.13**) could support the proposed phenomenon. As described in section 3.4.5.1, fitting a plateau followed by a one-phase exponential decay to the data provided parameters describing the acoustic emission power over time that could be compared. The results shown in **Figure 5.14** indicate that lowering the duty cycle significantly decreased the plateau of both ultraharmonic and broadband emissions although it also significantly lengthened the time over which the initial rise in emissions

occurred (**Table 5.5**). While the change in the pulse repetition frequency did not lead to such clear differences in the power of acoustic emissions recorded, some of the parameters were still significantly different between some of the pulse repetition frequencies tested (**Table 5.6**).

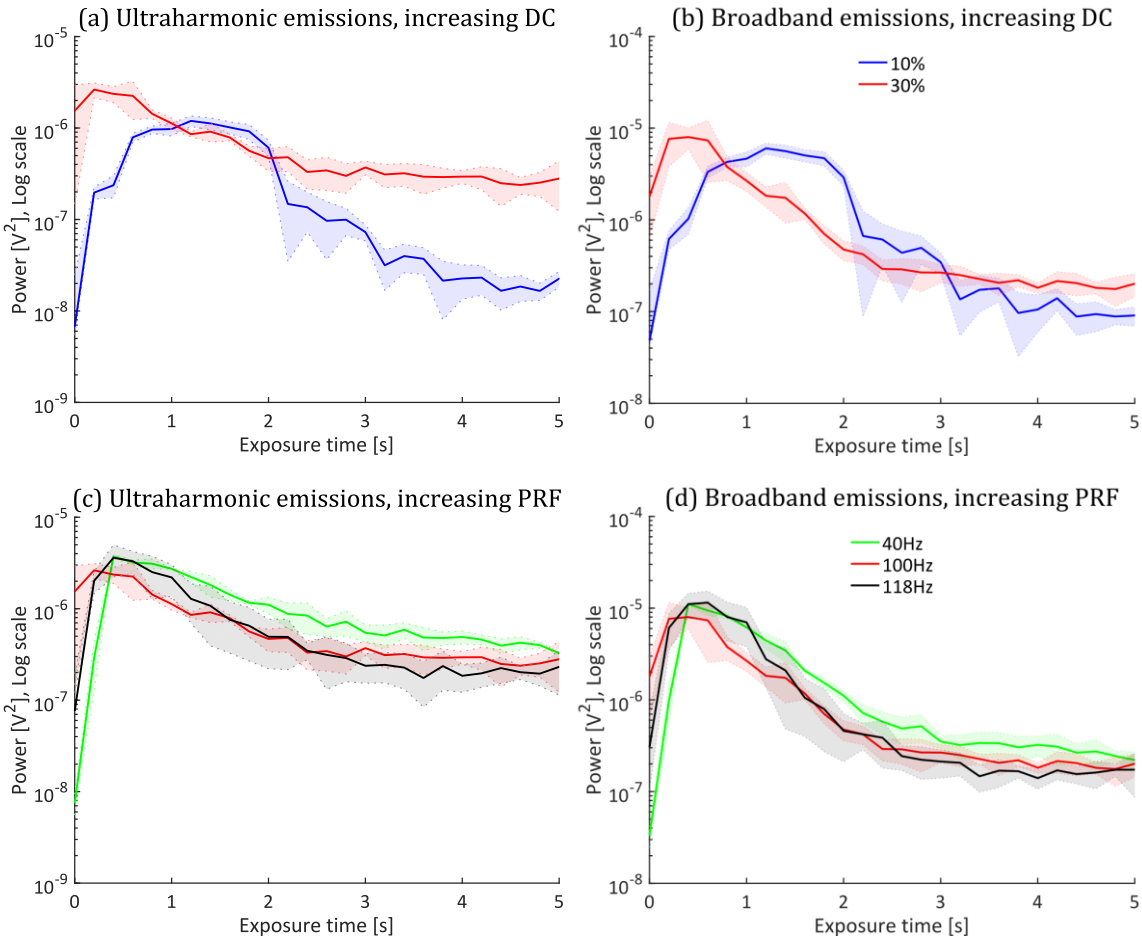

Figure 5.13. *The effects of increasing ultrasound* ***(a,b)*** *duty cycle [%] and* ***(b,c)*** *pulse repetition frequency [Hz] on the power of* ***(a,c)*** *ultraharmonic and* ***(b,d)*** *broadband emissions over the first 5 seconds of ultrasound exposure. The constant parameters were: f = 1 MHz, P = 1.4 MPa$_{pk\text{-}pk}$, total number of cycles = 9x10^6. Changing DC was done with a PRF of 100 Hz. Changing PRF was done with a DC of 30%. The samples were prepared (n = 3) in degassed PBS with 1.25 µM SOSG, 2.5 µM RB, + 5x10^7 O$_2$MB/mL.*

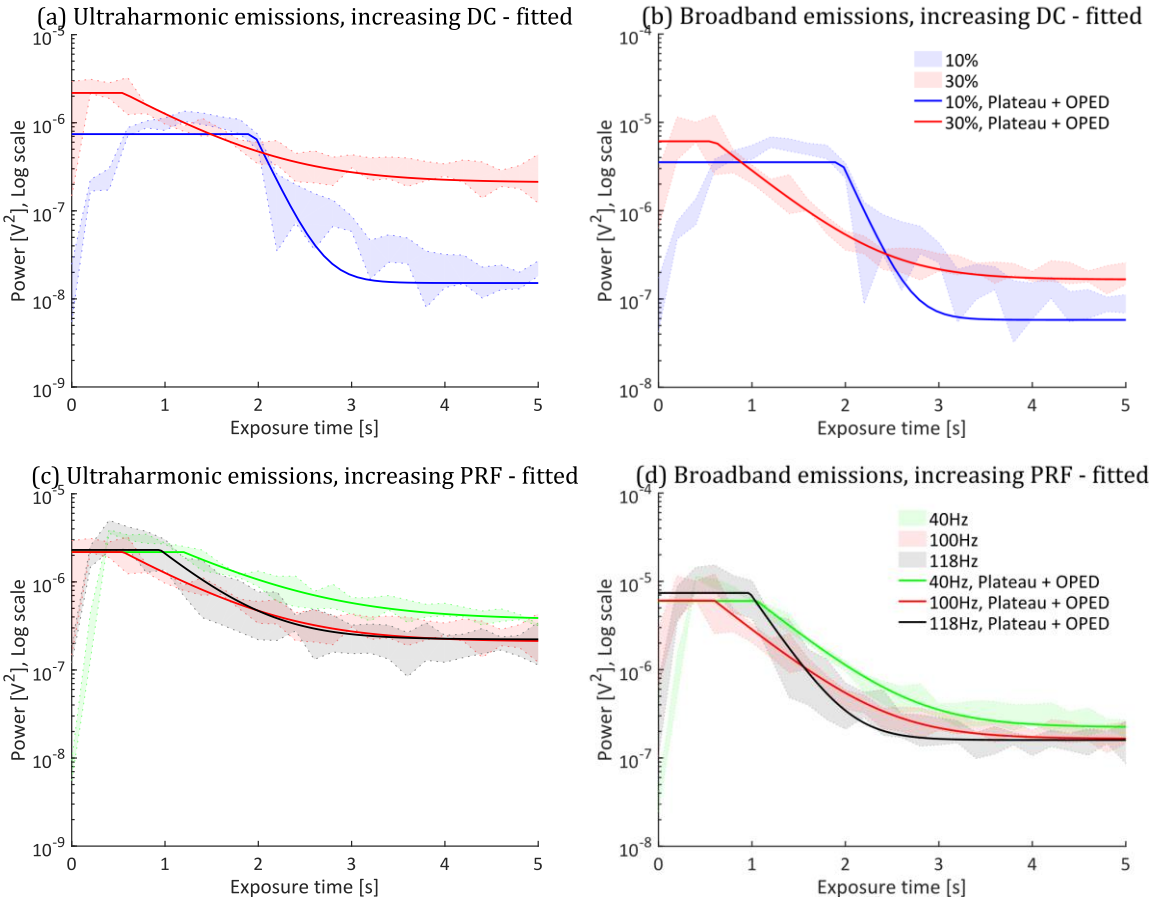

Figure 5.14. *Fitting a plateau followed by one-phase exponential decay (OPED) on the acoustic emissions available for increasing ultrasound* ***(a,b)*** *duty cycle [%] and* ***(b,c)*** *pulse repetition frequency [Hz].*

Table 5.5. *Parameters summary for fitting the plateau followed by the one-phase exponential decay to the emission power over time for increasing duty cycle (%).*

PARAMETERS	Ultraharmonics		Broadband	
Duty cycle	10%	30%	10%	30%
Adjusted R^2	0.74	0.82	0.72	0.74
t_0 [s]	1.96 **	0.55	1.96 **	0.60
Half-life, $t_{1/2}$ [s]	0.14 **	0.50	0.13 **	0.35
$t_{1/2,\ adjusted} = t_0 + t_{1/2}$ [s]	2.10 **	1.05	2.09 **	0.95
P_0 [x10^{-6} V^2]	0.74 **	2.18	3.54 **	6.10
Plateau [x10^{-7} V^2]	0.15 **	2.09	0.58 **	1.66

** $p < 0.01$ compared to all other parameter within the same ultrasound frequency subset (ultraharmonic or broadband). The parameters referred to in this table were previously described in Chapter 3, section 3.4.5.

Table 5.6. *Parameters summary for fitting the plateau followed by the one-phase exponential decay to the emission power over time for increasing pulse repetition frequency.*

PARAMETERS	Ultraharmonics			Broadband		
PRF	40 Hz	100 Hz	118 Hz	40 Hz	100 Hz	118 Hz
Adjusted R^2	0.64	0.82	0.66	0.67	0.74	0.71
t_0 [s]	1.20 **	0.55	0.95 **	1.05	0.60 **	0.98
Half-life, $t_{1/2}$ [s]	0.57	0.50	0.34	0.35	0.35	0.19 *
$t_{1/2,\ adjusted} = t_0 + t_{1/2}$ [s]	1.57	1.05	1.29	1.40	0.95	1.17
P_0 [x10^{-6} V^2]	2.18	2.18	2.30	5.99	6.04	7.39 **
Plateau [x10^{-7} V^2]	3.70 **	2.09	2.22	2.23	1.65	1.60

* $p < 0.05$, ** $p < 0.01$ compared to all other parameter within the same ultrasound frequency subset (ultraharmonic or broadband). The parameters referred to in this table were previously described in Chapter 3, section 3.4.5.

In vivo, an adequate "OFF time" during ultrasound exposure is necessary in order to enable (1) microbubble replenishment and (2) avoid heating. Thus, although currently most parameter-tuning to address these effects appears to be done by adjusting the ultrasound duty cycle (**Appendix Table A.1**), an improved therapeutic result might be achievable by adjusting the pulse repetition frequency with a reasonable duty cycle. Additionally, as the generation of singlet oxygen during sonodynamic therapy mediated by oxygen microbubbles increased with the acoustic energy delivered, a balance between acoustic pressure and exposure time is necessary to provide an efficient treatment protocol. The activation of Rose Bengal with oxygen microbubbles and 1 MHz ultrasound was found above background levels starting at 0.85 MPa_{pkpk} with a microbubble concentration of $5x10^7$ MB/mL, duty cycle of 30% and exposure time of 30 seconds. However, these results might be improved with a higher duty cycle compensated with a lower pulse repetition frequency. Due to the small range of parameters tested in this thesis, the differences caused by varying the parameters might not appear clearly, and further evaluation of these effects are needed to understand their impact on Rose Bengal

activation. Firstly, completing the preliminary results presented in this thesis to include the acoustic emissions for all parameters is necessary. Secondly, an examination of the effect of ultrasound frequency on sensitiser activation is important to help determine which ultrasonic device would be more appropriate for the clinical translation of this method. Additionally, a study on the required ultrasound parameters to enable the same sonodynamic effect in a flowing sample would be worthwhile to better represent biological conditions. Finally, an investigation focusing on the parameters necessary to allow for sufficient cavitation activity in order to promote the distribution of therapeutic effect further away from the vasculature would also be valuable.

With the parameters used in this investigation, oxygen microbubbles were necessary to enable the activation of Rose Bengal during ultrasound exposure. **Appendix Table A.1**, however, shows that others have reported the activation of sensitisers without the use of microbubbles. The results in Chapter 4 suggest the mechanism for sonodynamic therapy with Rose Bengal could involve sonoluminescence events. Then, Rose Bengal activation without the use of cavitation nuclei presumably would require (1) longer exposure times, (2) higher acoustic intensity, or (3) the use of non-degassed solutions in order to lower the cavitation threshold and produce sonoluminescence. Therefore, added oxygen microbubbles can lower the threshold at which Rose Bengal can be activated during sonodynamic therapy and this combination could increase the efficacy of treatment and while minimising the exposure conditions.

Nonetheless, the assessment of Rose Bengal activation was solely based on singlet oxygen generation, characteristic of Type-II reaction with the activated sensitiser. Thus, this work does not account for other reactive oxygen species potentially generated during microbubble cavitation or other reactions with sensitiser mentioned in Chapter 4. An

examination of the reactive oxygen species population produced during sonodynamic therapy in normal or degassed solution, with and without cavitation nuclei would therefore be useful. Finally, further examination of the acoustic emissions from microbubbles is worthwhile to determine whether cavitation monitoring during sonodynamic therapy could be used to predict treatment outcome.

5.5. Conclusions

The effects of ultrasound drive pressure, duty cycle, and pulse repetition frequency were investigated for the activation of Rose Bengal in degassed solutions to mimic the conditions found in hypoxic tumours. In these experiments, oxygen microbubbles were necessary to enable Rose Bengal activation, which was found to increase with the ultrasonic energy delivered, and the duty cycle used. However, changes in the pulse repetition frequency did not affect the production of singlet oxygen from the sensitiser. The work presented in this chapter aims to provide a greater insight as to how ultrasound parameters can be optimised to improve the treatment protocol of sonodynamic therapy and allow an easier translation of this method into clinical practice.

5.5.1. Contributions

This chapter first provides a comparison of techniques to produce lipid-coated oxygen microbubbles, followed by a characterisation of Rose Bengal activation through oxygen microbubble-mediated sonodynamic therapy and corresponding acoustic emissions for different ultrasound exposure conditions.

5.5.2. Limitations

The experiments presented in this chapter were subject to several limitations. In the examination of the encapsulated oxygen stability using *sparged* O_2MBs, improvements on the *in vitro* experimental set-up would allow a better reflection of biological effects. For example, the effect of degassed surrounding solution and temperature on the stability of the encapsulated oxygen would be valuable.

Additionally, the results presented for the activation of Rose Bengal with oxygen microbubble-mediated sonodynamic therapy at different ultrasound parameters were obtained for the exposure of a static sample. Continuation of this study focusing on a flowing sample at higher temperature would be more representative of biological conditions.

Chapter 6
Magnetic targeting of sonodynamic and antimetabolite therapies to hypoxic tumours

---

Chapter 6 investigates magnetic targeting of oxygen and drug loaded microbubbles for the combined delivery of sonodynamic and antimetabolite therapies. Following an in vitro characterisation of the microbubbles, and a novel magnetic-acoustic device, their combined effect on hypoxic pancreatic tumours in a murine model is evaluated.

Parts of the results presented in this chapter have been published, presented, or are in preparation for publication as indicated below. The collaborative work undertaken to produce these results is acknowledged in the following sections.

L.C. Barnsley, M.D. Gray, E. Beguin, D. Carugo, E. Stride, A Combined Magnetic-Acoustic Device for Simultaneous, Coaligned Application of Magnetic and Ultrasonic Fields, Adv. Mater. Technol. 3 (2018) 1800081. doi:10.1002/admt.201800081.

M. Gray, E. Beguin, E.P. Stride, H. Nesbitt, K. Logan, S. Kamila, A. McHale, J. Callan, L. Barnsley, Prototypical madness: Design and demonstration of a magnetic-acoustic targeted drug delivery system, in: J. Acoust. Soc. Am., Acoustical Society of America, 2018: pp. 1824–1824. doi:10.1121/1.5068042.

E. Beguin, M.D. Gray*, K.A. Logan*, H. Nesbitt, Y. Sheng, S. Kamila, L.C. Barnsley, A.P. McHale, J.F. Callan, E. Stride, Delivery of magnetic microbubble mediated sonodynamic therapy using a combined magnetic-acoustic device, J. Control. Release. (2019). In review. * first co-authors.*

Contents

6.1. Introduction

An investigation of magnetic microbubble formulations in Chapter 3 demonstrated a local increase in microbubble concentration with the application of an external magnetic field. This targeting method can therefore help to enhance the level and duration of cavitation events by increasing the local concentration of microbubbles. This has previously been correlated to an improved therapeutic effect [252–254]. Additionally, this method could help minimise off-target drug accumulation and hence undesirable side effects. Chapter 4 and Chapter 5 both confirmed that the presence of microbubbles enhances the effect of sonodynamic therapy. More specifically, in Chapter 4, this was related to an increased occurrence of sonoluminescence events, allowing sensitiser activation with mild ultrasound exposure conditions. These results were supported by those shown in Chapter 5, where the addition of oxygen microbubbles enabled the generation of cytotoxic singlet oxygen from the activated sensitiser during sonodynamic treatment in degassed solution. In contrast, the production of reactive species was not observed when the sensitiser alone was exposed to ultrasound.

Previous work on the use of oxygen microbubbles loaded with Rose Bengal (O_2MB-RB) for the treatment of hypoxic pancreatic tumours in mice was reviewed in section 2.3.5.2. These studies reported an improved therapeutic effect when oxygen microbubbles were used as carriers for Rose Bengal compared to sulphur hexafluoride microbubbles [4]. Additionally, treatment enhancement was also achieved through the incorporation of an antimetabolite therapy such as 5-fluorouracil or Gemcitabine in combination with sonodynamic therapy [182,220]. Finally, the introductory *in vivo* work presented in Chapter 3 demonstrated that magnetic targeting can also improve the delivery and hence the efficacy of combined sonodynamic and antimetabolite therapies

for hypoxic tumours [86]. While the combination of magnetic and ultrasound fields demonstrated an improved tumour growth delay and increased apoptotic cell signalling compared to the treatment with ultrasound only, there were three shortcomings in this study. First, the simultaneous application of magnetic and ultrasound fields represented a significant practical challenge *in vivo*; one that is particularly acute in small animal models due to space constraints. Second, it was necessary to use a mixture of bubbles with different surface functionalisation to deliver the combination of drugs, making it difficult to ensure the uniform delivery of both therapies to malignant cells. Finally, the stability of magnetic microbubbles used (**LipMB-LαPC**) was significantly lower than for the newly proposed formulations presented in Chapter 3.

6.1.1. Objectives, scope, and statement of collaborative work

In this chapter, the first shortcoming was addressed by using a novel ultrasound probe with an integrated co-aligned magnetic array. This device enabled the application of both magnetic and acoustic fields at the focus, thereby ensuring the accurate targeting and excitation of magnetic microbubbles during therapy. **Figure 6.1** illustrates this method used on a murine model compared to the use of two separate devices.

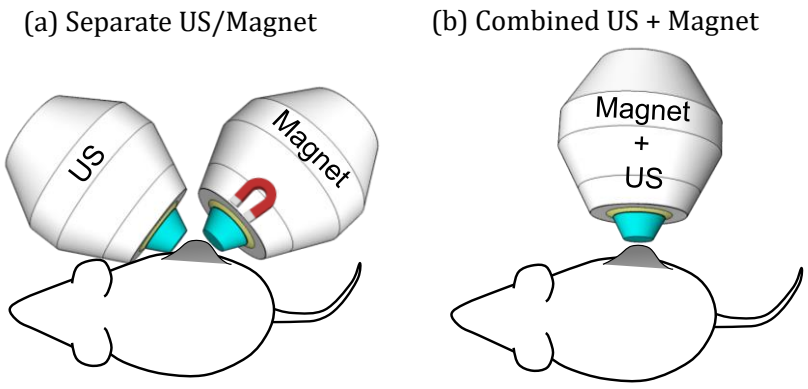

Figure 6.1. *Schematic for the use of* ***(a)*** *separate ultrasound and magnet devices compared to* ***(b)*** *one device providing both fields co-aligned. Drawings were provided by Dr. Michael Gray.*

The magnetic acoustic device (MAD) was designed by Dr. Lester Barnsley and Dr. Michael Gray and described in [303]. Further characterisation on the drug delivery it can achieve was completed in collaboration with Dr. Michael Gray and reported in this Chapter.

For the second challenge, a novel therapeutic agent was developed wherein both the sonodynamic (RB) and antimetabolite (Gem) drugs were linked to a single biotin moiety (biotin-RB-Gem). This compound then allows the attachment of both drugs onto a single microbubble formulation. Biotin-RB-Gem was developed, synthesised and purified by Dr. Sukanta Kamila. It was then characterised by Keiran Logan to determine the cytotoxicity of its antimetabolite moiety on several pancreatic cancer cell lines compared to Gem treatment alone. The results in **Figure 6.2** highlight the comparable antimetabolite profile of biotin-RB-Gem and Gem when the sensitiser Rose Bengal was not activated. Thus, the scope of this chapter was to investigate the drug loading of biotin-RB-Gem onto oxygen microbubbles and if it affects the activity of Rose Bengal during sonodynamic therapy.

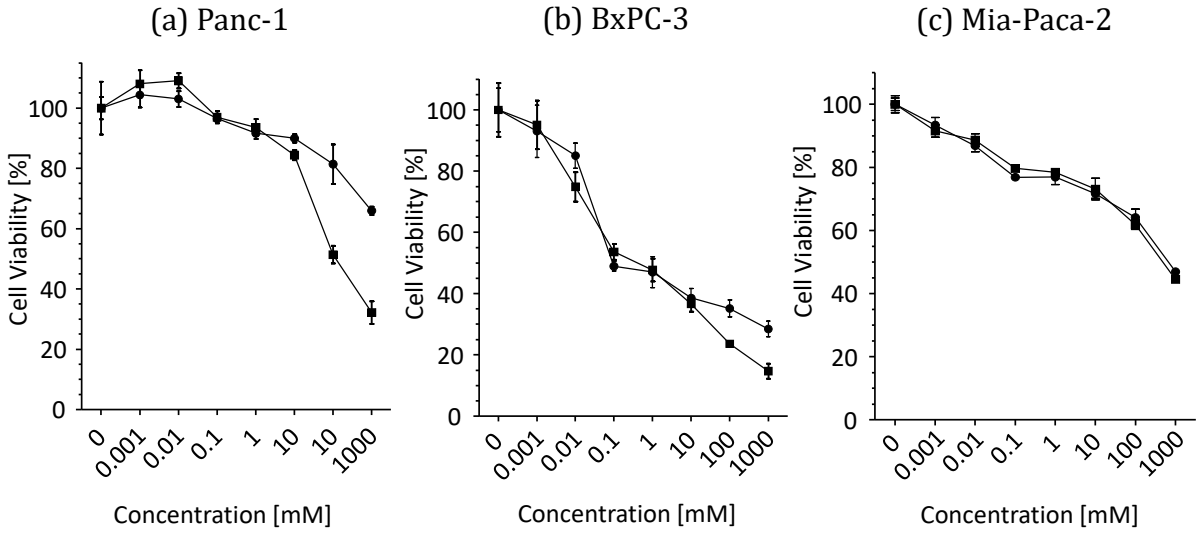

Figure 6.2. *MTT cell viability assay comparing the effects of biotin-RB-Gem (squares) and gemcitabine hydrochloride (circles) on human primary pancreatic adenocarcinoma* ***(a)*** *Panc-1,* ***(b)*** *BxPC-3, and* ***(c)*** *Mia-PaCa-2 cell lines. Data acquired and analysed by Keiran Logan.*

For the last challenge, the **LipMB-DBPC** formulation developed in Chapter 3 was used as the drug carrier on account of its superior stability compared to the previous formulation used (**LipMB-LαPC**) and its ability to carry the modified biotin described above. The loading of **LipMB-DPBC** with the new therapeutic agent is depicted in **Figure 6.3** which also shows the difference compared to the previously tested formulation presented in Chapter 3.

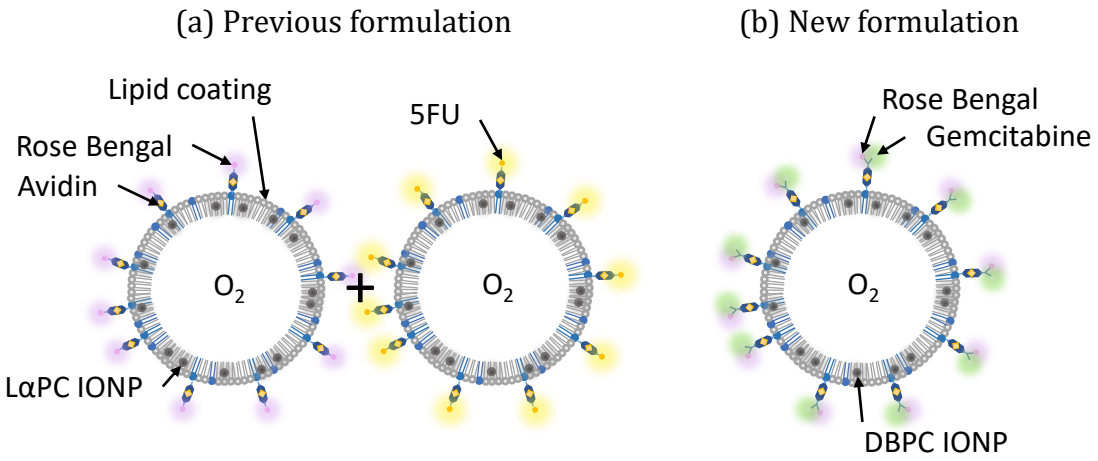

Figure 6.3. *Illustrations of magnetic and therapeutic microbubbles* ***(a)*** *previously used in [86] incorporating Rose Bengal and 5-fluorouracil on two separate LipMB-LαPC compared to* ***(b)*** *incorporating both Rose Bengal and Gemcitabine onto one LipMB-DBPC.*

It was then hypothesised that the combined use of the new magnetic-acoustic device and the incorporation of the two therapeutics onto a more stable magnetic microbubble formulation should increase the therapeutic benefit compared to previous work.

6.2. Methods

The magnetic microbubble formulation (**LipMB-DBPC**) used in this chapter was characterised *in vitro* to confirm its iron and drug loading, bubble size distribution and concentration, and acoustic response as described in Chapter 3. The generation of

cytotoxic singlet oxygen upon ultrasound exposure of Rose Bengal-loaded magnetic microbubbles was investigated to confirm the activation of the sensitiser. For part of this work, biotinylated Rose Bengal (biotin-RB) was used instead of the novel therapeutic biotin-RB-Gem in order to avoid wastage of this difficult to synthesize ligand. In effect, the *in vitro* characterisation completed in this chapter focused on the activation and delivery of Rose Bengal, and the addition of the gemcitabine moiety on biotin-RB-Gem was assumed to not affect the bubble dynamics. *In vitro* tests were also performed to compare the quantity of drug delivered to a target site within a tissue mimicking phantom using the MAD compared to separate magnetic and acoustic devices. Finally, the performance of the combined and targeted therapy was assessed *in vivo* in mice bearing human ectopic xenograft pancreatic BxPC-3 tumours for several ultrasound and magnet device configurations. The *in vivo* work was completed with the collaboration of Dr. Michael Gray, Keiran Logan, Dr. Heather Nesbitt and Dr. Yingjie Sheng.

6.2.1. Reagents and equipment

The materials used for magnetic microbubble production and cleaning were as reported in section 3.3.4. The biotinylated therapeutics were synthesized and purified by Dr. Sukanta Kamila. To determine the drug loading on microbubbles, these were ruptured using an ultrasound bath (Eumax UD150SH-6L, 40 kHz, 150 W). The absorbance of the sample was then measured on a FLUOstar Omega multi-purpose plate reader from BMG Labtech (Aylesbury, Bucks, UK) and compared to a standard curve (**Appendix Figure E.1** or **Appendix Figure E.2** when biotin-RB or biotin-RB-Gem was used respectively). The iron loading of microbubbles was determined through inductively coupled plasma - optical emission spectroscopy (ICP-OES) using an Optima 8000 from Perkin Elmer. The

experimental set-up used to expose microbubbles to 1 MHz ultrasound and record their acoustic emissions was described in section 3.4.5.1. The generation of singlet oxygen and thus the activation of Rose Bengal were determined based on the fluorescence intensity of SOSG (Ex: 490 nm/Em: 520 nm) purchased from Thermo Fischer Scientific (Loughborough, UK). The perfluorobutane (PFB) gas was obtained from The BOC Group (Guilford, Surrey, UK).

The design of the MAD was first presented in [303]. The paraffin wax used during testing in this chapter was obtained from FullMoons Cauldron (Berkshire, UK), and the ultrasound gel used was the product Anagel from Ana Wiz Ltd. (Surrey, UK). To compare the different device configurations, a drug delivery study in an agar phantom was completed using the holder described in [303]. UltraPure low melting point agarose was purchased from Thermo Fischer Scientific (Loughborough, UK) and the syringe pump was an AL-1000 from World Precision Instruments (Sarasota, FL, USA).

6.2.2. Preparation of drug-loaded **LipMB-DBPC**

Lipid-based magnetic microbubbles incorporating DBPC-IONPs with potential for external drug loading were prepared following the general protocol for **LipMB** (section 3.3.4) with the following changes: a lipid mix of DBPC:PEG40S:DSPE-PEG2000-biotin, 82:9:9 molar ratio was used. To promote microbubble stability, the resuspending aqueous solution was made of PBS:propylene glycol:glycerol (8:1:1 v/v), thereafter referred to a “PPG solution”, and PFB was used as the flowing gas during sonication [225].

The biotinylated- and pegylated- phospholipid DSPE-PEG2000-biotin was used in the lipid mix to enable the coating of **LipMB-DBPC** with avidin, a linker to subsequently allow the loading of biotinylated therapeutics on the outer surface of microbubbles. This

process was carried out during the centrifugal cleaning of the suspension. Similar to the cleaning steps indicated in the *general protocol* for microbubble manufacturing, the solution was cleaned once by centrifugation (100 g, 5 minutes, 4°C). The subnatant with excess material was removed and the remaining microbubble were resuspended in PPG solution, before the addition of avidin (1 mL, 10 mg/mL in PBS) and sample mixing for 5 minutes on ice. The centrifugation step was then repeated to produce cleaned avidin-functionalised magnetic microbubbles. These were resuspended and biotin-RB-Gem or biotin-RB (1 mL, 5.2 mM in PBS with 0.5% (v/v) DMSO) was added and mixed under reduced light exposure for 5 minutes on ice. The microbubble solution was then cleaned once more and resuspended in 5 mL PPG. The resultant sample was then referred to as MagMB-RB-Gem or MagMB-RB, depending on which drug product was added.

For oxygenation of the sample, 1 mL stocks of cleaned MagMB-RB-Gem or MagMB-RB were prepared and each one was sparged with oxygen for 2 minutes, before sealing and crimping the glass vial. The samples were kept in reduced light conditions on ice until further use and were then referred as $MagO_2$MB-RB-Gem or $MagO_2$MB-RB.

6.2.3. Microbubble characterisation

The microbubbles were characterised for their size and concentration following the protocol outlined in section 3.4.1 and their iron content was obtained as described in section 3.4.6.1.2.

The drug loading on microbubbles and remaining free drug in solution were also established after following the microbubble cleaning protocol with three centrifugation steps. For this, three batches of drug loaded bubbles were cleaned by centrifugation and the absorbance of the subnatant was measured. This procedure was then repeated, and

the decreasing amounts of Rose Bengal in the subnatant was measured until a background level was recorded. This defines the plateau achieved for the absorbance of Rose Bengal at 559 nm in the subnatant and indicates that a minimum has been reached for the Rose Bengal in the solution surrounding bubbles. The remaining absorbance of these samples then reflected the loading capacity of biotinylated Rose Bengal on microbubbles, [biotin-RB]$_{loaded}$. This data then allowed the calculation of free drug [biotin-RB]$_{free}$ remaining in subsequent batches following only three centrifugal cleaning steps [biotin-RB] as:

$$[biotin\text{-}RB]_{free} = [biotin\text{-}RB] - [biotin\text{-}RB]_{loaded}$$

To measure the activation of $MagO_2$MB-RB under ultrasound exposure, 12 mL samples of degassed PBS with SOSG (1.25 µM) and $MagO_2$MB-RB (5 x 10^7 MB/mL, [biotin-RB] = 541 µM), were exposed to 1.17 MHz ultrasound, 0.7 MPa peak negative pressure, 30% duty cycle, and 100 Hz pulse repetition frequency for 3.5 minutes. Sample exposure and acoustic emission acquisition were undertaken in a custom-made tank as described in section 3.4.5.1 and Appendix C. The built-in transducer was, however, driven at 1.17 MHz to reflect the centre frequency used by the MAD. The waveform generator input amplitude was adjusted to obtain the same pressure output at the focus as for the transducer in Chapter 3. The cumulative energy calculated for ultraharmonic frequencies of the recorded acoustic emissions are reported.

The production of singlet oxygen from activated Rose Bengal exposed to ultrasound was determined using SOSG as described in section 5.2.4.2.

6.2.4. Magnetic acoustic device and control device

The MAD was designed by Barnsley *et al.* and assembled as shown in **Figure 6.4** [303]. Briefly, the magnetic body consisted of N52 grade NdFeB permanent magnet material

whose geometry was optimized to have a maximum magnetic field of 0.2 T at a distance of 10 mm from the body's leading edge. An integrated ultrasonic element with a focal distance also of 10 mm provided a pressure field that spatially overlapped with the magnetic field peak, with sufficient amplitude to cause inertial cavitation of microbubbles. Side ports in the magnet body allowed airflow for passive cooling around the acoustic element (although this feature was not necessary for the drive conditions used in this chapter), as well as a path for the element drive cable. An aluminium-bodied copy of the MAD (hereafter referred to as "aMAD") was produced to provide an ultrasound-only control for *in vitro* and *in vivo* experimentation.

(a) MAD cross-section facing down

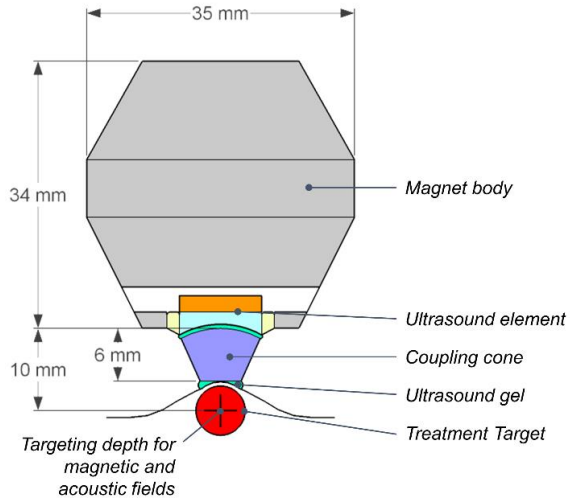

(b) Built MAD facing up

Figure 6.4. *Illustration of* ***(a)*** *MAD configuration and* ***(b)*** *photograph as tested with Perspex holder*

In order to span the gap between the ultrasound element and the delivery site of interest, a coupling cone was cast from paraffin wax and secured with ultrasound gel as shown in **Figure 6.4a**. The cone material was chosen for its ease of casting and minimal transmission loss in the 1 MHz frequency range as determined by conventional through-transmission measurements. Since the acoustic boundary conditions for this configuration

were different from those used in the initial characterisation [303], both the MAD and the aMAD were recalibrated by Dr. Michael Gray with the results shown in Appendix C.

Table 6.1 and **Table 6.2** show the different device configurations used in the *in vitro* and *in vivo* tests respectively. The MAD was used for: (1) its co-aligned magnetic and acoustic fields (group: "MAD" shown in **Figure 6.5a**), (2) its magnetic field only (group: "Mag"), and (3) its magnetic field combined with the acoustic field of the aMAD to study the non-coaligned fields (group: "US + Mag" shown in **Figure 6.5b**). The aMAD was also used on its own for the ultrasound only control (group: "US").

Table 6.1. *In vitro drug delivery experiment groups*

GROUP NAME	WATER	MAGMB-RB*	ULTRASOUND**	MAGNET***
Untreated	X			
MB		X		
US		X	X (aMAD)	
Mag		X		X (MAD)
US + Mag		X	X (aMAD)	X (MAD)
MAD		X	X (MAD)	X (MAD)

* MagMB-RB: MB = (1.7±0.6) x10^8 MB/mL and [RB] = 500±50 µM
** Ultrasound: 1.17 MHz, 30% duty cycle, peak negative pressure 0.7 MPa, 3.5 minutes
*** Magnet: 0.2 T at 10 mm

Table 6.2. *In vivo drug delivery experiment groups*

GROUP NAME	NO TREATMENT	MAGO_2MB-RB-GEM*	ULTRASOUND**	MAGNET***
Untreated	X			
MB		X		
US		X	X (aMAD)	
US + Mag		X	X (aMAD)	X (MAD)
MAD		X	X (MAD)	X (MAD)

* MagO2MB-RB-Gem: [MB] = (1.3±0.4) x 10^9 MB/mL, [biotin-RB-Gem] = 520±80 µM
** Ultrasound: 1.17 MHz, 30% duty cycle, peak negative pressure 0.7 MPa, 3.5 minutes
*** Magnet: 0.2 T at 10 mm

(a) *In vitro* setup with Dual Probe

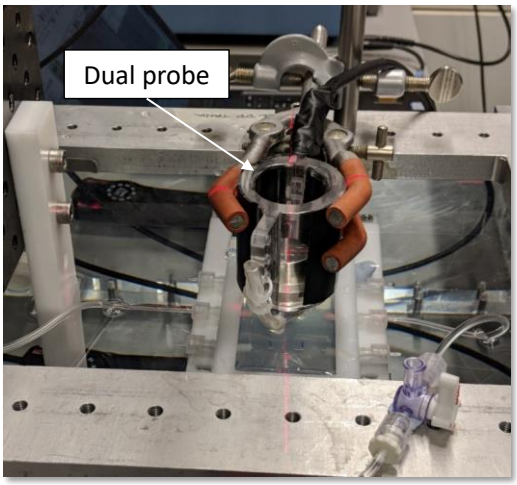

(b) *In vitro* setup with US + Mag

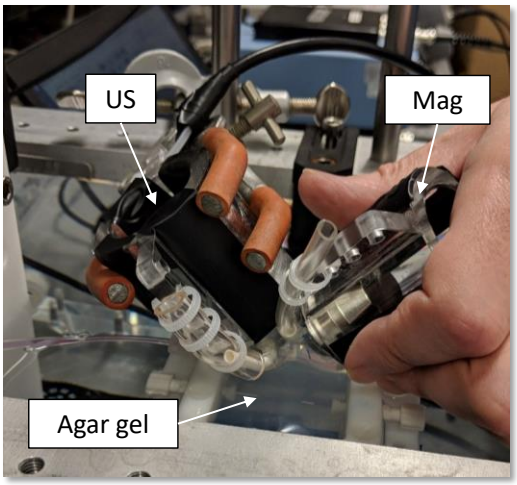

Figure 6.5. *Photographs of in vitro ultrasound and magnet set-up for* ***(a)*** *the MAD with co-aligned fields compared to* ***(b)*** *the US + Mag group with separate field applications.*

6.2.5. Drug delivery comparison in agar between devices

Drug delivery was quantified *in vitro* by flowing $MagO_2$MB-RB through a tissue mimicking agar phantom. The phantom body was formed within a Delrin frame filled with 1.25% agar gel. The cured agar phantom was 7 mm thick and covered in clear and acoustically transparent Mylar films on each side. Each phantom contained at least one straight channel of 1.2 mm diameter, with fittings on the frame for connection to a syringe pump and drain tubing. During testing, the phantom was partially immersed in a water bath heated to 36±1°C, with the upper phantom surface in air so that acoustic boundary conditions would be similar to those in the *in vivo* experiments. The phantom assembly was free of ferrous metal parts in order to minimize the likelihood of secondary magnetic fields influencing the results.

For acoustic treatments (MAD or aMAD), the device was held in place with a lab clamp, and the cone tip was coupled to the phantom face with water. Acoustic drive pulses (3000 cycles, 1.17 MHz, 30% duty cycle) were provided by a waveform generator

(33500B, Keysight, Santa Rosa, CA, USA) and passed to a power amplifier (1040L, E&I Ltd., Rochester, NY, USA) so that the peak negative pressure 10 mm in front of the device would be 0.7 MPa. This level matched the spatial peak value from the Sonidel (SP100, 1 MHz, Ø = 16 mm) transducer that was used in previous SDT studies [4,86], and in the sonoluminescence experiments presented in Chapter 4. Pressure calibrations for this device are presented in Appendix C.

The ultrasonic emissions from the channel were observed using a spherically focused single element transducer (7.5 MHz center frequency, 12.7 mm diameter, 75 mm focal distance, Olympus NDT) operating as a PCD. Signal conditioning was performed using the same procedures and instrumentation as in section 3.4.5.1. PCD signals were post-processed in MATLAB to yield power spectral density for each acquisition, and the responses at ultraharmonic frequencies were used to quantify cavitation activity during each exposure. Initial positioning of the agar flow channel and the acoustic instrumentation was guided by a crosshair laser to ensure proper alignment.

Data were collected for six groups as in **Table 6.1**, with three separate phantoms tested per group. For all treatment groups, 100 µL of MagMB-RB ((1.74±0.62) x 10^8 MB/mL, [biotin-RB] = 506±53 µM) were injected at a flow rate of 0.2 mL/min. Ultrasound was applied for 3.5 minutes, after which the treated channel was rinsed with 1 mL deionised water. The agar channel was immediately cut out (0.7 mL volume) and reserved for analysis after the experiment. After all groups were completed in a single test day, the reserved cut out agar channels were melted, sampled onto a pre-heated 96-well plate and left to equilibrate at 45°C for 15 minutes. Absorbance spectra were acquired at that temperature using a plate reader to measure the amount of Rose Bengal delivered in the agar volume. Spectra were normalised to no-treatment controls and the samples'

absorption intensities at 559 nm were compared to a standard curve for biotin-RB in melted 1.25% agar at 45°C (R^2 = 0.9991, **Appendix Figure E.3**).

6.2.6. Treatment of xenograft ectopic BxPC-3 tumours in SCID mice

BxPC-3 cells (1×10^6) in 50 µL Matrigel and 50 µL media were sub-cutaneously implanted into the rear dorsum of SCID (C·B-17/IcrHan®Hsd-*Prkdcscid*) mice. Tumours started to form approximately 2 weeks after cell implantation, and once they became palpable, they were measured using the Peira TM900 tumour measuring device. When the tumours reached an average of 113 mm^3, the animals were distributed into 5 groups (**Table 6.2**). They were then anaesthetized with intraperitoneal injections of Hypnorm / Hypnovel. A 100 µL mixture of PBS with $MagO_2$MB-RB-Gem ((1.25±0.41) $x10^9$ MB/mL, [biotin-RB-Gem] = 521±80 µM) was administered by tail vein injection to the animals in groups receiving treatments. The drive instrumentation and settings were the same as those used for the *in vitro* drug delivery experiments described in section 6.2.5. The cone of the MAD (or aMAD) was coupled to the skin of the animal using ultrasound gel. In order to minimise acoustic field uncertainties due to possible reflections and tissue damage risk, the subjects were treated lying prone over a mat of ultrasound absorbing material (Aptflex F28, Precision Acoustics, Dorset, UK). To improve free transmission of sound into the absorber, the abdominal hair was removed from the animals, and their skin coupled to the mat with ultrasound gel. Using this method, treatments were given on days 0, 2 and 4.

6.2.7. Statistical analysis

Errors are expressed as ± the standard deviation for all data shown. Statistical significance and comparisons were established using a 1-way analysis of variance (ANOVA) followed by Tukey's post hoc test.

6.3. Results and Discussion

6.3.1. Microbubble characterisation

Magnetic microbubbles (**Figure 6.6a**) were manufactured through the sonication of a mixture of phospholipids, surfactants and phospholipid-coated IONPs under PFB gas flow which resulted in a microbubble concentration of (2.1±0.3) x 10^9 MB/mL of 1.6 µm mean diameter. The removal of excess material through centrifugation decreased the microbubble concentration (**Figure 6.6b-c**) to an average of (7.2±2.0) x 10^8 MB/mL, of 1.8 µm diameter. A comparison of the size distributions shows that the loading and washing of biotin-RB-Gem mostly removes the small microbubbles (**Figure 6.6c**). However, the 1 to 8 µm sized bubbles appeared stable during this process.

(a) LipMB-DBPC before cleaning (b) MagMB-RB-Gem after cleaning (c) Size distribution

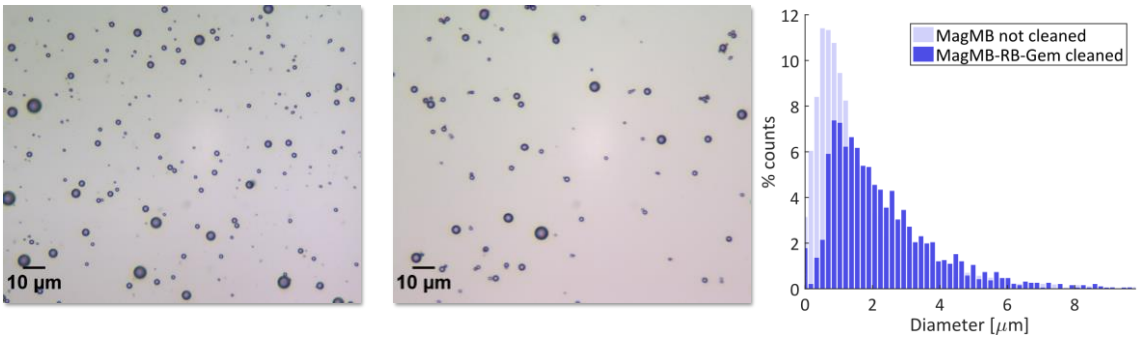

Figure 6.6. *Size comparison of magnetic microbubbles before and after drug loading. Photomicrographs or* ***(a)*** *LipMB-DBPC before cleaning and conjugation of biotin-RB-Gem and* ***(b)*** *after processing. Scale bars are 10 µm.* ***(c)*** *Microbubble size distribution before and after drug loading. The concentration of MagMB-RB-Gem after cleaning was (7.2±2.0) x10^8 MB/mL.*

To complete the *in vitro* studies, the iron content of **LipMB-DBPC** after three centrifugation steps (**Figure 6.7**) was measured and found to be higher than the results presented in Chapter 3 (**Figure 3.28a**) with an average of 0.07 pg iron per microbubble over three batches. The difference between these results could be associated with manipulation variations during the centrifugation cleaning steps.

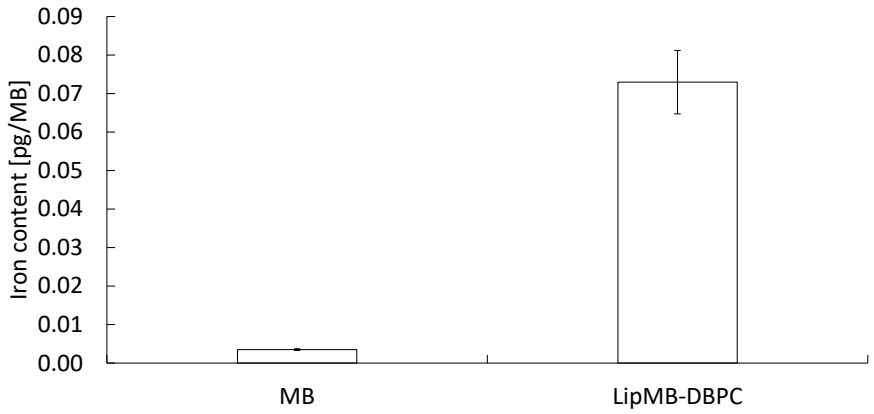

Figure 6.7. *Iron loading of cleaned lipid-based microbubbles ± DBPC-IONPs forming* ***LipMB-DBPC****; measured for n = 3 batches in each group.*

Considering the size distribution of these **LipMB-DBPC** batches, the available surface area of microbubbles and the theoretical maximum loading of nanoparticles on this surface were computed as described in section 3.4.6. The results from these calculations, presented in **Table 6.3**, indicate that a higher loading compared to the data presented in Chapter 3 was achieved with a loading of 10%. This difference was again attributed to the variable nature of the centrifugation and resuspension steps used for cleaning microbubbles.

Table 6.3. *Calculated particle loading per microbubble based on the measurement of iron loading per microbubble and IONP properties.*

PARAMETER	LipMB-DBPC
Measured iron loading / MB [pg/MB]	0.07
IONP/MB [a]	~ 1 000
Mean MB surface area [μm^2/MB] [b]	19
IONP area if considered a square [10^{-3} μm^2] [c]	2.5
Theoretical maximum loading [IONP/MB]	~ 8 000
Percent loading achieved [%]	~ 10%

[a] using results reported in **Table 3.5** for pg of iron per nanoparticle.
[b] considering the sample size distribution.
[c] based on the hydrodynamic diameter of the nanoparticles as reported in **Table 3.5**.

The drug concentration in the suspension after centrifuging the microbubbles three times was approximately 490±100 µM or 520±50 µM for biotin-RB-Gem or biotin-RB respectively. This was found to correspond to approximately 80% of the drug in solution and 20% on the surface of bubbles (**Figure 6.8**). Although most of the drug remains free in solution, an injection of 4.5 mL of the suspension would equate to an average dose of 0.6 mg Gemcitabine, which is still orders of magnitude lower than the 1000 mg/m^2 administered intravenously weekly over 7 weeks for pancreatic cancer patients [222,304]. Although clinically the toxicity of Rose Bengal has mostly been tested topically through intralesional injections [305,306], no indications of systemic toxicity were observed in mice receiving intravenous injections of $MagO_2MB$-RB ([biotin-RB] = 350 to 557 µM) individually or in combination with $MagO_2MB$-5FU ([biotin-5-FU] = 700 µM) [86] or O_2MB-Gem ([biotin-Gem] = 443 µM) [182].

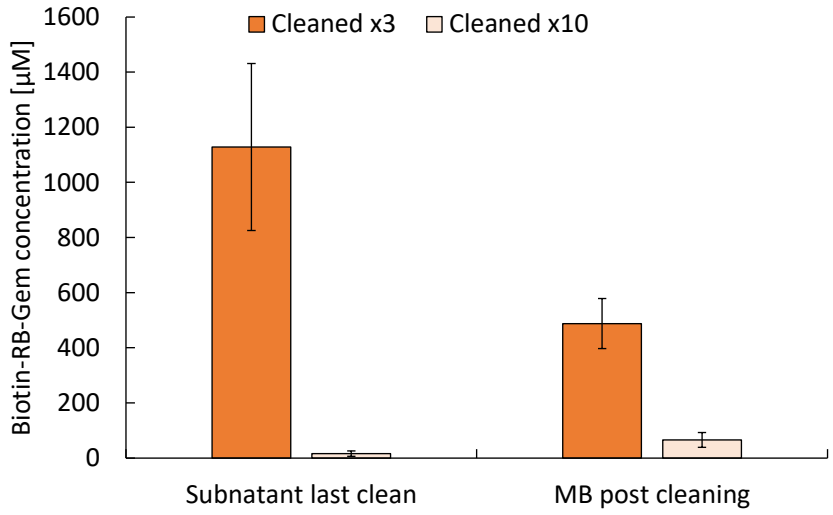

Figure 6.8. *Concentration of biotin-RB-Gem remaining in subnatant solution and on microbubbles after three and ten centrifugation steps. After being cleaned three times, the overall drug loading was found to be 488±91 µM. After ten times, the drug loading was 97±27 µM and minimal levels of biotin-RB-Gem was found remaining in the solution, indicating that the overall drug content reported after cleaning three times had approximately 20% of the drug on the microbubbles and 80% unbound in solution.*

6.3.2. *In vitro* results

Using the ultrasound parameters indicated in **Table 6.1**, the results from the *in vitro* activation of $MagO_2MB$-RB using ultrasound are shown in **Figure 6.9**. The generation of cytotoxic singlet oxygen was significantly enhanced for $MagO_2MB$-RB compared to $MagO_2MB$s or RB alone when exposed to ultrasound in a degassed solution ($p < 0.01$). A similar trend was observed for the ultraharmonic energy of microbubbles recorded from the PCD, but the emissions from the two types of microbubbles and Rose Bengal alone were all significantly different ($p < 0.01$). Although most of the cavitation activity occurred in the first five seconds of ultrasound, the emissions were computed by the integration of the ultraharmonic power over the entire 3.5 minutes to be comparable to the characterisation of singlet oxygen generation, obtained after the entire ultrasound exposure. Nonetheless, the energy calculations were also computed over the first 5 seconds of ultrasound exposure and presented similar results (data not shown). An analysis of the emission power over time in **Figure 6.10** and the fitting parameters in **Table 6.4** highlight a significant delay before the decay of the $MagO_2MB$-RB ultraharmonic emissions and a significant increase in the plateau level reached, compared to $MagO_2MB$. The increased cavitation activity of $MagO_2MB$-RB compared to $MagO_2MB$ could be associated with an enhanced stabilisation of $MagO_2MB$-RB due to the surface functionalisation of the sensitiser inhibiting bubble dissolution in the degassed medium [307].

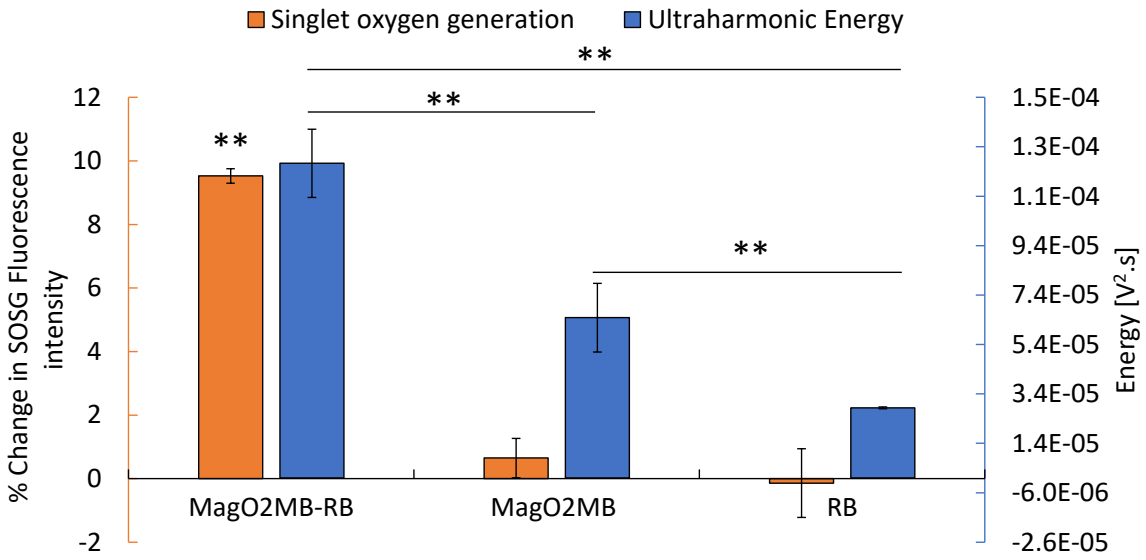

Figure 6.9. *Results (n = 3) from singlet oxygen characterisation (orange) from Rose Bengal activation after ultrasound exposure relative to unexposed sample, with associated ultraharmonic emissions from microbubbles (blue) indicating the nonlinear oscillations of bubbles undergoing cavitation (** = p < 0.01). A sample was prepared in degassed PBS with SOSG (1.25 µM), ± $MagO_2$MB-RB (541 µM, 5x10^7 MB/mL). Ultrasound parameters were 1.17 MHz, 0.7 MPa peak negative pressure, 30% duty cycle, 100 Hz pulse repetition frequency ultrasound for 3.5 minutes.*

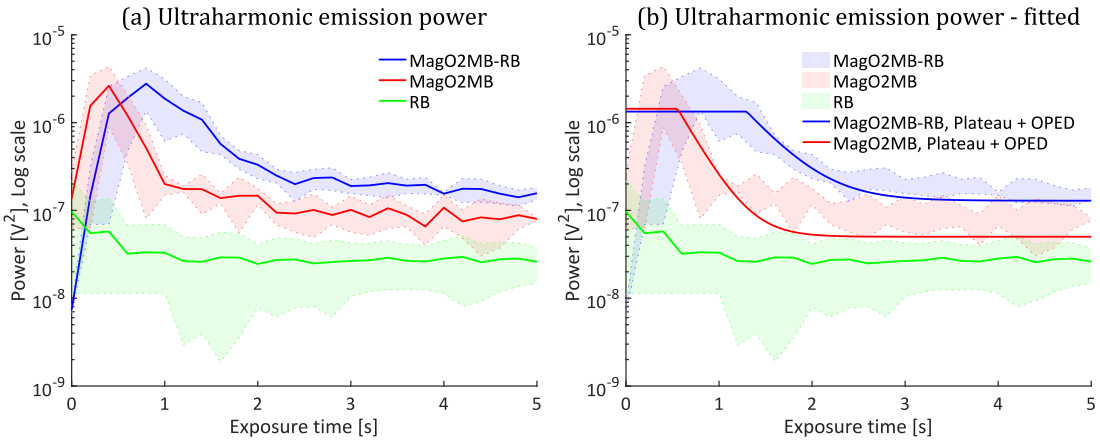

Figure 6.10. *The power of ultraharmonic emissions over the first 5 seconds of ultrasound exposure **(a)** mean and standard deviation, **(b)** runs with microbubbles were fitted with a plateau followed by one-phase exponential decay (OPED).*

Table 6.4. *Parameters summary for fitting the plateau followed by the one-phase exponential decay to the ultraharmonic emission power over time for $MagO_2MB$-RB and $MagO_2MB$.*

PARAMETERS	$MagO_2MB$-RB	$MagO_2MB$
Adjusted R^2	0.48	0.46
t_0 [s]	1.30	0.56 **
Half-life, $t_{1/2}$ [s]	0.25	0.16
$t_{1/2,\ adjusted} = t_0 + t_{1/2}$ [s]	1.55	0.72
P_0 [$x10^{-6}$ V^2]	1.34	1.44
Plateau [$x10^{-7}$ V^2]	1.29	0.50 **

** $p < 0.01$ compared to $MagO_2MB$-RB, determined by an unpaired t-test. The parameters referred to in this table were previously described in Chapter 3, section 3.4.5.

The performance of the MAD compared to the use of two separate devices was assessed in an agar phantom as pictured in **Figure 6.11**. The concentration of Rose Bengal delivered was determined based on the absorbance of a set volume of agar gel surrounding a channel after flowing 100 µL of MagMB-RB through it while exposed to one of the device configurations.

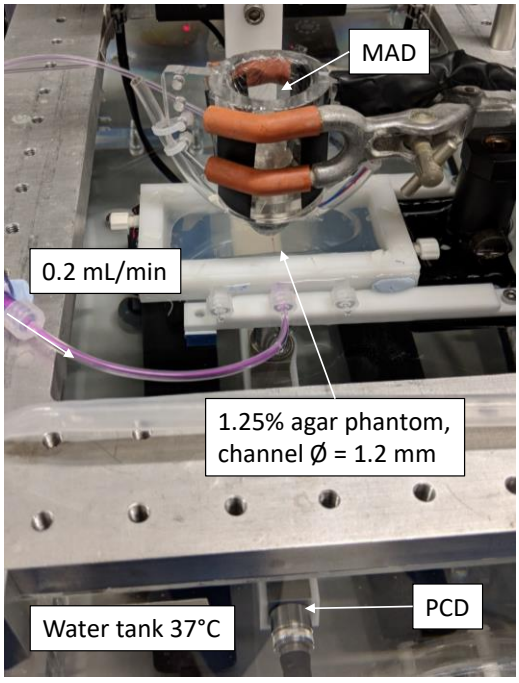

Figure 6.11. *Picture of experimental set-up used to test the performance of the MAD focused on a 1.2 mm inner diameter channel in a 1.25% agar phantom placed at the water level in order to allow the recording of acoustic emissions with a PCD at the bottom of tank. The microbubbles were flown at 0.2 mL/min through the channel.*

Figure 6.12 then reports the concentration of Rose Bengal delivered for the different groups considered. When ultrasound was used, the associated cavitation activity is also provided. A significantly higher concentration of Rose Bengal was delivered ($p < 0.01$) using the MAD; more specifically the MAD led to 1.6x and 1.4x more Rose Bengal compared to US only and US + Mag groups respectively. Moreover, a comparison between the MAD and US groups indicates a significant increase in delivery ($p < 0.01$) with the addition of magnetic targeting. The minimal enhancement observed for the US + Mag group compared to US only, however, highlights the difficulty in device alignment when using two separate units. The ultraharmonic emissions reported for the untreated group indicates the level found in water only, for reference. The delivery recorded for $MagO_2$MB-RB suspensions alone can be associated with the high concentration of free Rose Bengal in solution diffusing into the porous agar gel [308] without external stimulus and was found to be significant compared to the untreated group ($p < 0.01$). Individually, US and Mag fields enhanced delivery to a similar degree, in agreement with previous results from Stride *et al* [199]. The application of a magnetic field alone could potentially disrupt the coating of magnetic microbubbles causing the release of Rose Bengal or coating fragments, thereby increasing the delivery compared to the MB group.

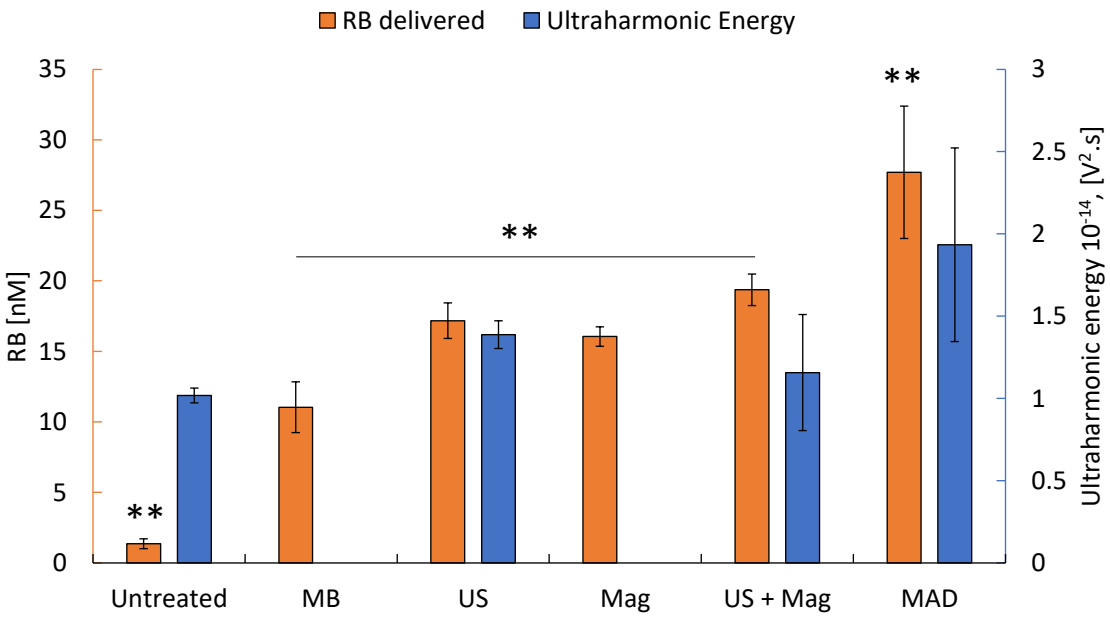

Figure 6.12. *Rose Bengal drug delivery (orange, n = 3) comparison using different ultrasound and magnetic device configurations as listed with Table 6.1, determined in a volume of 0.7 mL agar (1.25% w/w) (** = p < 0.01). The corresponding energies of ultraharmonic emissions from microbubbles (blue) when ultrasound was present are provided. For the treatment receiving groups, 100 µL of MagMB-RB ([MB] = (1.74±0.62) x10^{8} MB/mL, [biotin-RB] = 506±53 µM) were administered and flowed at a rate of 0.2 mL/min. When a magnet was used, a 0.2 T magnetic field was applied at the focus of the probe, and when ultrasound was applied, the parameters were: 1.17 MHz, 0.7 MPa peak negative pressure, 30% duty cycle, 3000 cycles, for 3.5 minutes. The ultraharmonic emissions plotted for the untreated group reflects the background emissions recorded for just water flowing in the agar channel.*

6.3.3. *In vivo* results

The co-aligned fields of the MAD were then tested for the delivery of MagO$_2$MB-RB-Gem *in vivo* in SCID mice bearing ectopic xenograft human pancreatic BxPC-3 tumours. The microbubble suspension produced for treatments were verified as before to determine their size distribution, iron content, and drug concentration (**Figure 6.13**) which were found to be comparable with the previous results.

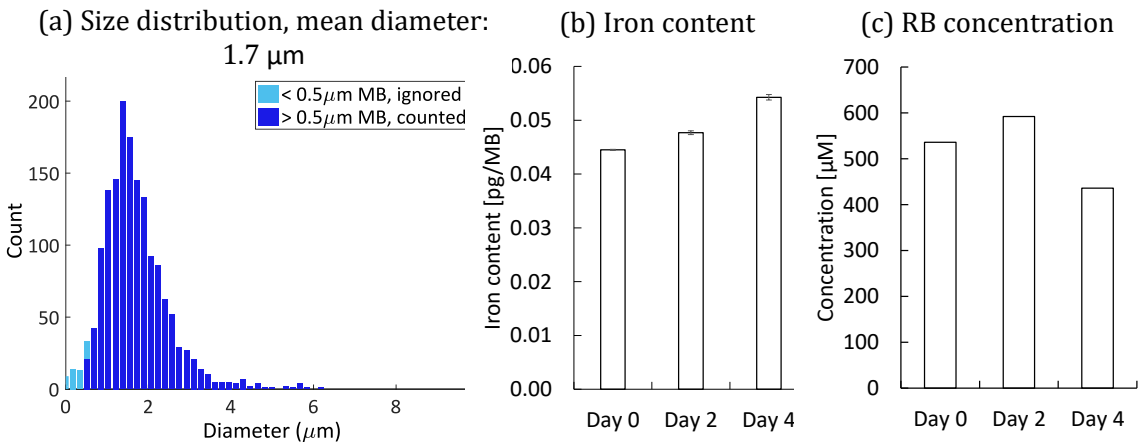

Figure 6.13. *Characterisation of $MagO_2MB$-RB-Gem used for in vivo treatment with a* ***(a)*** *size distribution,* ***(b)*** *iron content, and* ***(c)*** *Rose Bengal concentration in agreement with in vitro microbubble data.*

For this study, 25 animals with implanted tumours were randomly distributed into the five groups described in **Table 6.2**, and received injections on day 0, 2, and 4. Although the treatment appeared well tolerated with negligible mice weight change (**Figure 6.14a**) and normal iron content in faeces (**Figure 6.14b**) [309], four animals were lost during and following treatment as indicated in **Figure 6.15**. The reason is still unknown, but darkened skin in the bowel and genital area was observed on the mice that died in the US group. Iron toxicity was, however, unlikely according to the characterisation of mice faeces which would have indicated a rise in iron post-treatment if an excess was administered. Additionally, as an ultrasound absorbing mat and ultrasound gel were used underneath the mice receiving treatment, it is also unlikely that the exposure to ultrasound would have caused irritation or haemorrhage in the bowels further away from the face of the transducer. As it was two male mice that died in the US group with marked darkened skin, this might have been caused by irritation from the hair shaving process to enable the coupling to the absorber with ultrasound gel. Nevertheless, further toxicology examinations are required to determine if other factors in the handling procedure or

treatment suspension could have caused the high mortality rate observed. Tumour volume data including all treatment groups are presented in **Figure 6.16**. However, the US group was only left with 3 mice at the end of day 4 which explains the sudden increase in the reported standard deviation from this day due to one subject presenting a good response to treatment. Therefore, the US group was not included in the statistical analysis of the *in vivo* investigation with final results presented in **Figure 6.17**.

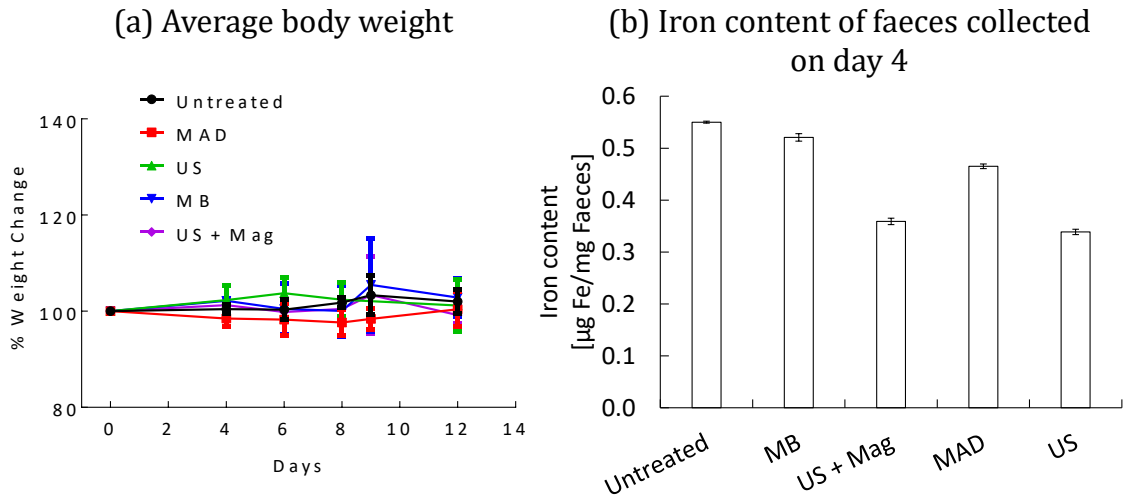

Figure 6.14. *Treatment tolerance in mice with* ***(a)*** *average body weight recorded during the study with black arrows indicating treatment days, and* ***(b)*** *faeces iron content determined through ICP-OES measurement in 0.2% nitric acid for faeces collected on day 4.*

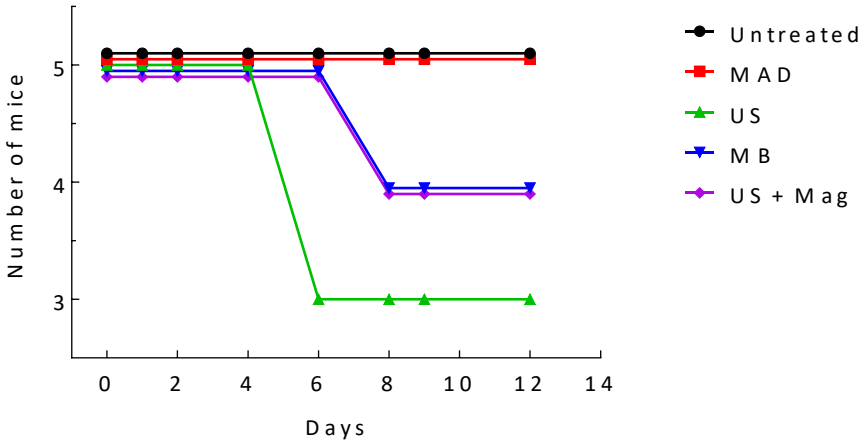

Figure 6.15. *Number of mice per treatment group over the study.*

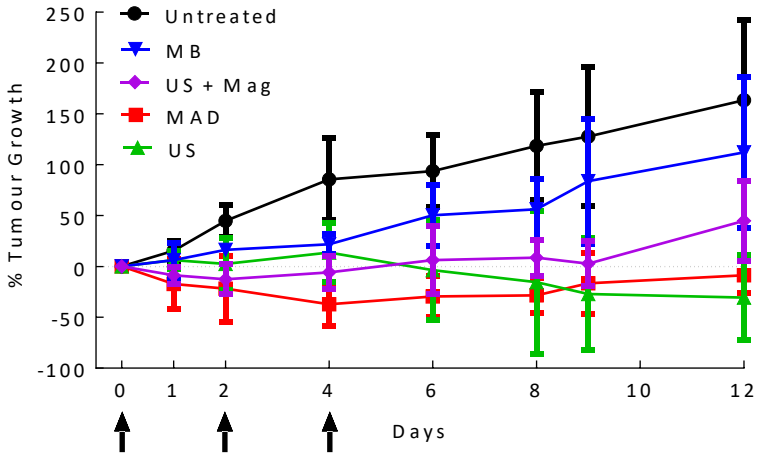

Figure 6.16. *In vivo results with % tumour growth over time relative to day 0. Arrows indicate treatment days, including US group. The increase in standard deviation after day 4 in the US group was explained by the death of two mice within that group following the last day of treatment.*

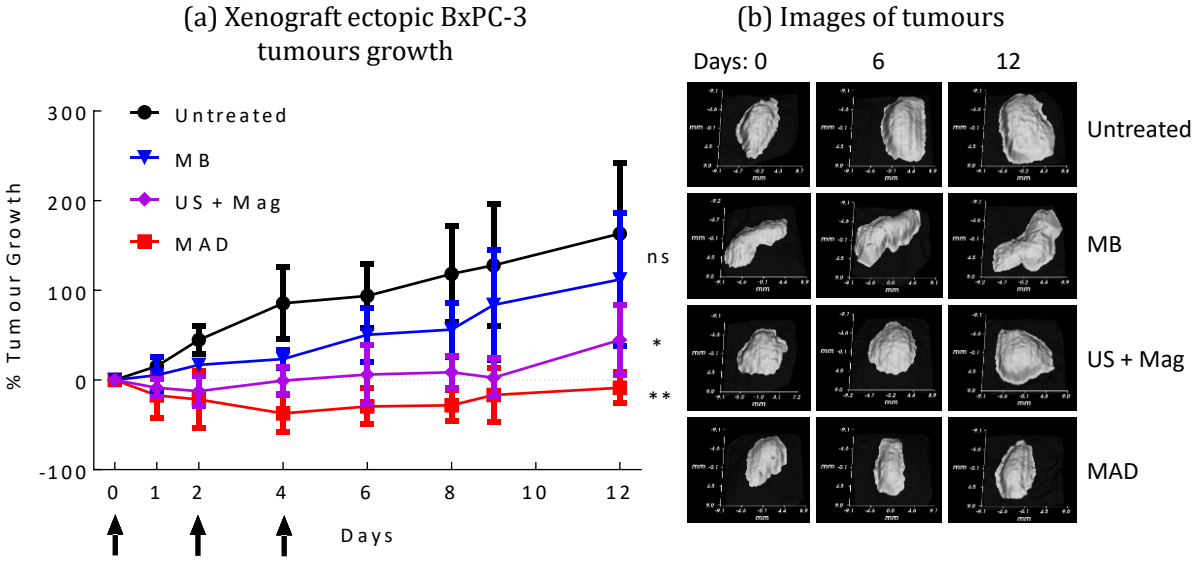

Figure 6.17. *In vivo results with **(a)** % tumour growth over time relative to day 0. **(b)** Images of tumours on day 0, 6, and 12. Arrows indicate treatment days. * $p < 0.05$, ** $p < 0.01$. Error bars indicate standard deviations.*

Considering **Figure 6.17**, the percent tumour growth data demonstrated a 37% decrease in tumour volume relative to pre-treatment values for animals in the MAD group, 4 days after the first treatment. Whereas a 9% reduction was recorded for subjects in the US + Mag group. Then 12 days after the first treatment, the animal exposed to the

MAD still presented tumours 9% smaller than their pre-treatment values and 54% smaller than animals in the US + Mag group. This data was, however, not significantly different due to the wide range of tumour volumes recorded in the US + Mag group. This was associated to the variability in aligning the US and magnetic fields when two separate devices were used leading to wide differences in tumour response to this treatment. Still, compared to the untreated group, the MAD enabled a more significant reduction in tumour volume sustained to day 12 with a p-value of 0.0028, while the US + Mag group presented a p-value of 0.0346. In addition, although the MB group has smaller tumours than untreated animals, the difference was not significant. Overall, the *in vivo* data corroborates with *in vitro* results indicating that the co-aligned magnetic-acoustic device allowed a consistent increase in drug delivery and hence treatment efficacy.

6.3.4. Study limitations

The results presented in this chapter improved on prior investigations by using a novel therapeutic to increase drug loading, a more stable magnetic microbubble to deliver the payload, and a more reliable device for the application of co-aligned magnetic and acoustic fields.

The *in vivo* study was, however, very limited by the number of animals per treatment groups which lowered the power of the statistical analysis completed. Additionally, uncertainties in the toxicology profile of the novel therapeutic are especially important to address in the next preclinical investigation. The processing of microbubbles could also be further improved to diminish the proportion of free drug in solution and minimise the risk of side effects. Although the MAD significantly enhanced the therapeutic effect, the addition of cavitation monitoring in subsequent device generations would provide a

valuable feedback to optimise the treatment protocol. Finally, as the *in vivo* work presented in this chapter was completed on ectopic xenograft tumours, questions arising from the relationship between this preclinical model and the targeted indication are important. For instance, biologically relevant tumour vasculature and depth are both critical factors that can be further investigated *in vitro* to determine the potential of co-aligned magnetic targeting and ultrasound activation for the sonodynamic treatment of pancreatic tumours in patients.

6.4. Conclusions

Overall, the MAD with co-aligned fields enabled the targeting and activation of **LipMB-DBPC** loaded with oxygen and a novel therapeutic incorporating both Rose Bengal and Gemcitabine. This combination significantly increased the averaged drug delivery by 1.6-fold in an agar flow phantom ($p < 0.01$) compared to the use of two separate devices, and an increase in the energy of microbubble ultraharmonic emissions was also observed. These results indicate that the MAD enabled the precise application of both targeting and activation fields to promote drug delivery. An examination of this method *in vivo* demonstrated a significant decrease in tumour size 12 days after treatment ($p < 0.05$) compared to the use of two separate devices. Further, the MAD allowed for a substantial 37% decrease in tumour size after 4 days of treatment compared to pre-treatment values, highlighting that this approach could become an ideal neo-adjuvant therapy to downstage tumours prior to surgery. This is especially important in the case of pancreatic cancer where 20% of patients present border-line resectable lesions at the time of diagnosis for whom the downstaging of tumours could change their eligibility to undergo curative surgical resection. Nonetheless, an examination of the MAD on an *in vitro* or *ex vivo*

system representative of human length scales, and a toxicology study of the injected suspension are both required to further advance this approach towards clinical use.

6.4.1. Contributions

This chapter provides a method for the characterisation of drug-loaded magnetic microbubbles and the amount of drug they deliver in an agar gel flow phantom upon exposure to magnetic and acoustic fields. The MAD was further evaluated *in vitro* and enabled a significant enhancement in drug delivery compared to the application of separate magnetic and ultrasound fields. These results were confirmed in an *in vivo* study.

Chapter 7
Conclusions and future work

7.1. Thesis overview

Sonodynamic therapy has recently been developed for the treatment of hypoxic tumours using the local activation of sensitising drugs to produce reactive oxygen species, cytotoxic to the surrounding cancer cells. In this thesis, it was demonstrated that sonoluminescence could be involved in the activation pathway of sensitisers during sonodynamic therapy. In addition, microbubbles facilitate the generation sonoluminescence when exposed to certain ultrasound conditions. Thus, the combination of these could provide a way to remotely produce light in a target location in the body. Magnetic microbubbles were then researched to increase the local concentration of microbubbles and therapeutics, and enhance the production of reactive oxygen species in a targeted manner.

In Chapter 3, several methods were compared to produce microbubbles for magnetic targeting. While different formulations have been reported to enhance drug delivery when a magnetic field is applied, a study comparing their performance was necessary in order to determine which magnetic microbubbles would be appropriate to combine with sonodynamic therapy. For this, the loading of iron oxide nanoparticles on the outer surface, within, and in an oil phase on the inner surface of the microbubble coating were

compared. Externally-bound particles significantly improved the stability of microbubbles (**SurfMB**), enabled more sustained acoustic emissions compared to all other formulations and presented the highest magnetic response. This method, however, challenged the further attachment of hydrophilic drugs such as the sensitiser Rose Bengal on the surface of microbubbles. Thus, the loading of lipid-coated iron oxide nanoparticles within the microbubble shell was preferred as it allowed the subsequent surface addition of the sensitiser for sonodynamic therapy. Although these magnetic microbubbles presented a weak magnetic response, they still demonstrated a significantly improved stability compared to unloaded systems when the coating on the iron oxide nanoparticles was composed of the same phospholipid as in the microbubble shell (**LipMB-DBPC**).

The performance *in vitro* and *in vivo* of these magnetic microbubbles for targeted sonodynamic therapy was evaluated in Chapter 6. The results showed a significant increase in Rose Bengal delivery *in vitro* using **LipMB-DBPC** with externally-bound Rose Bengal targeted and activated using a magnetic acoustic device. In effect, when several device configurations were compared, the use of a co-aligned magnetic and acoustic device enabled the accurate application of both fields compared to the use of separate probes. An improved therapeutic effect was then observed *in vivo* with a decrease in the tumour volume for mice bearing hypoxic pancreatic tumours and receiving magnetically targeted sonodynamic and antimetabolite therapies.

While the therapeutic effects of this method are the focus of current developments, the advancement of sonodynamic therapy towards clinical use requires additional characterisation. As previously mentioned, the mechanisms for sensitiser activation and

ultrasound parameters are critical factors that can help the optimisation of this approach. These were evaluated in Chapter 4 and Chapter 5 respectively.

In Chapter 4, an investigation of several proposed mechanisms for the activation of Rose Bengal using ultrasound was undertaken. First, as pyrolysis events during bubble cavitation can produce a range of reactive species, several of these were examined for their effect on Rose Bengal in solution to determine whether oxidative pathways could explain the production of cytotoxic agents during sonodynamic therapy. The presence of hydroxyl radicals, hydrogen peroxide, and singlet oxygen, however, did not alter the activity of the sensitiser. Additionally, the characterisation of Rose Bengal concentrations in solution before and after ultrasound exposures did not show significiant Rose Bengal degradation through pyrolysis. Although these results don't explain the activation of the sensitiser, they demonstrate that Rose Bengal can withstand the exposure to microbubble-induced cavitation and reactive oxygen species without degrading, thus confirming the utility of this sensitiser for sonodynamic therapy.

The second mechanism investigated was the generation of light i.e. sonoluminescence during cavitation which could be of appropriate wavelength to activate Rose Bengal also known for its photosensitivity. Sonoluminescence events were detected when sulphur hexafluoride or oxygen microbubbles were exposed to ultrasound conditions relevant for therapy and diagnostic techniques at 37°C. Photons were recorded over broad range of wavelengths (350, 470, 520, 560 nm) which included the absorption wavelength of Rose Bengal (560 nm). Confirmation of multi-bubble sonoluminescence as the activation mechanism for sonodynamic therapy at 1 MHz was provided by the reduction in the sonoluminescence recorded at 560 nm when Rose Bengal was added to the solution. The findings reported in this chapter demonstrate that light can be produced

when microbubbles are exposed to low intensity ultrasound, for in-house produced microbubbles as well as for imaging contrast agent Sonovue®. The implications of these results are important for the development of therapeutic ultrasound, not necessarily because of the amount of light produced, but mainly because of the conditions that are generated during microbubble collapse. In effect, multi-bubble sonoluminescence is associated with extreme temperatures and pressures [38]. Thus, additional investigations are necessary to determine whether these conditions are also produced during ultrasound diagnostic imaging. Further, therapeutic applications of ultrasound should also provide a careful examination of the chosen parameters and exposure conditions to estimate the conditions generated during cavitation and how these might affect the therapy or the surrounding biological functions.

In Chapter 5, degassed solutions were used to mimic the lack of oxygen in hypoxic tumours and a method of producing oxygen loaded microbubbles was established to provide the oxygen required for the generation of singlet oxygen during sonodynamic therapy in these conditions. The ultrasound drive pressure, duty cycle, and pulse repetition frequency were then varied to observe their effects on the activation of Rose Bengal at 1 MHz with oxygen microbubbles in degassed solutions. The results indicated that increasing the ultrasonic energy increased the sensitiser activation when oxygen microbubbles were added. In contrast, no activation was observed without the addition of cavitation nuclei. This indicates microbubbles can be used to lower the activation threshold of the sensitiser during ultrasound exposure and thus enable the use of milder ultrasound conditions during sonodynamic therapy.

The effects of changing duty cycle and pulse repetition frequency indicated that the timing of ultrasound cycles can affect the therapy. In effect, with a constant amount

energy and number of acoustic cycles delivered, increasing the duty cycle increased the activation of the sensitiser. In contrast, changes to the pulse repetition frequency from 20 to 118 Hz did not alter the activation level of Rose Bengal. Although only a small range of parameter was investigated, these results could suggest that a decrease in the OFF time between the ultrasound bursts of the exposure can promote bubble cavitation. The difference observed between these two parameters may then be useful to optimise the treatment protocol of sonodynamic therapy.

Overall, hypoxia has rendered the treatment of certain cancers challenging through an increase in tumour resistance and metastasis. To address this problem, sonodynamic therapy with Rose Bengal was enhanced using oxygen loaded microbubbles. This approach was designed to enable the treatment of hypoxic tumours by providing the oxygen and cavitation nuclei necessary for a therapeutic effect. Further improvement was then achieved through the magnetic targeting of the therapy. In effect, an increased concentration of microbubbles could enhance sonoluminescence production when exposed to ultrasound parameters relevant for sonodynamic therapy. While the amount of light generated is well below the levels used during laser therapy, the work presented in this thesis demonstrated that sonoluminescence might be involved in the activation of sensitisers during sonodynamic treatment. Thus, a method allowing the monitoring of light production *in vivo* will become important for the translation of this therapy. Initial development for this could focus on evaluating whether cavitation emission features can be indicative of sonoluminescence events *in vitro* and *in vivo*. Although an optimisation of sonodynamic therapy is still necessary, the results presented in this thesis have confirmed

the potential of this approach to enable the treatment of hypoxic tumours and provide important contributions for the advancement of this method towards clinical use.

7.2. Future work and translation considerations

There are several limitations to the results presented in this thesis and multiple areas for future development. These are summarised in this section.

7.2.1. Functionalisation of microbubbles for magnetic targeting

The formulations considered in Chapter 3 were solely based on previously reported magnetic microbubbles and the investigation mainly focused on the loading of iron oxide nanoparticles into microbubbles. Therefore, the main limitation of this study comes from the charge, composition, size, and magnetic properties of these particles which were not matched between the magnetic microbubble formulations considered. Additionally, circulation studies for these systems are also needed. Particularly, focusing on clearance mechanisms found *in vivo* to determine whether stabilising or stealth properties could be incorporated. For instance, an examination *in vivo* of the distribution obtained using radio-labelled microbubbles would be valuable. Finally, an investigation on how the magnetic functionalisation of microbubbles would affect subsequent drug loading becomes important as an increasing number of therapeutics added to microbubbles are being proposed.

7.2.2. Mechanisms

Chapter 4 characterised the mechanisms for Rose Bengal activation during sonodynamic therapy with samples at 37°C. Nonetheless, the results presented were limited to a static

environment. Thus, this work could be continued by repeating these measurements in a more biologically representative system which would provide further insight on the likelihood of these events to occurs during treatment. For this, a study on sonoluminescence events under flow at 37°C and for a confined sample volume is necessary.

Further, the current work solely focused on the generation of singlet oxygen as a cytotoxic agent during sonodynamic therapy. However, a study on the reactive oxygen species population produced during cavitation and what affects these processes are necessary to understand the overall bioeffects associated with this therapy.

7.2.3. Oxygen microbubbles and ultrasound parameters

An examination on the effectiveness of microbubbles at delivering oxygen to hypoxic regions is required to further complement the results presented in Chapter 5. This work would, therefore, have to consider oxygen delivery at larger length scales to determine the potential for treating hypoxic tumours in human. In effect, gas exchange using oxygen microbubbles was demonstrated to occur within the first few minutes when injected into a system with ambient oxygen partial pressures. Although this time scale might not be a problem for the treatment of hypoxic tumours in mice, the length scale of human vasculatures and the variability in tumour vasculatures might become challenges.

The investigation of varying ultrasound parameters for sonodynamic therapy also must be continued to further understand the effects of ultrasound frequency, pressure, duty cycle, and pulse repetition frequency on the activation of the sensitiser. The experimental set-up could then be improved using a sample under flow and at 37°C, to provide a better representation of how these parameters affect the therapy *in vivo*.

7.2.4. Magnetic targeting

The results of two *in vivo* studies demonstrated the benefit of targeting sonodynamic therapy using an externally applied magnetic field and responsive microbubbles. These results were, however, obtained on a small animal model and the characterisation of microbubble magnetic targeting at human length scales is necessary to understand the feasibility of this approach.

7.2.5. Clinical translation

To ease the clinical translation of sonodynamic therapy, a controlled- and repeatable-activation of the sensitiser is necessary. Therefore, Chapter 4 and Chapter 5 provide a starting point for the advancement of this approach to determine how ultrasound is activating the sensitiser and which parameters are necessary for this to occur consistently. Nonetheless, the sonodynamic treatment of hypoxic tumours might face an accelerated translation to clinical trials due to the poor prognosis given to these patients, the resistance of this disease to current therapies and promising preclinical results. In that event, the injected treatment should be chosen to ease the clinical approval while maintaining its therapeutic effect by using ingredients previously incorporated in ultrasound contrast agents or in other therapies. Additionally, an ultrasound device with feedback monitoring could be used to maximise the treatment and approval of the method. Thus, a trial using oxygen microbubbles loaded or co-injected with Rose Bengal and exposed to ultrasound would be prioritised to minimise the risk for failure. The addition of magnetic targeting is then a consideration that is further down the line in the clinical translation of approach.

Appendices

These appendices provide additional tables, methods, and results further referred to and discussed in the main document.

Contents

Appendix A. Review of sonodynamic therapy studies

Appendix Table A.1. *Review of sonodynamic therapy studies*

Sensitiser	Ultrasound f [MHz]	I [W/cm^2]	DC [%]	t [min]	*In vivo* biological model	Ref
Anticancer drug derived sensitisers						
Adriamycin *vs.* Daunomycin	1.92	0.7	-	10	**Rat:** Yoshida Rat sarcoma	[310]
Adriamycin	1.733	0.5, 2	-	30	**Mouse:** RIF-1 Mouse fibrosarcoma B-16 Mouse melanoma	[311]
Dihydroxy(oxybi-guanido) boron (III) *vs*. 5-FU	25	18.35	-	40 s	**Mouse:** Ehrlich cell Mouse mammary gland	[312]
5-FU	0.8	1,2,3	30, CW	1,3,5	**Mouse:** Ehrlich cell Mouse mammary gland	[313]
Porphyrin derived sensitisers						
ALA	1	2	50	5	**Mouse:** SAS Human tongue squamous cell carcinoma	[314]
ALA	1	0.5	10	15	**Mouse:** Atherosclerotic	[3]
Hp	1.92	1.7	CW	10	**Mouse:** Sarcoma 180 Mouse sarcoma	[315], [316]
Hp derivative	1.1	0.3	-	3	**Mouse:** Sarcoma 180 Mouse sarcoma	[317]
HMME	1	0.5	-	2	**Rat :** C-6 Rat malignant glioma	[318]
DEG	1	2	50	10	**Mouse:** MKN-74 Human gastric tubular adenocarcinoma	[11]
DCPH-P-Na(I)	1	1,2	50	10	**Mouse:** MKN-45 Human gastric adenocarcinoma	[294]
Metalloporphyrin	1	2.3	50	5	**Mouse:** 4T1 Mouse mammary gland	[319]
Sinoporphyrin sodium + (MBs)	0.996	2.94	30	1	**Mouse:** U87 MG-Red-FLuc Human Glioblastoma	[320]
ATX-70	1.92	1,2,3,5	-	15	**Rat:** Chemically induced rat mammary tumour	[321]
ATX-70	1.92	1,3,5	-	15	**Mouse:** Colon-26 Mouse colon adenocarcinoma	[322]
ATX-70	0.5 + 1	8 + 8 = 16	-	5	**Mouse:** Colon-26 Mouse colon adenocarcinoma	[323]
ATX-70	0.5 + 1	12	-	5	**Rat:** Walker 256 Rat Mammary gland adenocarcinoma	[324]
Photofrin II	1.92	1,2,3,5	-	15	**Mouse:** Colon-26 Mouse colon adenocarcinoma	[325]
Photofrin II	1.92	3	-	15	**Rat:** AH130 Rat sarcoma	[326]
Photofrin	0.150 + 1	2.2	-	30	**Mouse:** Breast adenocarcinoma	[327]
ppIX	1	3	10	4	**Mouse:** SCC7 Mouse squamous cell carcinoma	[328]
ppIX vs. Hp	2.2	3,5,7	-	3	**Mouse:** Sarcoma 180 Mouse sarcoma	[15]
AlPcTS	1.92	3	-	15	**Mouse:** Colon-26 Mouse colon adenocarcinoma	[329]
PAD-S31	1	0.3		15	**Rabbit:** Decreased neointimal hyperplasia after stenting	[330]

Appendix Table A.1. continued. Review of sonodynamic therapy studies

Sensitiser	Ultrasound f [MHz]	I [W/cm^2]	DC [%]	t [min]	*In vivo* biological model	Ref
Other sensitisers						
ICG	1	3.5	40	3	**Mouse:** RIF-1 Mouse fibrosarcoma	[331]
RB	1	3	50	0.5	**Mouse:** B16 Mouse melanoma	[2]
RB + (MBs)	1	3.5	30	3	**Mouse:** RIF-1 Mouse fibrosarcoma	[216]
RB + (MBs)	1	3	50	3.5	**Mouse:** BxPC-3 Human pancreatic ductal adenocarcinoma	[12]
RB + (MBs)	1	3.5	30	3.5	**Mouse:** BxPC-3 Human pancreatic ductal adenocarcinoma	[4]
RB derivative	1	1	100	3	**Mouse:** MDA-MB-468 Human breast adenocarcinoma	[332]
B-TiO_2-PEG	1	1.5	50	5	**Mouse:** 4T1 Mouse mammary gland	[333]
Piroxicam	2	3		2	**Mouse:** Sarcoma 180 Mouse sarcoma	[334]
Combination treatment						
RB + 5-FU + (MBs)	1	3.5	30	3.5	**Mouse:** BxPC-3 Human pancreatic ductal adenocarcinoma	[86,220]
RB + Gem + (MBs)	1	3.5	30	3.5	**Mouse:** MIA PaCa-2 Human pancreatic ductal adenocarcinoma	[182]
ALA + Bleomycin	1 3	1 3	50	3	**Mouse:** EMT-6Mouse mammary gland	[335]
Bleomycin + $AlPcS_{2a}$	3	3	50	3	**Mouse:** Colon-26 Mouse colon adenocarcinoma	[296]
Ce6 + Docetaxel	1	1	70	3	**Mouse:** B16-F10 Mouse melanoma	[336]
Hp + ICG	1	3.5	50	3.5	**Mouse:** RIF-1 Mouse fibrosarcoma	[337]
PTX MSN	1	0.8	CW	3 + 2	**Mouse:** 4T1 Mouse mammary gland	[338]
DOX/Mn-TPPS@RBC	1	1	CW	3	**Mouse:** MCF-7 Human Invasive ductal carcinoma	[339]

Abbreviations: f = frequency, I = intensity, DC = duty cycle, t = time, CW = continuous wave ultrasound, 5-FU = 5-fluorouracil, ALA = 5-aminolevulinic acid, Hp = hematoporphyrin, HMME = hematoporphyrin monomethyl ether, DEG = porphyrin-derived sonosensitizer with minimal photosensitivity, DCPH-P-Na(I) = porphyrin-derived sonosensitiser devoid of photosensitivity, Metalloporphyrin = HMONs-MnPpIX-PEG = PEGylated, manganese and protoporphyrin-loaded hollow mesoporous organosilica nanoparticles, ATX-70 = photosensitive gallium porphyrin complex, Photofrin = sodium porfimer, ppIX = protoporphyrin IX, AlPcTS = chloroaluminium phthalocyanine tetrasulfonate, PAD-S31 = chlorin derivative = 13,17-bis[1-carboxypropionyl] carbamoylethyl-3-ethenyl-8-ethoxyiminoethylidene-7- hydroxy-2,7,12,18-tetramethyl porphyrin sodium, ICG = indocyanine-Green, RB = rose Bengal, (MBs) = microbubbles, RB derivative = rose bengal derivative with minimal photosensitivity, B-TiO2-PEG = PEGylated black titania nanoparticle, Gem = gemcitabine, AlPcS2a = aluminum phthalocyanine disulfonate, Ce6 = Chlorin e6, PTX MSN = paclitaxel loaded mesoporous silica nanoparticles with folic acid functionalised β-cyclodextrin coating. DOX/Mn-TPPS = Doxorubicin and meso-tetra (4-sulphonatephenyl) porphyrinate manganese (III) complex loaded red blood cell carrier system.

Appendix B. Biotinylation of dextran IONPs

Dextran-coated IONPs were modified to have pegylated biotin anchors on their surface in order to functionalise biotinylated microbubbles for magnetic targeting with an avidin bridge.

B.1. Materials

Hydrochloric acid, 4-methylmorpholine (NMM) and 4-(4,6-dimethoxy-1,3,5-triazin-2-yl)-4-methylmorpholinium chloride (DMTMM) were purchased from Sigma Aldrich Ltd. (Gillingham, Dorset, UK). N-biotin-tetra(ethylene glycol)-diamine (Biotin-TEG-NH2·TFA) was obtained from Iris Biotech GmbH (Marktredwitz, Germany). IONPs coated with carboxymethyl dextran were purchased as FluidMAG-CMX (50 nm hydrodynamic diameter) from Chemicell GmbH (Berlin, Germany).

B.2. Methods

To a solution of biotin-TEG-NH_2 (22 mg, 50 µmol) in 0.5 mL of 0.3 M NMM buffer (pH 8) were added 0.5 mL of a 25 mg /mL solution of dextran-IONP (~5 µmol COOH) and DMTMM chloride (14 mg, 50 µmol) in this order. The reaction was shaken at 800 rpm at 23°C for 24 hours. The functionalised particles were then isolated by washing with MilliQ water by six cycles of 20-fold concentration followed by dilution to the original volume in Millipore Amicon Ultra 0.5 mL centrifugal filters (MWCO 100 kDa, 10 mins, 14000 g) to remove buffer and unbound reagents.

B.3. Characterisation and results

The product of this reaction was characterised pre- and post-cleaning by dynamic light scattering (DLS, Zetasizer Nano-ZS, Malvern Instruments Ltd. Worcestershire, UK) and transmission electron microscopy (TEM, FEI Tecnai 12) to obtain nanoparticle size and morphology (**Appendix Figure B.1**). The hydrodynamic diameter of the nanoparticles post-cleaning was found to be 51 nm with a PDI of 0.182 ± 0.006.

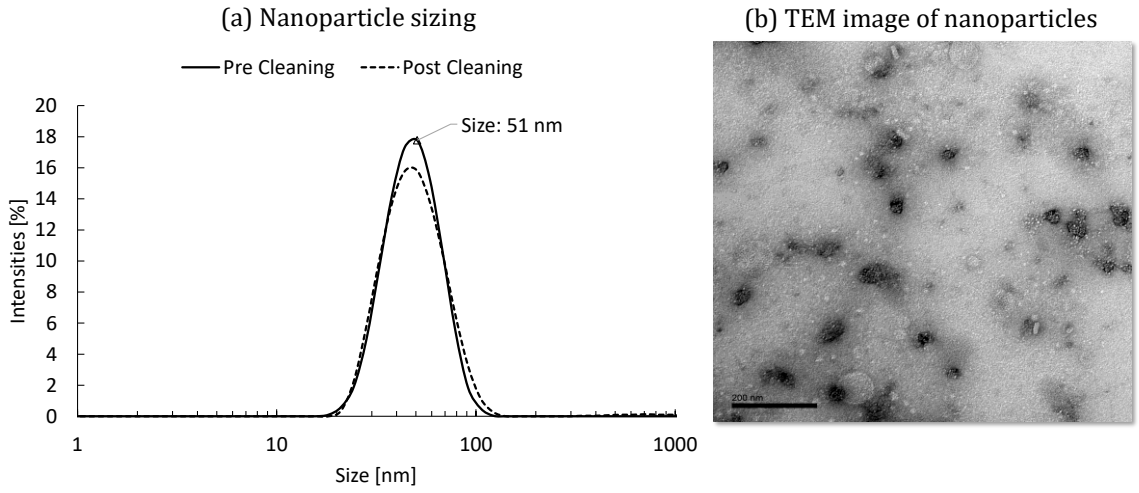

Appendix Figure B.1. (a) *Dynamic light scattering measurements of biotinylated dextran IONPs pre- and post- centrifugal cleaning, and* ***(b)*** *TEM images of the nanoparticles were obtained by negatively staining samples with 2% w/v uranyl acetate, and imaging them at 120 kV.*

Appendix C. Device calibrations

C.1. Standalone tank with built-in transducer

Transmitted pressures were computed for the transducer (Imasonic MR compatible transducer, Ø = 40 mm, ROC = 120 mm) at the bottom of the tank depicted in **Appendix Figure C.1**. Measurements were done along the indicated axes relevant for a sample positioned at z = 31 mm. Some of the measurements were provided by Dr. Michael Gray.

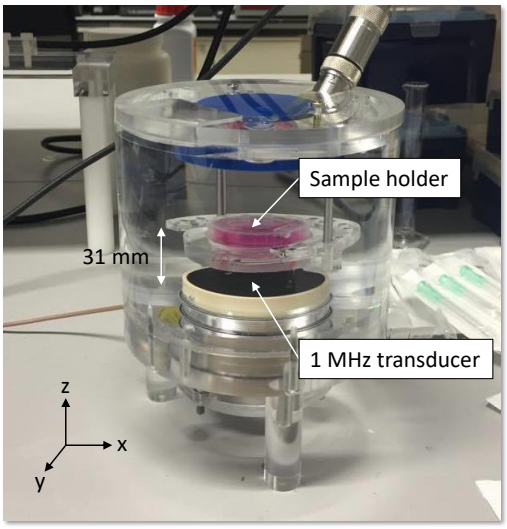

Appendix Figure C.1. *Picture of the tank with built-in transducer indicating the axis referred to in the pressure scans results.*

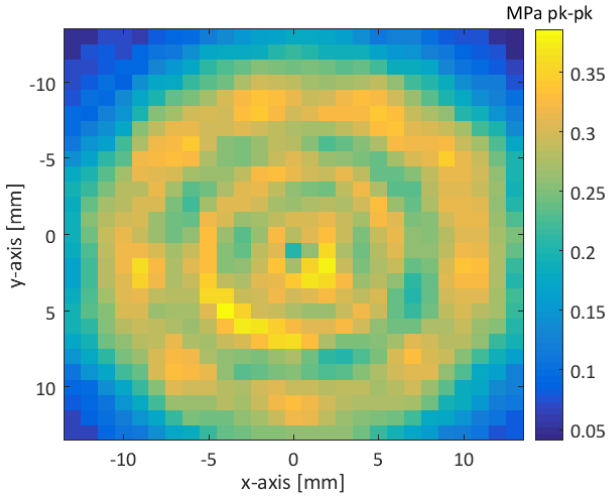

Appendix Figure C.2. *Planar pressure map, z = 31 mm, frequency of 1 MHz, voltage input 44 V_{pp}.*

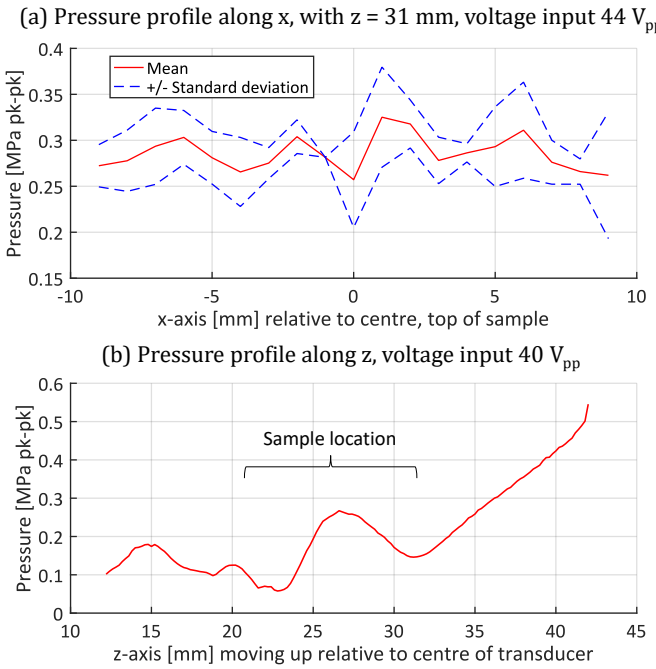

Appendix Figure C.3. *Pressure along* ***(a)*** *x, with z = 31 mm and input voltage of 44 V_{pp}, n = 3 lines over 18 mm were analysed, and* ***(b)*** *z, moving up relative to the centre of the transducer, with input voltage of 40 V_{pp}. A frequency of 1 MHz was used.*

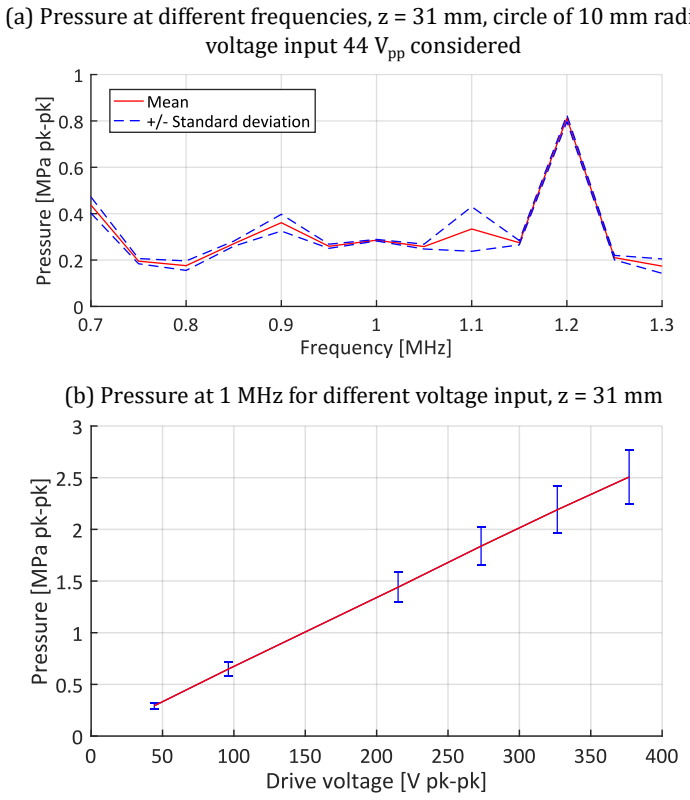

Appendix Figure C.4. *Pressure at z = 31 mm* ***(a)*** *for a range of frequencies* ***(b)*** *for a range of input voltage (power ramp) with a frequency of 1 MHz. n = 3 lines over 20 mm were analysed.*

C.2. Sonidel SP100 1 MHz transducer

The 1 MHz transducer (Sonidel Limited SP100, Ø = 16 mm) pictured in **Appendix Figure C.5** was characterised using a ONDA 1214 needle hydrophone with pre-amplifier and high 20 dB gain along the indicated axes.

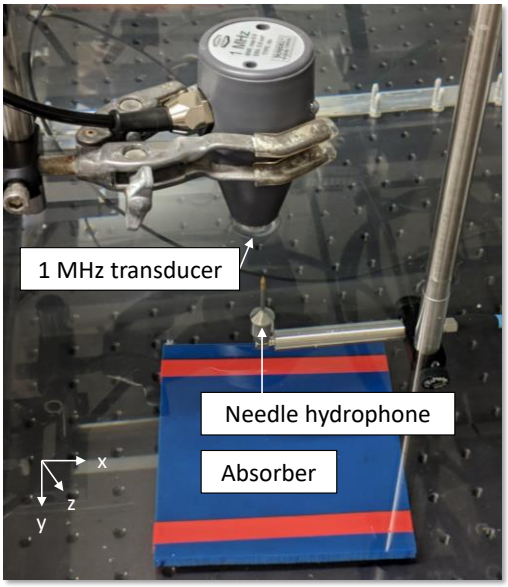

Appendix Figure C.5. *Picture of the 1 MHz transducer with axis referred to in pressure scans.*

(a) Planar x-y pressure field, z = 6 mm

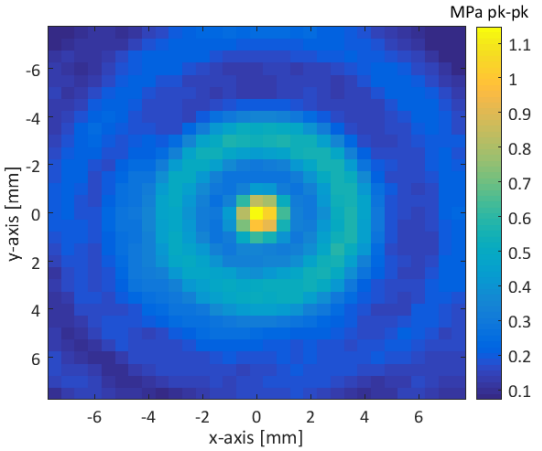

(b) Lateral planar x-z pressure field

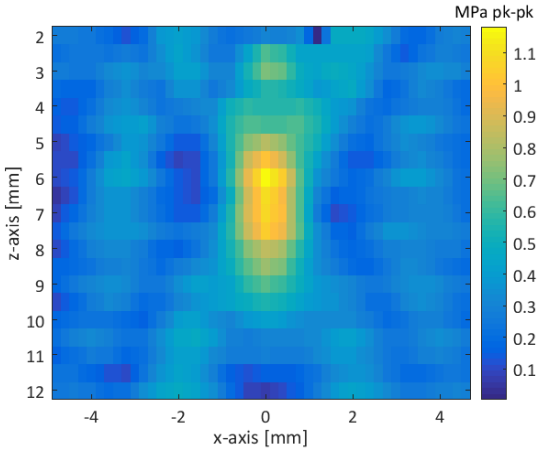

Appendix Figure C.6. *Pressure map* ***(a)*** *planar over x-y at z = 6 mm,* ***(b)*** *lateral over x-z. Sonidel intensity of 3.5 W/cm².*

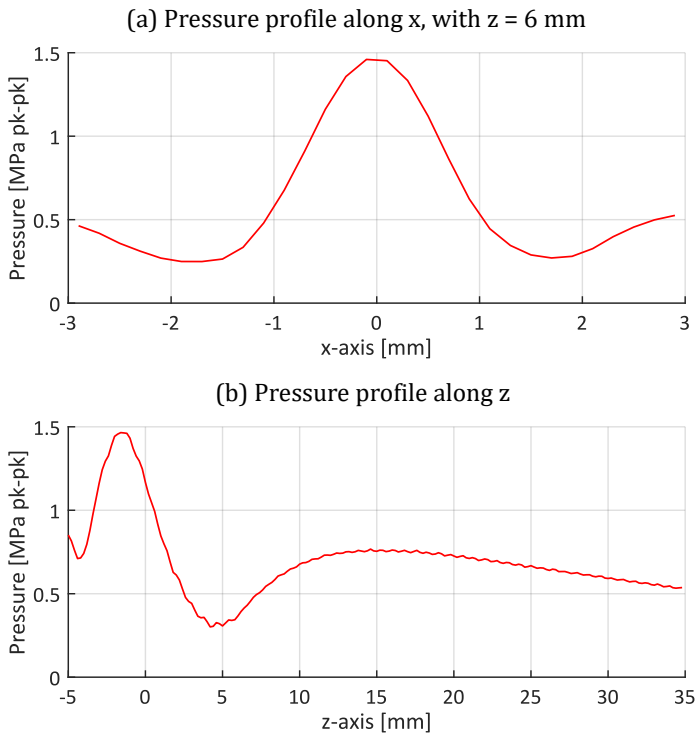

Appendix Figure C.7. *Pressure along* ***(a)*** *x, with z = 6 mm and* ***(b)*** *z moving down relative to the centre of the transducer. Sonidel intensity of 3.5 W/cm².*

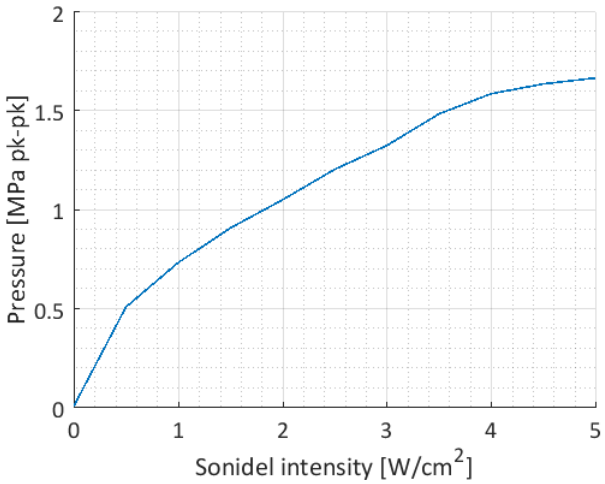

Appendix Figure C.8. *Power ramp at z = 6 mm for increasing Sonidel input intensity (spatial average temporal peak).*

C.3. Magnetic acoustic device

The magnetic acoustic device described in [303] shown the magnetic and acoustic results shown in **Appendix Figure C.9**. The focus of the acoustic field is located 10 mm away from the leading edge of the device. In this work, however, the MAD was used with a gelwax coupling cone of 6 mm in length to enable the treatment of subcutaneous tumours in the *in vivo* study. Thus, the device was measured once more to determine the effect of the coupling cone of the acoustic field. This data was acquired by Dr. Michael Gray and the results are presented in **Appendix Figure C.10** demonstrating an unchanged ultrasound focus for the MAD with and without coupling cone.

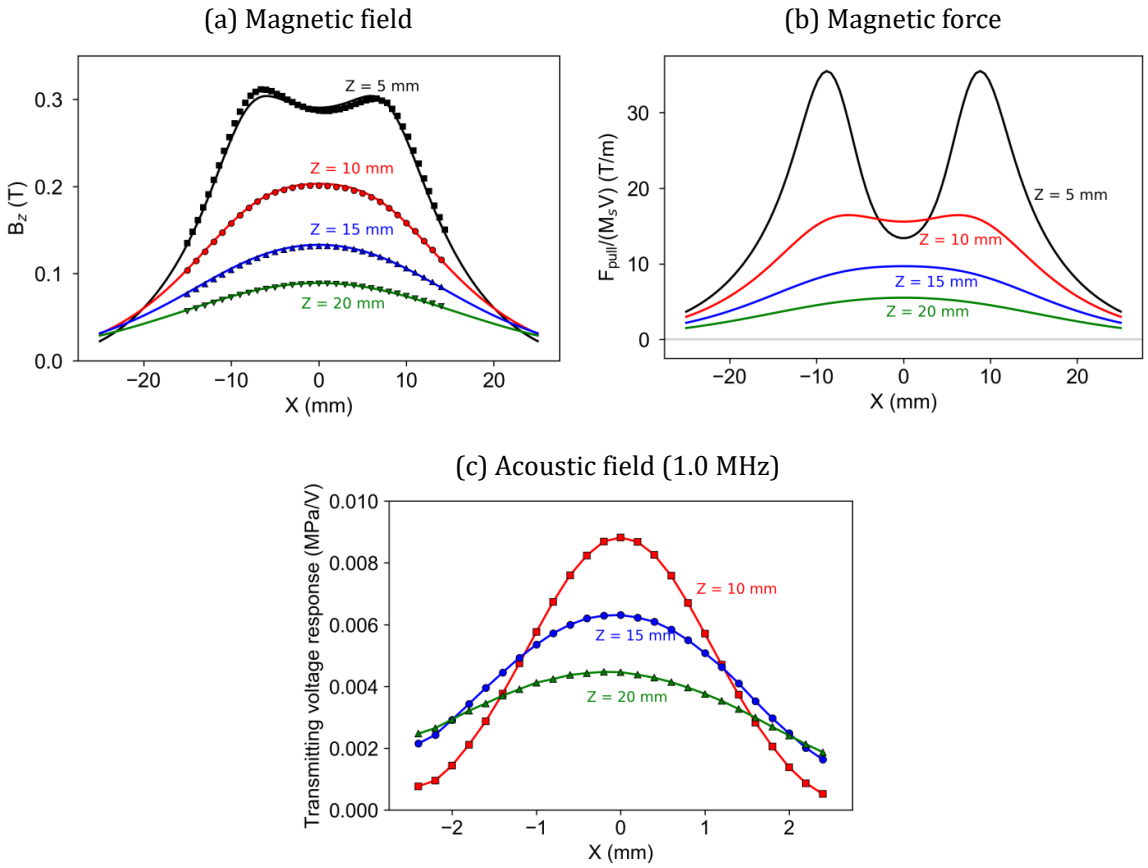

Appendix Figure C.9. *The magnetic acoustic device characterised over several depths for its* ***(a)*** *magnetic field,* ***(b)*** *magnetic force, and* ***(c)*** *acoustic field at 1 MHz. Figures reproduced from* [303].

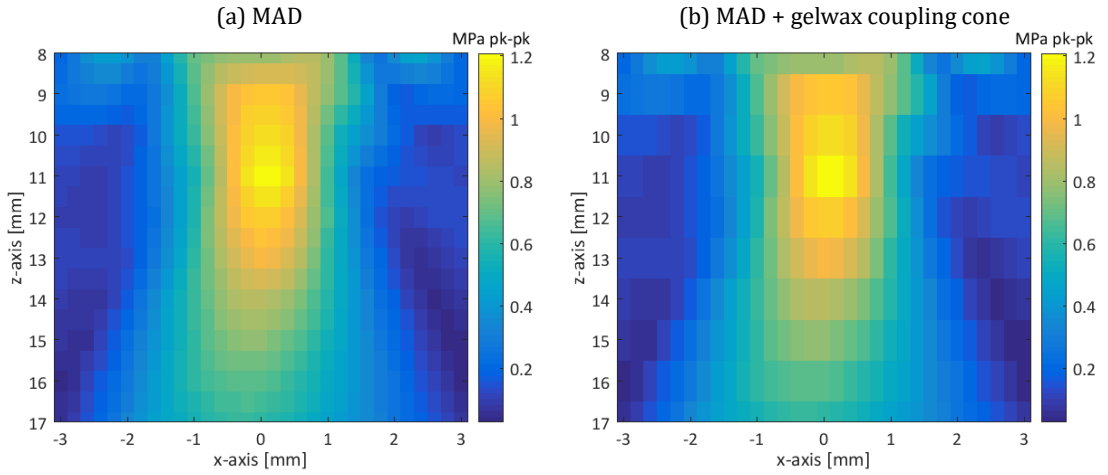

Appendix Figure C.10. *Lateral pressure scan over x-z for the* ***(a)*** *magnetic acoustic device as presented in* [303] *and* ***(b)*** *magnetic acoustic device with gelwax coupling cone. Driving voltage of 100* V_{pp}*, frequency of 1.17 MHz.*

Appendix D. Additional passive cavitation data

The duty cycle was varied for the ultrasound exposure of Rose Bengal and SOSG in degassed PBS ± oxygen microbubbles. Due to limitations of the TiePie Handyscope HS3 however, the acoustic emissions could only be recorded for the 10 and 30% duty cycles. Although no conclusion could be drawn from these preliminary results, the available data are reported in **Appendix Figure D.1** for completeness alongside the percent change in the SOSG fluorescence intensity induced by the exposure conditions.

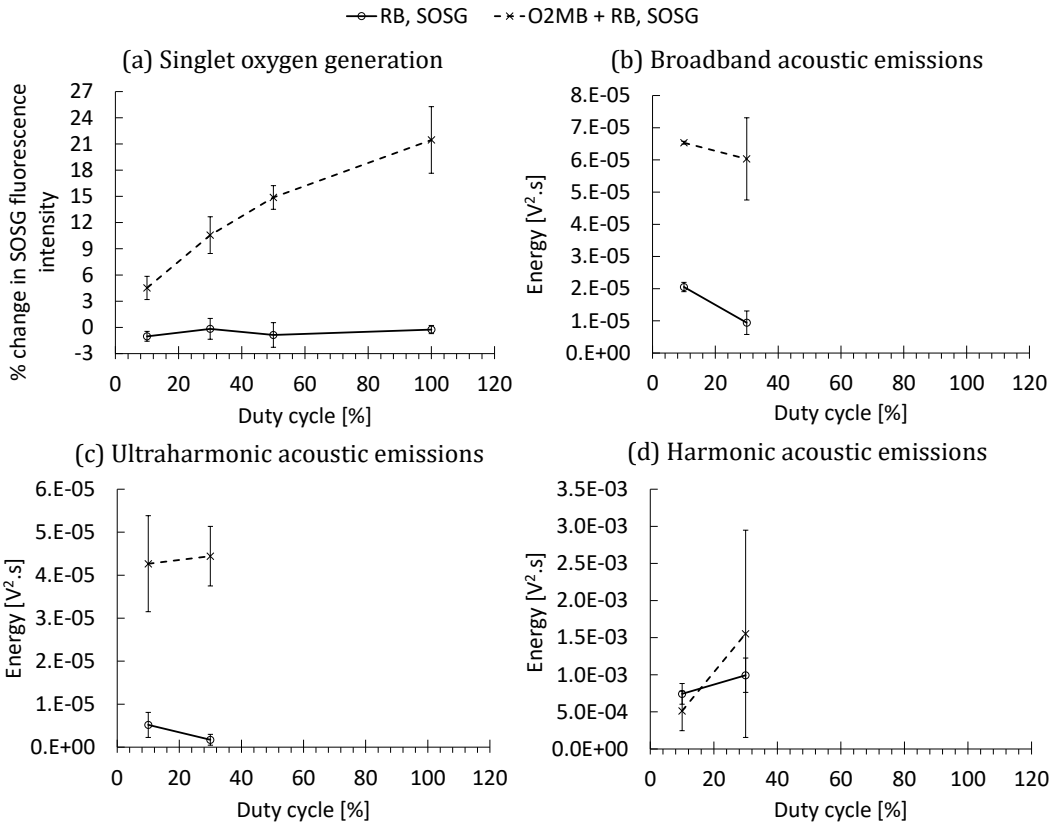

Appendix Figure D.1. *Additional PCD data on the effect of increasing ultrasound duty cycle [%] on the activation of Rose Bengal* ***(a)*** *determined by the generation of singlet oxygen, and the energy associated with* ***(b)*** *broadband,* ***(c)*** *ultraharmonic, and* ***(d)*** *harmonic acoustic emissions computed for the entire exposure time for 10 and 30% DC. Other parameters were: f = 1 MHz, PRF = 100 Hz, P = 1.4 MPa$_{pkpk}$, total number of cycles = 9x10^6. The samples were prepared (n = 3) in degassed PBS with 1.25 µM SOSG, 2.5 µM RB, ± 5x10^7 MB/mL.*

Similarly, while changing the pulse repetition frequency from 20 to 120 Hz only the acoustic emissions from 40 to 120 Hz PRF could be recorded. Nonetheless, the available results reported in **Appendix Figure D.2** did not demonstrate significant change in energy over these parameters and the activation of Rose Bengal with or without the presence of microbubbles did not appear affected by these changes in parameters based on the fluorescence intensity change of SOSG.

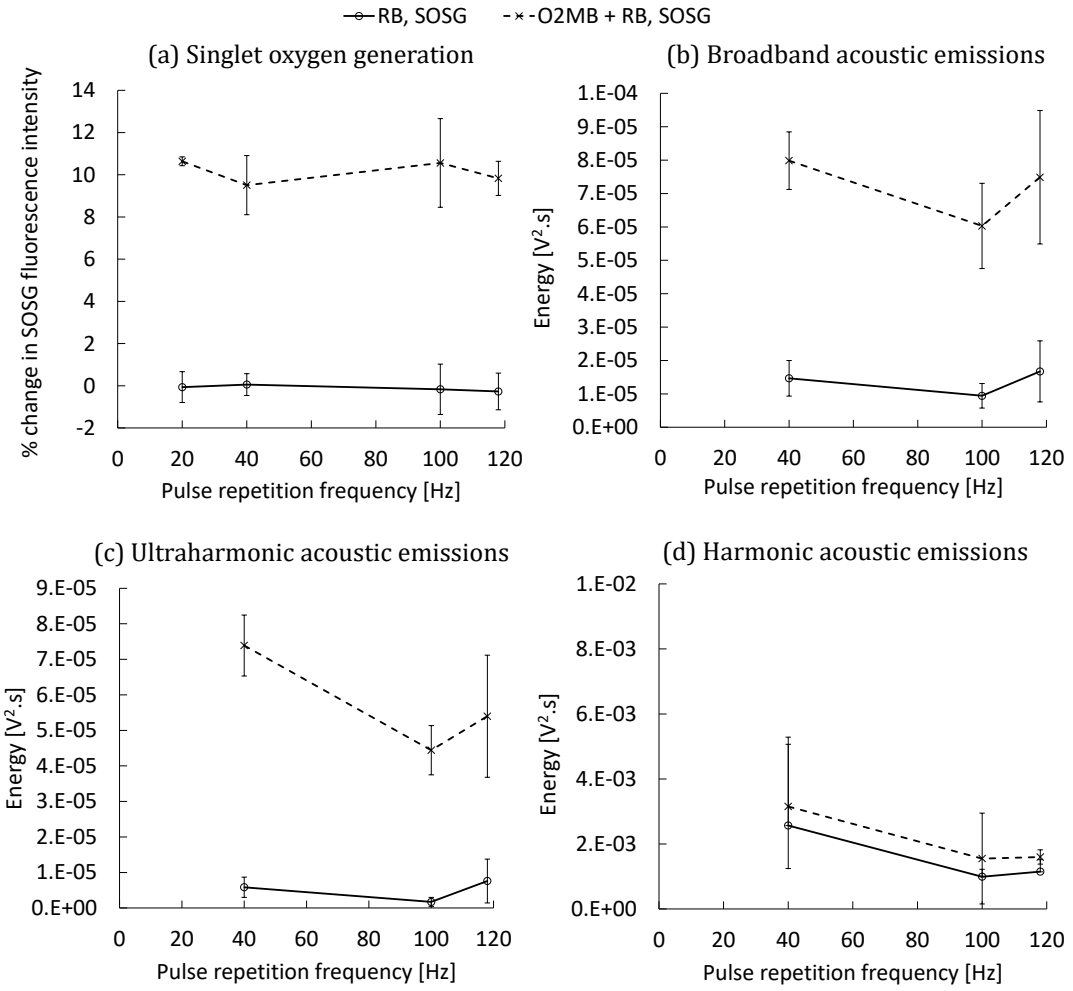

Appendix Figure D.2. *Additional PCD data on the effects of increasing ultrasound pulse repetition frequency [Hz] on the activation of Rose Bengal* ***(a)*** *determined by the generation of singlet oxygen, and the energy associated with* ***(b)*** *broadband,* ***(c)*** *ultraharmonic, and* ***(d)*** *harmonic acoustic emissions computed for the entire exposure time for 40 to 118 Hz PRF. The constant ultrasound parameters were: f = 1 MHz, DC = 30%, P = 1.4 MPa$_{pk-pk}$, t = 30 s, total number of cycles = 9x10^6. The samples were prepared (n = 3) in degassed PBS with 1.25 µM SOSG, 2.5 µM RB, ± 5x10^7 MB/mL.*

Appendix E. Absorbance standard curves

Absorbance standard curves were acquired on a FLUOstar Omega multi-purpose plate reader from BMG Labtech (Aylesbury, Bucks, UK) for the several dyes considered in this thesis.

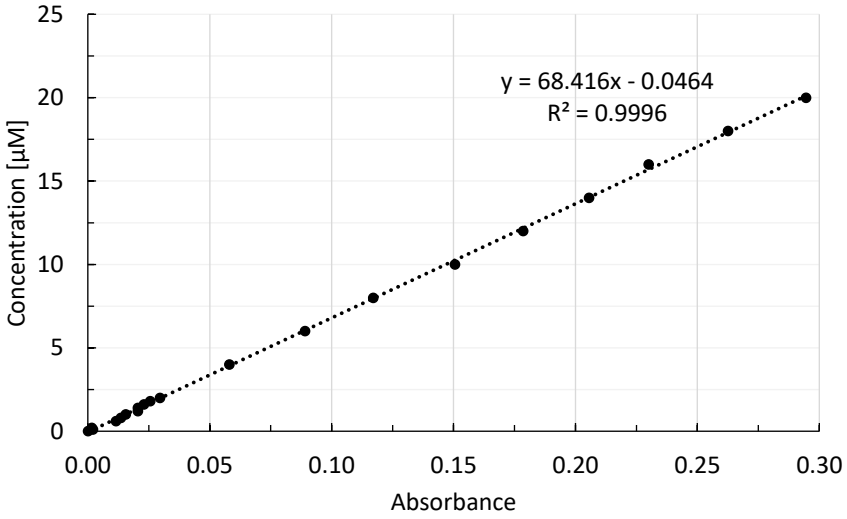

Appendix Figure E.1 *Absorbance standard curve of biotin-Rose Bengal in PBS at 559 nm and 21°C*

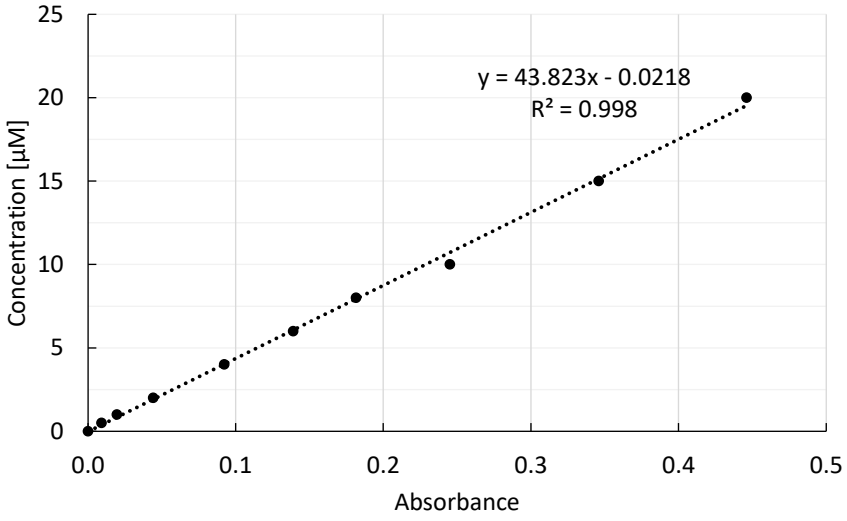

Appendix Figure E.2. *Absorbance standard curve of biotin-Rose Bengal-Gemcitabine in PPG (PBS:propylene glycol:glycerol, 80:10:10 v:v:v) at 559 nm and 21°C.*

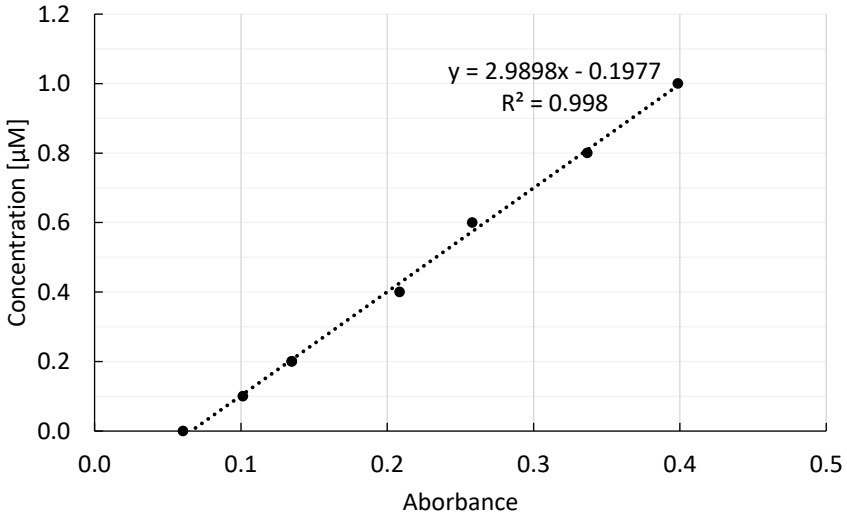

Appendix Figure E.3. *Absorbance standard curve of biotin-Rose Bengal in melted 1.25% agar at 559 nm and 45°C*

References

[1] N. Yumita, R. Nishigaki, K. Umemura, S. -i Umemura, Hematoporphyrin as a Sensitizer of Cell-damaging Effect of Ultrasound, Japanese J. Cancer Res. 80 (1989) 219–222. doi:10.1111/j.1349-7006.1989.tb02295.x.

[2] C. McEwan, H. Nesbitt, D. Nicholas, O.N. Kavanagh, K. McKenna, P. Loan, I.G. Jack, A.P. McHale, J.F. Callan, Comparing the Efficacy of Photodynamic and Sonodynamic Therapy in Non-Melanoma and Melanoma Skin Cancer, Bioorg. Med. Chem. (2016). doi:10.1016/j.bmc.2016.05.015.

[3] H. Wang, Y. Yang, X. Sun, F. Tian, S. Guo, W. Wang, Z. Tian, H. Jin, Z. Zhang, Y. Tian, Sonodynamic therapy-induced foam cells apoptosis activates the phagocytic PPARγ-LXRα-ABCA1/ABCG1 pathway and promotes cholesterol efflux in advanced plaque, Theranostics. 8 (2018) 4969–4984. doi:10.7150/thno.26193.

[4] C. McEwan, J. Owen, E. Stride, C. Fowley, H. Nesbitt, D. Cochrane, C.C. Coussios, M. Borden, N. Nomikou, A.P. McHale, J.F. Callan, Oxygen carrying microbubbles for enhanced sonodynamic therapy of hypoxic tumours., J. Control. Release. 203 (2015) 51–6. doi:10.1016/j.jconrel.2015.02.004.

[5] D. Costley, C. Mc Ewan, C. Fowley, A.P. McHale, J. Atchison, N. Nomikou, J.F. Callan, Treating cancer with sonodynamic therapy: A review, Int. J. Hyperth. 6736 (2015) 1–11. doi:10.3109/02656736.2014.992484.

[6] S.R. McKeown, Defining normoxia, physoxia and hypoxia in tumours—implications for treatment response, Br. J. Radiol. 87 (2014) 20130676. doi:10.1259/bjr.20130676.

[7] S. Umemura, N. Yumita, R. Nishigaki, K. Umemura, Mechanism of Cell Damage by Ultrasound in Combination with Hematoporphyrin, Japanese J. Cancer Res. 81 (1990) 962–966.

[8] I. Rosenthal, J.Z. Sostaric, P. Riesz, Sonodynamic therapy - a review of the synergistic effects of drugs and ultrasound, Ultrason. Sonochem. 11 (2004) 349–363. doi:10.1016/j.ultsonch.2004.03.004.

[9] H. Chen, X. Zhou, Y. Gao, B. Zheng, F. Tang, J. Huang, Recent progress in development of new sonosensitizers for sonodynamic cancer therapy, Drug Discov. Today. 19 (2014) 502–509. doi:10.1016/j.drudis.2014.01.010.

[10] A.P. McHale, J.F. Callan, N. Nomikou, C. Fowley, B. Callan, Sonodynamic Therapy: Concept, Mechanism and Application to Cancer Treatment, in: Ther. Ultrasound, 2016: pp. 429–450. doi:10.1007/978-3-319-22536-4.

[11] H. Tsuru, H. Shibaguchi, M. Kuroki, Y. Yamashita, M. Kuroki, Tumor growth inhibition by sonodynamic therapy using a novel sonosensitizer, Free Radic. Biol. Med. 53 (2012) 464–472. doi:10.1016/j.freeradbiomed.2012.04.025.

[12] C. McEwan, C. Fowley, N. Nomikou, B. McCaughan, A.P. McHale, J.F. Callan, Polymeric microbubbles as delivery vehicles for sensitizers in sonodynamic therapy, Langmuir. 30 (2014) 14926–30. doi:10.1021/la503929c.

[13] M. Prescott, J. Mitchell, S. Totti, J. Lee, E. Velliou, M. Bussemaker, Sonodynamic therapy combined with novel anti-cancer agents, sanguinarine and ginger root extract: Synergistic increase in toxicity in the presence of PANC-1 cells in vitro, Ultrason. Sonochem. (2016) 0–1. doi:10.1016/j.ultsonch.2017.05.018.

[14] M. Maeda, Y. Muragaki, J. Okamoto, S. Yoshizawa, N. Abe, H. Nakamoto, H. Ishii, K.

Kawabata, S. Umemura, N. Nishiyama, K. Kataoka, H. Iseki, Sonodynamic Therapy Based on Combined Use of Low Dose Administration of Epirubicin-Incorporating Drug Delivery System and Focused Ultrasound, Ultrasound Med. Biol. (2017) 1–7. doi:10.1016/j.ultrasmedbio.2017.06.003.

[15] Q. Liu, X. Wang, P. Wang, L. Xiao, Q. Hao, Comparison between sonodynamic effect with protoporphyrin IX and hematoporphyrin on sarcoma 180, Cancer Chemother. Pharmacol. 60 (2007) 671–680. doi:10.1007/s00280-006-0413-4.

[16] M. Roll, The Use of 5-aminolevulinic Acid (ALA) as an Intraoperative Tumor Marker for Resection of Pediatric Central Nervous System (CNS) Tumors, ClinicalTrials.Gov. (2014). https://clinicaltrials.gov/ct2/show/NCT02050243?term=porphyrin&draw=3&rank=20 (accessed November 2, 2018).

[17] L. University College, Treatment of Primary Breast Cancer Using PDT, ClinicalTrials.Gov. (2016). https://clinicaltrials.gov/ct2/show/NCT02872064?term=porphyrin&draw=5&rank=34 (accessed November 2, 2018).

[18] Y. Tian, Sonodynamic Therapy Manipulates Atherosclerosis Regression Trial on Patients With PAD and Claudication, ClinicalTrials.Gov. (2018). https://clinicaltrials.gov/ct2/show/NCT03457662?term=sonodynamic&rank=3 (accessed November 2, 2018).

[19] N. Sugita, Y. Iwase, N. Yumita, Sonodynamically Induced Cell Damage Using Rose Bengal Derivative, Anticancer Res. 30 (2010) 3361–3366.

[20] E. Panzarini, V. Inguscio, B.A. Tenuzzo, L. Dini, In vitro and in vivo clearance of Rose Bengal Acetate- Photodynamic Therapy-induced autophagic and apoptotic cells, Exp. Biol. Med. 238 (2013) 765–778. doi:10.1177/1535370213494552.

[21] C.H. Bastomsky, P.W. Horton, J. Shimmins, Gamma-camera study of the hepato-biliary excretion of 131I-thyroxine-glucuronide and 131I-Rose Bengal in the rat, J. Nucl. Med. (1972) 34–40.

[22] L.A. Sapirstein, A.M. Simpson, Plasma Clearance of Rose Bengal (Tetraiodotetrabromfluorescein), Am. Physiol. (1955).

[23] C.D. Klaassen, Pharmacokinetics of Rose Bengal in the Rat, Rabbit, Dog, and Guinea Pig, Toxicol. Appl. Pharmacol. 38 (1976) 85–100.

[24] Provectus Pharmaceuticals, A Phase 1 Study of PV-10 Chemoablation of Neuroendocrine Tumours (NET) Metastatic to the Liver, ClinicalTrials.Gov. (2016). https://clinicaltrials.gov/ct2/show/NCT02693067?term=rose+bengal&draw=2&rank=2 (accessed November 2, 2018).

[25] R.P.G. Feenstra, S.C.G. Tseng, Comparison of Fluorescein and Rose Bengal Staining, Ophthalmology. 99 (1992) 605–617. doi:10.1016/S0161-6420(92)31947-5.

[26] T.G. Leighton, The Acoustic Bubble, 1994. doi:10.1121/1.410082.

[27] F. Giuntini, F. Foglietta, A.M. Marucco, A. Troia, N. V. Dezhkunov, A. Pozzoli, G. Durando, I. Fenoglio, L. Serpe, R. Canaparo, Insight into ultrasound-mediated reactive oxygen species generation by various metal-porphyrin complexes, Free Radic. Biol. Med. 121 (2018) 190–201. doi:10.1016/j.freeradbiomed.2018.05.002.

[28] V. Misík, P. Riesz, Free radical intermediates in sonodynamic therapy, Ann. N. Y. Acad. Sci. 899 (2000) 335–348.

[29] N. Marinesco, J.J. Trillat, Actions des ultrasons sur les plaques photographiques, Proc. R. Acad. Sci. (1933) 858–860.

[30] K.S. Suslick, S.J. Doktycz, E.B. Flint, On the origin of sonoluminescence and sonochemistry, Ultrasonics. 28 (1990) 280–290. doi:10.1016/0041-624X(90)90033-K.

[31] D.F. Gaitan, L.A. Crum, C.C. Church, R.A. Roy, Sonoluminescence and bubble dynamics for a single, stable, cavitation bubble, J. Acoust. Soc. Am. 91 (1992) 3166–3183.

[32] L.A. Crum, Sonoluminescence, Sonochemistry, and Sonophysics, J. Acoust. Soc. Am. 95

(1994) 559–562. doi:10.1121/1.408351.
[33] T.J. Matula, R.A. Roy, P.D. Mourad, W.B. McNamara, K.S. Suslick, Comparison of multibubble and single-bubble sonoluminescence spectra, Phys. Rev. Lett. 75 (1995) 2602–2605. doi:10.1103/PhysRevLett.75.2602.
[34] W.B. McNamara, Y.T. Didenko, K.S. Suslick, Sonoluminescence temperatures during multi-bubble cavitation, Nature. 401 (1999) 772–775. doi:10.1038/44536.
[35] M.P. Brenner, Single-bubble sonoluminescence, Rev. Mod. Phys. 74 (2002) 425–484.
[36] Y.T. Didenko, K.S. Suslick, The energy efficiency of formation of photons, radicals and ions during single-bubble cavitation., Nature. 418 (2002) 394–397. doi:10.1038/nature00895.
[37] Y.T. Didenko, W.B. McNamara, K.S. Suslick, Molecular emission from single-bubble sonoluminescence., Nature. 407 (2000) 877–879. doi:10.1038/35038020.
[38] K.S. Suslick, Y. Didenko, M.M. Fang, T. Hyeon, K.J. Kolbeck, W.B. McNamara III, M.M. Mdleleni, M. Wong, Acoustic cavitation and its consequences, Philos. Trans. R. Soc. A. 357 (1999) 335–353. doi:10.1098/rsta.1999.0330.
[39] R.A. Craig, C.P. Mccoy, S.P. Gorman, S. David, R.A. Craig, C.P. Mccoy, S.P. Gorman, D.S. Jones, Photosensitisers – the progression from photodynamic therapy to anti-infective surfaces, Expert Opin. Drug Deliv. 5247 (2016) 85–101. doi:10.1517/17425247.2015.962512.
[40] M.A. Margulis, Sonoluminescence and sonochemical reactions in cavitation fields. A review, Ultrasonics. 23 (1985) 157–169. doi:10.1016/0041-624X(85)90024-1.
[41] G. Vazquez, C. Camara, S. Putterman, K. Weninger, Sonoluminescence : nature's smallest blackbody, Opt. Lett. 26 (2001) 575–577.
[42] W.C. Moss, D.B. Clarke, D.A. Young, Calculated pulse widths and spectra of a single sonoluminescing bubble, Science (80-.). 276 (1997) 1398–1401. doi:10.1126/science.276.5317.1398.
[43] S. Hilgenfeldt, S. Grossmann, D. Lohse, A simple explanation of light emission in sonoluminescence, Nature. 398 (1999) 402–405. doi:10.1038/18842.
[44] R. Hiller, K. Weninger, S.J. Putterman, B.P. Barber, Effect of Noble Gas Doping in Single-Bubble Sonoluminescence, Science (80-.). 266 (1994) 3–5.
[45] E.B. Flint, K.S. Suslick, Sonoluminescence from Nonaqueous Liquids: Emission from Small Molecules, J. Am. Chem. Soc. 976 (1989) 6987–6992. doi:10.1021/ja00200a014.
[46] L.S. Bernstein, M.R. Zakin, E.B. Flint, K.S. Suslick, Cavitation thermometry using molecular and continuum sonoluminescence, J. Acoust. Soc. Am. 100 (1996) 2679. doi:10.1121/1.416956.
[47] K.S. Suslick, Sonoluminescence and Sonochemistry, in: Encycl. Phys. Sci. Technol. 3rd Ed., 2001.
[48] D. Srinivasan, L. V. Holroyd, Optical spectrum of the sonoluminescence emitted by cavitated water, J. Appl. Phys. 32 (1961) 449–453. doi:10.1063/1.1736023.
[49] M.A. Beckett, I. Hua, Impact of ultrasonic frequency on aqueous sonoluminescence and sonochemistry, J. Phys. Chem. A. 105 (2001) 3796–3802. doi:10.1021/jp003226x.
[50] M.J.W. Pickworth, P.P. Dendy, T.G. Leighton, A.J. Walton, Studies of the cavitational effects of clinical ultrasound by sonoluminescence: 2. Thresholds for sonoluminescence from a therapeutic ultrasound beam and the effect of temperature and duty cycle, Phys. Med. Biol. 33 (1988) 1249–1260. doi:10.1088/0031-9155/33/11/003.
[51] Sascha Hilgenfeldt Detlef Lohse, W.C. Moss, Water Temperature Dependence of Single Bubble Sonoluminescence, Phys. Rev. Lett. 80 (1998) 1332–1335.
[52] E.B. Flint, K.S. Suslick, The temperature of cavitation, Science (80-.). 253 (1991) 1397–1399. doi:10.1126/science.253.5026.1397.
[53] W.B. McNamara, Y.T. Didenko, K.S. Suslick, Pressure during sonoluminescence, J. Phys. Chem. B. 107 (2003) 7303–7306. doi:10.1021/jp034236b.
[54] N. Miyoshi, T. Igarashi, P. Riesz, Evidence against singlet oxygen formation by sonolysis of

aqueous oxygen-saturated solutions of Hematoporphyrin and Rose Bengal. The mechanism of sonodynamic therapy, Ultrason. Sonochem. 7 (2000) 121–124. doi:10.1016/S1350-4177(99)00042-5.

[55] K. Makino, M. Mossoba, P. Riesz, Chemical effects of ultrasound on aqueous solutions. Formation of hydroxyl radicals and hydrogen atoms, J. Phys. …. (1983) 1369–1377. doi:10.1021/j100231a020.

[56] P. Riesz, T. Kondo, Free radical formation induced by ultrasound and its biological implications, Free Radic. Biol. Med. 13 (1992) 247–270. doi:10.1016/0891-5849(92)90021-8.

[57] Q. Hong, J.L. Hardcastle, R.A.J. Mckeown, F. Marken, R.G. Compton, The 20 kHz sonochemical degradation of trace cyanide and dye stuffs in aqueous media, New J. Chem. 23 (1999) 845–849. doi:10.1039/a903990b.

[58] O. Hamdaoui, S. Merouani, Improvement of Sonochemical Degradation of Brilliant Blue R in Water Using Periodate Ions: Implication of Iodine Radicals in the Oxidation Process, Ultrason. Sonochem. (2017). doi:10.1016/j.ultsonch.2017.01.025.

[59] R. Lall, R. Mutharasan, Y.T. Shah, P. Dhurjati, Decolorization of the dye, Reactive Blue 19, using ozonation, ultrasound, and ultrasound-enhanced ozonation, Water Environ. Res. 75 (1995) 171–9. doi:10.2175/106143003X140953.

[60] M.A. Elsayed, Ultrasonic removal of pyridine from wastewater: optimization of the operating conditions, Appl. Water Sci. 5 (2015) 221–227. doi:10.1007/s13201-014-0182-x.

[61] Y.S. Kim, V. Rubio, J. Qi, R. Xia, Z.Z. Shi, L. Peterson, C.H. Tung, B.E. O'Neill, Cancer treatment using an optically inert Rose Bengal derivative combined with pulsed focused ultrasound, AIP Conf. Proc. 1481 (2012) 175–179. doi:10.1063/1.4757330.

[62] J.F. Turrens, Mitochondrial formation of reactive oxygen species., J. Physiol. 552 (2003) 335–344. doi:10.1113/jphysiol.2003.049478.

[63] S. Saito, Y.-C. Lin, M.-H. Tsai, C.-S. Lin, Y. Murayama, R. Sato, K.K. Yokoyama, Emerging roles of hypoxia-inducible factors and reactive oxygen species in cancer and pluripotent stem cells, Kaohsiung J. Med. Sci. 31 (2015) 279–286. doi:10.1016/j.kjms.2015.03.002.

[64] S.C. Gupta, D. Hevia, S. Patchva, B. Park, W. Koh, B.B. Aggarwal, Upsides and Downsides of Reactive Oxygen Species for Cancer: The Roles of Reactive Oxygen Species in Tumorigenesis, Prevention, and Therapy, Antioxid. Redox Signal. 16 (2012) 1295–1322. doi:10.1089/ars.2011.4414.

[65] E. Gandin, Y. Lion, A. Van de Vorst, Quantum Yield of Singlet Oxygen Production By Xanthene Derivatives, Photochem. Photobiol. 37 (1983) 271–278. doi:10.1111/j.1751-1097.1983.tb04472.x.

[66] C. Lambert, T. Sarna, T.G. Truscott, Rose bengal radicals and their reactivity, J. Chem. Soc. Faraday Trans. 86 (1990) 3879–3882. doi:10.1039/ft9908603879.

[67] M. Niedre, M.S. Patterson, B.C. Wilson, Direct near-infrared luminescence detection of singlet oxygen generated by photodynamic therapy in cells in vitro and tissues in vivo., Photochem. Photobiol. 75 (2002) 382–91. doi:10.1562/0031-8655(2002)0750382DNILDO2.0.CO2.

[68] A.P. Castano, T.N. Demidova, M.R. Hamblin, Mechanism in photodynamic therapy: part two-cellular signaling, cell metabolism and modes of cell death, Photodiagnosis Photodyn. Ther. 2 (2005) 1–23. doi:10.1016/j.pmrj.2014.02.014.Lumbar.

[69] T.I. Rokitskaya, E.A. Kotova, I.I. Agapov, M.M. Moisenovich, Y.N. Antonenko, Unsaturated lipids protect the integral membrane peptide gramicidin A from singlet oxygen, FEBS Lett. 588 (2014) 1590–1595. doi:10.1016/j.febslet.2014.02.046.

[70] M. Morita, Y. Naito, T. Yoshikawa, E. Niki, Plasma lipid oxidation induced by peroxynitrite, hypochlorite, lipoxygenase and peroxyl radicals and its inhibition by antioxidants as assessed by diphenyl-1-pyrenylphosphine, Redox Biol. 8 (2016) 127–135. doi:10.1016/j.redox.2016.01.005.

[71] M. Dellinger, Apoptosis or necrosis following photofrin® photosensitization: Influence of the incubation protocol, Photochem. Photobiol. 64 (1996) 182–187. doi:10.1111/j.1751-1097.1996.tb02440.x.

[72] N.L. Oleinick, R.L. Morris, I. Belichenko, The role of apoptosis in response to photodynamic therapy: What, where, why, and how, Photochem. Photobiol. Sci. 1 (2002) 1–21. doi:10.1039/b108586g.

[73] N. Yumita, Q.S. Han, I. Kitazumi, S.I. Umemura, Sonodynamically-induced apoptosis, necrosis, and active oxygen generation by mono-l-aspartyl chlorin e6, Cancer Sci. 99 (2008) 166–172. doi:10.1111/j.1349-7006.2007.00653.x.

[74] X. Pang, C. Xu, Y. Jiang, Q. Xiao, A.W. Leung, Natural products in the discovery of novel sonosensitizers, Pharmacol. Ther. (2015). doi:10.1016/j.pharmthera.2015.12.004.

[75] M. Trendowski, The promise of sonodynamic therapy, Cancer Metastasis Rev. 33 (2014) 143–160. doi:10.1007/s10555-013-9461-5.

[76] M. Trendowski, Using the Promise of Sonodynamic Therapy in the Clinical Setting against Disseminated Cancers, Chemother. Res. Pract. 2015 (2015) 1–16. doi:10.1155/2015/316015.

[77] X. Liu, S. Li, M. Wang, Z. Dai, Current Status and Future Perspectives of Sonodynamic Therapy and Sonosensitiers, Asian Pacific J. Cancer Prev. 16 (2015) 4489–4492.

[78] J.I.T. Nofiele, R. Karshafian, M. Furukawa, A. Al Mahrouki, A. Giles, S. Wong, G.J. Czarnota, Ultrasound-Activated Microbubble Cancer Therapy: Ceramide Production Leading to Enhanced Radiation Effect in vitro, Technol. Cancer Res. Treat. 12 (2012). doi:10.7785/tcrt.2012.500253.

[79] M. Kuroki, K. Hachimine, H. Abe, H. Shibaguchi, M. Kuroki, S. Maekawa, J. Yanagisawa, T. Kinugasa, T. Tanaka, Y. Yamashita, Sonodynamic therapy of cancer using novel sonosensitizers, Anticancer Res. 27 (2007) 3673–3678.

[80] M.-Y. Liou, P. Storz, Reactive oxygen species in cancer, Free Radic Res. 44 (2010). doi:10.3109/10715761003667554.Reactive.

[81] M.P. Murphy, How mitochondria produce reactive oxygen species, Biochem. J. 417 (2009) 1–13. doi:10.1042/BJ20081386.

[82] Y. Huang, Z. Qiu, Y. Yang, C. Liu, L. Sun, Study of Cell Death Induced by Cell Membrane Localized Sonodynamic Therapy, IEEE Int. Ultrason. Symp. Proc. (2015) 6–9.

[83] D. Kessel, M.G.H. Vicente, J.J. Reiners, Initiation of apoptosis and autophagy by photodynamic therapy, Autophagy. 2 (2006) 289–290. doi:10.4161/auto.2792.

[84] X. Wang, Q. Liu, Z. Wang, P. Wang, P. Zhao, X. Zhao, L. Yang, Y. Li, Role of autophagy in sonodynamic therapy-induced cytotoxicity in S180 cells, Ultrasound Med. Biol. 36 (2010) 1933–1946. doi:10.1016/j.ultrasmedbio.2010.06.022.

[85] X. Su, P. Wang, S. Yang, K. Zhang, Q. Liu, X. Wang, Sonodynamic therapy induces the interplay between apoptosis and autophagy in K562 cells through ROS, Int. J. Biochem. Cell Biol. 60 (2015) 82–92. doi:10.1016/j.biocel.2014.12.023.

[86] Y. Sheng, E. Beguin, H. Nesbitt, S. Kamila, J. Owen, L.C. Barnsley, B. Callan, C. O'Kane, N. Nomikou, R. Hamoudi, M.A. Taylor, M. Love, P. Kelly, D. O'Rourke, E. Stride, A.P. McHale, J.F. Callan, Magnetically responsive microbubbles as delivery vehicles for targeted sonodynamic and antimetabolite therapy of pancreatic cancer, J. Control. Release. 262 (2017) 192–200. doi:10.1016/j.jconrel.2017.07.040.

[87] M. Hockel, P. Vaupel, Tumor Hypoxia : Definitions and Current Clinical Biologic, and Molecular Aspects, J. Natl. Cancer Inst. 93 (2001) 266–276.

[88] S. Rockwell, I.T. Dobrucki, E.Y. Kim, S.T. Marrison, V.T. Vu, Hypoxia and radiation therapy: past history, ongoing research, and future promise, Curr. Mol. Med. 9 (2009) 442–458. doi:10.2174/156652409788167087.

[89] R. Greger, U. Windhorst, Blood, Plasma Proteins, Coagulation, Fibrinolysis, and Thrombocyte Function, in: Compr. Hum. Physiol., 1996: pp. 1651–1659.

[90] F.B. Jensen, The dual roles of red blood cells in tissue oxygen delivery: oxygen carriers and regulators of local blood flow, J. Exp. Biol. 212 (2009) 3387–3393. doi:10.1242/jeb.023697.
[91] A.S. Popel, Theory of oxygen transport to tissue, Crit. Rev. Biotechnol. 17 (1989) 257–321. doi:10.1126/scisignal.274pe36.Insulin.
[92] R. Wheeler, Hemoglobin created with en:pymol from en:PDB enzyme 1GZX, Wikipedia. (2007). https://commons.wikimedia.org/wiki/File:1GZX_Haemoglobin.png (accessed December 15, 2018).
[93] Smokefoot, Oxygenation of heme protein, Wikipedia2. (2017). https://commons.wikimedia.org/wiki/File:Mboxygenation.png (accessed December 15, 2018).
[94] R.N. Pittman, Oxygen Gradients in the Microcirculation, Acta Physiol. 202 (2011) 311–322. doi:10.1152/physrev.00034.2002.
[95] R.N. Pittman, Oxygen Transport in the Microcirculation and Its Regulation, Microcirculation. 20 (2013) 117–137. doi:10.1111/micc.12017.
[96] J.M. Brown, W.R. Wilson, Exploiting tumour hypoxia in cancer treatment., Nat. Rev. Cancer. 4 (2004) 437–47. doi:10.1038/nrc1367.
[97] Y. Cai, J. Zhang, J. Wu, Z.Y. Li, Oxygen transport in a three-dimensional microvascular network incorporated with early tumour growth and preexisting vessel cooption: Numerical simulation study, Biomed Res. Int. 2015 (2015). doi:10.1155/2015/476964.
[98] A. Carreau, B. El Hafny-Rahbi, A. Matejuk, C. Grillon, C. Kieda, Why is the partial oxygen pressure of human tissues a crucial parameter? Small molecules and hypoxia, J. Cell. Mol. Med. 15 (2011) 1239–1253. doi:10.1111/j.1582-4934.2011.01258.x.
[99] J.J. Kwan, M. Kaya, M.A. Borden, P.A. Dayton, Theranostic oxygen delivery using ultrasound and microbubbles, Theranostics. 2 (2012) 1174–1184. doi:10.7150/thno.4410.
[100] S.M. Fix, M. a. Borden, P. a. Dayton, Therapeutic gas delivery via microbubbles and liposomes, J. Control. Release. 209 (2015) 139–149. doi:10.1016/j.jconrel.2015.04.027.
[101] J. Mathieu, W. Zhou, Y. Xing, H. Sperber, A. Ferreccio, Z. Agoston, K.T. Kuppusamy, R.T. Moon, H. Ruohola-Baker, Hypoxia-inducible factors have distinct and stage-specific roles during reprogramming of human cells to pluripotency, Cell Stem Cell. 14 (2014) 592–605. doi:10.1016/j.stem.2014.02.012.
[102] M. Mimeault, S.K. Batra, Hypoxia-inducing factors as master regulators of stemness properties and altered metabolism of cancer- and metastasis-initiating cells, J. Cell. Mol. Med. 17 (2013) 30–54. doi:10.1111/jcmm.12004.
[103] Y. Kim, Q. Lin, P.M. Glazer, Z. Yun, Hypoxic tumor microenvironment and cancer cell differentiation, Curr. Mol. Med. 9 (2009) 425–34. http://www.pubmedcentral.nih.gov/articlerender.fcgi?artid=2824923&tool=pmcentrez&rendertype=abstract.
[104] S.M. Grist, L. Chrostowski, K.C. Cheung, Optical Oxygen Sensors for Applications in Microfluidic Cell Culture, Sensors. 10 (2010) 9286–9316. doi:10.3390/s101009286.
[105] S. Badger, J. Brant, J.C. McClements, M. Loughrey, M. Taylor, T. Diamond, L. McKie, The role of surgery for pancreatic cancer: a 12-year review of patient outcome, Ulster Med J. 79 (2010) 70–75. www.ums.ac.uk.
[106] I. Garrido-Laguna, M. Hidalgo, Pancreatic cancer: from state-of-the-art treatments to promising novel therapies, Nat. Rev. Clin. Oncol. 12 (2015) 319–334. doi:10.1038/nrclinonc.2015.53.
[107] J. Li, M.G. Wientjes, J.L.-S. Au, Pancreatic cancer: pathobiology, treatment options, and drug delivery., AAPS J. 12 (2010) 223–232. doi:10.1208/s12248-010-9181-5.
[108] H. Tajima, I. Makino, Y. Ohbatake, S. Nakanuma, H. Hayashi, H. Nakagawara, T. Miyashita, H. Takamura, T. Ohta, Neoadjuvant chemotherapy for pancreatic cancer: Effects on cancer tissue and novel perspectives, Oncol. Lett. 13 (2017) 3975–3981. doi:10.3892/ol.2017.6008.

[109] M.H.G. Katz, P.W.T. Pisters, D.B. Evans, C.C. Sun, J.E. Lee, J.B. Fleming, J.N. Vauthey, E.K. Abdalla, C.H. Crane, R.A. Wolff, G.R. Varadhachary, R.F. Hwang, Borderline Resectable Pancreatic Cancer: The Importance of This Emerging Stage of Disease, J. Am. Coll. Surg. 206 (2008) 833–846. doi:10.1016/j.jamcollsurg.2007.12.020.

[110] M. Tachezy, F. Gebauer, C. Petersen, D. Arnold, M. Trepel, K. Wegscheider, P. Schafhausen, M. Bockhorn, J.R. Izbicki, E. Yekebas, Sequential neoadjuvant chemoradiotherapy (CRT) followed by curative surgery vs. primary surgery alone for resectable, non-metastasized pancreatic adenocarcinoma: NEOPA- a randomized multicenter phase III study (NCT01900327, DRKS00003893, ISRCTN82191749), BMC Cancer. 14 (2014) 1–9. doi:10.1186/1471-2407-14-411.

[111] P. Cabrales, M. Intaglietta, Blood Substitutes: Evolution From Non-Carrying To Oxygen and Gas Carrying Fluids, ASAIO K. 59 (2013) 337–354. doi:10.1097/MAT.0b013e318291fbaa.

[112] I. Moen, L.E.B. Stuhr, Hyperbaric oxygen therapy and cancer—a review, Target. Oncol. 7 (2012) 233–242. doi:10.1007/s11523-012-0233-x.

[113] J. Varlotto, M.A. Stevenson, Anemia, tumor hypoxemia, and the cancer patient, Int. J. Radiat. Oncol. Biol. Phys. 63 (2005) 25–36. doi:10.1016/j.ijrobp.2005.04.049.

[114] C. Plafki, P. Peters, M. Almeling, W. Welslau, R. Busch, Complications and side effects of hyperbaric oxygen therapy, Aviat Sp. Env. Med. 71 (2000) 119–124. http://www.ncbi.nlm.nih.gov/entrez/query.fcgi?cmd=Retrieve&db=PubMed&dopt=Citation&list_uids=10685584.

[115] T. Henkel-Hanke, M. Oleck, Artificial Oxygen Carriers - A Current Review, Am. Assoc. Nurse Anesth. 75 (2007) 205–211. http://www.aana.com/newsandjournal/documents/henkelhanke205-211.pdf (accessed June 10, 2015).

[116] Z. Tao, P.P. Ghoroghchian, Microparticle, nanoparticle, and stem cell-based oxygen carriers as advanced blood substitutes, Trends Biotechnol. 32 (2014) 466–473. doi:10.1016/j.tibtech.2014.05.001.

[117] A. Paciello, G. Amalfitano, A. Garziano, F. Urciuolo, P.A. Netti, Hemoglobin-Conjugated Gelatin Microsphere as a Smart Oxygen Releasing Biomaterial, Adv. Healthc. Mater. (2016). doi:10.1002/adhm.201600559.

[118] S. Wang, F. Yuan, K. Chen, G. Chen, K. Tu, H. Wang, L.-Q. Wang, Synthesis of hemoglobin conjugated polymeric micelle: a ZnPc carrier with oxygen self-compensating ability for photodynamic therapy, Biomacromolecules. (2015) 150724130703006. doi:10.1021/acs.biomac.5b00571.

[119] J.G. Riess, M.P. Krafft, Fluorinated materials for in vivo oxygen transport (blood substitutes), diagnosis and drug delivery, Biomaterials. 19 (1998) 1529–1539. doi:10.1016/S0142-9612(98)00071-4.

[120] M.P. Krafft, Fluorocarbons and fluorinated amphiphiles in drug delivery and biomedical research, Adv. Drug Deliv. Rev. 47 (2001) 209–228. doi:10.1016/S0169-409X(01)00107-7.

[121] J. Owen, P. Bovornchutichai, C. McEwan, J. Callan, M. Borden, R. Averre, H. Nesbitt, E. Stride, Reducing Tumour Hypoxia via Oral Administration of Oxygen Nanobubbles, Cancer Res. (2016) 2–13. doi:10.1371/journal.pone.0168088.

[122] M.A. Borden, M.L. Longo, Dissolution behavior of lipid monolayer-coated, air-filled microbubbles: Effect of lipid hydrophobic chain length, Langmuir. 18 (2002) 9225–9233. doi:10.1021/la026082h.

[123] M.A. Borden, M.L. Longo, Oxygen Permeability of Fully Condensed Lipid Monolayers, J Phys Chem B. 108 (2004) 6009–6016. doi:10.1021/jp037815p.

[124] L. Mullin, R. Gessner, J. Kwan, M. Kaya, M.A. Borden, P.A. Dayton, Effect of anesthesia carrier gas on in vivo circulation times of ultrasound microbubble contrast agents in rats, Contrast Media Mol. Imaging. 6 (2011) 126–131. doi:10.1002/cmmi.414.

[125] M. Schneider, Characteristics of SonoVue™, Echocardiography. 16 (1999) 743–746.

doi:10.1111/j.1540-8175.1999.tb00144.x.

[126] N. Matsuki, S. Ichiba, T. Ishikawa, O. Nagano, M. Takeda, Y. Ujike, T. Yamaguchi, Blood oxygenation using microbubble suspensions, Eur. Biophys. J. 41 (2012) 571–578. doi:10.1007/s00249-012-0811-y.

[127] Y. Sheng, H. Nesbitt, B. Callan, M.A. Taylor, M. Love, A.P. McHale, J.F. Callan, Oxygen generating nanoparticles for improved photodynamic therapy of hypoxic tumours, J. Control. Release. (2017). doi:10.1016/j.jconrel.2017.09.004.

[128] T. Lin, X. Zhao, S. Zhao, H. Yu, W. Cao, W. Chen, H. Wei, H. Guo, O2-generating MnO2 nanoparticles for enhanced photodynamic therapy of bladder cancer by ameliorating hypoxia, Theranostics. 8 (2018) 990–1004. doi:10.7150/thno.22465.

[129] L. Yu, Y. Chen, H. Chen, H2O2-responsive theranostic nanomedicine, Chinese Chem. Lett. (2017). doi:10.1016/j.cclet.2017.05.023.

[130] D. Cosgrove, Ultrasound contrast agents: An overview, Eur. J. Radiol. 60 (2006) 324–330. doi:10.1016/j.ejrad.2006.06.022.

[131] L.J.M. Juffermans, P.A. Dijkmans, R.J.P. Musters, C.A. Visser, O. Kamp, Transient permeabilization of cell membranes by ultrasound-exposed microbubbles is related to formation of hydrogen peroxide, Am J Physiol Hear. Circ Physiol. 291 (2006) H1595-601. doi:01120.2005 [pii]\r10.1152/ajpheart.01120.2005.

[132] L.J.M. Juffermans, A. van Dijk, C.A.M. Jongenelen, B. Drukarch, A. Reijerkerk, H.E. de Vries, O. Kamp, R.J.P. Musters, Ultrasound and Microbubble-Induced Intra- and Intercellular Bioeffects in Primary Endothelial Cells, Ultrasound Med. Biol. 35 (2009) 1917–1927. doi:10.1016/j.ultrasmedbio.2009.06.1091.

[133] M.C. Cochran, J. Eisenbrey, R.O. Ouma, M. Soulen, M.A. Wheatley, Doxorubicin and paclitaxel loaded microbubbles for ultrasound triggered drug delivery, Int. J. Pharm. 414 (2011) 161–170. doi:10.1016/j.ijpharm.2011.05.030.

[134] J. Sun, M. Yin, S. Zhu, L. Liu, Y. Zhu, Z. Wang, R.X. Xu, S. Chang, Ultrasound-mediated destruction of oxygen and paclitaxel loaded lipid microbubbles for combination therapy in hypoxic ovarian cancer cells, Ultrason. Sonochem. 28 (2016) 319–326. doi:10.1016/j.ultsonch.2015.08.009.

[135] C. Niu, Z. Wang, G. Lu, T.M. Krupka, Y. Sun, Y. You, W. Song, H. Ran, P. Li, Y. Zheng, Doxorubicin loaded superparamagnetic PLGA-iron oxide multifunctional microbubbles for dual-mode US/MR imaging and therapy of metastasis in lymph nodes, Biomaterials. 34 (2013) 2307–2317. doi:10.1016/j.biomaterials.2012.12.003.

[136] Y. Li, H. An, X. Wang, P. Wang, F. Qu, Y. Jiao, K. Zhang, Q. Liu, Ultrasound-triggered release of sinoporphyrin sodium from liposome-microbubble complexes and its enhanced sonodynamic toxicity in breast cancer, Nano Res. (2017).

[137] M. a Borden, S. Qin, K.W. Ferrara, Ultrasound Contrast Agents, in: Mol. Imaging Princ. Pract., 2010: pp. 425–444.

[138] J.G. Riess, Highly fluorinated systems for oxygen transport, diagnosis and drug delivery, Colloids Surfaces A Physicochem. Eng. Asp. 84 (1994) 33–48. doi:10.1016/0927-7757(93)02696-C.

[139] M. Lee, E.Y. Lee, D. Lee, B.J. Park, Stabilization and fabrication of microbubbles: applications for medical purposes and functional materials, Soft Matter. 11 (2015) 2067–2079. doi:10.1039/C5SM00113G.

[140] N. De Jong, A. Bouakaz, P. Frinking, Basic acoustic properties of microbubbles, Echocardiography. 19 (2002) 229–240. doi:10.1046/j.1540-8175.2002.00229.x.

[141] J.R. Lindner, Microbubbles in medical imaging: current applications and future directions., Nat. Rev. Drug Discov. 3 (2004) 527–32. doi:10.1038/nrd1417.

[142] E. Stride, N. Saffari, Microbubble ultrasound contrast agents: a review., Proc. Inst. Mech. Eng. H. 217 (2003) 429–47. doi:10.1243/09544110360729072.

[143] S.R. Sirsi, M.A. Borden, Microbubble compositions, properties and biomedical applications,

Bubble Sci Eng Technol. 1 (2009) 3–17. doi:10.1179/175889709X446507.Microbubble.
[144] A. Upadhyay, S. V. Dalvi, G. Gupta, N. Khanna, Effect of PEGylation on performance of protein microbubbles and its comparison with lipid microbubbles, Mater. Sci. Eng. C. (2016). doi:10.1016/j.msec.2016.10.021.
[145] J. Bertolini, The purification of plasma proteins for therapeutic use, in: Ross. Princ. Transfus. Med., 2016: pp. 302–320.
[146] A.W. Appis, M.J. Tracy, S.B. Feinstein, Update on the safety and efficacy of commercial ultrasound contrast agents in cardiac applications, Echo Res. Pract. 2 (2015) R55–R62. doi:10.1530/ERP-15-0018.
[147] B.W. Ninham, K. Larsson, P. Lo Nostro, Two sides of the coin. Part 1. Lipid and surfactant self-assembly revisited, Colloids Surfaces B Biointerfaces. 152 (2017) 326–338. doi:10.1016/j.colsurfb.2017.01.022.
[148] G. Mohamedi, M. Azmin, I. Pastoriza-santos, V. Huang, J. Pe, L.M. Liz-marza, M. Edirisinghe, E. Stride, Effects of Gold Nanoparticles on the Stability of Microbubbles, Langmuir. 28 (2012) 13808–13815.
[149] T. van Rooij, Y. Luan, G. Renaud, A.F.W. van der Steen, M. Versluis, N. de Jong, K. Kooiman, Non-linear Response and Viscoelastic Properties of Lipid-Coated Microbubbles: DSPC versus DPPC, Ultrasound Med. Biol. 41 (2015) 1432–1445. doi:10.1016/j.ultrasmedbio.2015.01.004.
[150] W.Y. Wen, J.A. Muccitelli, Thermodynamics of some perfluorocarbon gases in water, J. Solution Chem. 8 (1979) 225–246. doi:10.1007/BF00648882.
[151] Hazardous Substances Data Bank (HSDB), (n.d.). https://toxnet.nlm.nih.gov/newtoxnet/hsdb.htm (accessed November 6, 2018).
[152] J.L. Bullister, D.P. Wisegarver, F.A. Menzia, The solubility of sulfur hexafluoride in water and seawater, Deep. Res. I. 49 (2002) 175–187. doi:10.1016/S0967-0637(01)00051-6.
[153] T. Park, T.R. Rettich, R. Battino, D. Peterson, E. Wilhelm, Solubility of Gases in Liquids. 14. Bunsen Coefficients for Several Fluorine-Containing Gases (Freons) Dissolved in Water at 298.15 K, J. Chem. Eng. Data. 27 (1982) 324–326. doi:10.1021/je00029a027.
[154] T.R. Rettich, Y.P. Handa, R. Battino, E. Wilhelm, Solubility of gases in liquids. 13. High-precision determination of Henry's constants for methane and ethane in liquid water at 275 to 328 K, J. Phys. Chem. 85 (1981) 3230–3237. doi:10.1021/j150622a006.
[155] B.B. Benson, D. Krause, M.A. Peterson, Solubility and isotopic fractionation of gases in dilute aqueous solution. I. Oxygen, J. Solution Chem. 8 (1979) 655–690.
[156] T.R. Rettich, R. Battino, E. Wilhelm, Solubility of gases in liquids. XVI. Henry's law coefficients for nitrogen in water at 5 to 50°C, J. Solution Chem. 13 (1984) 335–348. doi:10.1007/BF00645706.
[157] E. Unger, T. Porter, J. Lindner, P. Grayburn, Cardiovascular drug delivery with ultrasound and microbubbles, Adv. Drug Deliv. Rev. 72 (2014) 110–126. doi:10.1016/j.addr.2014.01.012.
[158] M. Azmin, G. Mohamedi, M. Edirisinghe, E.P. Stride, Dissolution of coated microbubbles: The effect of nanoparticles and surfactant concentration, Mater. Sci. Eng. C. 32 (2012) 2654–2658. doi:10.1016/j.msec.2012.06.019.
[159] K. Ferrara, R. Pollard, M. Borden, Ultrasound Microbubble Contrast Agents: Fundamentals and Application to Gene and Drug Delivery, Annu. Rev. Biomed. Eng. 9 (2007) 415–447. doi:10.1146/annurev.bioeng.8.061505.095852.
[160] B.D.M. Meijering, L.J.M. Juffermans, A. Van Wamel, R.H. Henning, I.S. Zuhorn, M. Emmer, A.M.G. Versteilen, W.J. Paulus, W.H. Van Gilst, K. Kooiman, N. De Jong, R.J.P. Musters, L.E. Deelman, O. Kamp, Ultrasound and microbubble-targeted delivery of macromolecules is regulated by induction of endocytosis and pore formation, Circ. Res. 104 (2009) 679–687. doi:10.1161/CIRCRESAHA.108.183806.
[161] R. Karshafian, P.D. Bevan, R. Williams, S. Samac, P.N. Burns, Sonoporation by Ultrasound-

Activated Microbubble Contrast Agents: Effect of Acoustic Exposure Parameters on Cell Membrane Permeability and Cell Viability, Ultrasound Med. Biol. 35 (2009) 847–860. doi:10.1016/j.ultrasmedbio.2008.10.013.

[162] K. Kooiman, A.F.W. Van Der Steen, N. De Jong, Role of intracellular calcium and reactive oxygen species in microbubble-mediated alterations of endothelial layer permeability, IEEE Trans. Ultrason. Ferroelectr. Freq. Control. 60 (2013) 1811–1815. doi:10.1109/TUFFC.2013.2767.

[163] I. Skachkov, Y. Luan, A.F.W. Van Der Steen, N. De Jong, K. Kooiman, Targeted microbubble mediated sonoporation of endothelial cells in vivo, IEEE Trans. Ultrason. Ferroelectr. Freq. Control. 61 (2014) 1661–1667. doi:10.1109/TUFFC.2014.006440.

[164] R. Bolaños-Jiménez, M. Rossi, D. Fernandez Rivas, C.J. Kähler, A. Marin, Streaming flow by oscillating bubbles: quantitative diagnostics via particle tracking velocimetry, J. Fluid Mech. 820 (2017) 529–548. doi:10.1017/jfm.2017.229.

[165] P. Qin, T. Han, A.C.H. Yu, L. Xu, Mechanistic understanding the bioeffects of ultrasound-driven microbubbles to enhance macromolecule delivery, J. Control. Release. (2018). doi:10.1016/j.jconrel.2018.01.001.

[166] N. Mizrahi, E.H. Zhou, G. Lenormand, R. Krishnan, D. Weihs, J.P. Butler, D.A. Weitz, J.J. Fredberg, E. Kimmel, Low intensity ultrasound perturbs cytoskeleton dynamics, Soft Matter. 8 (2012) 2438–2443. doi:10.1039/c2sm07246g.

[167] S. Zhang, J. Cheng, Y.X. Qin, Mechanobiological modulation of cytoskeleton and calcium influx in osteoblastic cells by short-term focused acoustic radiation force, PLoS One. 7 (2012) 1–11. doi:10.1371/journal.pone.0038343.

[168] W. Zhong, X. Chen, P. Jiang, J.M.F. Wan, P. Qin, A.C.H. Yu, Induction of Endoplasmic Reticulum Stress by Sonoporation: Linkage to Mitochondria-Mediated Apoptosis Initiation, Ultrasound Med. Biol. 39 (2013) 2382–2392. doi:10.1016/j.ultrasmedbio.2013.08.005.

[169] H. Honda, T. Kondo, Q.-L. Zhao, L.B. Feril, H. Kitagawa, Role of intracellular calcium ions and reactive oxygen species in apoptosis induced by ultrasound., Ultrasound Med. Biol. 30 (2004) 683–692. doi:10.1016/j.ultrasmedbio.2004.02.008.

[170] Y. Luan, G. Lajoinie, E. Gelderblom, I. Skachkov, A.F.W. van der Steen, H.J. Vos, M. Versluis, N. De Jong, Lipid shedding from single oscillating microbubbles, Ultrasound Med. Biol. 40 (2014) 1834–1846. doi:10.1016/j.ultrasmedbio.2014.02.031.

[171] I. De Cock, G. Lajoinie, M. Versluis, S.C. De Smedt, I. Lentacker, Sonoprinting and the importance of microbubble loading for the ultrasound mediated cellular delivery of nanoparticles, Biomaterials. (2016). doi:10.1053/j.gastro.2012.12.021.This.

[172] C. Der Loughian, P. Muleki Seya, C. Pirat, C. Inserra, J.-C. Bera, J.-P. Rieu, Jumping acoustic bubbles on lipid bilayers, 2Soft Matter. 11 (2015) 3460–3469. doi:10.1039/C5SM00427F.

[173] M.S. Tartis, D.E. Kruse, H. Zheng, H. Zhang, A. Kheirolomoom, J. Marik, K.W. Ferrara, Dynamic microPET imaging of ultrasound contrast agents and lipid delivery, J. Control. Release. 131 (2008) 160–166. doi:10.1016/j.jconrel.2008.07.030.

[174] J.J. Kwan, R. Myers, C.M. Coviello, S.M. Graham, A.R. Shah, E. Stride, R.C. Carlisle, C.C. Coussios, Ultrasound-Propelled Nanocups for Drug Delivery, Small. (2015) n/a-n/a. doi:10.1002/smll.201501322.

[175] R. Myers, C. Coviello, P. Erbs, J. Foloppe, C. Rowe, J. Kwan, C. Crake, S. Finn, E. Jackson, J.-M. Balloul, C. Story, C. Coussios, R. Carlisle, Polymeric cups for cavitation mediated delivery of oncolytic vaccinia virus, Mol. Ther. (2016). doi:10.1038/mt.2016.139.

[176] J.J. Kwan, G. Lajoinie, N. de Jong, E. Stride, M. Versluis, C.C. Coussios, Ultrahigh-Speed Dynamics of Micrometer-Scale Inertial Cavitation from Nanoparticles, Phys. Rev. Appl. 6 (2016) 044004. doi:10.1103/PhysRevApplied.6.044004.

[177] J.L. Paris, C. Mannaris, M.V. Cabañas, R. Carlisle, M. Manzano, M. Vallet-Regí, C.C. Coussios, Ultrasound-Mediated Cavitation-Enhanced Extravasation of Mesoporous Silica Nanoparticles for Controlled-Release Drug Delivery, Chem. Eng. J. (2017).

doi:10.1016/j.cej.2017.12.051.

[178] I. Lentacker, S.C. De Smedt, J. Demeester, V. Van Marck, M. Bracke, N.N. Sanders, Lipoplex-loaded microbubbles for gene delivery: A trojan horse controlled by ultrasound, Adv. Funct. Mater. 17 (2007) 1910–1916. doi:10.1002/adfm.200700106.

[179] A. Kheirolomoom, P.A. Dayton, A.F.H. Lum, E. Little, E.E. Paoli, H. Zheng, K.W. Ferrara, Acoustically-active microbubbles conjugated to liposomes: Characterization of a proposed drug delivery vehicle, J. Control. Release. 118 (2007) 275–284. doi:10.1016/j.jconrel.2006.12.015.

[180] Y. Li, X. Zhang, W. Luo, D. Wang, L. Yang, J. Wang, L. Zhang, S. Zhang, S. Luo, Y. Wang, Dual-functionalized Nanoparticles Loaded Microbubbles for Enhancement of Drug Uptake, Ultrasonics. (2018). doi:10.1016/j.ultras.2018.02.003.

[181] I. Lentacker, S.C. De Smedt, N.N. Sanders, Drug loaded microbubble design for ultrasound triggered delivery, Soft Matter. 5 (2009) 2161. doi:10.1039/b823051j.

[182] H. Nesbitt, Y. Sheng, S. Kamila, K. Logan, K. Thomas, B. Callan, M.A. Taylor, M. Love, D. O'Rourke, P. Kelly, E. Beguin, E. Stride, A.P. McHale, J.F. Callan, Gemcitabine loaded microbubbles for targeted chemo-sonodynamic therapy of pancreatic cancer, J. Control. Release. 279 (2018) 8–16. doi:10.1016/j.jconrel.2018.04.018.

[183] M.A. Borden, M.R. Sarantos, S.M. Stieger, S.I. Simon, K.W. Ferrara, P.A. Dayton, Ultrasound radiation force modulates ligand availability on targeted contrast agents., Mol. Imaging Off. J. Soc. Mol. Imaging. 5 (2006) 139–147. doi:10.2310/7290.2006.00016.

[184] P. Dayton, A. Klibanov, G. Brandenburger, K. Ferrara, Acoustic radiation force in vivo: A mechanism to assist targeting of microbubbles, Ultrasound Med. Biol. 25 (1999) 1195–1201. doi:10.1016/S0301-5629(99)00062-9.

[185] J. Owen, Q. Pankhurst, E. Stride, Magnetic targeting and ultrasound mediated drug delivery: Benefits, limitations and combination, Int. J. Hyperth. 28 (2012) 362–373. doi:10.3109/02656736.2012.668639.

[186] F. Yang, Z.X. Gu, X. Jin, H.Y. Wang, N. Gu, Magnetic microbubble: A biomedical platform co-constructed from magnetics and acoustics, Chinese Phys. B. 22 (2013). doi:10.1088/1674-1056/22/10/104301.

[187] F. Yang, L. Li, Y. Li, Z. Chen, J. Wu, N. Gu, Superparamagnetic nanoparticle-inclusion microbubbles for ultrasound contrast agents, Phys. Med. Biol. 53 (2008) 6129–6141. doi:10.1088/0031-9155/53/21/016.

[188] F. Yang, Y. Li, Z. Chen, Y. Zhang, J. Wu, N. Gu, Superparamagnetic iron oxide nanoparticle-embedded encapsulated microbubbles as dual contrast agents of magnetic resonance and ultrasound imaging, Biomaterials. 30 (2009) 3882–3890. doi:10.1016/j.biomaterials.2009.03.051.

[189] Z. Liu, T. Lammers, J. Ehling, S. Fokong, J. Bornemann, F. Kiessling, J. Gätjens, Iron oxide nanoparticle-containing microbubble composites as contrast agents for MR and ultrasound dual-modality imaging, Biomaterials. 32 (2011) 6155–6163. doi:10.1016/j.biomaterials.2011.05.019.

[190] F. Yang, M. Zhang, W. He, P. Chen, X. Cai, L. Yang, N. Gu, J. Wu, Controlled release of Fe3O4 nanoparticles in encapsulated microbubbles to tumor cells via sonoporation and associated cellular bioeffects, Small. 7 (2011) 902–910. doi:10.1002/smll.201002185.

[191] T.B. Brismar, D. Grishenkov, B. Gustafsson, J. Härmark, Å. Barrefelt, S.V.V.N. Kothapalli, S. Margheritelli, L. Oddo, K. Caidahl, H. Hebert, G. Paradossi, Magnetite nanoparticles can be coupled to microbubbles to support multimodal imaging, Biomacromolecules. 13 (2012) 1390–1399. doi:10.1021/bm300099f.

[192] S. Gun, M. Edirisinghe, E. Stride, Encapsulation of superparamagnetic iron oxide nanoparticles in poly-(lactide-co-glycolic acid) microspheres for biomedical applications, Mater. Sci. Eng. C. 33 (2013) 3129–3137. doi:10.1016/j.msec.2013.03.001.

[193] M. Poehlmann, D. Grishenkov, S.V.V.N. Kothapalli, J. Härmark, H. Hebert, A. Philipp, R.

Hoeller, M. Seuss, C. Kuttner, S. Margheritelli, G. Paradossi, A. Fery, On the interplay of shell structure with low- and high-frequency mechanics of multifunctional magnetic microbubbles, Soft Matter. 10 (2014) 214–26. doi:10.1039/c3sm51560e.

[194] W. Song, Y. Luo, Y. Zhao, X. Liu, J. Zhao, J. Luo, Q. Zhang, H. Ran, Z. Wang, D. Guo, Magnetic nanobubbles with potential for targeted drug delivery and trimodal imaging in breast cancer: an in vitro study, Nanomedicine. (2017).

[195] W. He, F. Yang, Y. Wu, S. Wen, P. Chen, Y. Zhang, N. Gu, Microbubbles with surface coated by superparamagnetic iron oxide nanoparticles, Mater. Lett. 68 (2012) 64–67. doi:10.1016/j.matlet.2011.10.013.

[196] C. Sciallero, A. Trucco, Ultrasound assessment of polymer-shelled magnetic microbubbles used as dual contrast agents, J. Acoust. Soc. Am. 133 (2013). doi:10.1121/1.4804942.

[197] L. Duan, F. Yang, L. Song, K. Fang, J. Tian, Y. Liang, M. Li, N. Xu, Z. Chen, Y. Zhang, N. Gu, Controlled assembly of magnetic nanoparticles on microbubbles for multimodal imaging, Soft Matter. 11 (2015) 5492–5500. doi:10.1039/C5SM00864F.

[198] M. Ahmed, B. Cerroni, A. Razuvaev, J. Härmark, G. Paradossi, K. Caidahl, B. Gustafsson, Cellular Uptake of Plain and SPION-Modified Microbubbles for Potential Use in Molecular Imaging, Cell. Mol. Bioeng. (2017) 1–12. doi:10.1007/s12195-017-0504-9.

[199] E. Stride, C. Porter, A.G. Prieto, Q. Pankhurst, Enhancement of Microbubble Mediated Gene Delivery by Simultaneous Exposure to Ultrasonic and Magnetic Fields, Ultrasound Med. Biol. 35 (2009) 861–868. doi:10.1016/j.ultrasmedbio.2008.11.010.

[200] H. Mulvana, R.J. Eckersley, R. Browning, J. V Hajnal, E. Stride, T. Barrack, M. Tang, Q. Pankhurst, D. Wells, Enhanced gene transfection in vivo using magnetic localisation of ultrasound contrast agents: Preliminary results, 2010 IEEE Int. Ultrason. Symp. Proc. (2010) 670–673. doi:10.1109/ULTSYM.2010.5935952.

[201] M. de Saint Victor, D. Carugo, L.C. Barnsley, J. Owen, C.-C. Coussios, E. Stride, Magnetic targeting to enhance microbubble delivery in an occluded microarterial bifurcation, Phys. Med. Biol. (2017). doi:10.1016/j.colsurfa.2007.04.052.

[202] D. Vlaskou, O. Mykhaylyk, F. Krötz, N. Hellwig, R. Renner, U. Schillinger, B. Gleich, A. Heidsieck, G. Schmitz, K. Hensel, C. Plank, Magnetic and acoustically active lipospheres for magnetically targeted nucleic acid delivery, Adv. Funct. Mater. 20 (2010) 3881–3894. doi:10.1002/adfm.200902388.

[203] D. Vlaskou, P. Pradhan, C. Bergemann, A.L. Klibanov, K. Hensel, G. Schmitz, C. Plank, O. Mykhaylyk, Magnetic microbubbles: Magnetically targeted and ultrasound-triggered vectors for gene delivery in vitro, AIP Conf. Proc. 1311 (2010) 485–494. doi:10.1063/1.3530059.

[204] H. Mannell, J. Pircher, F. Fochler, Y. Stampnik, T. Räthel, B. Gleich, C. Plank, O. Mykhaylyk, C. Dahmani, M. Wörnle, A. Ribeiro, U. Pohl, F. Krötz, Site directed vascular gene delivery in vivo by ultrasonic destruction of magnetic nanoparticle coated microbubbles, Nanomedicine Nanotechnology, Biol. Med. 8 (2012) 1309–1318. doi:10.1016/j.nano.2012.03.007.

[205] H. Mannell, J. Pircher, T. Räthel, K. Schilberg, K. Zimmermann, A. Pfeifer, O. Mykhaylyk, B. Gleich, U. Pohl, F. Krötz, Targeted endothelial gene delivery by ultrasonic destruction of magnetic microbubbles carrying lentiviral vectors, Pharm. Res. 29 (2012) 1282–1294. doi:10.1007/s11095-012-0678-8.

[206] Y. Heun, S. Hildebrand, A. Heidsieck, B. Gleich, M. Anton, A. Ribeiro, O. Mykhaylyk, D. Eberbeck, D. Wenzel, A. Pfeifer, Targeting of Magnetic Nanoparticle-coated Microbubbles to the Vascular Wall Empowers Site-specific Lentiviral Gene Delivery in vivo, Theranostics. 7 (2017). doi:10.7150/thno.16192.

[207] T. Räthel, H. Mannell, J. Pircher, B. Gleich, U. Pohl, F. Krötz, Magnetic stents retain nanoparticle-bound antirestenotic drugs transported by lipid microbubbles, Pharm. Res. 29 (2012) 1295–1307. doi:10.1007/s11095-011-0643-y.

[208] J.D. Dove, T.W. Murray, M.A. Borden, Enhanced photoacoustic response with plasmonic nanoparticle-templated microbubbles, Soft Matter. 9 (2013) 7743. doi:10.1039/c3sm51690c.

[209] J.D. Dove, M. a Borden, T.W. Murray, Optically induced resonance of nanoparticle-loaded microbubbles, Opt. Lett. 39 (2014) 3732–5. doi:10.1364/OL.39.003732.

[210] B. Chertok, R. Langer, Circulating Magnetic Microbubbles for Localized Real-Time Control of Drug Delivery by Ultrasonography-Guided Magnetic Targeting and Ultrasound, Theranostics. 8 (2018) 341–357. doi:10.7150/thno.20781.

[211] K. Soetanto, H. Watarai, Development of magnetic microbubbles for drug delivery system (DDS), Jpn. J. Appl. Phys. 39 (2000) 3230–3232. doi:10.1143/JJAP.39.3230.

[212] X. Zhao, P.A. Quinto-Su, C.D. Ohl, Dynamics of magnetic bubbles in acoustic and magnetic fields, Phys. Rev. Lett. 102 (2009). doi:10.1103/PhysRevLett.102.024501.

[213] A. Kovalenko, J. Jouhannaud, P. Polavarapu, M.P. Krafft, G. Waton, G. Pourroy, Hollow magnetic microspheres obtained by nanoparticle adsorption on surfactant stabilized microbubbles, Soft Matter. 10 (2014) 5147–5156. doi:10.1039/c4sm00318g.

[214] A. Kovalenko, J. Jouhannaud, P. Polavarapu, M.P. Krafft, G. Waton, G. Pourroy, Incorporation of negatively charged iron oxide nanoparticles in the shell of anionic surfactant-stabilized microbubbles: The effect of NaCl concentration, J. Colloid Interface Sci. 472 (2016) 180–186. doi:10.1016/j.jcis.2016.02.016.

[215] Y. Gao, C.U. Chan, Q. Gu, X. Lin, W. Zhang, D.C.L. Yeo, A.M. Alsema, M. Arora, M.S.K. Chong, P. Shi, C.-D. Ohl, C. Xu, Controlled nanoparticle release from stable magnetic microbubble oscillations, NPG Asia Mater. 8 (2016) e260. doi:10.1038/am.2016.37.

[216] N. Nomikou, C. Fowley, N.M. Byrne, B. McCaughan, A.P. McHale, J.F. Callan, Microbubble-sonosensitiser conjugates as therapeutics in sonodynamic therapy., Chem. Commun. (Camb). 48 (2012) 8332–4. doi:10.1039/c2cc33913g.

[217] H. Wang, P. Wang, L. Li, K. Zhang, X. Wang, Q. Liu, Microbubbles Enhance the Antitumor Effects of Sino- porphyrin Sodium Mediated Sonodynamic Therapy both In Vitro and In Vivo, Int. J. Biol. Sci. 11 (2015) 1401–1409. doi:10.7150/ijbs.12802.

[218] A.K.W. Wood, C.M. Sehgal, A review of low-intensity ultrasound for cancer therapy, Ultrasound Med. Biol. 41 (2015) 905–928. doi:10.1016/j.ultrasmedbio.2014.11.019.

[219] M.M. Asuncion Valenzuela, J.W. Neidigh, N.R. Wall, Antimetabolite Treatment for Pancreatic Cancer, Chemother. (Los Angel). 03 (2014). doi:10.4172/2167-7700.1000137.

[220] C. Mcewan, S. Kamila, J. Owen, H. Nesbitt, B. Callan, M. Borden, N. Nomikou, R.A. Hamoudi, M.A. Taylor, E. Stride, A.P. Mchale, J.F. Callan, Combined Sonodynamic and Antimetabolite Therapy for the Improved Treatment of Pancreatic Cancer using Oxygen Loaded Microbubbles as a Delivery Vehicle, Biomaterials. 80 (2016) 20–32. doi:10.1016/j.biomaterials.2015.11.033.

[221] H.A. Burris, M.J. Moore, J. Andersen, M.R. Green, M.L. Rothenberg, M.R. Modiano, M.C. Cripps, R.K. Portenoy, A.M. Storniolo, P. Tarassoff, R. Nelson, F.A. Dorr, C.D. Stephens, D.D. Von Hoff, Improvements in survival and clinical benefit with gemcitabine as first-line therapy for patients with advanced pancreas cancer: a randomized trial., J. Clin. Oncol. 15 (1997) 2403–2413. doi:10.1126/science.1198443.

[222] S. Kotopoulis, G. Dimcevski, O. Helge Gilja, D. Hoem, M. Postema, Treatment of human pancreatic cancer using combined ultrasound, microbubbles, and gemcitabine: A clinical case study, Med. Phys. 40 (2013) 072902. doi:10.1118/1.4808149.

[223] G. Dimcevski, S. Kotopoulis, T. Bjånes, D. Hoem, J. Schjøt, B.T. Gjertsen, M. Biermann, A. Molven, H. Sorbye, E. McCormack, M. Postema, O.H. Gilja, A human clinical trial using ultrasound and microbubbles to enhance gemcitabine treatment of inoperable pancreatic cancer, J. Control. Release. (2016). doi:10.1016/j.jconrel.2016.10.007.

[224] J. Owen, S. Kamila, S. Shrivastava, D. Carugo, J. Bernadino de la Serna, C. Mannaris, V. Pereno, R. Browning, E. Beguin, A.P. McHale, J.F. Callan, E. Stride, The Role of PEG-40-

stearate in the production, morphology and stability of microbubbles, Langmuir. (2018). doi:10.1021/acs.langmuir.8b02516.

[225] E.C. Unger, T.P. McCreery, R.H. Sweitzer, V.E. Caldwell, Y. Wu, Acoustically active lipospheres containing paclitaxel: a new therapeutic ultrasound contrast agent, Invest. Radiol. 33 (1998) 886–92. https://ovidsp.tx.ovid.com/sp-3.31.1b/ovidweb.cgi?QS2=434f4e1a73d37e8ca2f1b1848b61e1eaf6a68641f78041e883202800f446d63fa54dbc67cb51126f237a3e8cb056f7438e181aa7b66e6cb55dd1a426b30ae5ae6da5d2b29e22b0bd14f5e6c0419b2f2456f7a2f333992cc90ba28a8a5f6af8ccc157e864e (accessed November 22, 2018).

[226] M.S. Tartis, J. McCallan, A.F.H. Lum, R. LaBell, S.M. Stieger, T.O. Matsunaga, K.W. Ferrara, Therapeutic effects of paclitaxel-containing ultrasound contrast agents, Ultrasound Med. Biol. 32 (2006) 1771–1780. doi:10.1016/j.ultrasmedbio.2006.03.017.

[227] C. Crake, J. Owen, S. Smart, C. Coviello, C.-C. Coussios, R. Carlisle, E. Stride, Enhancement and Passive Acoustic Mapping of Cavitation from Fluorescently Tagged Magnetic Resonance-Visible Magnetic Microbubbles In Vivo, Ultrasound Med. Biol. (2016) 1–15. doi:10.1016/j.ultrasmedbio.2016.08.002.

[228] J. Owen, C. Crake, J.Y. Lee, D. Carugo, E. Beguin, A.A. Khrapitchev, R.J. Browning, N. Sibson, E. Stride, A versatile method for the preparation of particle-loaded microbubbles for multimodality imaging and targeted drug delivery, Drug Deliv. Transl. Res. (2017). doi:10.5287/bodleian.

[229] FDA, Feraheme (ferumoxytol) Injection Label, (n.d.). https://www.accessdata.fda.gov/drugsatfda_docs/label/2009/022180lbl.pdf (accessed May 9, 2018).

[230] FDA, DEFINITY Injection Label, (2001) 1–18.

[231] I. European Medicines Agency, Sonovue - Annex I Summary of Product Characteristics, 2007. http://www.ema.europa.eu/docs/en_GB/document_library/EPAR_-_Product_Information/human/000303/WC500055380.pdf.

[232] M.A. Borden, G. Pu, G.J. Runner, M.L. Longo, Surface phase behavior and microstructure of lipid/PEG-emulsifier monolayer-coated microbubbles, Colloids Surfaces B Biointerfaces. 35 (2004) 209–223. doi:10.1016/j.colsurfb.2004.03.007.

[233] C. a. Sennoga, V. Mahue, J. Loughran, J. Casey, J.M. Seddon, M. Tang, R.J. Eckersley, On sizing and counting of microbubbles using optical microscopy, Ultrasound Med. Biol. 36 (2010) 2093–2096. doi:10.1016/j.ultrasmedbio.2010.09.004.

[234] S.J. Satinover, J.D. Dove, M. a. Borden, Single-particle optical sizing of microbubbles, Ultrasound Med. Biol. 40 (2014) 138–147. doi:10.1016/j.ultrasmedbio.2013.08.018.

[235] H. Mulvana, R.J. Browning, Y. Luan, N. De Jong, M.X. Tang, R.J. Eckersley, E. Stride, Characterization of contrast agent microbubbles for ultrasound imaging and therapy research, IEEE Trans. Ultrason. Ferroelectr. Freq. Control. 64 (2017) 232–251. doi:10.1109/TUFFC.2016.2613991.

[236] C.A. Sennoga, J.S.M. Yeh, J. Alter, E. Stride, P. Nihoyannopoulos, J.M. Seddon, D.O. Haskard, J. V. Hajnal, M.X. Tang, R.J. Eckersley, Evaluation of Methods for Sizing and Counting of Ultrasound Contrast Agents, Ultrasound Med. Biol. 38 (2012) 834–845. doi:10.1016/j.ultrasmedbio.2012.01.012.

[237] M.P. Savage, D.L. Fischman, R. Rake, M.B. Leon, R.A. Schatz, I. Penn, M. Nobuyoshi, J. Moses, J. Hirshfeld, R. Heuser, D. Baim, M. Cleman, J. Brinker, S. Gebhardt, S. Goldberg, Efficacy of Coronary Stenting Versus Balloon Angioplasty in Small Coronary Arteries, J. Am. Coll. Cardiol. 31 (1998) 307–311. doi:10.1016/s0735-1097(97)00511-1.

[238] K.A. Myers, D. Jolley, A. Clough, J. Kirwan, Outcome of Ultrasound-guided Sclerotherapy for Varicose Veins: Medium-term Results Assessed by Ultrasound Surveillance, Eur. J. Vasc. Endovasc. Surg. 33 (2007) 116–121. doi:10.1016/j.ejvs.2006.09.005.

[239] R. Greger, U. Windhorst, Peripheral Circulation: Fundamental Concepts, Comparative

Aspects of the Control in Specific Vascular Sections, and Lymph Flow, in: Compr. Hum. Physiol., 1996: pp. 1865–1873.

[240] M. Klarhöfer, B. Csapo, C. Balassy, J.C. Szeles, E. Moser, High-resolution blood flow velocity measurements in the human finger, Magn. Reson. Med. 45 (2001) 716–719. doi:10.1002/mrm.1096.

[241] E.M. Renkin, C. Crone, Microcirculation and Capillary Exchange, in: Compr. Hum. Physiol., 1996: pp. 1965–1979. doi:10.1007/978-3-642-60946-6_98.

[242] S. Garg, A.A. Thomas, M.A. Borden, The effect of lipid monolayer in-plane rigidity on in vivo microbubble circulation persistance, Biomaterials. 34 (2013) 6862–6870. doi:10.1097/MPG.0b013e3181a15ae8.Screening.

[243] S. Kilic, Quantification of PEG40S squeeze out from DSPC/PEG40S monolayers at higher molar ratios, Colloids Surfaces A. 551 (2018) 58–64. doi:10.1016/j.colsurfa.2018.05.001.

[244] G. Pu, M.A. Borden, M.L. Longo, Collapse and shedding transitions in binary lipid monolayers coating microbubbles, Langmuir. 22 (2006) 2993–2999. doi:10.1021/la0530337.

[245] A. Gopal, K.Y.C. Lee, Morphology and collapse transitions in binary phospholipid monolayers, J. Phys. Chem. B. 105 (2001) 10348–10354. doi:10.1021/jp012532n.

[246] V. Tsoukanova, C. Salesse, Mixing Behavior of a Poly(ethylene glycol)-Grafted Phospholipid in Monolayers at the Air/Water Interface, Langmuir. 24 (2008) 13019–13029. doi:10.1021/la801868j.

[247] D. Carugo, J. Owen, C. Crake, J.Y. Lee, E. Stride, Biologically and acoustically compatible chamber for studying ultrasound-mediated delivery of therapeutic compounds, Ultrasound Med. Biol. 41 (2015) 1927–1937. doi:10.1016/j.ultrasmedbio.2015.03.020.

[248] M. Chong, P.C. Freeny, U.P. Schmiedl, Pancreatic Depiction Helical Arterial Anatomy : with, Radiology. 208 (1998) 537–542.

[249] I. Hirai, W. Kimura, M. Kamiga, M. Mizutani, A. Takeshita, T. Watanabe, A. Fuse, The significance of intraoperative Doppler ultrasonography in evaluating hepatic arterial flow when assessing the indications for the Appleby procedure for pancreatic body cancer, J. Hepatobiliary. Pancreat. Surg. 12 (2005) 55–60. doi:10.1007/s00534-004-0939-y.

[250] P. Vaupel, F. Kallinowski, P. Okunieff, Blood-flow, oxygen and nutrient supply, and metabolic microenvironment of human tumors : a review, Cancer Res. 49 (1989) 6449–6465.

[251] T.W. Secomb, Hemodynamics, Compr. Physiol. 6 (2017) 975–1003. doi:10.1002/cphy.c150038.Hemodynamics.

[252] N. McDannold, N. Vykhodtseva, K. Hynynen, Targeted disruption of the blood-brain barrier with focused ultrasound: Association with cavitation activity, Phys. Med. Biol. 51 (2006) 793–807. doi:10.1088/0031-9155/51/4/003.

[253] J.H. Hwang, J. Tu, A.A. Brayman, T.J. Matula, L.A. Crum, Correlation between inertial cavitation dose and endothelial cell damage in vivo, Ultrasound Med. Biol. 32 (2006) 1611–1619. doi:10.1016/j.ultrasmedbio.2006.07.016.

[254] Y. Qiu, Y. Luo, Y. Zhang, W. Cui, D. Zhang, J. Wu, J. Zhang, J. Tu, The correlation between acoustic cavitation and sonoporation involved in ultrasound-mediated DNA transfection with polyethylenimine (PEI) in vitro, J. Control. Release. 145 (2010) 40–48. doi:10.1016/j.jconrel.2010.04.010.

[255] J.J. Kwan, M.A. Borden, Lipid monolayer dilatational mechanics during microbubble gas exchange, Soft Matter. 8 (2012) 4756–4766. doi:10.1039/c2sm07437k.

[256] J. Owen, E. Stride, Technique for the Characterization of Phospholipid Microbubbles Coatings by Transmission Electron Microscopy, Ultrasound Med. Biol. 41 (2015) 3253–3258. doi:10.1016/j.ultrasmedbio.2015.07.024.

[257] R. Tietze, H. Unterweger, C. Alexiou, Magnetic nanoparticles for drug delivery, in: Handb. Nanobiomedical Res. Fundam. Appl. Recent Dev. (Vol. 1), 2014: pp. 595–620.

[258] C.-C. Huang, Z.-X. Liao, H.-M. Lu, W.-Y. Pan, W.-L. Wan, C.-C. Chen, H.-W. Sung, Cellular Organelle-Dependent Cytotoxicity of Iron Oxide Nanoparticles and Its Implications for Cancer Diagnosis and Treatment: A Mechanistic Investigation, Chem. Mater. (2016) acs.chemmater.6b03905. doi:10.1021/acs.chemmater.6b03905.

[259] U.S. Patil, S. Adireddy, A. Jaiswal, S. Mandava, B.R. Lee, D.B. Chrisey, In vitro/in vivo toxicity evaluation and quantification of iron oxide nanoparticles, 2015. doi:10.3390/ijms161024417.

[260] FDA, LUMASON / Sonovue Injection Label, n.d. https://www.accessdata.fda.gov/drugsatfda_docs/label/2016/203684s001lbl.pdf (accessed May 9, 2018).

[261] P.K. Hristov, L.A. Petrov, E.M. Russanov, Lipid peroxidation induced by ultrasonication in Ehrlich ascitic tumor cells, Cancer Lett. 121 (1997) 7–10. doi:10.1016/S0304-3835(97)00318-2.

[262] A. Vysniauskas, M. Qurashi, M.K. Kuimova, A Molecular Rotor that Measures Dynamic Changes of Lipid Bilayer Viscosity Caused by Oxidative Stress, Chem. - A Eur. J. 22 (2016) 13210–13217. doi:10.1002/chem.201601925.

[263] A. Lassenberger, A. Scheberl, A. Stadlbauer, A. Stiglbauer, T. Helbich, E. Reimhult, Individually stabilized, superparamagnetic nanoparticles with controlled shell and size leading to exceptional stealth properties and high relaxivities, ACS Appl. Mater. Interfaces. 9 (2017) 3343–3353. doi:10.1021/acsami.6b12932.

[264] M.A. Borden, S. Qin, K.W. Ferrara, Ultrasound contrast agents, in: Mol. Imaging Princ. Pract., 2010: pp. 425–444.

[265] J.K. Willmann, Z. Cheng, C. Davis, A.M. Lutz, M.L. Schipper, C.H. Nielsen, S.S. Gambhir, Targeted Microbubbles for Imaging Tumor Angiogenesis: Assessment of Whole-Body Biodistribution with Dynamic Micro-PET in Mice, Radiology. 249 (2008) 212–219. doi:10.1148/radiol.2491072050.

[266] Å. Barrefelt, M. Saghafian, R. Kuiper, F. Ye, G. Egri, M. Klickermann, T.B. Brismar, P. Aspelin, M. Muhammed, L. Dähne, M. Hassan, Biodistribution, kinetics, and biological fate of SPION microbubbles in the rat, Int. J. Nanomedicine. 8 (2013) 3241–3254. doi:10.2147/IJN.S49948.

[267] K. Yanagisawa, F. Moriyasu, T. Miyahara, M. Yuki, H. Iijima, Phagocytosis of ultrasound contrast agent microbubbles by Kupffer cells, Ultrasound Med. Biol. 33 (2007) 318–325. doi:10.1016/j.ultrasmedbio.2006.08.008.

[268] S. Palchetti, V. Colapicchioni, L. Digiacomo, G. Caracciolo, D. Pozzi, A.L. Capriotti, G. La Barbera, A. Laganà, The protein corona of circulating PEGylated liposomes, Biochim. Biophys. Acta - Biomembr. 1858 (2016) 189–196. doi:10.1016/j.bbamem.2015.11.012.

[269] J. Owen, P. Rademeyer, D. Chung, Q. Cheng, D. Holroyd, C. Coussios, P. Friend, Q.A. Pankhurst, E. Stride, Magnetic targeting of microbubbles against physiologically relevant flow conditions, Interface Focus. 5 (2015) 1–12.

[270] D.E.J.G.J. Dolmans, D. Fukumura, R.K. Jain, Photodynamic therapy for cancer, Semin. Cancer Biol. 3 (2003). doi:10.1016/j.semcancer.2003.11.001.

[271] L. Ludvíková, P. Friš, D. Heger, P. Šebej, J. Wirz, P. Klán, I.E. Kochevar, R.W. Redmond, M.C. DeRosa, R.J. Crutchley, D.C. Neckers, P. Murasecco-Suardi, E. Gassmann, A.M. Braun, E. Oliveros, E. Chesneau, D.C. Neckers, C.R. Lambert, I.E. Kochevar, H. Görner, V. Wintgens, J.C. Scaiano, S.M. Linden, D.C. Neckers, P.C.C. Lee, M.A.J. Rodgers, F. Vatansever, W. de Melo, P. Avci, D. Vecchio, M. Sadasivam, A. Gupta, R. Chandran, M. Karimi, N.A. Parizotto, R. Yin, G.P. Tegos, M.R. Hamblin, H.R. Shen, J.D. Spikes, C.J. Smith, J. Kopecek, A. Posadaz, A. Biasutti, C. Casale, J. Sanz, F. Amat-Guerri, N.A. Garcia, T.S. Johnson, A.C. O'Neill, P.M. Motarjem, C. Amann, T. Nguyen, M.A. Randolph, J.M. Winograd, I.E. Kochevar, R.W. Redmond, Y. Wang, I.E. Kochevar, R.W. Redmond, M. Yao, M. Yao, A. Yaroslavsky, F.P. Henry, R.W. Redmond, I.E. Kochevar, V. Kasche, L. Lindqvist, V. Kasche, L. Lindqvist, E.F.

Zwicker, L.I. Grossweiner, E. Klimtchuk, M.A.J. Rodgers, D.C. Neckers, D. Burget, J.P. Fouassier, S.D.M. Islam, O. Ito, A. Mills, C. Lawrence, P. Douglas, C.R. Lambert, I.E. Kochevar, X.F. Zhang, I. Zhang, L.H. Liu, C. Lambert, T. Sarna, T.G. Truscott, A. Penzkofer, M. Simmel, D. Riedl, T. Sarna, J. Zajac, M.K. Bowman, T.G. Truscott, F. Stracke, M. Heupel, E. Thiel, C.R. Lambert, I.E. Kochevar, R.W. Redmond, P. Bilski, R. Dabestani, C.F. Chignell, L.E. Cramer, K.G. Spears, G.R. Fleming, A.W.E. Knight, J.M. Morris, R.J.S. Morrison, G.W. Robinson, M.A. Rauf, J.P. Graham, S.B. Bukallah, M.A.S. Al-Saedi, O. Berndt, F. Bandt, I. Eichwurzel, H. Stiel, E. Slyusareva, A. Sizykh, A. Tyagi, A. Penzkofer, C.R. Lambert, H. Stiel, D. Leupold, M.C. Lynch, I.E. Kochevar, M. Gisin, J. Wirz, A. Seret, A. Vandevorst, J.M. Larkin, W.R. Donaldson, T.H. Foster, R.S. Knox, T. Shimidzu, T. Iyoda, Y. Koide, P. Zhang, M. Wang, J.F. Dong, X.Q. Li, F. Wang, L.Z. Wu, L.C. Sun, X.J. Zhang, Z.L. Jin, Y.X. Li, S.B. Li, G.X. Lu, Photochemistry of rose bengal in water and acetonitrile: a comprehensive kinetic analysis, Phys. Chem. Chem. Phys. 18 (2016) 16266–16273. doi:10.1039/C6CP01710J.

[272] L.A. MacManus-Spencer, B.L. Edhlund, K. McNeill, Singlet oxygen production in the reaction of superoxide with organic peroxides, J. Org. Chem. 71 (2006) 796–799. doi:10.1021/jo051736n.

[273] J.R. Kanofsky, H. Hoogland, R. Wever, S.J. Weiss, Singlet oxygen production by human eosinophils, J. Biol. Chem. 263 (1988) 9692–9696.

[274] W.H. Koppenol, Reactions involving singlet oxygen and the superoxide anion, Nature. 262 (1976). doi:10.1038/260170a0.

[275] K. Brieger, S. Schiavone, F.J. Miller, K.H. Krause, Reactive oxygen species: From health to disease, Swiss Med. Wkly. 142 (2012) 1–14. doi:10.4414/smw.2012.13659.

[276] S. Miyamoto, G.R. Martinez, M.H.G. Medeiros, P. Di Mascio, Singlet molecular oxygen generated by biological hydroperoxides, J. Photochem. Photobiol. B Biol. 139 (2014) 24–33. doi:10.1016/j.jphotobiol.2014.03.028.

[277] A. Gollmer, J. Arnbjerg, F.H. Blaikie, B.W. Pedersen, T. Breitenbach, K. Daasbjerg, M. Glasius, P.R. Ogilby, Singlet oxygen sensor green®: Photochemical behavior in solution and in a mammalian cell, Photochem. Photobiol. 87 (2011) 671–679. doi:10.1111/j.1751-1097.2011.00900.x.

[278] H. Lin, Y. Shen, D. Chen, L. Lin, B.C. Wilson, B. Li, S. Xie, Feasibility Study on quantitative measurements of singlet oxygen generation using singlet oxygen sensor green, J. Fluoresc. 23 (2013) 41–47. doi:10.1007/s10895-012-1114-5.

[279] M. Wozniak, F. Tanfani, E. Bertoli, G. Zolese, J. Antosiewicz, A new fluorescence method to detect singlet oxygen inside phospholipid model membranes, Biochim. Biophys. Acta (BBA)/Lipids Lipid Metab. 1082 (1991) 94–100. doi:10.1016/0005-2760(91)90304-Z.

[280] T. Ohyashiki, M. Nunomura, T. Katoh, Detection of superoxide anion radical in phospholipid liposomal membrane by fluorescence quenching method using 1,3-diphenylisobenzofuran, Biochim. Biophys. Acta - Biomembr. 1421 (1999) 131–139. doi:10.1016/S0005-2736(99)00119-4.

[281] W. Spiller, H. Kliesch, D. Wöhrle, S. Hackbarth, B. Röder, G. Schnurpfeil, Singlet Oxygen Quantum Yields of Different Photosensitizers in Polar Solvents and Micellar Solutions, J. Porphyrins Phthalocyanines. 02 (1998) 145–158. doi:10.1002/(SICI)1099-1409(199803/04)2:2<145::AID-JPP60>3.0.CO;2-2.

[282] A. Gomes, E. Fernandes, J.L.F.C. Lima, Fluorescence probes used for detection of reactive oxygen species, J. Biochem. Biophys. Methods. 65 (2005) 45–80. doi:10.1016/j.jbbm.2005.10.003.

[283] X.F. Zhang, X. Li, The photostability and fluorescence properties of diphenylisobenzofuran, J. Lumin. 131 (2011) 2263–2266. doi:10.1016/j.jlumin.2011.05.048.

[284] S. Leichnitz, J. Heinrich, N. Kulak, A Fluorescence Assay for the Detection of Hydrogen Peroxide and Hydroxyl Radical Production by Metallonucleases - Supporting Information, Chem. Commun. (2018).

[285] P.K. Choi, K. Fuayama, Multibubble sonoluminescence and Na atom emission in sodium dodecyl sulfate surfactant solutions, Japanese J. Appl. Physics, Part 1 Regul. Pap. Short Notes Rev. Pap. 46 (2007) 4768–4770. doi:10.1143/JJAP.46.4768.

[286] Y.T. Didenko, D.N. Nastich, S.P. Pugach, Y.A. Polovinka, V.I. Kvochka, The effect of bulk solution temperature on the intensity and spectra of water sonoluminescence, Ultrasonics. 32 (1994) 71–76. doi:10.1016/0041-624X(94)90083-3.

[287] C. Sehgal, R.G. Sutherland, R.E. Verrall, Optical spectra of sonoluminescence from transient and stable cavitation in water saturated with various gases, J. Phys. Chem. 84 (1980) 388–395. doi:10.1021/j100441a009.

[288] J. Escoffre, P. Campomanes, M. Tarek, A. Bouakaz, New insights in the role of reactive oxygen species in mechanisms of sonoporation: in-vitro validation and molecular dynamic simulations, in: IEEE Int. Ultrason. Symp. Proc., 2017.

[289] A.H. Barati, M. Mokhtari-Dizaji, H. Mozdarani, S.Z. Bathaei, Z.M. Hassan, Free hydroxyl radical dosimetry by using 1 MHz low level ultrasound waves, Iran. J. Radiat. Res. 3 (2006) 163–169.

[290] F. Lepoint-Mullie, N. Voglet, T. Lepoint, R. Avni, Evidence for the emission of “alkali-metal-noble-gas” van der Waals molecules from cavitation bubbles, Ultrason. Sonochem. 8 (2001) 151–158. doi:10.1016/S1350-4177(00)00030-4.

[291] D.L. Miller, N.B. Smith, M.R. Bailey, G.J. Czarnota, K. Hynynen, I.R.S. Makin, Overview of therapeutic ultrasound applications and safety considerations., J. Ultrasound Med. 31 (2012) 623–34. doi:10.1016/j.biotechadv.2011.08.021.Secreted.

[292] P. Ciuti, N.V. Dezhkunov, G. Iernetti, A.I. Kulak, Cavitation phenomena in pulse modulated ultrasound fields, Ultrasonics. 36 (1998) 569–574. doi:10.1016/S0041-624X(97)00114-5.

[293] K.R. Weninger, C.G. Camara, S.J. Putterman, Observation of bubble dynamics within luminescent cavitation clouds: Sonoluminescence at the nano-scale, Phys. Rev. E - Stat. Physics, Plasmas, Fluids, Relat. Interdiscip. Top. 63 (2001) 1–7. doi:10.1103/PhysRevE.63.016310.

[294] K. Hachimine, H. Shibaguchi, M. Kuroki, H. Yamada, T. Kinugasa, Y. Nakae, R. Asano, I. Sakata, Y. Yamashita, T. Shirakusa, M. Kuroki, Sonodynamic therapy of cancer using a novel porphyrin derivative, DCPH-P-Na(I), which is devoid of photosensitivity, Cancer Sci. 98 (2007) 916–920. doi:10.1111/j.1349-7006.2007.00468.x.

[295] K. Ninomiya, K. Noda, C. Ogino, S.I. Kuroda, N. Shimizu, Enhanced OH radical generation by dual-frequency ultrasound with TiO 2 nanoparticles: Its application to targeted sonodynamic therapy, Ultrason. Sonochem. 21 (2014) 289–294. doi:10.1016/j.ultsonch.2013.05.005.

[296] T. Osaki, I. Yokoe, Y. Uto, M. Ishizuka, T. Tanaka, N. Yamanaka, T. Kurahashi, K. Azuma, Y. Murahata, T. Tsuka, N. Ito, T. Imagawa, Y. Okamoto, Bleomycin enhances the efficacy of sonodynamic therapy using aluminum phthalocyanine disulfonate, Ultrason. Sonochem. 28 (2016) 161–168. doi:10.1016/j.ultsonch.2015.07.013.

[297] N. Sakusabe, K. Okada, K. Sato, S. Kamada, Y. Yoshida, T. Suzuki, Enhanced sonodynamic antitumor effect of ultrasound in the presence of nonsteroidal anti-inflammatory drugs, Japanese J. Cancer Res. 90 (1999) 1146–1151. doi:10.1111/j.1349-7006.1999.tb00689.x.

[298] H. Chen, J.H. Hwang, Ultrasound-targeted microbubble destruction for chemotherapeutic drug delivery to solid tumors, J. Ther. Ultrasound. 1 (2013) 1. doi:10.1186/2050-5736-1-10.

[299] M. Asano, M. Doi, K. Baba, M. Taniguchi, M. Shibano, S. Tanaka, M. Sakaguchi, M. Takaoka, M. Hirata, R. Yanagihara, R. Nakahara, Y. Hayashi, T. Yamaguchi, H. Matsumura, Y. Fujita, Bio-imaging of hydroxyl radicals in plant cells using the fluorescent molecular probe rhodamine B hydrazide, without any pretreatment, J. Biosci. Bioeng. 118 (2014) 98–100. doi:10.1016/j.jbiosc.2013.12.015.

[300] G. ter Haar, C. Coussios, High intensity focused ultrasound: Physical principles and devices, Int. J. Hyperth. 23 (2007) 89–104. doi:10.1080/02656730601186138.

[301] S. Sridhar, A. Patel, S. V. Dalvi, Estimation of Storage Stability of Aqueous Microbubble Suspensions, Colloids Surfaces A Physicochem. Eng. Asp. (2015). doi:10.1016/j.colsurfa.2015.10.044.

[302] W.T. Shi, F. Forsberg, P. Vaidyanathan, A. Tornes, J. Østensen, B.B. Goldberg, The influence of acoustic transmit parameters on the destruction of contrast microbubbles in vitro, Phys. Med. Biol. 51 (2006) 4031–4045. doi:10.1088/0031-9155/51/16/010.

[303] L.C. Barnsley, M.D. Gray, E. Beguin, D. Carugo, E. Stride, A Combined Magnetic-Acoustic Device for Simultaneous, Coaligned Application of Magnetic and Ultrasonic Fields, Adv. Mater. Technol. 3 (2018) 1800081. doi:10.1002/admt.201800081.

[304] Ely Lilly and Company, GEMZAR (gemcitabine for injection) - Highlights of prescribing information, 1996.

[305] J.F. Thompson, P. Hersey, E. Wachter, Chemoablation of metastatic melanoma using intralesional Rose Bengal, Melanoma Res. 18 (2008) 405–411. doi:10.1097/CMR.0b013e32831328c7.

[306] T.A. Read, A. Smith, J. Thomas, M. David, M. Foote, M. Wagels, A. Barbour, B.M. Smithers, Intralesional PV-10 for the treatment of in-transit melanoma metastases—Results of a prospective, non-randomized, single center study, J. Surg. Oncol. 117 (2018) 579–587. doi:10.1002/jso.24921.

[307] Y. Chevalier, M.-A. Bolzinger, Emulsions stabilized with solid nanoparticles: Pickering emulsions, Colloids Surfaces A Physicochem. Eng. Asp. 439 (2013) 23–34. doi:10.1016/j.colsurfa.2013.02.054.

[308] J. Narayanan, J.Y. Xiong, X.Y. Liu, Determination of agarose gel pore size: Absorbance measurements vis a vis other techniques, J. Phys. Conf. Ser. 28 (2006) 83–86. doi:10.1088/1742-6596/28/1/017.

[309] K. Buhnik-Rosenblau, S. Moshe-Belizowski, Y. Danin-Poleg, E.G. Meyron-Holtz, Genetic modification of iron metabolism in mice affects the gut microbiota, BioMetals. 25 (2012) 883–892. doi:10.1007/s10534-012-9555-5.

[310] N. Yumita, A. Okumura, R. Nishigaki, K. Umemura, S. Umemura, The combination treatment of ultrasound and antitumor drugs on Yoshida sarcoma.pdf, Jpn. J. Hyperthermic Oncol. 3 (1987) 175–182.

[311] A.H. Saad, G.M. Hahn, Ultrasound-enhanced effects of adriamycin against murine tumors, Ultrasound Med. Biol. 18 (1992) 715–723. doi:10.1016/0301-5629(92)90122-Q.

[312] P. Sur, P. Ghosh, S.P. Bag, B. Sur, S.N. Chatterjee, On the Inhibitory Activities of a New Boron Compound and Ultrasound against the Mouse Ascites Tumour, Chemotherapy. 45 (1999) 360–369.

[313] M.M. Mohamed, M.A. Mohamed, N.M. Fikry, Enhancement of antitumor effects of 5-fluorouracil combined with ultrasound on Ehrlich ascites tumor in vivo, Ultrasound Med. Biol. 29 (2003) 1635–1643. doi:10.1016/j.ultrasmedbio.2003.08.001.

[314] Z. Gao, J. Zheng, B. Yang, Z. Wang, H. Fan, Y. Lv, H. Li, L. Jia, W. Cao, Sonodynamic therapy inhibits angiogenesis and tumor growth in a xenograft mouse model, Cancer Lett. 335 (2013) 93–99. doi:10.1016/j.canlet.2013.02.006.

[315] S. Umemura, N. Yumita, R. Nishigaki, K. Umemura, Sonochemical activation of hematoporphyrin: a potential modality for cancer treatment, IEEE Int. Ultrason. Symp. Proc. (1989) 955–960.

[316] N. Yumita, R. Nishigaki, K. Umemura, S. -i Umemura, Synergistic Effect of Ultrasound and Hematoporphyrin on Sarcoma 180, Japanese J. Cancer Res. 81 (1990) 304–308. doi:10.1111/j.1349-7006.1990.tb02565.x.

[317] Q. Liu, S. Sun, Y. Xiao, H. Qi, Z. Shang, J. Zhang, J. Zhang, Y. Ren, M. Li, Q. Li, Study of cell killing and morphology on S180 by ultrasound activating hematoporphyrin derivatives., Sci. China. C. Life Sci. 46 (2003) 253–62. doi:10.1360/03yc9027.

[318] D. Song, Z. Li, J. Zhao, N. Zhang, W. Yue, J. Li, Study of the mechanism of sonodynamic

therapy in a rat glioma model, Onco. Targets. Ther. 7 (2014) 1801–1810. doi:10.2147/OTT.S52426.

[319] P. Huang, X. Qian, Y. Chen, L. Yu, H. Lin, L. Wang, Y. Zhu, J. Shi, Metalloporphyrin-encapsulated Biodegradable Nanosystems for Highly Efficient MRI-Guided Sonodynamic Cancer Therapy, J. Am. Chem. Soc. (2016) jacs.6b11846. doi:10.1021/jacs.6b11846.

[320] Z. Pi, Y. Huang, Y. Shen, X. Zeng, Y. Hu, T. Chen, C. Li, H. Yu, S. Chen, X. Chen, Sonodynamic Therapy on Intracranial Glioblastoma Xenografts Using Sinoporphyrin Sodium Delivered by Ultrasound with Microbubbles, Ann. Biomed. Eng. (2018). doi:10.1007/s10439-018-02141-9.

[321] N. Yumita, N. Okuyama, K. Sasaki, S.I. Umemura, Sonodynamic therapy on chemically induced mammary tumor: Pharmacokinetics, tissue distribution and sonodynamically induced antitumor effect of porfimer sodium, Cancer Sci. 95 (2007) 765–769. doi:10.1111/j.1349-7006.2004.tb03259.x.

[322] N. Yumita, K. Sasaki, S. Umemura, R. Nishigaki, Sonodynamically Induced Antitumor Effect of a Gallium-Porphyrin Complex, ATX-70, Jpn. J. Cancer Res. 87 (1996) 310–316.

[323] N. Yumita, K. Sasaki, S. Umemura, A. Yukawa, R. Nishigaki, Sonodynamically induced antitumor effect of gallium-porphyrin complex by focused ultrasound on experimental kidney tumor, Cancer Lett. 112 (1997) 79–86.

[324] K. Sasaki, N. Yumita, R. Nishigaki, S.I. Umemura, Antitumor effect sonodynamically induced by focused ultrasound in combination with Ga-porphyrin complex, Japanese J. Cancer Res. 89 (1998) 452–456. doi:10.1111/j.1349-7006.1998.tb00584.x.

[325] N. Yumita, R. Nishigaki, S.I. Umemura, Sonodynamically induced antitumor effect of Photofrin II on colon 26 carcinoma, J. Cancer Res. Clin. Oncol. 126 (2000) 601–606. doi:10.1007/PL00008471.

[326] N. Yumita, S. Umemura, Sonodynamic therapy with photofrin II on AH130 solid tumor. Pharmacokinetics, tissue distribution and sonodynamic antitumoral efficacy of photofrin II., Cancer Chemother. Pharmacol. 51 (2003) 174–8. doi:10.1007/s00280-002-0523-6.

[327] A.H. Barati, M. Mokhtari-Dizaji, Ultrasound dose fractionation in sonodynamic therapy, Ultrasound Med. Biol. 36 (2010) 880–887. doi:10.1016/j.ultrasmedbio.2010.03.010.

[328] X. Chen, B. Qin, D. Whitehurst, B. Helfield, L. Lavery, F.S. Villanueva, Sonodynamic therapy using protoporphyrin IX encapsulated microbubbles inhibits tumor growth, IEEE. (2017).

[329] N. Yumita, S. Umemura, Sonodynamic antitumour effect of chloroaluminum phthalocyanine tetrasulfonate on murine solid tumour, J. Pharm. Pharmacol. 56 (2004) 85–90. doi:10.1211/0022357022412.

[330] K. Arakawa, K. Hagisawa, H. Kusano, S. Yoneyama, A. Kurita, T. Arai, M. Kikuchi, I. Sakata, S.I. Umenura, F. Ohsuzu, Sonodynamic therapy decreased neointimal hyperplasia after stenting in the rabbit iliac artery, Circulation. 105 (2002) 149–151. doi:10.1161/hc0202.102921.

[331] N. Nomikou, C. Sterrett, C. Arthur, B. Mccaughan, J.F. Callan, A.P. Mchale, The Effects of Ultrasound and Light on Indocyanine-Green-Treated Tumour Cells and Tissues, ChemMedChem. 7 (2012) 1465–1471. doi:10.1002/cmdc.201200233.

[332] C.H. Tung, M.S. Han, Y. Kim, J. Qi, B.E. O'Neill, Tumor ablation using low-intensity ultrasound and sound excitable drug, J. Control. Release. 258 (2017) 67–72. doi:10.1016/j.jconrel.2017.05.009.

[333] X. Han, J. Huang, X. Jing, D. Yang, H. Lin, Z. Wang, P. Li, Y. Chen, Oxygen-Deficient Black Titania for Synergistic / Enhanced Sonodynamic and Photo-Induced Cancer Therapy at Near Infrared-II Biowindow, ACS Nano. (2018). doi:10.1021/acsnano.8b00899.

[334] K. Okada, E. Itoi, N. Miyakoshi, M. Nakajima, T. Suzuki, J. Nishida, Enhanced antitumor effect of ultrasound in the presence of piroxicam in a mouse air pouch model, Japanese J. Cancer Res. 93 (2002) 216–222. doi:10.1111/j.1349-7006.2002.tb01261.x.

[335] T. Osaki, M. Ono, Y. Uto, M. Ishizuka, T. Tanaka, N. Yamanaka, T. Kurahashi, K. Azuma, Y.

Murahata, T. Tsuka, N. Ito, T. Imagawa, Y. Okamoto, Sonodynamic therapy using 5-aminolevulinic acid enhances the efficacy of bleomycin, Ultrasonics. (2016) 1–9. doi:10.1016/j.ultras.2016.01.003.

[336] M. Liu, A.R. Khan, J. Ji, G. Lin, X. Zhao, G. Zhai, Crosslinked self-assembled nanoparticles for chemo-sonodynamic combination therapy favoring antitumor, antimetastasis management and immune responses, J. Control. Release. (2018). doi:10.1016/j.jconrel.2018.10.007.

[337] N. Nomikou, K. Curtis, C. McEwan, B.M.G. O'Hagan, B. Callan, J.F. Callan, A.P. McHale, A versatile, stimulus-responsive nanoparticle-based platform for use in both sonodynamic and photodynamic cancer therapy, Acta Biomater. (2016). doi:10.1016/j.actbio.2016.11.031.

[338] J. Wang, Y. Jiao, Y. Shao, Mesoporous Silica Nanoparticles for Dual-Mode Chemo-Sonodynamic Therapy by Low-Energy Ultrasound, Materials (Basel). 11 (2018) 2041. doi:10.3390/ma11102041.

[339] B. Du, X. Yan, X. Ding, Q. Wang, Q. Du, T. Xu, G. Shen, H. Yao, J. Zhou, Oxygen Self-production Red Blood Cell Carrier System for MRI Mediated Cancer Therapy: Ferryl-Hb, Sonodynamic and Chemical Therapy, ACS Biomater. Sci. Eng. (2018). doi:10.1021/acsbiomaterials.8b00497.